Spatio-temporal precipitation patterns: from teleconnections to improved long-term forecasts

Dissertation

zur Erlangung des akademischen Grades
Doktor der Naturwissenschaften
am Fachbereich Geowissenschaften
der Freien Universität Berlin

vorgelegt von

Diliara Willink

Berlin, 2019

1. Gutachter: Prof. Dr. Henning Rust, *Freie Universität Berlin*
2. Gutachter: Prof. Dr. Reik V. Donner, *Magdeburg-Stendal University of Applied Sciences*

Disputation: 14 Januar 2020

Weather proverbs

„Red sky at night, sailors' delight, red sky at morning, sailors take warning."

by folks. Old way of short-range storm predictions, works even now

„Wenn's um Neujahr Regen gibt, oft um Ostern Schnee noch stiebt."

Deutsche Bauernregeln für eine langfristige Regenvorhersage

„На Татьяну снег - к дождливому лету, а проглянет солнце -
к раннему прилету птиц."

Русская народная примета

List of Publications

Utkuzova (Willink) D., Khan V., Vilfand R. (2015). "Statistical analysis of extreme drought and wet events in Russia". In: *Atmospheric and Oceanic Optics* 28(4), pp. 336-346.

Utkuzova (Willink) D., Vilfand R., Khan V., Ganieva E. (2015). "Synoptical analysis of wet and drought extremes over the territory of Russian Federation". In: *Biosphere* 7(1), pp. 50-60.

Vilfand R., Martazinova V., Tsepelev V., Khan V., Mironicheva N., Eliseev G., Ivanova E., Tishchenko V., **Utkuzova (Willink) D.** (2017). "Integration of synoptic and hydrodynamic monthly air temperature forecasts". In: *Russian Meteorology and Hydrology* 42(8), pp. 485-493.

Willink D., Khan V., Donner R.V. (2017). "Improved one-month lead-time forecasting of the SPI over Russia with pressure covariates based on the SL-AV model". In: *Quartely Journal of the Royal Meteorological Society* 143(707), pp. 2636-2649.

Erklärung zu inhaltlichen Beiträgen der Co-Autoren an verschiedenen Publikationen innerhalb der Dissertation

This thesis is based on the publications, where I have been the first author.

Utkuzova (Willink) D., Khan V., Vilfand R. (2015). "Statistical analysis of extreme drought and wet events in Russia". In: Atmospheric and Oceanic Optics 28(4), pp. 336-346.

My contribution to this paper was in finding reliable data sources of observed rain gauge data, collecting and processing data, calculating the SPI index for whole Russia, as well as the idea of identifying the extreme events and provide the statistical analysis of previously identified cases. The question about the possibility of using the SPI index for this study came from Valentina Khan. At that time, WMO recommended to use the SPI index for all weather agencies in order to quantify and monitor dry and wet events. Together with the two co-authors, we also decided to test other drought and wet indices and provide a short description of them in the paper. Roman Vilfand helped with the discussion of the obtained results. The manuscript has been fully written by myself.

Utkuzova (Willink) D., Vilfand R., Khan V., Ganieva E. (2015). "Synoptical analysis of wet and drought extremes over the territory of Russian Federation". In: Biosphere 7(1), pp. 50-60.

This paper is the logical continuation of the previous one, in which the synoptical analysis of the previously identified extreme dry and wet events has been performed. The idea of this paper has been put forward by me, which also applies to the implementation and documentation. In addition, the way of creating and visualizing the “composite maps” (representing superposed fields of mean sea level pressure and SPI index) used in the synoptical analysis for the current paper has been developed by me as well.

Based on my experience as weather forecaster, the obtained extreme cases were synoptically analysed. With the help of Ekaterina Ganieva, I was able to associate certain types of weather processes (according to Katz' classification of atmospheric processes, cf. Katz 1960) with each previously identified extreme dry and wet event. Valentina Khan and Roman Vilfand helped with the logical presentation of the paper and text improvements.

Vilfand R., Martazinova V., Tsepelev V., Khan V., Mironicheva N., Eliseev G., Ivanova E., Tishchenko V., Utkuzova (Willink) D. (2017). "Integration of synoptic and hydrodynamic monthly air temperature forecasts". In: Russian Meteorology and Hydrology 42(8), pp. 485-493.

This paper is a collaborative paper of several authors, where I contributed in the data collection and provided some important calculations used further for air temperature forecasts. The results of this paper have not been included in my PhD thesis.

Willink D., Khan V., Donner R.V. (2017). "Improved one-month lead-time forecasting of the SPI over Russia with pressure covariates based on the SL-AV model". In: Quartely Journal of the Royal Meteorological Society 143(707), pp. 2636-2649.

The concept, implementation and documentation of this study have been exclusively performed by me. Hindcast data from the SL-AV model used for this work was obtained by the help of Valentina Khan, while all other data sets used have been open source. Reik Donner supported me with the discussions on full paper structure, suggestions for figures improvements and further important calculations. He also recommended including some teleconnection analysis and expanding the verification section by adding extra important verification metrics. He helped with the logical presentation of the paper and text construction according to the requirements of the journal.

Abstract

The standardized precipitation index (SPI) is an important yet easy-to-calculate means to describe wet or dry conditions in very different climates. In this work, a new scheme for obtaining improved forecasts of this index is developed. The methodology is tested over Russia and West Africa, proving that it can be successfully applied to different forecasting models and world regions. For testing, we use two forecasting models: the semi-implicit semi-Lagrangian vorticity-divergence (SL–AV) model of the Hydrometeorological Centre of Russia and the Institute of Numerical Mathematics of the Russian Academy of Sciences for Russia and the Climate Forecast System Version 2 (CFSv2) of the National Center for Environmental Prediction (NCEP) for West Africa. Based on hindcast simulations of both models, we demonstrate relatively poor skills in obtaining direct zero to three month lead-time SPI forecasts in the regions of interest during summer season. In order to improve the accuracy of these forecasts, we utilize surface temperature, mean sea level pressure and 500 hPa geopotential height fields, obtained from the outputs of both models. The spatial patterns of cross-correlations between previously obtained climatological fields and our target variable (SPI-1) are studied to identify informative co-variates, potentially affecting monthly-scale precipitation variability. The cross-correlation structures between the different fields reveal relevant interdependencies between SPI-1, sea surface temperature, mean sea level pressure and 500 hPa geopotential height in different regions. Subsequently, we employ two different regression models based on statistical post-processing of regional climate model output. In the first model, we consider all combinations of pairs of the previously identified predictors in a set of linear regression equations, which generates an ensemble of individual SPI-1 forecasts. The second model is based on a multiple linear regression approach comprising the dependency between all predictor variables and the predictand (SPI-1) in a single equation. The resulting SPI-1 forecasts obtained from both regression models are subsequently analysed in both deterministic and probabilistic ways and checked by various verification metrics. We identify that the first proposed model provides a significant improvement in the SPI forecasting, pointing to the potential for its implementation in operational monthly precipitation forecasts.

Abstract

Der Standardisierte Niederschlagsindex (SPI) ist ein wichtiges und leicht berechenbares Maß, um feuchte oder trockene Bedingungen in sehr unterschiedlichen Klimazonen zu beschreiben. Im Zuge dieser Arbeit wurde eine neue Methode zur verbesserten Vorhersage dieses Indexes entwickelt. Diese Methodik wurde für Russland und Westafrika getestet; es konnte gezeigt werden, dass sie für verschiedene Weltregionen und in Kombination mit verschiedenen Vorhersage-Modellen genutzt werden kann. Für den Test wurden zwei Vorhersage-Modelle genutzt: das semi-implizite semi-Lagrange'sche Vortizitäts-Divergenz-Modell (SL–AV) des Hydrometeorologischen Zentrums Russlands und des Instituts für Numerische Mathematik der Russischen Akademie der Wissenschaften für Russland sowie das Klima-Vorhersage-System 2 (CFSv2) des Nationalen Zentrums zur Umweltvorhersage der Vereinigten Staaten (NCEP) für Westafrika. Basierend auf Hindcast-Simulationen beider Modelle konnte bei einer direkten null- bis dreimonatigen SPI-Vorhersage während der Sommermonate nur eine jeweils relativ geringe Vorhersagequalität erzielt werden. Um die Genauigkeit dieser Vorhersagen zu verbessern, wurden die Meeresoberflächentemperatur, der durchschnittliche barometrische Druck auf Meereshöhe sowie die geopotentiellen Höhenfelder bei 500 hPa der jeweiligen Modelle genutzt. Die räumlichen Muster der Kreuzkorrelationen zwischen diesen klimatologischen Feldern und unserer Zielvariablen (SPI-1) wurden untersucht, um informative Kovariaten zu identifizieren, die möglicherweise die Niederschlagsvariabilität im monatlichen Maßstab beeinflussen. Die Kreuzkorrelationsstruktur zwischen den verschiedenen Feldern zeigte relevante Abhängigkeiten zwischen SPI-1, Meeresoberflächentemperatur, mittlerem barometrischem Druck auf Meereshöhe und geopotentielle Höhen von 500 hPa in verschiedenen Regionen. In Anschluss wurden zwei unterschiedliche Regressionsmodelle verwendet, die auf der statistischen Nachbearbeitung der regionalen Klimamodellausgabe basieren. Im ersten Modell wurden Kombinationen von Paaren der zuvor identifizierten Prädiktoren in einem Satz linearer Regressionsgleichungen betrachtet, die ein Ensemble einzelner SPI-1-Vorhersagen erzeugen. Das zweite Modell basierte auf einem Ansatz der multiplen linearen Regression, der die Abhängigkeit zwischen allen Prädiktorvariablen und dem Prädiktand (SPI-1) in einer einzigen Gleichung umfasste. Die resultierenden SPI-1-Vorhersagen, die aus beiden Regressionsmodellen erhalten wurden, wurden anschließend auf deterministische und probabilistische Weise analysiert und durch verschiedene Verifikationsmetriken überprüft.

Contents

Chapter 1

Introduction

In recent decades, global warming and the associated changes in climate variability have led to an increasing frequency and economic impact of hydro-meteorological hazards (Pachauri et al. 2014). The most recent Fifth Assessment Report (AR5) of the Intergovernmental Panel on Climate Change (IPCC) concluded that, global temperature has risen on average by 0.12°C per decade (IPCC 2013) since 1951. Other types of extreme deviations from the mean climatology such as the sustained absence of precipitation and excess evapotranspiration from soils and vegetation, can lead to severe droughts.
In general, hydro-meteorological extreme events, such as droughts or floods, can affect numerous sectors (Singh et al. 2014). In the context of future climate change, there are rising concerns that climatic extremes are likely to increase in frequency, severity and duration (Cook et al. 2007). Therefore, it is essential to investigate the dynamics of precipitation changes around the globe, and to predict their variations with sufficient lead-time. For this purpose, the improvement of long-term precipitation forecasts becomes increasingly essential.
In this thesis, an improved monthly-scale precipitation forecasting scheme using the Standardized Precipitation Index (SPI) is developed, starting at the initialization time and operating at different lead-times. Subsequently, this approach is applied to two regional case studies in Russia and West Africa and based on two numerical weather prediction models: the semi-Lagrangian vorticity divergence (SL-AV) operational model of the Hydrometeorological Center of Russia (Hydrometcenter) and the Institute of Numerical Mathematics of the Russian Academy of Sciences (Tolstykh et al. 2014, INM RAS; for the Russian case study), and the second generation Climate Forecasting System (CFSv2) operated by the National Center for Environmental Prediction (NCEP; for the West African case study).

1.1 Motivation

Precipitation is a main element of the hydrological cycle and water balance, playing a crucial role in the climate system. The formation of the precipitation regime is

controlled by a number of factors, such as the local physiographic conditions, atmospheric circulation patterns, and global and regional features of climate change. These factors, including their significant inhomogeneity in space and time, add complexity to the problems of monitoring and forecasting precipitation patterns. The long-term observations of precipitation in some regions in Russia and West Africa, reveal significant variations in the regimes of extreme dry and wet conditions (Dutra et al. 2013; Groisman et al. 2005). As it is important to understand the behaviour and variability of precipitation patterns, these issues have become of major significance to modern meteorology.

Recently, the problem of hydrodynamical long-range precipitation modelling has become critical. Current global and regional precipitation simulations provide evidence for the correct description of basic boundary-layer processes. For example, the comparison of simulated monthly and seasonal precipitation in the framework of the DEMETER, ENSEMBLES, and APCC projects, has demonstrated successful precipitation modelling over tropical regions (Parker 2017). However, the simulation of precipitation variability at the monthly-to-seasonal scale at extratropical latitudes does not give reliable results. For instance, in Russia, where complex combination of large-scale processes and local physiographic conditions are present, the accuracy of long-term precipitation forecasts commonly does not exceed 65%. In this case, to solve the problem of increasing the accuracy of such precipitation predictions, there are two possible solutions: the first is to improve the weather forecasting models (e.g., their physical description, data assimilation processes, forecasting speed, and boundary-layer description); the second is the implementation of statistical post-processing methods, applied immediately to the model outputs, which effectively improves the quality of the issued forecasts. These types of statistical schemes are built upon long-term interdependencies between predictors and forecasted values. Currently, developing and applying statistical post-processing methods to ensemble forecasts is the most promising direction in the forecasting practices of many weather services (Williams 2016). This thesis therefore proposes a new statistical post-processing method for reconstructing precipitation with a lead-time of 0-3 months. By implementing this methodology for Russia and West Africa which have complex weather conditions, the flexibility of the scheme is demonstrated. Since the interdependencies between precipitation and predictors can in fact be acquired for any region, the methodology may be applied to improve monthly precipitation forecasts for different lead-times, obtained from any weather forecasting model, for all regions, as well as for different predictors.

1.2 Aim

The aim of this study is to improve the accuracy of long-term precipitation forecasts with different lead-times, by developing implementing and testing a new postprocessing forecasting scheme. The new scheme uses spatial-temporal patterns of air pressure and surface temperature covariates, which are implemented into regression models for

obtaining deterministic and probabilistic forecasts in terms of the SPI.
In pursuing this general objective, three subjects are investigated:

- Since numerical weather prediction (NWP) models do not produce good precipitation estimates, are there further statistical methods to improve precipitation predictions?
- Can we construct statistical forecasting models for predicting precipitation based on large-scale predictors?
- Can the statistical forecasting models be implemented for any region and be constructed by various NWP models?

1.3 Structure of this thesis

The remainder of this thesis is organized as follows. Chapter 2 presents the climatological background, including the precipitation regimes in Russia and West Africa, as well as the teleconnection patterns influencing the precipitation formation in both regions. In Chapter 3, all statistical methods are presented including the SPI-1 calculation, spatial predictor selecting by means of correlation and cluster analysis. The proposed statistical post-processing based forecasting methods are described in Chapter 4. Chapters 5 and 6 discuss the utilisation of the corresponding regression models, the observed results and associated forecast verifications for Russia and West Africa, respectively. Finally, Chapter 7 summarizes the main strategy and findings, providing conclusions and an outlook to future work.

Chapter 2

Climatological background

Precipitation is one of the most important meteorological variables, since huge hazards can result from its deficit or surplus. Floods cause loss of life, property damage, and lasting environmental issues. Droughts may initially appear less destructive, but this is in fact not the case. The drying of rivers and forests can cause fires and death for humans, many animal and plant species, with a corresponding negative effect on biodiversity. Notably, agricultural losses due to both, flood and drought can leave millions of people without food. Furthermore they can cause large-scale problems for both population and governments, by increasing food prices and raising the necessity to import from foreign countries. Thus, it is important to study the precipitation regime, the reasons for its fluctuations, and to identify potential flood and drought landmarks.
The main problem of precipitation is its inhomogeneous distribution. This can be explained by the transfer of air masses, heat, and moisture controlled by radiation conditions, the distribution of land and ocean, the location of polar ice, dynamic processes (Coriolis force and friction) and air pressure fields. Terrain exerts considerable influence on the precipitation pattern; even a relatively flat underlying surface affects air masses in the zone of an atmospheric front, which in turns disturbs the course of atmospheric processes. The atmospheric front evolves, then passes from one underlying surface to another, e.g. when passing from land to sea, over the sea (or over big water reservoirs), the front gets saturated with moisture (Jacob 1999). Therefore, it is essential to take orography into account when producing weather forecasts. The spatial distribution and the overall climatic variability should also be considered when studying precipitation patterns.
This chapter introduces the precipitation regimes in Russia and West Africa, including an overview of weather processes causing different types of precipitation on both regions. Since precipitation is a very sensitive variable, it can be strongly influenced by long-term spatial and temporal fluctuations. Temperature changes in the Pacific Ocean can cause severe droughts or floods in many areas of the world. That is why, this chapter also contains a short description of the most prominent teleconnection indices, which affect precipitation fluctuations in both Russia and West Africa.

Figure 2.1: Physical Map of Russia [1]

2.1 Precipitation in Russia

The amount of precipitation that falls in Russia starts to increase in the spring from the subtropical to the mid latitudes and continues growing until autumn. This is influenced by the physical characteristics of the region (Fig. 2.1). In the lowlands, most precipitation is observed between 55° and 65°N. Precipitation in the Far East of Russia is characterized by regional differences (Matveev 1984); there, precipitation is largely caused by monsoon circulation and by extratropical cyclones (Arkhangelskiy 1956). The following spatial pattern of precipitation is observed in Russia: in the European part, the amount of precipitation is approximately 750 mm/year, originating from the Atlantic Ocean and moving inland. In Siberia the total annual precipitation is roughly 300-500 mm/year. However, the amount of precipitation in the Far East increases up to 1000 mm/year due to its close proximity of the Pacific Ocean (Khromov et al. 1994). Further towards the north or south, the monthly amount of precipitation decreases. Towards the north, the total year precipitation is only up to 100 mm, which is caused by low temperature and low humidity of air masses generated over cold seas. Similar behavior is observed in the more southern areas, where the amount of precipitation is slightly higher and varies around 300 mm/year. This can be explained by dry continental southern air, moving from the deserts in Central Asia and frequently generating weather conditions in the region (Kononova 2009).

[1] The figure is taken from: https://www.ezilon.com/maps/europe/russ and reproduced with the permission of the original publisher.

Figure 2.2: Map of Russia showing the two macroregions EPR (purple) and APR (yellow).

Since the nature of weather formation in different parts of Russia varies vastly, the whole country has been divided into two large macroregions for the purposes of this study - EPR, the European part of Russia (circa 42-69°N, 20-80°E; the natural border is the Ural Mountains), and APR, the Asian part of Russia (circa 42-69°N, 81-170°E; Fig. 2.2). These macroregions have a strong connection with natural synoptic regions (NSR), first introduced by Multanovsky (1933), which have all been incorporated into long-range weather forecasts. It is found, that NSRs present large areas with similar synoptic processes characterising the described region. Within NSR the thermobaric field in the troposphere stays relatively stable and, therefore, provides the possibility of creating a certain synoptic period with similar weather within the region. Multanovsky (1954) distinguished three NSRs in the Northern Hemisphere. The fist covers the area from Greenland to the Taymyr Peninsula, 0°- 80°E (including the EPR), the second from Taymyr to the Bering Strait, 81° - 170°E (including the APR) and the third from Bering Strait to Greenland. That is why, the weather conditions in EPR and APR are so different (Pagava et al. 1966).

2.1.1 European part of Russia (EPR)

In the EPR, comprising the area from the Black Sea coast and the Caucasus Mountains to the Ural Mountains, the total amount of precipitation from May to August varies from 75–100 mm/month and occasionally even more (Zverev 1977). In May, the sea-level pressure patterns present the displacement of the zones of global maxima and minima, within the isobars having northwest direction. During that time, east winds

prevail in the southern part of the EPR and isobars in the summer have the northwest direction (Zanina 1968).
Zonal circulation usually prevails in the EPR, so the region is permanently affected by atmospheric processes developing over the North Atlantic. A significant number of cyclones and anticyclones move through the Baltic Sea and the Gulf of Finland. This often causes dramatic weather differences between the areas situated to the north and south of 60°N. Another cyclonic trajectory commonly passes the Scandinavian Mountains. When crossing the mountains, cyclones can split into two separated perturbations. The leeward side of the mountains normally contains different weather conditions than the luv side, which can cause the transformation of the cyclone. These perturbations, in turn, form new cyclones, continuing to move further as independent formations. The inland Baltic and Black Seas are also affected by wind, air temperature, cloudiness, and precipitation in the coastal areas. In general, the intensity of cyclones over the EPR is higher in the warm season than in the cold season (Zverev 1977). The cyclones over EPR are divided into three types:

1. *Western cyclones* are active in this region in summer, are less-developed in comparison to those in other seasons, and mainly manifest in the form of low-activity cyclones and fronts.

2. *Southern cyclones* are characterized by high temperature contrasts and usually transport warmer humid air from the sea, which causes heavy precipitation. Such cyclones are typical for *meridional* circulation, which blocks west-to-east air propagation. In view of this, these cyclones are quasi-stationary until they are filled or supplemented with new warm air. According to their prevalent geographic trajectories, the Southern cyclones are further classified according to their association to the Mediterranean, Black, or Caspian Seas.

3. *Diving cyclones* are generated by meridional circulation patterns and have specific trajectories associated only with this type of cyclone. These cyclones move from north to south with high speed and are associated with cold intrusion; in some dramatic scenarios, the cold air masses reach the subtropics. In these cases, cold air is transported by such cyclones to the heated surface in the summer, pushing sharpening of atmospheric fronts and brings rapid changes in weather, e.g. heavy rainfall, strong winds, hailstorms, squalls, and thunderstorms.

The rapid movements of southern and diving cyclones result in the formation of significant temperature contrasts which intensify the atmospheric fronts and cause heavy precipitation. Usually, an anticyclone contributes to the formation of a precipitation deficit. Severe aridity can be caused by the meridional circulation patterns that arise when anticyclones are quasi-stationary. Examples of the negative effects of such blocking anticyclones include the droughts of 1972 or 2010, and many others (Coumou et al. 2014; Lupo et al. 2012; Mokhov et al. 2014; Shakina et al. 2010). The following classes of anticyclones characteristic for the EPR in the summer are based on the Matveev (1984), Zanina (1960), and Zverev (1977):

1. *Anticyclones moving from the west, north, and south*.
2. *Terminated anticyclones* formed after a series of cyclones. A high-pressure zone can form along with cold air mass in the northeast which is rapidly transformed into an independent zone of high pressure and then moves on to the southeast. Thus, the anticyclone becomes quasi-stationary in the southeast of EPR. At the same time, a cyclone is generated over the southeast of the Black Sea.
3. *Local anticyclones:*
   - Anticyclones in the eastern part of the Black Sea region;
   - Carpathian and Pannonian anticyclones;
   - Orographic anticyclogenesis over the North Caucasus formed due to the orographic slowdown of air mass transport by the Caucasus Mountains.

2.1.2 Asian part of Russia (APR)

The specific features of the terrain and the difference in thermal conditions between the land and oceans cause the formation of steady meridional tropospheric flows in this region. Thus, zonal flow in the troposphere is perturbed more significantly in comparison to other regions. The pressure field in the summer is mainly characterized by the extensive zone of high values of submeridional direction, spreading from north-east China to Yakutia and the Magadan region. There are two zones of low values on both sides of these regions: one stretches from the polar basin to the Bering Sea, and the other from the Taimyr Peninsula to Transbaikalia (Pagava et al. 1966). As noted by Arkhangelskiy (1956), the cyclones in the summer move slower over the continent than over the sea due to thermal conditions, though they gather speed near the coastline.

2.1.2.1 Ural and Western Siberia

The Ural Mountains divide Russia into two macroregions not only geographically, but also synoptically. Therefore, the weather-generating processes in these regions display unique properties. In view of this, the pressure centres move to the APR either from the EPR or from the east of the APR.
Apart from relatively high mountains causing weather changes in the region, the south of the region is affected by the Central Asian Low, causing minimum air pressure over Western Siberia and high precipitation amounts. However in the late summer, the Asian High starts being manifested. As a result, the amount of precipitation starts to decrease in this region, especially in Western Siberia, with 90 mm/month on average by the late autumn (Zverev 1977). Weather conditions in Western Siberia are affected by Atlantic processes and by Central Asia. The moisture is transported from the north, leading to an increasing amount of aridity towards the south. Thus in Western Siberia, precipitation is formed by moisture recycling (Berezhnykh et al. 2012).
The cyclones defining the weather in the region can be classified as:

1. *Western cyclones* move across the region from west to east.

2. *Southern cyclones* come to the region from the south or southwest, such as the Black, Caspian, and Aral Seas, but rarely from the Mediterranean Sea. The cyclones transport warm humid air to the colder and drier surfaces. This causes the sharpening of fronts and cyclogenesis. The most severe types of cyclones in this region originate from the South Caspian and Karakum. Southern cyclones move with great velocity towards the central areas of Western Siberia and transform into deep cyclones. In general, the southern Siberia is more influenced by cyclones which transport heavy precipitation to the region. Southern cyclones can also be generated within meridional circulation patterns.

3. *Diving cyclones* develop on the Arctic front and often come from the northwest or directly from the Northern seas. They are formed by meridional circulation patterns.

According to Zanina (1960) and Zverev (1977), anticyclones are similarly divided by their trajectories and types:

1. *moving from the west;*

2. *moving from the north and northwest;*

3. *moving along the ultrapolar axis from the Taimyr Peninsula or Yakutia;*

4. *blocking ridges.*

2.1.2.2 East Siberia, Transbaikalia, Far East

A considerable lack of precipitation is observed in these areas due to the great distance from the Atlantic Ocean, the complex terrain, and the presence of circulation features that impede the transport of humid air masses from the Pacific Ocean (Shakina et al. 2010). In the summer, heating of the continent induces temperature differences, that influence the cyclonic activity at the Arctic boundary. At the same time pressure gradients and cloud cover decrease in inland areas, increasing the radiative heating of the region (Mazin et al. 1989). Thus, only a small amount of precipitation such as 40–50 mm/month, is registered in the early summer. Thereafter the precipitation increases due to the increase in cloud cover.
The precipitation patterns are also inhomogeneous in the Far East. The continental part of the Far East is less moist than the marine areas (Zanina 1968). In Transbaikalia, the maximum summer precipitation is caused by the influence of the Mongolian cyclones. The warm sector in these cyclones is filled by the continental tropical air from Northern China. Therefore, the amount of precipitation in the region does not exceed 100–200 mm/month. The Mongolian cyclones coming to this region transport drier warm air from the heated continental Central Asia, and as a result, the amount of precipitation is small. Air masses transported with the marine tropical air are usually more humid.

Therefore, about 70% of summer precipitation falls in the presence of such conditions. Thus, the formation of abundant precipitation in the Far East takes place as a result of circulation processes and seasonal variability and these are due to the effects of continental and oceanic air masses (Shver 1976).
In the marine regions of the Far East, precipitation forms under the influence of cyclonic processes in the Pacific Ocean. These types of processes rarely move inland due to the mountainous topography, which normally prevents the development and westward movement of cyclones (Kiktev et al. 2015). For example, the 2 km elevation of the mountain range Sikhote-Alin, around the Primorsky and Khabarovsk regions, presents a natural obstacle to the free movement of anticyclonic ridges from the southwest. They therefore do not spread westward of the eastern slopes of the range or even go beyond the limits of the coastal zone.
In general, total precipitation in the Far East of Russia is greater in the summer than for the rest of the year. Localisation of the Far East ridge is a typical feature of large-scale processes formed over this region. The ridge influences the zonal transport of wind over Eastern Siberia and blocks in the Far East. Zonal processes in the summer are accompanied by the preservation of the Pacific subtropical high ridge in the area of Japan and the Far East upper - air trough. This supports the intensification of anticyclones and filling of cyclones after their movement from the land to the sea (Arkhangelskiy 1956; Zanina 1968). Cyclones in this area are divided into several groups:

1. *Northern cyclones* passing north of 65°N;
2. *Western cyclones* mainly passing between 50 and 65°N are most likely to penetrate Transbaikalia, Yakutia, and the Far East. Some cyclones of this type cause significant rainfall over the Amur and Ussuri rivers;
3. *Southern cyclones*:
    - intensive cyclones moving in from the Seas of Japan and Okhotsk. These occur when the upper-air trough spreads far to the south, up to 30–35°N;
    - cyclone tracking from the southwest over the Far Eastern seas.
4. *Local cyclones*:
    - orographic cyclogenesis in Southern Cisbaikalia causes cyclones to develop south of Lake Baikal due to the orographic regeneration in upper-air troughs, moving from the western part of the APR through Siberia toward the southeast. These cyclones progress when cold air masses cross over the Altai and Sayan Mountains;
    - cyclonic activity over the Amur River basin covers the eastern part of Transbaikalia, the northeastern provinces of China, the Amur region, the west of Khabarovsk and the Primorsky region. This is triggered when western cyclones move towards the Amur River basin. In some cases, these

lows move from the Amur River basin to the Sea of Okhotsk. Deep cyclones are rarely generated in the summer. The intrusion of cold air masses is required for the active development of cyclonic processes to occur over this region;

5. *Extratropical cyclones (mid-latitude cyclones)* initially originating from the tropics, is a very powerful type. In some cases, their power is so strong, that they continue moving towards the north and reach the mid-latitudes. Usually this occurs in July-September, when the differences in ocean surface temperature between tropics and extratropics are not so high. This type of cyclones are formed as a result of seasonal changes in the North Pacific and usually dissipate over land or colder oceans. Entering tropical cyclones in the mid-latitudes is usually dangerous and can have destructive consequences, including strong gusts of wind and heavy rainfalls.

According to Arkhangelskiy (1956), the summer anticyclones are divided into:

1. *Anticyclones with northern trajectories* follow sublatitudinal trajectories and move from west to east. In the second half of the summer they follow the submeridional directions and move from the northwest to the southeast;

2. *Anticyclogenesis in the area of the Sea of Okhotsk* in the period from April to September governs weather conditions for almost the entire Far East. The anticyclone is formed due to the stabilization of high-pressure centres originating from the north. Since this anticyclone transports cold air, it forms clouds, fog and drizzle even in high-pressure zones;

3. *Anticyclones moving from the Kolyma River basin* towards the south of the Sea of Okhotsk may further move to:

   - the north of the Sea of Japan;
   - the Kuril Islands;
   - the Pacific Ocean.

4. *quasi-stationary anticyclones* observed over the northeastern edge of Asia, the adjacent part of the Bering Sea, and the Eastern Sayan Mountains.

To sum up, the atmospheric circulation with active fronts plays a crucial role in precipitation formation over Russia. Modern climate researcher‘s pay little attention to the variability of planetary atmospheric circulation patterns, although its peculiarities strongly influence the variations in air pressure, air temperature, and precipitation in different regions. For example, Byshev et al. (2002) estimated the variability of atmospheric circulation using the classification for the Northern Hemisphere created by the Russian scientist B. L. Dzerdzeevskii. He came to the conclusion that the surface air

Figure 2.3: Physical map of West Africa.[2]

temperature in the Northern Hemisphere and even the whole globe, responds closely to variations in atmospheric circulation. In the periods of blocking processes (Palmén et al. 1969; Pelly 2001) the quantity and intensity of anticyclones increases, together with the frequency of extreme events (Petoukhov et al. 2013). Thus, to predict more accurately the regime of precipitation in different regions with different lead-times, spatial patterns and synoptic conditions, teleconnections and long-term dependencies must be taken into consideration.

2.2 Precipitation in West Africa

West Africa (WA) is a subregion of Africa containing 18 countries. It is normally considered to be confined to 0-20°N, and 20°W-25°E. In this study, the southern boundary is increased by 8°; thus, the area of interest falls within 8°S-20°N, 20°W-25°E (Fig. 2.3). Life in this region heavily relies on the water supplied by rainfall for agriculture (Rockström et al. 2010). Shower rainfalls have a critical impact in this region. Many areas have very low resilience and limited capabilities to mitigate the effects of drought. The annual rainfall normally has a north-to-south gradient of 1 mm/km, ranging from about 100 mm at 17°N, 800 mm at 10°N and 2000-3000 mm in some areas (Gulf of Guinea) south of 10°N (Lebel et al. 2003).
Notably, rainfall variability is modulated by oceanic (between 0°and 10°N) and continental (between 10°and 20°N) convergence, by variations in movements of the Intertropical Convergence Zone (ITCZ), and by land-atmosphere interactions, respectively (Polo et al. 2008). The ITCZ is formed by the convergence of the trade winds of the two hemispheres. This zone is characterized by low pressure, rising air motion, clouds and precipitation. From the viewpoint of the global atmosphere, the ITCZ forms the ascending branch of the Hadley cell (Nicholson 2009). The West African Monsoon

[2]The figure is taken from: https://eros.usgs.gov/westafrica/node/157

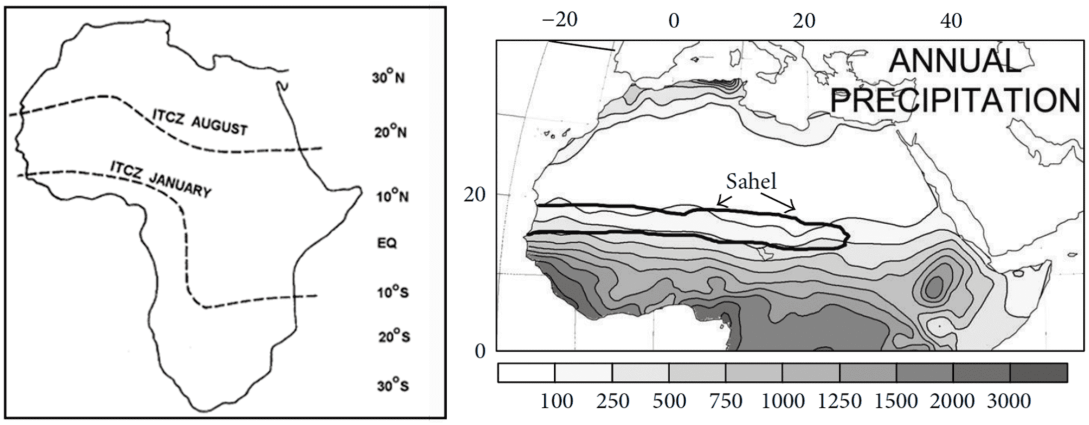

Figure 2.4: Left: map of the mean position of the ITCZ over Africa in January and August, taken from (Nicholson 2009). Right: mean annual precipitation over WA (rainfall in mm), with the location of the Sahel indicated (Nicholson 2013).

(WAM) is driven by sea-land contrasts of temperature and surface pressure between the Gulf of Guinea and the Sahara Desert. During the summer months, North African continental areas heat up more rapidly than oceanic waters (Fontaine et al. 1998). The ITCZ over Africa is conceptualized as a band of rainfall. This band advances into the Northern Hemisphere in the boreal summer and retreats into the Southern Hemisphere in winter (Fig. 2.4 a).

This phenomenon explains the latitudinal gradient of precipitation over WA as well as the seasonality of rainfall throughout the tropical regions of the continent. The ITCZ is pushed northward and provides humidity to Sahel via monsoon moisture (Gómara et al. 2017). The most important feature is that the ITCZ is effectively independent of the system that produces most of the rainfall (Nicholson 2009). Over WA, the ITCZ is distorted and moves northward from the coast of the Gulf of Guinea as the Sahara Desert becomes increasingly hotter during the lengthening days. The distortion is so strong that the Meteorological Equator (ME) separates the area of deep convection south of the Intertropical Front (ITF) and associated thunderstorms with strong showers. In the beginning of the monsoon season, convection occurs periodically over land and continues over the Gulf of Guinea. In June, the ME becomes confined to the land, north of 5°N, as the waters of the Gulf of Guinea cool down. By the beginning of August, the convection takes place over northern Africa (Galvin 2008).

The WAM has local features due orography. The monsoon flow reaches no further north than roughly 20°N, and deep convection is only occasionally seen north of 15°N. It should be mentioned that the monsoon flow and deep instability spread inland quickly. Initially, convection is scattered, but by late June, as a warm dome develops over North Africa, with easterly winds of about 3 km/hour, southwesterly winds at low levels bring more frequent rains to the northern parts of the region (Galvin 2008). There are notable variations in the northward extent of the deep humid zone. To the south of the ME, there is a moist flow crossing the equator. It picks up moisture as

it flows towards the south-facing coast of the Gulf of Guinea. The direction of the Coriolis force changes as the southeasterly flow crosses the equator, causing the flow to become southwesterly.
In the beginning of the summer, the increase in pressure gradients between the warm Gulf and northern Africa is relatively weak; the flow is unstable and intensive rains may appear over the sea as well as on the land. The wind strengthens, and the pressure gradients increase from south to north as the summer progresses. By the end of June, the flow across the Gulf is relatively cool, heat has been used for evaporation and cloud formation (Nicholson 1980). The cooling plays a crucial role in supplying moisture to the monsoon. Therefore, the moist monsoon flow is heated and diverges, bringing significant deep convection with thunderstorms and heavy showers above the land. Its large spatial scale means that stability can not be maintained as it passes inland.
Within the monsoon rain, moisture normally occurs south of the ME, from near the coast of the Gulf of Guinea to about 10°N (Fig. 2.4 b; Galvin 2008). This area is called the Sahel; it is identified by different authors in terms of vegetation and rainfall (Tanaka et al. 1975). In the dry areas of Sahelian countries, life revolves around the occurrence or non-occurrence of rainfall and its temporal and spatial distribution (Sivakumar 1992). Normally the region receives 200-600 mm/year. It is bordered to the north by sub-deserts (100-200 mm/year) and to the south by the Sudan vegetation zone (600-900 mm/year). In this region, the 400-500 mm isoheight has been generally accepted as a boundary range north of which only irrigated crops should be grown. Rainfall in this area occurs during a 4-5 month period from the beginning of June till the end of October, with the maximum rainfall occurring in August. The region is arid to semiarid, and in such climates the interannual precipitation variability is high (Glantz 1977). However, even in this area, droughts are expected as part of the climate regime (Dutra et al. 2013).
The northern part of WA is characterized by only one rainy season, with the highest values recorded in July and August, while the southern (Guinean Coast) has two rainy seasons per year, with the highest amount of precipitation falling in May/June and August/September (Siegmund et al. 2015). In the current study a period from June to September of 1982-2016 is considered. For June, two areas with the highest amount of monthly precipitation are identified. One covers the coastal areas south of Nigeria and the coastal west of Cameroon; it receives 320-340 mm/month (CAMS data set, Fig. 2.5). The second covers the coastal parts of Liberia and the Ivory Coast (C*ô*te d′Ivoire) with an average rainfall of 400-420 mm/month. In July (Fig. 2.5 b), the precipitation in Nigeria/Cameroon increases by 350-400 mm/month, and the second area moves towards the western coast of Sierra Leone, Guinea and Guinea-Bissau, with the rainfall reaching up to 300-450 mm/month (the majority falling in Sierra Leone). Actually, this area of high precipitation is fixed from June till September. August (Fig. 2.5 c) is the most humid month in WA. The intensity of precipitation greatly increases in both areas, thus the rainfall in Nigeria and West Cameroon is 400-550 mm/month, and 500-700 mm/month are normally observed in Sierra Leone, Guinea and Guinea-Bissau. In September (Fig. 2.5 d), when the ITCZ begins to move southward, the precipi-

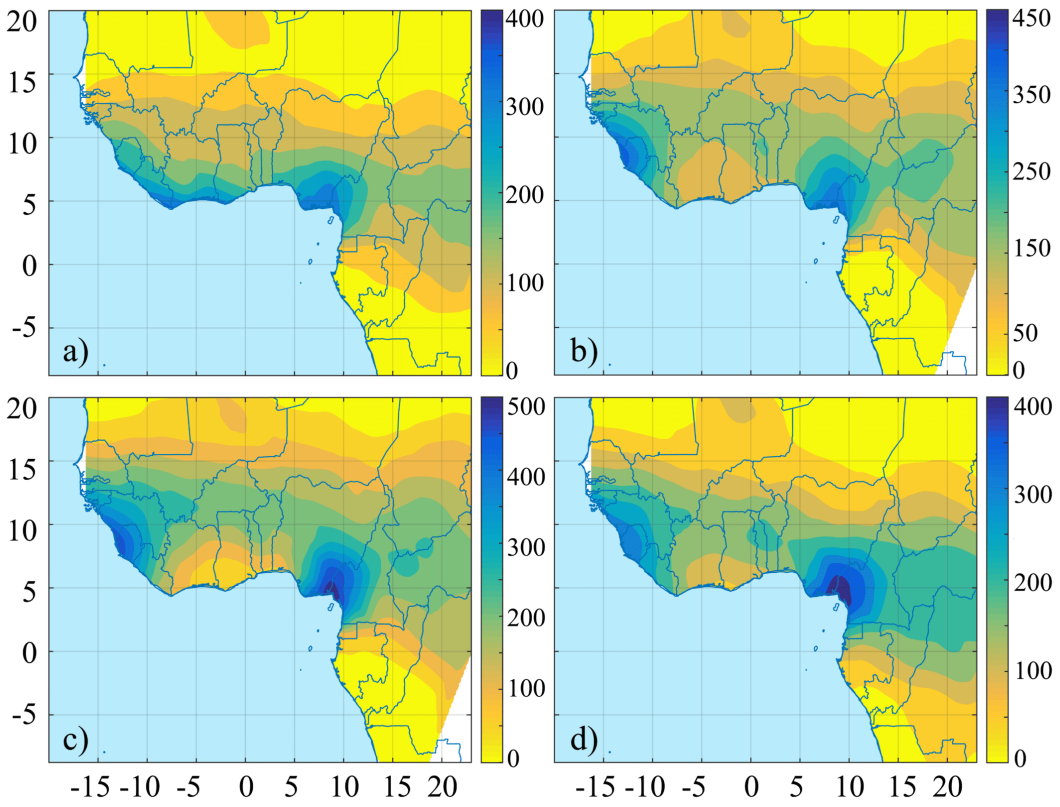

Figure 2.5: Climatological map of monthly precipitation (in mm) in West Africa for the period 1982–2016 (data from CAMS-OPI): a) June, b) July, c) August, d) September.

tation intensity starts to decrease, but intensive rains are still observed, with 350-450 mm/month observed in Nigeria/Cameroon and in Sierra Leone/Guinea/Guinea-Bissau. In summary, WA can be divided into 5 zones (Fig. 2.6): the Saharan region, which stretches across the whole northern extent of WA, is formed by the Sahara Desert, and has an annual rainfall of about 0-150 mm; the Sahelian/Sahel Region, a semiarid belt extending from the Atlantic Ocean to Sudan, averaging about 350 km in width, with an annual rainfall of 150-600 mm and a dry season lasting about 8-9 months; the Sudanian Region, which consists of a very large belt immediately south of the Sahel, with annual rainfall of about 600-1200 mm and a dry season lasting 5-7 months; the Guinean Region, which lies to the south of the Sudanian Region and is defined by its precipitation average of 1200-2200 mm/year with a dry season lasting 7-8 months; and the Guineo-Congolian Region, the wettest in WA, with an annual average rainfall of 2200-5000 mm, with rainfall nearly uniformly distributed over the year (Fig. 2.6; Cotillon et al. 2016).

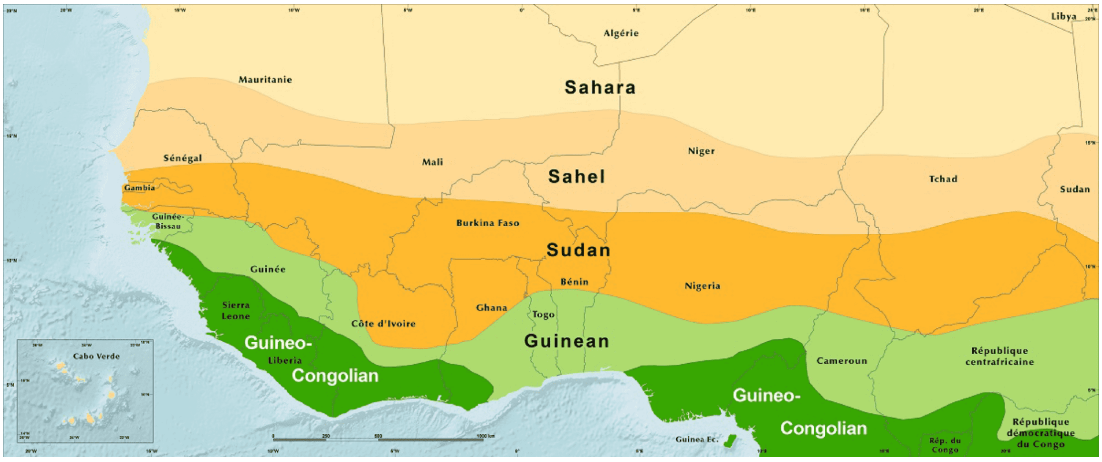

Figure 2.6: Bioclimatic regions in West Africa taken from (Cotillon et al. 2016).

2.3 Teleconnection indices

The term "teleconnection" was introduced by the Swedish geologist Gerard de Geer in 1925. With this term he described the relationships between annual clay deposits in remote parts of the globe and solar radiation mechanisms (De Geer 1926). In general, teleconnections are characterised by interdependences between one or more sets of events and the effects of one set on the behaviour of another. The distance between events or the time of the response are not significant.

Some progress in the area of identification and implementation of this phenomenon in meteorology was achieved by Wallace et al. (1981). The authors provided significant research on teleconnections, they checked the correlation between 500 mb geopotential height fluctuations at selected points and every other grid point in the Northern Hemisphere. They also performed the same analysis for sea level pressure. In this way, large-scale atmospheric centres of action were identified for both tested variables. For example, sea level pressure has a high negative correlation between the polar region and temperature latitudes, whereas the 500 mb height is showing a high correlation more at the regional scale, which displays a nearly equivalent baratropic structure with amplitudes increasing with height. At the Earth's surface the majority of regional patterns have only one or two well-defined centres, however, at the level of the mid-troposphere they appear more wavelike and are characterized by multiple centres of action.

Another influential paper in this field was written by Barnston et al. (1987). In this work, the authors used an orthogonally rotated principal component analysis of the Northern Hemisphere 700 mb geopotential height field to identify and describe the seasonality and stability of the major modes of inter-annual variability. They also found two north-south dipole patterns in the Pacific Ocean (the West Pacific Oscillation and East Pacific pattern), the Atlantic Ocean (the North Atlantic Oscillation and the East Atlantic pattern), as well as two uncorrelated modes with three centres: ap-

proximately east-west wave trains over the Eurasian and North American continents (the Pacific/North American and the Tropical/Northern Hemisphere pattern) and the Siberian north-south dipole (the Northern Asian pattern). The authors outlined the inter-monthly and inter-seasonal distribution of the patterns and their fluctuations during the seasons. In teleconnections, the investigation of long-term memory signals plays a crucial role, necessitating observation and the development of models that can suitably present the impact mechanisms of these signals. It is found that the prevailing variability modes in the Earth's free atmosphere are characterized by different general spatial patterns (Wallace et al. 1981). In this case, since the formation of precipitation is controlled by atmospheric dynamics on different scales and for long-range forecasting purposes, it is necessary to identify interdependencies between meteorological variables and precipitation formation.
NOAA's Climate Prediction Center[3] has identified and stored historical information about individual teleconnection patterns. According to the area of influence, those that are of interest in this thesis can be divided into two groups: the *Northern Hemisphere extratropical indices* and the *tropical indices*.

2.3.1 Northern Hemisphere extratropical indices

The indices listed below are important for specific regions of Russia.

- The *Pacific North American pattern* (PNA; Fig. 2.7 a) is one of the major factors affecting temperature and precipitation formation in North America. It has four centres of action over the Hawaiian Islands, North Pacific, Alberta (Canada), and in the southeast of the USA, near the Gulf of Mexico (Barnston et al. 1987; Wallace et al. 1981)

- The *East Pacific/North Pacific pattern* (EP/NP; Fig. 2.7 b) can be expressed as a western north Pacific monsoon and SST differences in the tropical to subtropical Pacific sector (Bell et al. 1995).

- The *West Pacific pattern* (WP; Fig. 2.7 c) in its positive phase leads to positive temperature and precipitation anomalies in the Chukchi Peninsula, Kamchatka, and Magadan region, as well as a weakening of the Pacific High, generating about 100 mm/month precipitation excess in the summer. In the negative phase, it has the opposite effect (Barnston et al. 1987; Wallace et al. 1981).

- The *East Atlantic/West Russian pattern* (EA/WR; Fig. 2.7 d) has a connection observed over the Canary Islands, in Great Britain, and the Black Sea region. The positive phase of EA/WR is characterised by the formation of a pronounced ridge at the level of 500 hPa in the east of the North Atlantic and the Barents Sea. In November and December, precipitation deficits are observed over Great

[3] www.cpc.ncep.noaa.gov/data/teledoc/telecontents.shtml

Britain, while at the same time excess precipitation falls over the Canary Islands. In the spring and summer, a weak signal is observed only in Great Britain (Barnston et al. 1987; Wallace et al. 1981).

- The *East Atlantic pattern* (EA; Fig. 2.7 f) in a positive phase leads to the weakening of the jet stream in the west of the North Atlantic, to the strengthening of the Azores High, and thereby to a weakening of the Icelandic Low, and vice versa for the negative phase. The lower-latitude centre contains a strong subtropical link in association with modulations in the subtropical ridge intensity and location. The pattern has an effect on temperature and precipitation in the north of Europe in winter (Wallace et al. 1981).

- The *North Atlantic Oscillation* (NAO; Fig. 2.7 e) is a dipole between the Azores high and the Icelandic Low. This pattern is commonly used when analysing climate change as it indicates planetary oscillations in the atmosphere-ocean system and it is the most significant indicator of circulation conditions in the North Atlantic mid-latitudes (Wallace et al. 1981). The index is pronounced in all seasons and is manifested at time-scales ranging from several days to several centuries. The essence of the NAO consists of the redistribution of air masses between the Arctic and subtropical Atlantic. The transition from one phase of NAO to another causes significant variations in wind, heat, and moisture transfer, the intensity, number, and trajectories of cyclones, etc. The maximum response is observed mainly in winter and in the regions of the North Atlantic, Europe and in the northern parts of Russia, mainly in winter. From April to December the correlation between NAO and precipitation decreases, but the connection can still be identified (Hurrell et al. 1995; Ulbrich et al. 1999; Wallace et al. 1981).

- The *Scandinavia pattern* (SCAND; Fig. 2.7 g) is a dipole between the Scandinavian Peninsula and the south of Europe/east of Mongolia. The positive phase corresponds to high positive anomalies, sometimes related to blocking anticyclones over the Scandinavian Peninsula or the EPR that lead to droughts. The negative phase causes negative anomalies, stationary cyclones, and heavy precipitation in these regions (Barnston et al. 1987; Wallace et al. 1981).

- The *Polar Eurasian pattern* (POL) exists between the south of Scandinavia, north of Poland, Siberia, and Japan, displaying a long-term correlation from the Atlantic Ocean to Eurasia. An intensification of cyclonic activity over Europe takes place in the positive phase of POL, when a low with its axis in the area of 20–30°E is observed (Barnston et al. 1987; Wallace et al. 1981).

- The *Arctic Oscillation* (AO) is one of the major climate indices, characterising the nonseasonal sea level pressure variations northward of 20°N. The positive phase of the index is characterised by positive temperature anomalies in Europe, Siberia, Yakutia, and in the south of the Russian Far East during the period from

March to November. The index affects precipitation variations over the oceans in winter (November-March Higgins et al. 2002; Larson et al. 2005).

2.3.2 Tropical indices

The indices listed below are important for specific regions in West Africa.

- The *El Niño Southern Oscillation* (ENSO; Fig. 2.8) is a cyclic fluctuation in sea surface temperature (SST) and the air pressure of the atmosphere (the Southern Oscillation) overlying the equatorial Pacific Ocean that recurs every few years as part of a naturally occurring cycle. It reaches its full strength by the end of the year and can last several seasons. The Southern Oscillation also describes a bimodal variation in the sea level barometric pressure between Darwin (Australia) and Tahiti. Normally, the El Niño phase starts with SST rising in the central/east Pacific. The opposite of the El Niño phase event, called La Niña, is characterised by a decrease in SST. It should be mentioned that not only the Pacific Ocean, but the Atlantic and Indian oceans have been noted as involved in the ENSO phenomenon. In this work we used the NINO3.4 index as representative of ENSO. The effects vary considerably with season and location[6] (Trenberth et al. 2001; Wolter et al. 2011; Yeh et al. 2009).

- The *Southern Oscillation Index* (SOI) is an indicator of the development and intensity of the El Niño or the La Niña in the Pacific. It captures the atmospheric component of ENSO and serves as an indicator. Low negative values (-8,-7) indicate the appearance of the El Niño, with warming of the central and eastern tropical Pacific and at the same time, a decrease in the strength of the Pacific trade winds, causing a decrease of precipitation in Australia[7].

- The *Eastern Mediterranean Pattern Index* (EMPI) is a part of the Mediterranean Oscilliation (MO) index that was introduced by Conte et al. (1989). The authors suggested the existence of a teleconnection pattern in the annual geopotential height field at 500 hPa between the western and eastern Mediterranean basin. The EMPI is defined as the difference between standardized geopotential height in Algiers and Cairo. It also proves the existence of the MO in the Mediteranean Meridional Circulation pattern (between British Isles and Italy in winter and spring). The EMPI, being a part of the MO, in one of its phases can bring warm air in the eastern basin of Mediterranean, and increase evaporation, so that it enhances the moisture advection towards the Sahel region in WA (Polo et al. 2008; Rowell 2001).

[4]The figure is taken from: http://www.cpc.ncep.noaa.gov/data/teledoc/

[5]The figure is taken from: http://www.noaa.gov/understanding-el-nino

[6]https://www.metoffice.gov.uk/research/climate/seasonal-to-decadal/gpc-outlooks/el-nino-la-nina/enso-description

[7]http://www.bom.gov.au/climate/glossary/soi.shtml

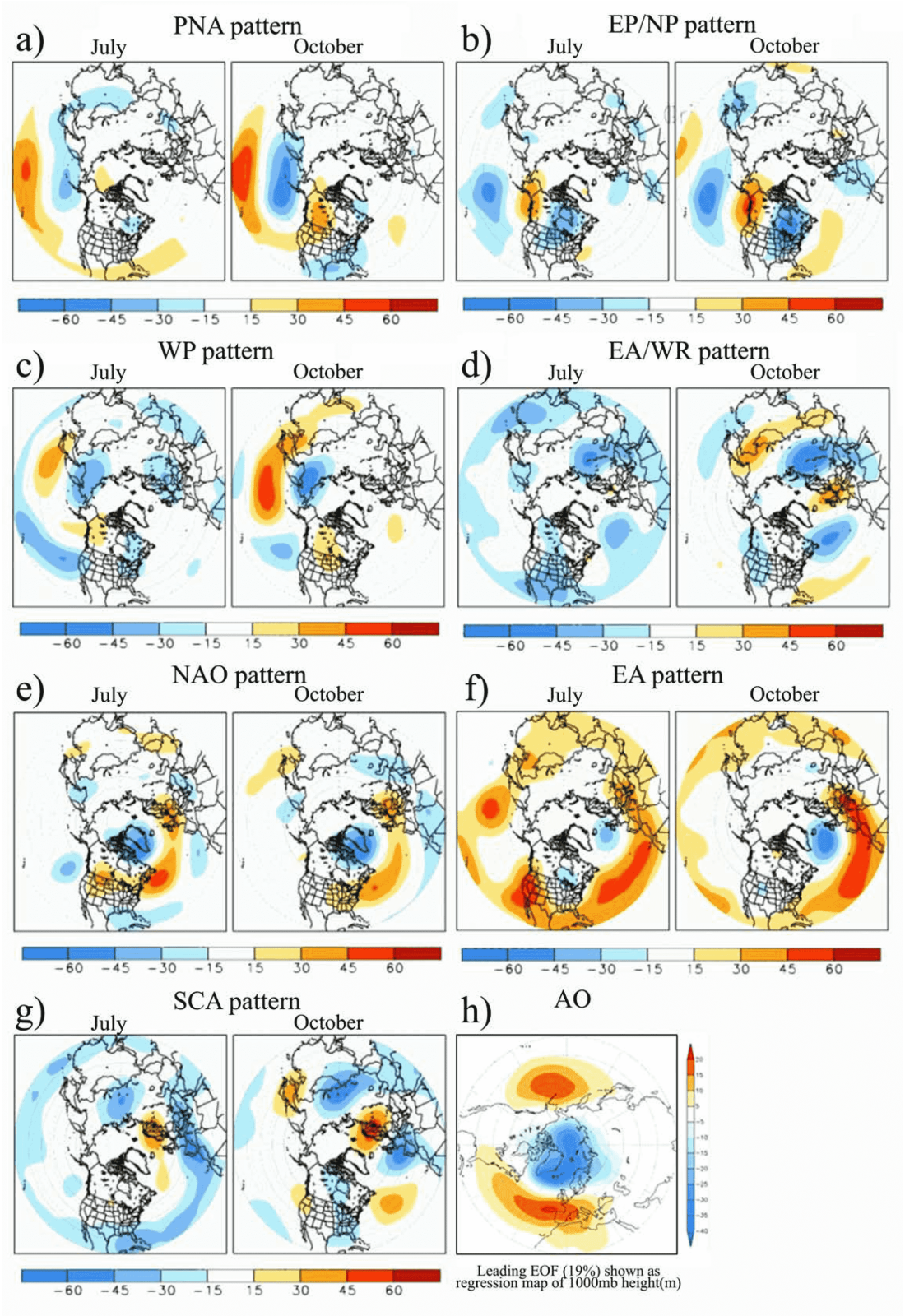

Figure 2.7: Teleconnection patterns for July and October, showing the temporal correlation between the monthly standardized geopotential height anomalies at each point and the teleconnection pattern time series valid for the specified month. a) PNA pattern, b) EP/NP pattern, c) WP pattern, d) EA/WR pattern, e) NAO pattern, f) EA pattern, g) SCA pattern and h) AO pattern.[4]

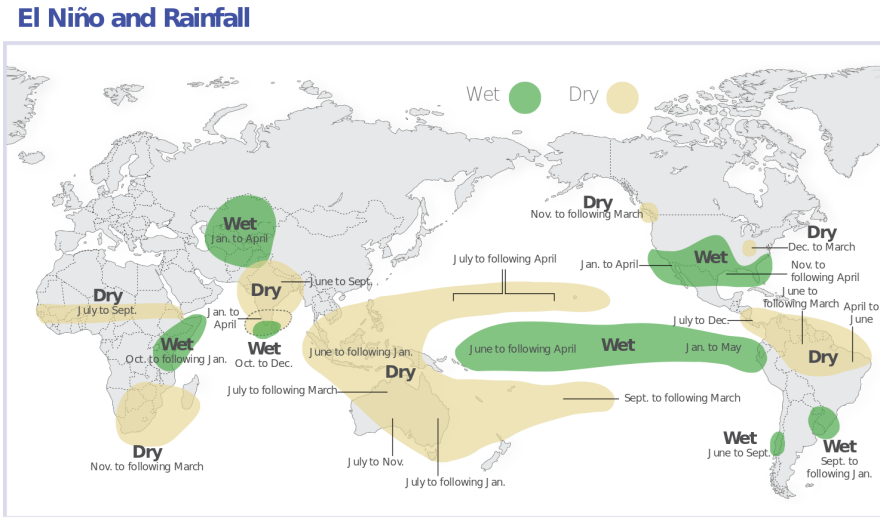

Figure 2.8: El Niño and strong continental rainfall anomalies.[5]

- The *Atlantic Equatorial Model* (ATL3) is a quasi-periodic inter-annual pattern appearing in the equatorial basin of the Atlantic Ocean. The ATL3 influences the SST by episodic cooling, which most certainly causes atmospheric circulation changes. It is strongly related to atmospheric climate anomalies, especially in West African countries near the Gulf of Guinea. It mitigates the pressure gradient between the Gulf of Guinea and the Sahara during the boreal summer (Gómara et al. 2017; Zebiak 1993).

- The *Atlantic Meridional Model* (AMM) SST index describes a coupled ocean-atmosphere variability in the Atlantic Ocean. The SST in the tropical North Atlantic in the positive AMM phase becomes warmer and pushes the ITCZ northward, thereby continuing to warm up both, the sea and the air. Thus, the surface air pressure response to the SST, wind shear becomes weaker and tropical cyclones start to develop in the Tropical North Atlantic. With the negative phase, the consequences are opposite (Kossin et al. 2007; Rugg et al. 2016).

- The *Quasi-Biennial Oscillation* (QBO) is a quasi-periodic oscillation of the stratospheric winds high above the equator which form a belt around the planet and change direction approximately every 14th months. It is driven by atmospheric waves and produced by intensive tropical systems. By that, the QBO affects the Atlantic jet stream[8].

- The *Tropical North Atlantic* (TNA) index is a dipole non-periodic index, which is defined over the region 5.5-23.5°N and 57.5-15°W and can be identified on the north of the ITCZ (Enfield et al. 1999). It presents an average of the SST

[8]https://www.metoffice.gov.uk/learning/quasi-biennial-oscillation

anomalies occurring in the defined area, however it influences the weather conditions in a large area, from northern Brazil as far as southeastern Europe (Hatzaki et al. 2015). It has been shown the TNA has a strong influence on the variability of tropical cyclone frequency in the Pacific Ocean, especially during the boreal summer (Huo et al. 2015). The TNA SST has a strong connection with the ENSO events in the succeeding winter time and when warm SST anomalies are observed in the TNA region, the La Niña event happens, normally in spring. However, the connection between TNA and climate is tenuous: the mean period is 8-12 years for the boreal winter-spring and 2-3 years for the summer-autum (Chen et al. 2017; Huang et al. 2002; B. Wang et al. 2000).

- For *Tropical Southern Atlantic* (TSA) index, the SST anomalies are calculated as for the TNA, but in the domain of 0-20°S, 30°W-10°E, i.e., the south of the ITCZ. The index shows the SST anomalies in the Gulf of Guinea, but the general idea is similar with TNA. The mean period keeps the same as for the TNA: 8-12 years (Enfield et al. 1999).

- The *Western Hemisphere Warm Pool* (WHWP) index presents monthly anomalies in the ocean surface area warmer than 28.5°C, ranging from the eastern North Pacific to the Gulf of Mexico and the Caribbean. The WHWP approaches its highest temperature values by the end of the summer and the beginning of autumn and is closely associated with hurricane activity and rainfall in the surrounding areas. The importance of this index lies in its ability to measure the stage of the SST, when even small anomalies lead to large impacts on tropical convection. It has been observed with the increase of the SST anomalies there is a decrease of atmospheric sea level pressure, together with an increase of convection and cloudiness (C. Wang et al. 2001).

- The *Madden-Julian Oscillation* (MJO) describes a tropical planetary wave propagating from west to east with rainfall activity associated with upward motion and divergence in the upper troposphere, followed by an area of rainfall associated with descending motion. It is also known as a dominant mode of tropical variability at interseasonal times scale. The MJO appears episodically, has a period of 30-60 days, and is mostly centred along the equator, influencing both hemispheres. Its primary area of influence is noticed in the Western Hemisphere, extending from the eastern Pacific to central Africa, over the Indian Ocean and the central Pacific, where strong convection occurs. Also, the effect of the MJO on precipitation is noticed in WA (Madden et al. 1971).

- The *Indian Ocean Dipole Zonal Mode* (IOD) is a coupled ocean-atmospheric variability mode, which in its positive phases increases the SST in the western Indian Ocean and brings heavy precipitation to the sub-continent. In its negative phase, the SST cooling is observed along with less precipitation on the sub-continent and heavy precipitation in the eastern Indian Ocean. Links to pre-

cipitation behaviour in WA have also been identified (Nnamchi et al. 2011; Saji et al. 1999; Williams et al. 2011).

Chapter 3

Methods

Statistics is an integral aspect of meteorology and weather forecasting; however, the complexity and implementation requirements of statistical techniques vary. Different statistical methods are implemented to help solving complex issues regarding observation data, integrating initial data into weather models, teleconnections, and pre- and post-processing, among many others. In this chapter, the detailed descriptions of all statistical methods used in this thesis are provided, including the SPI calculation, traditional and new spatial verification methods.

3.1 Standardized Precipitation Index

In this thesis, the terms "drought" and "wet" events characterise atmospheric processes caused by cyclones and anticyclones. Based on the context, droughts are typically distinguished into: meteorological, hydrological, agricultural and socio-economical droughts (Dutra et al. 2013). Here, we focus only on meteorological droughts.
By definition, a *meteorological drought* is based on precipitation deficiency accompanied by reduced surface runoff and ground water recharge, high air temperature, low relative humidity and high solar radiation for a specific region and specific period of time (Dracup et al. 1980). Thereby, dry conditions, in comparison with normal situations, depend on a deficit in precipitation and increased evapotranspiration. In the middle latitudes of the Northern Hemisphere, this type of drought appears due to stable (blocking) anticyclone(s) (Shakina et al. 2010).
As an alternative to the use of direct meteorological observations of precipitation amounts, which are commonly hard to obtain reliably, drought and wetness indices can be applied as quantitative approximations of precipitation variability. Over the last few decades, a multitude of such indices have been developed, with the SPI (Standardized Precipitation Index) as probably the most commonly used example (McKee et al. 1993). It was developed for monitoring drought situations as well as wet events on a particular time scale and location (i.e., it can be defined for any location in the world). In 2012, the World Meteorological Organisation (WMO) developed a user guide for the usage of the SPI by weather services (Svoboda et al. 2012).

The computation of the SPI follows a relatively simple procedure based on precipitation sums taken over a certain time period (1–48 months) that is selected according to the specific problem under study (Lloyd-Hughes et al. 2002). The time period is defined depending on the particular application and data availability, with the typical values of 1, 3, 6, 12, ..., 48 months, and the SPI indices in each case being named SPI-1, SPI-3, SPI-6, SPI-12, ..., SPI-48, respectively.
Since precipitation is distributed in a non-Gaussian fashion, the SPI overcomes the associated statistical challenges by transforming the data to a standard Gaussian distribution. Let us assume that our precipitation means follow a gamma distribution (e.g., for monthly precipitation sums). Then, to compute the SPI we need to fit a gamma probability density function to the empirical frequency distribution of precipitation for the station (grid point) of interest. This probability density function is defined as:

$$g(x) = \frac{1}{\beta^{\alpha}\Gamma(\alpha)} x^{\alpha-1} e^{-x/\beta}, \tag{3.1}$$

where $x > 0$ is the amount of precipitation, (otherwise, $g(x) = 0$ for $x < 0$), $\alpha > 0$ is a shape parameter, $\beta > 0$ is a scale parameter and

$$\Gamma(\alpha) = \lim_{n\to\infty} \prod_{v=0}^{n-1} \frac{n! n^{x-1}}{x+v} \equiv \int_0^{\infty} y^{\alpha-1} \mathrm{e}^{-x} \mathrm{d}x. \tag{3.2}$$

The empirical parameters α and β of the probability density function are estimated following an approximation developed by Thom (1958). In the investigations described in this thesis, such estimates are obtained for each point and time period of interest (in the case of SPI-1, they are obtained for each month of the year during the whole calculation period). The corresponding estimates are:

$$\hat{\alpha} = \frac{1}{4A}\left(1 + \sqrt{\frac{4A}{3}}\right), \tag{3.3}$$

$$\hat{\beta} = \frac{\overline{x}}{\hat{\alpha}}, \tag{3.4}$$

with

$$A = \ln(\overline{x}) - \frac{\sum \ln(x)}{n}, \tag{3.5}$$

where $\overline{x}$ is the climatological mean precipitation for the given point, and n is the number of precipitation observations. To describe the probability distribution function for observed precipitation, the resulting parameters are used:

$$G(x) = \int_0^x g(x)dx = \frac{1}{\hat{\beta}^{\hat{\alpha}}\Gamma(\hat{\alpha})} \int_0^x x^{\hat{\alpha}-1} e^{-x/\hat{\beta}} dx. \tag{3.6}$$

If we assume $t = x/\hat{\beta}$, the equation for the probability distribution can be simplified to an incomplete Gamma function,

$$G(x) = \frac{1}{\Gamma(\hat{\alpha})} \int_0^x t^{\hat{\alpha}-1} e^{-t} dt. \tag{3.7}$$

The reason for using the probability distribution in this step can be explained by the necessity of some analytical treatment, which will be shown below. In this way, the gamma function is undefined for $x = 0$. With $q = P(x = 0) > 0$, where $P(x = 0)$ is the probability of zero precipitation, the cumulative probability distribution takes the final form:

$$H(x) = q + (1 - q)G(x), \quad \text{for} \quad x > 0. \tag{3.8}$$

Finally, this cumulative probability distribution is transformed into a standard normal random variable Z, yielding the SPI values. Notably, Z variable has a mean of zero and a variance of one (Karavitis et al. 2011; Lloyd-Hughes et al. 2002; McKee et al. 1993).

The process of obtaining the SPI values is illustrated in Fig. 3.1 with an example of precipitation amounts taken over 1 month, September, for the precipitation average during 35 years (1982–2016) for a point in West Africa with coordinates 1.25°N, 11.25°E. The left panel shows the probability density function of precipitation during the sampling period, while the central and right panels show the process of obtaining the SPI values from the cumulative probability distribution function. The dotted blue line in the central panel indicates the empirical cumulative probability distribution obtained for the study period (a detailed explanation of the procedure of obtaining the empirical cumulative probability is given in Panofsky et al. 1958). The red pluses in the same figure represent the probability distribution function of the fitted gamma distribution associated with the actual precipitation values.

Let us take one point on line formed by the red pluses, characterising a certain precipitation amount, and convert it to the corresponding SPI values. For that, we project the associated cumulative probability horizontally until it intersects with the curve on the right panel (standard normal cumulative probability distribution). Then we take the associated value on the x-axis to determine the corresponding SPI value. In this particular example, 228 mm per month is 0.65 in terms of the SPI (characterising a normal event for the considered point and observation period).

However, the graphical approach is not convenient to use for a large number of data points, which is why McKee et al. (1993) and Lloyd-Hughes et al. (2002) proposed an alternative procedure for easier SPI computation. In those papers, the authors converted the cumulative probability to a standard normal random variable Z using an approximation provided by Abramowitz et al. (1965):

$$Z = \text{SPI} = -\left(t - \frac{c_0 + c_1 t + c_2 t^2}{1 + d_1 t + d_2 t^2 + d_3 t^3}\right) \quad \text{for} \quad 0 < H(x) \leq 0.5,$$

$$Z = \text{SPI} = +\left(t - \frac{c_0 + c_1 t + c_2 t^2}{1 + d_1 t + d_2 t^2 + d_3 t^3}\right) \quad \text{for} \quad 0.5 < H(x) < 1,$$

with

$$t = \sqrt{\ln\left[\frac{1}{(H(x))^2}\right]} \quad \text{for} \quad 0 < H(x) \leq 0.5, \tag{3.9}$$

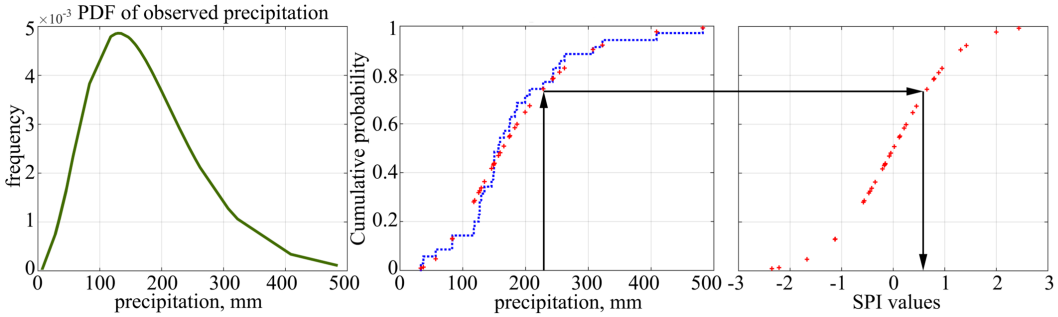

Figure 3.1: Example of an equiprobability transformation from a fitted gamma distribution to the standard normal distribution. Data are taken for the September precipitation during 1982-2016, for the point in West Africa with coordinates 1.25°N, 11.25°E.

$$t = \sqrt{\ln\left[\frac{1}{(1-H(x))^2}\right]} \quad \text{for} \quad 0.5 < H(x) < 1, \tag{3.10}$$

and

$$c_0 = 2.515517, c_1 = 0.802853, c_2 = 0.010328,$$
$$d_1 = 1.432788, d_2 = 0.189269, d_3 = 0.001308.$$

As a result, the SPI gives the number of standard deviations an observation deviates from the mean; negative SPI values indicate drought ($SPI \leq -2$) and positive values represent wet extremes ($SPI \geq +2$).

Table 3.1: Drought and wet events classification according to SPI value.

SPI value	Category
-2.0 or less	Extreme drought
-1.5 to -1.99	Severe drought
-1.0 to -1.49	Moderate drought
-1 to 1	Normal events
1.0 to 1.49	Moderately wet
1.50 to 1.99	Severely wet
2.0 and more	Extremely wet

Different ranges of values represent moderate-to-extreme conditions (see Table 3.1). A drought classification by SPI values and corresponding event probabilities has been presented by Lloyd-Hughes et al. (2002). The SPI is generally suited to map wet and dry conditions; its values are specific to the considered time scale of aggregation

of precipitation amounts and should not be compared quantitatively among regions, since it measures wet/dry conditions relative to the local climatology. Thus, at different locations, the same SPI value usually corresponds to different total amounts of precipitation.

3.2 Correlation and regression analysis

Correlation and regression analysis are standard statistical methods that are very popular in the natural sciences, since they help to identify and qualify the dependencies among paired data. Those two methods can be used separately or combined. Both methods are employed in this thesis.

3.2.1 Correlation analysis

Normally, in order to identify a linear dependence between two variables, the Pearson correlation is used, which is estimated as:

$$r_{xy} = \frac{\frac{1}{n-1}\sum_{i=1}^{n}[(x_i-\bar{x})(y_i-\bar{y})]}{\left[\frac{1}{n-1}\sum_{i=1}^{n}(x_i-\bar{x})^2\right]^{1/2}\left[\frac{1}{n-1}\sum_{i=1}^{n}(y_i-\bar{y})^2\right]^{1/2}} = \frac{\sum_{i=1}^{n}\left(x_i'y_i'\right)}{\left[\sum_{i=1}^{n}\left(x_i'\right)^2\right]^{1/2}\left[\sum_{i=1}^{n}\left(y_i'\right)^2\right]^{1/2}}, \quad (3.11)$$

where x and y are two sets of data, $\bar{x}$ and $\bar{y}$ are the mean values, and x_i' and y_i' denote anomalies obtained by subtraction of the mean values. The correlation coefficient $r_{x,y}$ is bounded by [-1, 1], with the perfect positive linear connection between variables expresed as $r_{x,y} = 1$ and perfect negative linear connection as $r_{x,y} = -1$ (A. Katz 1988; Wilks 2011). In this thesis two types of correlations are used (Willink et al. 2017):

- *Local (point-wise) correlation* is the classical Pearson correlation coefficient between two time series (e.g., station observations and the forecasts for the respective closest grid point); in other words, it is the correlation between points in space (taking information over time).

- *Field (spatial) correlation* is the correlation between the SPI-1 values of all stations/grid points taken into account at a given time (e.g., during one specific month).

In this regard, correlation analysis in this thesis is used for different purposes: 1) to establish statistical relations between predictors and predictands, as well as finding relevant predictors; 2) in teleconnection analysis, to identify strong connections between teleconnection patterns and local precipitation; and 3) in verification, to quantify agreement between observations and forecast data.

3.2.2 Linear regression analysis

This type of analysis is used here as a part of statistical forecasting, e.g., in long-range weather predictions. It describes the linear relationship between predictor and predictand. The predictor in regression analysis is an independent variable and the predictand fulfils the function of a dependent variable. Linear regression can be divided into two types: *simple linear regression* and *multiple linear regression*; this division is based on the number of predictors influencing the predictand. In this study, both regression types were used for different purposes.

3.2.2.1 Simple linear regression

The main problem of regression analysis is to estimate the parameters of a linear model describing the functional relationship between two datasets. The most common estimation procedure, the *ordinary least squares method*, aims to minimize the sum of squared vertical distances between the regression line and the observations. These vertical distances, called the *residuals* (e_i), describe the difference between observed and predicted values and are defined for a data pair (x_i, y_i) as:

$$e_i = y_i - \hat{y}(x_i), \tag{3.12}$$

where y_i is the observed value and $\hat{y}(x_i)$ is the predicted value. In such cases, the full regression equation, including the residuals reads:

$$y_i = \hat{y}(x_i) + e_i = \hat{a} + \hat{b}x_i + e_i. \tag{3.13}$$

Solving the regression equation implies to estimate the regression coefficients, where a is the intercept and b characterizes the dependence of y on x.
Hence, simple linear regression describes the relationship between predictor and predictand by a linear function with parameters estimated such that the error of the predictions of y is minimised for given observations of x. For this purpose, the most common approach is to minimise the sum of the squared errors, which is called the *ordinary least squares (OLS)* method (Wilks 2011). Of course, this criterion is not the only possible one; other approaches are also popular and used for different applications (e.g., least absolute deviation; Gray et al. 1992a). However, using the OLS criterion is useful, since it provides an analytically tractable solution.
Let us assume, that the quantities e_i are independent random variables with a mean of zero; the sample mean of the residuals is also zero ($\sum_{i=1}^{n} e_i = 0$), and the variance is constant. The constant variance assumption means that all conditional distributions of the residuals have the same variance. The regression equation can be regarded as specifying the conditional mean of the predictand by giving a specific value of the predictor. The estimated residual variance is then given by the following formula:

$$\hat{s}_e^2 = \frac{1}{n-2} \sum_{i=1}^{n} \left[y_i - \hat{y}\left(x_i\right) \right]^2. \tag{3.14}$$

The estimated residual variance is key to obtaining estimates of the sampling distributions of the regression coefficients. The regression coefficients a and b exhibit sampling variability, and different sets of data with size n will lead to different estimates of regression slopes and intercepts. Let us assume that the sampling distributions of the regression parameters are Gaussian.

$$a \sim N(\alpha, \sigma_a^2), \quad b \sim N(\beta, \sigma_b^2), \quad e \sim N(0, \sigma^2), \tag{3.15}$$

$$\text{with} \quad \alpha = \hat{a}, \quad \hat{\mu}_a = \alpha. \tag{3.16}$$

$$\beta = \hat{b}, \quad \hat{\mu}_b = \beta. \tag{3.17}$$

Then,

$$\hat{\sigma}_a = \hat{s}_e \left[\frac{\sum_{i=1}^{n} x_i^2}{n \sum_{i=1}^{n} (x_i - \bar{x})^2}, \right]^{1/2}, \tag{3.18}$$

and

$$\hat{\sigma}_b = \frac{\hat{s}_e}{\left[\sum_{i=1}^{n} (x_i - \bar{x})^2 \right]^{1/2}}, \tag{3.19}$$

Hence, the OLS estimates of the regression coefficients are unbiased, and equations (3.18) and (3.19) describe the precision with which the regression parameters can be estimated from the data. However, these equations apply only for simple linear regressions; for multiple linear regression, more complex expressions must be considered (Wilks 2011).

Another important notion in regression analysis is the *prediction interval*, containing a future value of the predictand with a specific probability. Following the assumption of residuals having a Gaussian distribution, we can expect a 95% confidence interval for a future value approximately being bounded by $\hat{y} \pm 1.96\hat{s}_e$. For a forecasted $\hat{y}$, the prediction variance can be written as:

$$\hat{s}_y^2 = \hat{s}_e^2 \left[1 + \frac{1}{n} + \frac{(x_0 - \bar{x})^2}{\sum_{i=1}^{n} (x_i - \bar{x})^2} \right]. \tag{3.20}$$

where x_0 is the predictor value. Here, the second term in the equation comes from the uncertainty in estimation of the true mean of the predictand from a sample size n. The third term describes the uncertainty of the slope, which means that predictions with large deviation from the centre of the distribution of the data used for the regression have larger uncertainty compared to the case where the predictions are made near the mean of the sample. If we remove the first term of 1 in Equation (3.20), we obtain the *confidence intervals*. If we compute and plot prediction and confidence intervals, the latter are more narrow compared with the prediction intervals reflecting a smaller variance. The variance of the conditional mean of the predictand given a particular predictor value x_0 is:

$$\hat{s}_{\bar{y}|x_0} = \hat{s}_e^2 = \left[\frac{1}{n} + \frac{(x_0 - \bar{x})^2}{\sum_{i=1}^{n} (x_i - \bar{x})^2} \right]. \tag{3.21}$$

3.2.2.2 Multiple linear regression

Multiple linear regression can be used to describe situations where more than one predictor influences the predictand. In the multiple regression equation, an arbitrary number of predictors can be taken. The general form of a multiple linear regression can be written as:

$$y = \hat{a}_0 + \hat{a}_1 x_1 + \hat{a}_2 x_2 + ... + \hat{a}_n x_n + e, \tag{3.22}$$

where $\hat{a}_1, \hat{a}_2, ..., \hat{a}_n$ are regression coefficients, $\hat{a}_0$ is the intercept (i.e., the value of y if $x_i = 0$ for all $i = 1, ..., n$), and e is the residual. Equation (3.12) is also valid for calculating the residuals of multiple linear regressions. In the least-squares method, the best fit for the observed data is again obtained by minimizing the sum of the squared residuals for each data point. Since deviations from the fitted model are first squared, then summed, there are no cancellations between positive and negative residuals (Parker 2017; Wilks 2011).

3.3 Cluster analysis

Cluster analysis is a standard method of multivariate statistical analysis for separating data into groups having similar properties, though, we usually don't know the exact number of groups beforehand. Cluster analysis is common in different applications. In the atmospheric sciences, it is used in such diverse areas as post-processing techniques, especially in order to investigate predictors (Bondell et al. 2008; Dormann et al. 2013; Gaffney et al. 1999), in weather typification analysis (Fovell et al. 1993; Huth et al. 2008; Kalkstein et al. 1987), and in grouping members of forecast ensembles (Legg et al. 2002; Molteni et al. 1996; Tracton et al. 1993), among many others. The main advantage of cluster analysis is that it identifies groups exhibiting high internal homogeneity and high external heterogeneity.

In cluster analysis, the Euclidean distance $d_{i,j} = \left[\sum_{k=1}^{K} w_k (x_{i,k} - x_{j,k})^2\right]^{1/2}$ between data points is often used, where x_i and x_j are the measured points (vectors), K is the number of dimensions and w_k are weights, which can balance the influence of variables with incommensurate units for each $k = 1, .., K$ (Wilks 2011). For both case studies considered in this thesis, the Euclidean distance is taken as a clustering criterion. Along with the resulting distance matrix, it is possible to implement different techniques of cluster analysis to identify strongly related groups of data.

Hierarchical cluster analysis is a very common approach. It starts with the assumption that n observations of x have no group structure or, equivalently, that the data set consist of n groups containing one observation each. Within the next steps, the two groups that are closest in K-dimensional space are identified in terms of their Euclidean distance (see below) and then combined into a single cluster. This procedure is iteratively repeated until all items have been considered into a single cluster. Several approaches are available to define cluster-to-cluster distances. The results can strongly depend on the technique chosen (Wilks 2011):

1. *Single-linkage/minimum-distance clustering* - the distance between two clusters G_1 and G_2 is the shortest distance between one member of G_1 and one member of G_2:
$$d_{G_1,G_2} = \min_{i \in G_i, j \in G_2} d_{i,j}. \tag{3.23}$$

2. *Complete-linkage/maximum distance clustering* - the distance between two groups of data points is given by the largest distance between points in the two groups G_1 and G_2:
$$d_{G_1,G_2} = \max_{i \in G_i, j \in G_2} d_{i,j}. \tag{3.24}$$

3. *Average-linkage clustering* - the distance between two clusters G_1 and G_2 is equal to the average distance from any member of one cluster to any member of another cluster:
$$d_{G_1,G_2} = \frac{1}{n_1 n_2} \sum_{i=1}^{n_1} \sum_{j=1}^{n_2} d_{i,j}. \tag{3.25}$$
where n_1, n_2 are the numbers of clusters in G_1, G_2 respectively.

4. *Centroid clustering* - here, the distance between centroids/vector averages of pairs of clusters is taken:
$$d_{G_1,G_2} = \|\bar{x}_{G_1} - \bar{x}_{G_2}\| \quad \text{with} \quad \bar{x}_{G_i} = \frac{1}{n_i} \sum_{k \in G_i} x_k, \tag{3.26}$$

When dealing with different scales and a large number of potentially important variables, different techniques such as principal components analysis (PCA; Preisendorfer 1988) and cross-correlation analysis (Wilks 2011) are frequently used in meteorology. PCA identifies new variables composed of mutually orthogonal linear combinations of the original ones, each accounting for a specific fraction of the original total variance of the data, as indicated by the size of their associated eigenvalue of the correlation matrix associated with data. These new variables can be used to generate component scores, those can be clustered instead of the raw data (Fovell et al. 1993; Richman et al. 1985).

3.4 Types of forecasts

Weather services and scientists produce different types of forecasts with different aims. A deterministic prediction gives an exact value of atmospheric parameters in the future, while a probabilistic forecast gives only certain probabilities of an occurence of the forecasted event. That is why deterministic and probabilistic forecasts are given for different ranges of predictions, purposes and parameters. However, when they are given together, they provide diverse forecasting information. Many studies of atmospheric predictability (J. Li et al. 2011; Lorenz 1969a,b; Shukla 1981; Slingo et al.

2011; Stockdale et al. 1998) have shown that there is a limit of deterministic forecast predictability of 14 days. Thus, a deterministic forecast is normally bounded by short- and middle-range periods. For longer ranges (month, season, year, decade), a probabilistic forecast is given.

3.4.1 Deterministic forecast

A deterministic forecast predicts the future state of the atmosphere by extrapolating the current situation using a fixed law or set of laws written in different ways (dynamical models, statistical models or others; Inness et al. 2012). Another important feature of deterministic forecasts is the absence of uncertainty. Weather forecasters occasionally use the terminology "most likely" or "probably" along with this type of forecast because of otherwise incorrect interpretation. However, these types of probabilities in deterministic forecasts must be considered as absolute. In any case, despite the simplicity of deterministic forecasts, the WMO (Gordon et al. 2000) defines it as follows:

- *Deterministic forecast for dichotomous events* - many meteorological events can be characterised as dichotomous events, or in other words, binary events. Such events either occur or do not occur (e.g., rain, fog, floods, thunderstorm, frost, tornado, etc.). These forecasts are normally issued with a statement that they will/will not occur, also described as a yes/no forecast (NCAR Research Applications Laboratory 2015).

- *Deterministic forecast for multiple categories* - this type can be subdivided into two types, *unranked forecast* and *ranked forecast*. The first represents situations with a number of different types of one event, for example, precipitation can be presented as rain, snow, or freezing rain, among others. More often in weather prediction, there are *ranked* forecasts that include an order (e.g., precipitation forecasts in gradations of intensity, visibility in categories, etc.).

- *Deterministic forecast for continuous variables* - a forecast results in a specific value of the variable which is possible to compare with the corresponding observation (e.g., temperature in degrees Celsius).

3.4.2 Probabilistic forecast

The main idea of probabilistic forecasts is to identify the joint probability distribution of future weather conditions or events. A probabilistic forecast gives the user the infromation about forecast's uncertainty. Like the deterministic forecast, it can be also divided into following types (Gordon et al. 2000):

- *Probabilistic forecast for two categories* - presents the forecasts limited by two possible outcomes. According to Wilks (2011) the most commonly used exam-

ple of this forecast is the probability of precipitation (PoP) forecast, where we can say about occurrence or nonoccurrence of the event.

- *Probabilistic forecast for multiple categories* - often used when the forecast must be presented with different categories and corresponding probabilities at the same time. Often, this type is used for long-term forecasts. Let us consider a monthly precipitation forecast. Normally, it has to be given in three gradations: below normal, normal and above normal with respect to the mean climatology, with certain probabilities for each gradation. The probabilities of all categories together add to 100%; thus, since we have 3 categories of this event, we have to find probabilities of occurrence of each gradation that combine to a total of 100%. Here, we give a small example for clarity: Assume that the monthly precipitation forecast for any random point *A* is given as a 25% probability of below normal values, 70% probability of normal values and 5% chance of above normal values. Thus, for point A, there is a 70% chance that precipitation in the next month will be within the normal range gradation according to the mean climatology.

- *Probabilistic forecast for continuous variables* - presents a forecast in the form of a probability distribution of continuous variables from, as an example, an ensemble system.

After implementing the forecasting schemes, we obtain deterministic and probabilistic forecasts for multiple categories. The deterministic forecast is obtained in terms of the SPI-1 index in seven categories as presented in Table 3.1. The probabilistic forecast is presented for 3 categories: below, normal, and above normal gradations, as recommended by WMO for long-range forecasts. The detailed descriptions of obtaining deterministic and probabilistic forecasts from the proposed scheme are given in the next sections (4.3.1) and (4.4.1).

3.5 Forecast verification

Forecast verification is the process of assessing the quality of statistical forecasts. The joint distribution of forecasts and observations provides the basis for a unified framework for verification (Murphy et al. 1987). The joint distribution can be written as $p(f,o)$, where f is a forecast and o is an observation. Thus, having forecast/observation data sets, the joint behaviour can be characterized in terms of the relative frequencies of all possible combinations of forecast/observation. This gives information about the forecast, the observation, and their relationship. The joint distribution can be used to create a conditional distribution for the observation, given a forecast. a Bayesian approach can be used to estimate the forecasting parameters.
Providing statistics obtained from verification analysis can help in the assessment of specific strengths and weaknesses of forecasts (Murphy et al. 1992). The usefulness

of forecasts to support decision making clearly depends on their error characteristics, which are explained through forecast verification methods. That is why forecasts must be verified quickly in order to provide it to users a useful time in advance of the forecast events. For forecasts relating to specific types of events (e.g., SPI classification from Table 3.1), following Wilks (2011) *the joint distribution* of the forecasts and observations can be written in the following way:

$$p(f_i, o_j) = Pr\{f_i, o_j\} = Pr\{f_i \cap o_j\}; i = 1, ..., I; j = 1, ..., J, \tag{3.27}$$

where f_i are the forecasts, which can take any of I values; o_j are the corresponding observations with any of J values, and Pr is the probability that a forecasted event will be observed. Equation (3.27) presents a discrete bivariate probability distribution function. Joint distributions can be factorized in two ways into *conditional distributions* and *marginal distributions*:

- *Calibration-refinement factorization* - involves the conditional distribution $p(o_j|f_i)$ of the observation given the forecasts and the marginal distribution $p(f_i)$ of the forecasts:

  $$p(f_i, o_j) = p(o_j|f_i)p(f_i); i = 1, ..., I; j = 1, ..., J. \tag{3.28}$$

  The conditional distribution characterises the frequency of different observations for given forecast value f_i; $p(f_i)$ is the frequency of different forecasted values. Notably, calibration and refinement are two important parts of the verification process and have to be considered together in order to achieve good forecasts. The ability of the forecast to predict extreme events is called *sharpness*, it is a property of the forecast only. It will be introduced later in this thesis by attribute diagrams (Section 3.5.2).

- *Likelihood-base rate factorization* - involves the conditional distribution $p(f_i|o_j)$ of the forecasts given the observation and the unconditional distribution $p(o_j)$ of the observation o_j:

  $$p(f_i, o_j) = p(f_i|o_j)p(o_j); i = 1, ..., I; j = 1, ..., J. \tag{3.29}$$

  The conditional distribution $p(f_i|o_j)$ is defined the likelihoods that the forecasted values would have been issued of each of the observed values with certain period in advance. As an example, let us take precipitation prediction. Here, in categorical predictions, we forecast the occurrence or non-occurrence of the precipitation event; therefore, two conditional distributions for such forecasts can be written as $p(f_j|1)$ for occurred and $p(f_j|0)$ non-occurred events. When the likelihoods are distinctive for different observed events, the forecast gives sparse results and is therefore very informative about observed events. The unconditional distribution $p(o_j)$ is the frequency of occurrence of observed o_j events in verification data sets, and is well-known as *sample climatological distribution*.

> Likelihood-base rate factorization provides a separation of two types of information that can be implemented in the forecast of observed events. The likelihood reflects the conditional distribution of the forecast for the given observation and base rate reflects historical observations.

These two factorizations can organize the verification more conceptually in an informative way (Murphy et al. 1987; Wilks 2011).
There are two verification approaches that can be derived based on the full information content of the joint distribution. The first is the *distribution oriented approach*, where verification methods are based on distributions, and the second is the *measures-oriented approach*, which is based on a few scalar verification measures. Below, we discuss different verification characteristics from these two classes of approaches and give a short computational description for each of them.
In order to select informative verification characteristics, we adopt the Standardized Verification System on Long-Range Forecasts (SVS-LRF) established by the World Meteorological Organization (WMO). To create this system, WMO collected the most popular verification methods for both deterministic and probabilistic forecasts (Mason 2016). SVS-LRF integrates several established verification approaches from the existing literature on this topic (Mariani et al. 2008; Murphy et al. 1992; Wilks 2011).
One of the foremost challenges in developing a new statistical forecasting method is obtaining a realistic estimate of its skills. Usually, the underlying regression equations are tested on a sample of independent data that have not been used during the development of the forecast equations. There are two approaches to obtaining such an independent data set, which we mention in this thesis, since one of them is used later to train both forecasting schemes.
The first approach splits the available period to create training and verification periods. For example, a data set covering 28 years splits sample into two parts: 23 years of data are used for training the forecasting model and 5 years of data for verification. This approach has some disadvantages. Normally, verifying a model with data from such a short period is not sufficient for the results to be informative. The short period cannot capture all possible diverse weather conditions, so it does not provide us with information on how the model will behave in rare situations.
The second approach does not have the problem of short data sets, due to using almost all available data from the study period with the exception of e.g., one year (depends on puposes of the forecaster); this method is called *cross-validation (CV)* (Wilks 2011). The most frequently applied procedure is known as "leave-one-out" cross-validation, in which the fitting procedure is repeated N times, each time with a sample of given size $(N-1)K$, where a subset of size K serves as the validation set and the remaining sample of size $(N-1)K$ as a training set. Therefore, the length of the initial data set is not reduced markedly and the model is checked more widely against more different types of past weather situations. Thus, we get more diverse information about the model's forecasting ability. This presents a reasonable solution and the approach has also been used in forecasting applications in other fields (e.g., Michaelsen 1987).

It has to be noted that cross-validation calls for some care when the underlying data are serially correlated. In this case, individual data that are adjacent or near the omitted observation(s) will tend to be more similar to them than randomly selected ones (Wilks 2011). In our case for both, Russia and West Africa case studies we use the "leave-one-out" method.
At this point, we should also introduce two important terms in the context of verification, *skill* and *skill score*. By *skill* (skillfull) we mean a relative accuracy of the forecast, normally with respect to observation data (Murphy 1973). A *skill score* is a metric that is used in order to quantify the skill of the forecast. Gneiting et al. (2007) define a skill score as: $S_n^{\text{skill}} = \frac{S_n^{\text{fcst}} - S_n^{\text{ref}}}{S_n^{\text{opt}} - S_n^{\text{ref}}}$, where S_n^{fcst} is the forecast's score, S_n^{Opt} is the hypothetical optimal forecast, and S_n^{ref} is the score for a reference forecast strategy. Skill scores are standardized, in such a way that 1 corresponds to a perfect (optimal) forecast, where the forecasted weather situation was fully observed. The reference forecast is normally a *climatological* forecast (but there are several available options for reference forecast), that in turn is the marginal distribution of the predictand. If $S_n^{\text{fcst}} = S_n^{\text{opt}}$, then the skill score is 1; if $S_n^{\text{fcst}} = S_n^{\text{ref}}$, then the skill score is 0, since there is no improvement according to the reference forecast. Skill scores can also take negative values, indicating that the forecast performing worse than the reference forecast.

3.5.1 Measures-oriented approaches

A reference forecast provides a benchmark against which a certain forecast accuracy is to be quantified. Normally, such a reference is based on climatological values of the predictand, persistence forecasts or random forecasts. The following gives a short description of parameters used in this thesis in order to evaluate the developed forecasting schemes for continuous forecasts.

- The *Mean Absolute Error (MAE)*

$$MAE = \frac{1}{n}\sum_{k=1}^{n}|f_k - o_k| \tag{3.30}$$

  is the arithmetic mean of the absolute values of the differences between forecasted and observed data, where a value of zero would indicate a perfect forecast. When the *MAE* is large, the distance between forecast and observation data is also large; thus, it can be interpreted as a magnitude of the forecast error in a given verification data set.

- The *Mean Squared Error (MSE)*

$$MSE = \frac{1}{n}\sum_{k=1}^{n}(f_k - o_k)^2 \tag{3.31}$$

  is based on the average squared difference between the forecast and observation data. By squaring the difference between forecast and observation values, by

definition, errors are always positive. This characteristic is more sensitive to larger errors, in contrast with the *MAE*.

If we take the root of the MSE, we achieve a new characteristic, the *RMSE*,

$$RMSE = \left(\frac{1}{n} \sum_{k=1}^{n} (f_k - o_k)^2 \right)^{1/2} \tag{3.32}$$

which measures the standard deviation of the prediction errors (or residuals in regression models).

To better understand the metrics given above and below, the following definitions are used. The term "hit" describes a forecasted event that is observed in a given range or within an acceptable range. For example, for precipitation forecasts, it is necessary to be within the gradation of intensity of precipitation and correctly say if a corresponding value will occur in the forecasted area. Similarly, a "miss" denotes that an event was not forecasted, but observed. A false alarm (FA) indicates a predicted event that did not occur (Jolliffe et al. 2012). With these terms, we can define the additional indices which are refer to general dichotomous events:

- The *reliability characteristic*

$$\rho = \frac{n_+ - n_-}{N} \tag{3.33}$$

  is the difference between the numbers of true (n_+) and false (n_-) forecasts, divided by the total number N of comparisons made. A "true" forecast means an event was forecasted and observed, and "false" means an event was not forecasted, but was observed, or a forecast was issued, but the forecasted event was not observed. In this thesis ρ will be used for comparing gridded data with station-based reference data and estimated for all stations and all years of observations.

- *Local (point-wise) correlation* - see Section 3.2.1.

- *Field (spatial) correlation* - see Section 3.2.1.

- False alarm rate (FAR):

$$FAR = \frac{\#FA}{\#hits + \#FA}; \tag{3.34}$$

  where *FA* is the number of false alarms.

Whereas the previously introduced measures are tailored to characterise the forecast of the dichotomous events, we consider generalising this to events following multiple classes.

- *The continuous ranked probability score (CRPS)* makes use of the main advantage of probabilistic forecasts, the opportunity to extract cumulative distribution functions (CDF) or probability density functions (PDF). It assesses the quality of weather forecasts by defining a distance between probabilistic forecast and observation. In other words, it compares the forecasted and observed CDF (Hersbach 2000; Jolliffe et al. 2012; Jordan et al. 2017; Wilks 2011). The corresponding equation can be written as

$$CRPS = \int_{-\infty}^{\infty} [P(f) - P_o(f)]^2 \, df, \tag{3.35}$$

where $P(f)$ is the cumulative distribution of the forecast f; P_o is the cumulative distribution of the observed value.

$$P_o(f) = \begin{cases} 0, & f < \text{observed value} \\ 1, & f \geq \text{observed value} \end{cases} \tag{3.36}$$

Equation (3.36) is a cumulative probability step function that varies from 0 to 1, and the best *CRPS* value is the smallest. Thus, for any cumulative distribution $P(f) \in [0,1], F(-\infty) = 0$ and $F(\infty) = 1$. For a Gaussian distribution, the classical view of Equation 3.35 translates into:

$$CRPS(\mu, \sigma^2, o) = \sigma \left\{ \frac{o-\mu}{\sigma} \left[2\Phi\left(\frac{o-\mu}{\sigma}\right) - 1 \right] + 2\varphi\left(\frac{o-\mu}{\sigma}\right) - \frac{1}{\sqrt{\pi}} \right\} \tag{3.37}$$

where μ is the mean, σ^2 the variance, o the observation, Φ the CDF, and φ the PDF.

Equation (3.37) significantly simplifies the calculation for the Gaussian case. This is of particular benefit for the SPI index. Since precipitation values are not normally distributed, transforming them to the SPI yields a Gaussian distribution of the resulting values and helps to implement most statistical metrics in a more simplified way, without the need for additional transformations. Cases for other distributions are not presented here; however, they can be found in Grimit et al. (2006). As mentioned by Hersbach (2000) and Wilks (2011), there is a direct link between *CRPS* and the *BS* for dichotomous events.

A list of further metrics can be found in Wilks (2011).

MAE, *RMSE*, ρ, *CRPS*, *local* and *field* correlation will be used for checking predictability of the deterministic forecasts provided by the new forecasting scheme described in this thesis, since these metrics are simple to implement and interpret the obtained results.
All abovementioned metrics require an exact match between observed and forecasted values in both space and time. This creates the "double penalty problem", where a false alarm is noted, but at the same time an event was observed at different site and was

missed in the forecast. Thus, two forecasts errors are recorded for one observed event in one location. Therefore, the above metrics do not provide information on the spatial distribution of false forecasts, how far the forecasted area is from the occured event, and whether the forecast over- or underestimated the true conditions. To overcome such problems, additional spatial forecasting methods have been developed (Casati 2010; Ebert et al. 2009, 2000; Gilleland et al. 2009; Marzban et al. 2009; Nachamkin et al. 2005; Roberts et al. 2008; Wernli et al. 2008), including:

- *Neighborhood (fuzzy)* methods give credit to spatially close forecasts, e.g., the Fractions Skill Score (*FSS*; Roberts et al. 2008) and other neighbourhood-based methods (Ebert 2009);
- *Scale-separation methods* measure a scale-dependent error, e.g., the intensity scale (*IS*; Casati 2010) or multi-scale variability (*MSV*; Brown et al. 2009);
- *Features-based methods* evaluate attributes of identifiable features, e.g., Contiguous rain area (*CRA*; Ebert et al. 2009); Structure, Amplitude and Location (*SAL*; Wernli et al. 2008); composite-composite method (Nachamkin et al. 2005), Method for Object-based Diagnostic Evaluation (*MODE*; Davis et al. 2009);
- In *Field deformation* methods the forecasted field is spatially manipulated in order to make it as close to the observation field as possible, e.g., Image warping (*IW*; Gilleland et al. 2009).

Neighbourhood methods require the forecasts and observations to be close in space, time, intensity, etc. They measure the strength of the relationship between forecast and observation. These techniques provide information on temporal or spatial scales used in the forecast to achieve appropriate accuracy. For such neighbourhood methods, object matching is not required (Ebert 2008; Roberts et al. 2008). One of the most popular neighbourhood metrics is the *Fractions Skill Score (FSS)*. Within this metric, the forecast is useful if the forecasted event frequency (F_f) is similar to the observed event frequency (F_o) and they have to be on the same grid. The similarity between forecast and observation is measured in terms of their fractional coverage of the event (the fraction of surrounding points within a given cell of the size n).
As the best example of generating the fractions, Figure 3.2 provides a schematic explanation of observed and forecasted binary fields on the same grid. Shaded grid cells show forecasted and observed events. Let us take the central grid cell highlighted with a black contour. For that particular case an event had been observed although it had not been forecasted. Then, the observation field at this grid cell has a value of 1 and the forecast field is 0. However, when computing the fractions of forecasted and observed events over the 5×5 domain (i.e., a neighbourhood size of $n = 5$) provides the same fractional event coverage of 6/25 (6 shaded grid cells with observed and predicted events out of 25), thus the forecast is correct over the area covered by that neighbourhood.

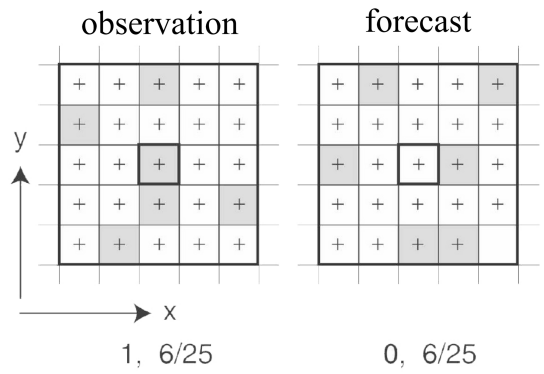

Figure 3.2: Schematic example of observed and forecasted fractional coverage of the event, taken from (Roberts et al. 2008).

Then let us define the MSE for the fractional coverages of the forecast P_f and observation P_o at each cell of size n for the domain size N, where $N = N_x \times N_y$, and N_x is the number of columns, N_y is the number of rows in the domain, then

$$MSE_{(n)} = \frac{1}{N_x N_y} \sum_{i=1}^{N_x} \sum_{j=1}^{N_y} \left[P_{o(n)_{i,j}} - P_{f(n)_{i,j}} \right]^2 \tag{3.38}$$

$$MSE_{(n)ref} = \frac{1}{N_x N_y} \left[\sum_{i=1}^{N_x} \sum_{j=1}^{N_y} P_{o(n)_{i,j}}^2 + \sum_{i=1}^{N_x} \sum_{j=1}^{N_y} P_{f(n)_{i,j}}^2 \right]. \tag{3.39}$$

with this equations, we can define the $FSS_{(n)}$ for a given neighbourhood size based on the classical definition of the *skill score* (given above), using MSE as follows:

$$FSS_{(n)} = \frac{MSE_{(n)} - MSE_{(n)ref}}{MSE_{(n)perfect} - MSE_{(n)ref}}, \tag{3.40}$$

For the perfect forecast, $MSE_{(n)perfect} = 0$ (the MSE of a perfect forecast on the neighbourhood length n), then the Equation (3.41) simplifies to:

$$FSS_{(n)} = 1 - \frac{MSE_{(n)}}{MSE_{(n)ref}}. \tag{3.41}$$

Now if we insert Equation (3.38) and (3.39) into (3.41) we get the definition of the FSS for a given neighbourhood length as follows:

$$FSS_{(n)} = 1 - \frac{\frac{1}{N}\sum_{i=1}^{N}(P_f - P_o)^2}{\frac{1}{N}\sum_{i=1}^{N} P_f^2 + \frac{1}{N}\sum_{i=1}^{N} P_o^2}. \tag{3.42}$$

All further computational formulas and details can be found in Roberts et al. (2008). For FSS to be implemented, the data must be of a high resolution, so that as many neighbouring points as possible can be taken into consideration for computing the fractional coverages of forecast and observations. The fractional coverages are generated for each possible spatial scale. The FSS is normally calculated for different thresholds (depending on the type of the forecast, if we use the FSS for precipitation forecasts, any threshold can be selected, depending on the purpose, e.g., 1, 2 or 5 mm). With $FSS_{random} = F_o$, the minimum FSS for a forecast to be useful is given by $FSS_{useful} = 0.5 + F_o/2$. $FSS = 0$ when the spatial extent of the considered neighborhood domain is smaller or equal to the displacement error of the event implying a complete mismatch. In turn, when the spatial scales is larger than the displacement error, the FSS increases with the scale and can reach the value of 1, meaning a complete match. By changing the value of n, the fractions are thus generated for different spatial scales, and n can be any odd value up to $2N-1$, where N is the number of grid points along the longest side of the research domain (e.g., if the domain is $5\times10^{\circ}$, as the longest side we take 10°, details can be found in Roberts et al. 2008). It has to be mentioned, that the $FSS = 1$ only in case of no bias in the forecast. If there is a bias, then the observed frequency (F_o) is not equal to the forecast frequency (F_f), and the resulting bias can be:

$$AFSS = 1 - \frac{\left(F_o - F_f\right)^2}{F_o^2 + F_f^2} = \frac{2F_oF_f}{F_o^2 + F_f^2}. \tag{3.43}$$

This approach is useful, since it relates the bias to the spatial accuracy of the forecast and provides a link to the conventional frequency bias (F_o/F_f).

3.5.2 Distribution-oriented approaches

Distribution-oriented approaches include not only statistical verification characteristics belonging to probabilistic forecasts, but also give information about the joint distribution for non-probabilistic forecasts and observations for continuous variables.

- *Conditional quantile plots* present the joint distribution of non-probabilistic forecast and observation for continuous variables. Information about two factors of the calibration-refinement factorization of the joint distribution of forecast and observation is represented in the plot. It is a convenient way of visually analysing the forecast model's performance and clearly shows the deviation of forecasted data from observations. It divides prediction and observation values into three bin pairs of the same length and identifies 10%, 25% and 50% quantiles for each bin, where the diagonal line represents perfect skill. In this sense, the conditional quantile plot characterises how well the distributions of observation and forecasted data agree with each other, especially at the lower and upper quantiles (Carslaw et al. 2012; Wilks 2011). The plot is rather different from a standard Q-Q plot and presents a modified version of it, avoiding two main disadvantages of

a Q-Q plot: firstly, a wavy appearance, and secondly, difficulties in quantifying linearity of the plot (Kafadar et al. 1986).

- The *Receiver Operating Characteristic (ROC) curve* describes the joint changes of true positive rate (TPR - corresponds to the previously discussed hit rate) and false alarm rate (FAR) when a certain parameter of the forecasting scheme used to identify the event type of interest is systematically varied. The ROC curve can characterise deterministic and probabilistic forecasts; however, in this thesis it will be used only for probabilistic forecasts. If the forecast probabilities Φ have been rounded to I discrete values, there are $I-1$ thresholds, excluding the case where the forecaster always observes/not observes the forecasted event. These probabilities can be used to select those thresholds for event definition that provide the best trade-off between hit rate and false alarm rate for a particular type of decision. A skilful forecast will achieve a hit rate that exceeds the false alarm rate, and therefore the ROC curve will move towards the top left corner in a (FPR, TPR) diagram, whereby further left represents a more skilful forecast. The forecast can be called without any skill (which is no better than guessing) if TPR equals FPR; thus, the ROC curve will be along the diagonal. The resulting prediction skills are then measured by the area under the ROC curve (AUC). Commonly, for AUC values between 0.9 and 1.0 the forecast accuracy is considered excellent, good to acceptable for 0.7 - 0.9, fair for 0.7 - 0.5, and poor for 0.5 (Wilks 2011).

- The *attributes (reliability) diagram* is a tool showing the full joint distribution of forecast and observation for probabilistic forecasts of a binary predictand in terms of calibration-refinement factorization. In other words, it shows the observed frequencies of a given type of event plotted against the forecast probability (Hartmann et al. 2002; Weisheimer et al. 2014; Wilks 2011). In an ideal case, when the predicted event probabilities and observed event frequencies are equal, the characteristic curve in the reliability diagram coincides with the main diagonal. However, in realistic weather forecasting systems, especially in long-term precipitation forecasts, it is hard to achieve this optimal result. Beyond the main diagonal corresponding to perfect forecast reliability, the attribute diagram comprises horizontal and vertical lines showing climatological event frequencies for the forecasted variable, as well as shaded areas indicating a positive Brier Skill Score (Wilks 2011). The latter a measure-oriented approach defined as:

$$BSS = 1 - BS/BSB \tag{3.44}$$

with

$$BS = \frac{1}{N}\sum_{i=1}^{N}(p_i - o_i)^2 \tag{3.45}$$

denoting the classical BS (where p_i is the forecast probability of a certain event to occur at time i and o_i is the actual outcome, i.e., $o_i = 1$ if the event actually

happened, and $o_i = 0$ otherwise) and the Brier score baseline (*BSB*) defined as the value of *BS* if the forecast is based only on the mean climatology obtained from all available observations. The *BS* is a verification tool for the occurrence of a specific event.

Chapter 4

Statistical post-processing-based forecasting schemes

Today, operational long-range forecasts are based on NWP models, which produce different future scenarios of the atmospheric dynamics, and as a result, provide information on the behaviour of forecasted meteorological parameters. However, complicated relationships between meteorological variables that are not precisely described in the model equations, and errors in the initial observation data (assimilated into the NWP model), make forecasting models and their outputs imperfect.
For example, the question of how to obtain an accurate representation of the atmospheric processes in terms of physical equations is a complicated question and our ability to model them improves slowly. While work on improving the various parts of the forecasting models is in the progress, forecasters work with the NWP outputs which contain large uncertainties.
Regardless of these input uncertainties, forecasters need to produce reliable forecasts. Statistical post-processing techniques have been developed in order to improve not the model, but its outputs, and to reduce uncertainties. Post-processing methods are relatively simplistic statistical approaches (compared to working with complex forecasting models, debugging potential mistakes, waiting for a long time to get computational results after applying new features, etc.). Their absence of direct representations of physical processes of the atmosphere and fast calculations increase the ease of their implementation, and in many cases, they achieve good results. These methods draw upon relationships between forecast and observation data and obtain a new, calibrated forecast as a result.
In this section, we discuss several basic post-processing methods developed for various applications and types of forecasts to improve the resulting prediction, aiming to provide the background for the new strategy developed and presented in this thesis. Subsequently, we provide a full description of a new forecasting scheme along with

two forecasting models that will be used in order to predict SPI-1 values in Russia and West Africa.

4.1 Statistical post-processing

According to Wilks (2011), there are two statistical approaches to weather forecasting, both based on regression equations. These two methods differ from classical statistical forecasting approaches by the range of available predictor variables.
The first approach is *perfect prognosis* (*perfect-prog*; Klein et al. 1959). It involves taking the forecast of future atmospheric variables as an initial value and assuming that this forecast is perfect. Developing regression equations for perfect-prog does not much differ from developing classical regression equations, where predictors are specifying observed predictands with a possible time lag, using climatological data. The forecast time lag is represented in the regression equations by connecting predictors available before the forecast to values of the predictand observed at a later time. To fit the regression model, predictand and predictor values are obtained at the same time. In the perfect-prog approach it is possible to use the forecasted predictor values obtained from the dynamical model at any time in advance. Quantities forecasted without a dynamical model cannot be taken as potential predictors, apart from those values already known. Of course, since predictors are coming from the dynamical model, their quality heavily influences the perfect-prog outputs - in this approach, the higher the quality of the forecasted predictors, the higher the quality of the output.
A second well known approach is *Model Output Statistics (MOS)* in which the dynamical forecast is used together with a statistical weather forecast. The statistical model is usually presented in terms of some regression equation (Carter et al. 1989; Glahn et al. 1972). The big advantage of MOS is the possibility to consider in the regression equation the influence of specific characteristics of the dynamical model forecast at different lead-times. It also gives an opportunity to compensate the systematic errors, while the forecast is computed.
Both perfect-prog and MOS use dynamical model outputs to derive the predictors. The only difference is that perfect-prog uses predictors only during the preparation of the forecast, while MOS uses the model's outputs to develop and produce the forecast equations. For constructing forecasting equations, both perfect-prog and MOS use a multiple linear regression approach based on correlations between predictand and predictor (Lemcke et al. 1988; Schuhen et al. 2012).
In one example of its application, Lemcke et al. (1988) used the MOS approach to forecast different weather parameters such as precipitation, frozen precipitation, thunderstorm, and sunshine. The authors created two statistical forecasting models - a multiple linear regression model for point forecasts and a logistic model for probabilistic forecasts - and showed that the approach exhibits good forecasting skills. The MOS approach was even used to provide forecasts of temperature, relative humidity, wind speed and wind direction for the Olympic and Paralympic Winter Games in Salt

Lake City in 2002, and is noted to be more accurate than the local forecasting 12- and 4-km grid models MM5 (Schuhen et al. 2012). It can be concluded that MOS can be used together with any forecasting model and can derive forecasts at any lead-time. However, the MOS equations must be renewed for each forecasting model.
Ensembles are commonly used for hydrometeorological forecasts and represent various types of uncertainties from climatology, models, parametrisations or initial conditions. In order to overcome these uncertainties, several post-processing methods for ensemble forecasts have been developed. One such method is *frequency-based probability forecasting*, which aims to estimate probability forecasts of binary events. The probability forecast is derived from the ensemble members based upon the PDF of the future observations. The number of ensemble members predicting an event is consistently an unbiased estimator of the probability of this event taking place. Thus, the corresponding fraction of members of the ensemble can be used to estimate the probabilities

$$Pr(y_t \leq q) = \frac{1}{N} \sum_{n=1}^{N} I\left(x_{n,t} \leq q\right), \tag{4.1}$$

where $Pr(y_t \leq q)$ is the probability of predicting an event y_t, N is the number of historical observations; q is the threshold of interest and can be set by the user, $x_t = (x_{1,t}, x_{2,t}, ..., x_{N,t})$ are the members of the forecast ensemble. As an alternative estimator, Equation (4.1) can be transformed to:

$$Pr\left(y_t \leq q\right) = \text{Rank}(q)_t/(N+1), \tag{4.2}$$

where $\text{Rank}(q)_t = \sum_{n=1}^{N} I\left(x_{n,t} \leq q\right) + 1$ is the rank of the threshold q, when brought together with all members of the forecast ensemble x_t. When all members of the ensemble are below q, then according to Duncan et al. (1978), $\text{Rank}(q)_t = N+1$.
A modified frequency based probability forecasts approach can be used to derive a new method called *direct model output (DMO)*. Here, the probability forecast is given by

$$\text{Rank}\left(y_t \leq q\right) = \frac{\text{Rank}(q)_t - 1/3}{N + 1 + 1/3}. \tag{4.3}$$

The probability forecast can range from $2/(3N+4)$, where $\text{Rank}(q_t) = 1$ to $(3M+2)/(3M+4)$, when $\text{Rank}(q)_t = N+1$. The adjustments introduced to the numerator $(-1/3)$ and to the denominator $(1/3)$ in the proposed equation are one among the possible corrections of frequency-based approaches (Wilks 2011; Williams 2016).
Hamill et al. (1997) presented another ensemble post-processing method using *rank histogram recalibration (RHR)* in ensemble location and dispersion. It uses historical training samples of ensemble forecast and observation. To generate the rank distribution histogram, quasi-independent sample points are used. To improve the quality of precipitation predictions, probabilistic ensemble forecasts are created by using the ensemble in conjunction with the probability information embedded in the rank histograms. Before constructing the probability forecast using the RHR method, it is

essential to remove any constant bias from the out-of-sample ensemble forecast x_t. Then we assume that the distribution between the ensemble members is uniform, thus we can find the appropriate weight for each member as:

$$w_j = \frac{1}{N}\sum_{i=1}^{N} I\left(\text{Rank}\left(y_i\right) = j\right) \text{for} j = 1, 2, \ldots, M+1, \tag{4.4}$$

where $\text{Rank}(y_i) = 1 + \sum_{m=1}^{M} I\left(\hat{x}_{im} \leq y_i\right)$ is the rank of the observation when merged together with the ensemble members, $M+1$ is the relative frequency of possible ranks taken by the N observations y_i. Hamill et al. (1997) assumed that the observations y_i are uniformly distributed in the range of [0, $\hat{x}_t^{(N)}$], where $\hat{x}_t^{(N)}$ is the largest ensemble member. However, if we fit a normal distribution for both tails of the RHR of the forecast distribution, then the probability forecast for observation in the lower part of the forecast distribution is weighed by w_1, and for the upper part by w_{N+1}. However, many observations fall in the tails of the probability forecast distribution, since operational ensemble forecasts possess low dispersity. Let us assume that g^{RHR} is the probability distribution for the tails of the RHR forecast distribution, G^{RHR} the cumulative distribution function and $\hat{x}_t$ the ensemble forecast. Then, the RHR forecast distribution is a weighted disjointed mixture of uniform distributions, chosen for quantities in the lower and upper tails and unbounded by the ensemble forecasts. Thus, the probability forecast of the binary event $y_t \leq q$ can be written as:

$$\Pr\left(y_t \leq q\right) = \begin{cases} \sum_{j=1}^{k} w_j + w_{k+1}\frac{q-\hat{x}_t^{(k)}}{\hat{x}_t^{(k+1)}-\hat{x}_t^{(k)}}, & \text{if} \quad \hat{x}_t^{(1)} < q \leq \hat{x}_t^{(N)} \\ w_1 \frac{G^{RHR}(q)}{G^{RHR}\left(\hat{x}_t^{(1)}\right)}, & \text{if} \quad q \leq \hat{x}_t^{(1)} \\ \sum_{j=1}^{N} w_j + w_{N+1}\frac{G^{RHR}(q)-G^{RHR}\left(\hat{x}_t^{(N)}\right)}{1-G^{\text{RHR}}\left(\hat{x}_t^{(N)}\right)}, & \text{if} \quad q > \hat{x}_t^{(M)} \end{cases} \tag{4.5}$$

where q is the threshold of interest.

Gneiting et al. (2005) presented another post-processing method, *nonhomogeneous Gaussian regression (NGR)*, which can be used when the forecast has a Gaussian distribution. The NGR is actually an extension of the MOS technique which accounts for the possible spread-skills relationships which appears between the forecast spread and the errors of the NGR forecast mean. Thus, the variance obtained from the post-processing method is given by a linear function of the ensemble mean, variance, and a weighted sum of the ensemble members. We expect that the NGR forecast distribution is a bias-corrected deterministic forecast, where the bias-correction is a linear function of the ensemble mean (Gneiting et al. 2005).

In this overview, we should also mention a method called *best member dressing (BMD)*, first introduced by Roulston et al. (2003). The idea behind the "dressing" method is providing each ensemble member with its own statistical error (taking into account the

impact of the residual errors in the forecast due to the finite size of the ensemble) in order to achieve a realistic comparison between different forecasts which can be made within the ensemble. The BMD method was developed by X. Wang et al. (2005). The authors dressed each ensemble member of a dynamical model with independent sets of N random 4D dressing perturbations in order to remove seasonal mean errors. In this approach, each member of an ensemble forecast is dressed with an extra, so-called "daughter ensemble" to derive a "hybrid" version of the ensemble. However, as Williams (2016) noted, the result of the method is more the construction of a continuous probability distribution of the forecast than an actual ensemble forecast. X. Wang et al. (2005) derived a Gaussian-distributed dressing kernel variance (mathematically it is a variance of the BMD forecast distribution, which has to be equal to that of the squared distance between the observations and ensemble members in the training sample; Williams 2016), which can be written for the one-dimensional case as

$$\sigma^2_{BMD} = \frac{1}{N}\sum_{i=1}^{N}\left\{\left(\overline{\hat{x}}_i - y_i\right)^2 - (1+1/M)s_i^2\right\} \tag{4.6}$$

where σ^2_{BMD} is the variance of the Gaussian-distributed dressing kernels, $\overline{\hat{x}}_i = M^{-1}\sum_{m=1}^{M}\hat{x}_{im}$ is the ensemble mean, and $s_i^2 = (M-1)^{-1}\sum_{m=1}^{M}\left(\hat{x}_{im} - \overline{\hat{x}}_i\right)^2$ is the ensemble variance of the bias corrected ensemble forecast, $m = 1,2,3,...,M$ are the ensemble members. Then the probability forecast of the binary event $y_t \leq q$ can be written as

$$\Pr(y_t \leq q) = \frac{1}{M}\sum_{m=1}^{M}\Phi\left(\frac{q-\hat{x}_{m,t}}{\sigma^{\mathrm{BMD}}}\right), \tag{4.7}$$

where Φ is the cumulative density function of the standard Gaussian distribution, $\hat{x}_{m,t}$ is the bias-corrected ensemble member, $m = 1,2,3,...,M$, and q is the threshold of interest. The method can be used even for systems with an additional member; however, this is possible only when the size of the ensemble is predefined.

Another important and frequently used method for probabilistic weather forecasting is *Bayesian model averaging* (*BMA*; Fraley et al. 2010; Hoeting et al. 1999; Raftery et al. 2005; Sloughter et al. 2007). It is used to address questions of model selection, combined estimation and prediction, and helps to identify the most obvious model selection criteria while at the same time leading to less risky predictions (Hoeting et al. 1999). In this method, each ensemble member is weighted and has its own kernel variance. Notably, the dressing kernel variance is estimated by an optimized objective function which is obtained over the training sample. The probability forecast of the binary event $y_t \leq q$ can be written as

$$\Pr(y_t \leq q) = \frac{1}{M}\sum_{m=1}^{M}\Phi\left(\frac{q-\hat{x}_{m,t}}{\sigma^{\mathrm{BMA}}}\right). \tag{4.8}$$

The BMA method can be used for parameters with a normally distributed PDF. In its original form, it cannot be applied for precipitation forecasts, since precipitation

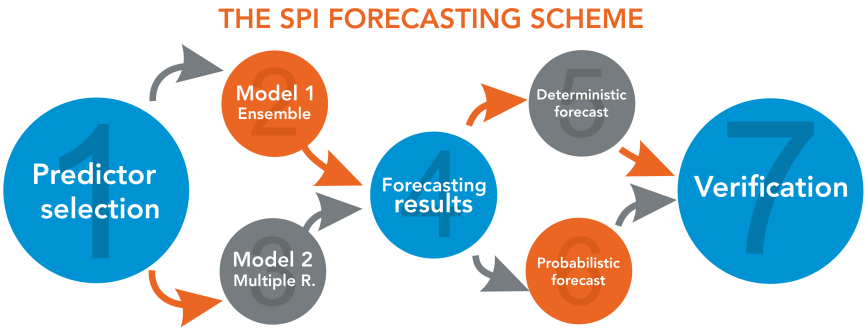

Figure 4.1: Schematic illustration of the SPI-1 forecasting scheme proposed in this thesis: (1) predictor selection, (2) forecasting model 1 - ensemble construction based on single linear regression equations, (3) model 2 - multiple linear regression, (4) final forecasting results, (5,6) deterministic/probabilistic forecast, (7) verification.

is non-Gaussian distributed. However, Sloughter et al. (2007) presented a modified BMA method which obtains a probabilistic precipitation forecast.

4.2 General strategy of the used foresting scheme

The SPI forecasting scheme presented in this thesis systematically exploits the existence of relevant statistical relationships between potential predictors and predictand. Hence, the identification and selection of informative predictors is a crucial aspect of this scheme. Wilby et al. (2000) provided a table with predictors and techniques used in different studies to investigate precipitation amounts. Notably, an absolute geopotential at 500 hPa level (H500) has been found to serve as a globally applicable predictor that can be used not only for weather classification (Bardossy et al. 1992), but also for predicting different meteorological variables and especially precipitation (Bardossy et al. 1992; Kilsby et al. 1998; Lang 2011; Wen et al. 2009; Yao et al. 2010). Using H500 as a predictor in post-processing schemes is a common approach, because it is a more stable parameter than others (precipitation, wind direction, temperature, etc.) and that is why it is forecasted by almost all models with higher skills (Kilsby et al. 1998; Yao et al. 2010).
Figure 4.1 shows a schematic representation of our approach. First, we identify predictors which exhibit a relevant statistical relationship with precipitation formation in different regions. Then, we decide, which model to utilize, model 1 or model 2 (see Sections 4.3.1 and 4.4.1 respectively). Both models are based on regression equations between predictors and predictand (SPI-1) obtained by investigating the statistical relationships among them in more detail, exploiting existing teleconnections in space. The difference between the presented models lies in the way, how the regression equations with the possible predictors are constructed. In model 1, we consider all combinations of previously identified predictors in a set of linear regression equations, which generates an ensemble of individual SPI-1 forecasts. Model 2 is based on a multiple linear

regression approach comprising the dependency between all predictor variables and the predictand (SPI-1) in a single equation. The resulting SPI-1 forecasts obtained from both regression models are subsequently analysed in both, deterministic and probabilistic ways, by means of various verification metrics. Finally, statistical verification procedures are performed to identify when and where the employed method provides acceptable skills.

4.3 Forecast model 1

4.3.1 Definition and description

We use multiple fields of potential predictors in order to investigate strong covariability with local SPI-1 changes over the respective region of interest, including H500, mean level pressure (MSLP) and surface temperature (ST). To identify strong statistical relationships between potential predictors and SPI-1, a cross-correlation analysis and then a cluster analysis are applied. Both types of analysis identify areas with strong statistical dependence between possible predictors and the predictand. Motivated by this, we hypothesize that combinations of the thus derived potential predictors can be utilized to constrain the expected SPI-1 values for any given grid point, together with their associated uncertainties.
Henceforth, as a first model we propose an SPI-1 forecasting scheme in which all possible combinations of individual predictors from each of the considered climatological fields are used to form a set of linear regression equations for the predictand (local SPI-1 value).
To this end, we use at most triplets of predictors - on the one hand, to reflect the fact that three predictor fields influence SPI-1 - and on the other hand, to keep the regression models as sparse as possible so that the corresponding regression parameters can be well-constrained and minimize numerical problems due to a possible collinearity of predictors. Instead, the maximally possible variety of combinations of predictors from the predictor fields is utilized to explore the full space of possibilities in the probabilistic forecasting task and capture as much as possible of the associated forecast uncertainty.
Following this rationale, we consider all combinations of previously identified individual predictors of the fields of interest to provide individual forecasts of the
SPI-1 (y_{ijk}) for any given forecasting region (FR) and month in terms of a set of linear regression equations

$$\hat{y}_{ijk} = a_{ijk}x_{1i} + b_{ijk}x_{2j} + c_{ijk}x_{3k} + d_{ijk} \tag{4.9}$$

where a_{ijk}, b_{ijk}, c_{ijk} and d_{ijk} are regression coefficients estimated from the available data. By this procedure, each forecasting site is associated with an individual set of linear equations, which are independently solved to generate an ensemble of individual SPI forecasts based on different lead-time predictors obtained from the model. The

resulting set of forecasts are suitable for exploitation in both deterministic and probabilistic ways.

4.3.2 Ensemble generation from model 1

A deterministic forecast is obtained by computing the mean over all ensemble members. As a result, we obtain a single SPI-1 estimate together with some possible further statistical characteristics, like its standard error. Specifically, by taking an average over the different ensemble members, we ensure that the resulting deterministic forecast represents the range of possible outcomes more reliably than each individual forecast. Moreover, the spread among the ensemble members can be used for assessing forecast uncertainty (in the spirit of multi-model ensembles) at least qualitatively, while the actual number of independent ensemble members might often be too small to obtain reliable quantitative uncertainty estimates. Note that the different predictor variables x_n exhibit different mean correlation values with the target SPI-1 value of the respective FR, suggesting that they will not be equally skilful. A natural extension of the approach presented here would therefore be replacing the unweighted mean over the individual forecasts of the different ensemble members by an accordingly weighted one. In contrast, the probabilistic forecasting procedure takes all ensemble members explicitly into account instead of using only the basic statistical properties of their distribution.

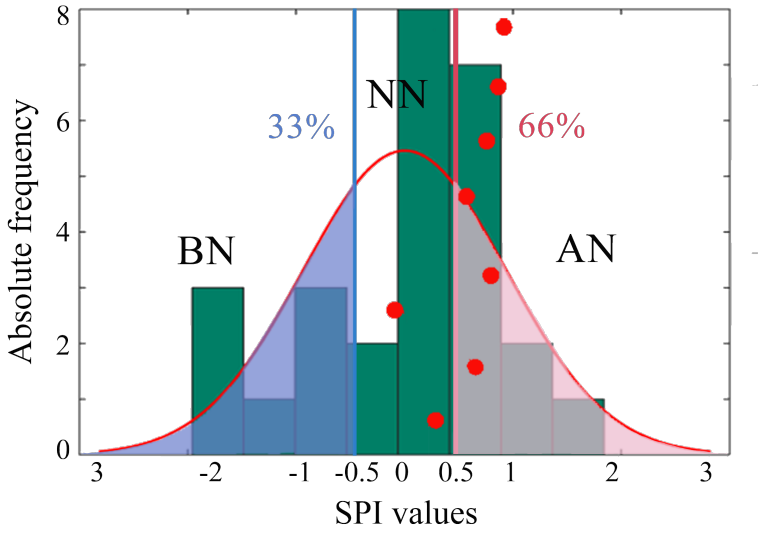

Figure 4.2: Schematic example for a forecast probability distribution based on the linear regression approach described in the text. Dark bars denote the histogram of observed SPI-1 values; the solid red line indicates a normal distribution with the same mean and standard deviation as the SPI-1 values; and dots show individual SPI-1 forecasts from the considered ensemble. In the presented case, 6 out of 8 ensemble members indicate wet (AN) rather than normal (NN) or dry (BN) conditions.

To obtain a coarse-grained classification of local SPI estimates, we utilize the empirical probability distribution function of all historical SPI-1 data at the given site during the study period. Based on this distribution, we select the 33th and 66th percentiles to classify the individual SPI-1 values of each FR into normal (NN), below normal (BN, dry conditions) and above normal (AN, wet conditions)[1]. Note that it would also be possible to instead adopt the WMO classification of different drought levels and proceed with this classification in the same way. However, in our case studies we prefer to utilize a coarser classification of SPI values.
Next, we take all members of the SPI-1 forecast ensemble and determine the empirical probabilities of forecasts in any of the three classes (NN, AN, BN). We refer to the estimated probabilities of these three classes of values as the probabilistic forecasts. The class (NN, AN, BN) containing most of the individual forecasts can be considered as a categorical SPI-1 forecast. If two or more classes are equally likely, no such categorical forecast can be made at the respective time step for the location under study. Figure 4.2 shows a corresponding example. In the end, the information derived from this kind of analysis is of the type "probability of a drought event to occur". Hence, such a probabilistic forecast provides the probabilities of occurrence of different types of (coarse-grained) events, while a deterministic forecast specifies an explicit expected SPI-1 value.

4.4 Forecast model 2

4.4.1 Definition and description

The forecast model 1 described above offers many advantages: to avoid the problem of multicollinearity (appearing in multiple linear regression models) and to achieve both probabilistic and deterministic forecasts in a simple and reliable way. However, it remains to be studied how the performance of such classical multiple linear regression models differs from that of the model 1. For this purpose, we compare the accuracy of the forecast made by model 1 with that of classical multiple linear regression (model 2) to provide a conclusion about the quality of both schemes in the particular case of long-range predictions with different lead-time. Here, model 2 is based on a multiple linear regression approach, containing the dependency between all predictors and predictand as:

$$\tilde{y} = a_0 + a_1 x_1 + a_2 x_2 +, ..., +a_n x_n, \tag{4.10}$$

where $\tilde{y}$ is the predicted variable, $x_1, x_2, ..., x_n$ are the potential predictors and $a_0, a_1, a_2, ..., a_n$ the corresponding regression coefficients (Parker 2017; Wilks 2011). Note that in model 1, each simple linear equation has individual coefficients. Thus, since we obtain N linear regression equations, we have N predictions and hence a

[1]The classification into normal, below normal and above normal conditions is a common strategy in long-term forecasting.

corresponding forecast uncertainty. In contrast, the model 2 contains only one equation and consequently one SPI-1 estimate, while also capturing the uncertainty of the system as described below.

4.4.2 Forecast generation for model 2

A deterministic forecast based on model 2 is obtained immediately and does not require extra calculations, due to the nature of model 2. Instead of an ensemble of linear regression equations we construct only one forecasting equation, and its result presents a pure deterministic forecast. However, for a probabilistic forecast, the computation is not so obvious.
To present a probabilistic forecast in below normal, normal, and above normal gradations, we estimate the regression parameters in the multiple regression Equation (4.10). It is important to mention, that we assume, the regression parameters have a Gaussian distribution and are chosen in order to obtain the best estimations, i.e., $e \sim N(0, \sigma^2)$. Thus, we can replace the single forecasted value ($\tilde{y}$) by its distribution, which is characterised by the forecasted value as the mean. Then the standard deviation is described by the standard deviation of the residuals obtained from the regression model. In such way, $\tilde{y} \sim N(\mu, \sigma^2)$ with $\mu = a_0 + a_1 x_1 + a_2 x_2 +, ..., + a_n x_n$. By assuming that our model has a Gaussian distribution, we can immediately obtain quantiles and probabilities for forecasts in the gradations BN, NN, and AN, which simplifies all calculations.

Chapter 5

Spatio-temporal pattern of extreme SPI and monthly SPI forecasts in Russia

Obtaining consistent and reliable precipitation forecasts beyond the time-scales of normal synoptic patterns is a challenging task. The results of such forecasts are very important for a variety of different applications. Accordingly, there is an increasing interest in the development of improved forecasting schemes in order to predict precipitation with higher accuracy. In this chapter we present an analysis of the SPI-1 index over Russia, focusing on the most extreme precipitation events during the period 1966-2010. The reasons for the occurrence of the identified extremes are explained by synoptical analysis. By means of statistical methods we identify their spatial distribution in different regions of Russia and frequency of occurrence. In order to predict extreme events, it is necessary to improve the long-range precipitation forecasts. In this chapter, we propose an implementation and verification of a new statistical forecasting scheme (model 1) in Russia.

5.1 Data and model

5.1.1 Precipitation data

The station-based observational data is used from the RIHMI-WDC[1]. Figure 5.1 shows the corresponding spatial distribution of rain gauge stations. It is clearly seen, that observation stations are not homogeneously distributed across Russia, especially huge gaps between stations are noticed in the Northern regions of APR. In those regions the distance between stations is more than 700 km and the total amount of observation stations with available data in Russia is only 518 (in 2012)[2]. In this way, the replacement

[1] http://meteo.ru/data

[2] http://meteo.ru/data

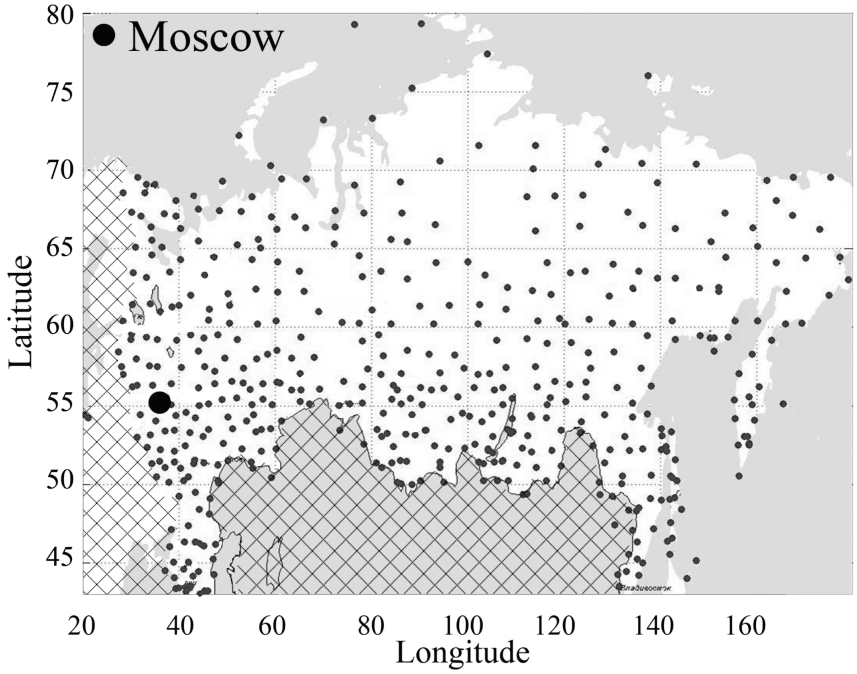

Figure 5.1: Spatial distribution of meteorological stations with continuous rain gauge records that are used as reference data in this chapter. Hatching indicates land area outside the Russian Federation, which is ignored in the following.

of these heterogeneously distributed station data with a realistic and spatially homogeneous data set of values across Russia is essential. We considered two candidate data sets, NOAA/NCEP CPC CAMS[3] and ERA-Interim[4], with the same horizontal resolution of $0.5^\circ \times 0.5^\circ$.

The *CAMS_CPC* data set of the Climate Prediction Center of the National Weather Service of USA provides global monthly gridded precipitation amounts and is available for the entire globe (excluding ocean areas). Within this data set, rain gauge observations (from the Climate Anomaly Monitoring System, CAMS) are combined with satellite data (Huffman et al. 1997; Janowiak et al. 1999, specifically, the Outgoing Long-Wave Radiation Precipitation Index). The data set is renewed every month at a resolution of 2.5°. When this work was started the CAMS data archive was available at three resolutions: 0.5°, 1° and 2.5° for the period from 1979 until present.

ERA-Interim is an operationally updated global reanalysis data set including meteorological records from 1979 to present. The data set is provided by the European Centre for Medium-Range Weather Forecasts (ECMWF, UK). The model is semi-Lagrangian with a semi-implicit scheme; it utilizes the hybrid sigma-pressure coordinate system to improve wind simulation in the upper troposphere and stratosphere, which allows a large improvement in forecasts of all other parameters, including pre-

[3] ftp://ftp.cpc.ncep.noaa.gov/precip

[4] http://www.ecmwf.int

cipitation. The data is assimilated using the 4D-VAR technique and operational data from the ECMWF data set. Therefore, in each cycle, the available observation data are integrated with the forecast data to reveal the most accurate current global atmospheric conditions (Balsamo et al. 2015; Dee et al. 2011).
Both data sets (CAMS and ERA-Interim) provide global coverage and are regularly extended up to the present day. In both cases, monthly precipitation data are taken for the period 1979–2014 to calculate the SPI-1 values.

5.1.2 Operational model description

To obtain values of the SPI-1 from raw NWP data, we use the SL–AV model. SL–AV is a global semi-Lagrangian semi-implicit model of the atmospheric general circulation based on the absolute vorticity equation. The model is run at the Hydrometeorological Center of Russia (Hydrometcenter) as an operational probabilistic long-range forecast system, and at the Siberian Hydrometeorological Institute (SibNIGMI) as an operational medium-range numerical weather prediction tool. The model's dynamic core was developed at the Institute of Numerical Mathematics, Russian Academy of Science, in cooperation with Hydrometcenter and using the subgrid-scale physics package from the ALADIN/ LACE NWP model (Shashkin et al. 2014). The main characteristic of SL–AV is that its dynamical core uses a finite-difference semi-implicit semi-Lagrangian implementation on the unstaggered grid, with horizontal divergence and the vertical component of the absolute vorticity as forecasted variables. The horizontal grid is regular in latitude and longitude with the options for variable latitude resolution and the use of a reduced latitude-longitude grid.
The SL–AV model uses a time-stepping scheme based on SETTLS (Hortal 2002) time approximation in combination with the semi-implicit approach and the pseudo-second-order decentering (Temperton et al. 2001). A semi-implicit time integration scheme within the semi-Lagrangian treatment of advection allows atmospheric simulations with time steps larger than the limits of the Courant - Friedrichs - Lewy (CFL) stability condition, and thus allows the creation of computationally efficient models. The model includes a set of parameterizations of the following sub-grid processes: short- and long-wave radiation, deep and shallow convection, planetary boundary layer, slow-down of gravity waves, heat and moisture exchange with the underlying surface.
The most recent version of the model couples the SL–AV model of general atmospheric circulation with the sigma model of general ocean circulation, INMOM, developed at the Institute of Numerical Mathematics of the Russian Academy of Sciences. The INMOM model is based on a closed system of nonlinear equations of ocean hydrodynamics in spherical coordinates using the hydrostatic and Boussinesq approximations (Tolstykh et al. 2014). A model of sea ice dynamics and thermodynamics was also incorporated into INMOM.
It should be noted that global models have a problem with meridian convergence in the geographic coordinate system. The model developers have therefore applied different methods to overcome the related shortcomings. For example, SL–AV uses a reduced

latitude-longitude grid and INMOM uses a curvilinear orthogonal grid. There is a time gap in SL–AV between the atmosphere and ocean models as the atmosphere is integrated with a time step of 36 minutes and the ocean with a time step of 72 minutes (Tolstykh et al. 2014). Spatial weight averaging is used to recompute SST generated by the ocean model to the atmospheric grid. The use of a new assimilation method improved the quality of initial data and thereby reduced the errors in the simulation in the field of 500 hPa geopotential height. In addition, the simulation of the precipitation field was improved, the mean error of temperature forecast decreased and the forecast of SST in the tropics performed much better (Tolstykh et al. 2014). Despite the fact that further work on improving the model is in progress, the results of the model can be also corrected by post-processing methods. For example, the application of statistical methods to separate forecast variables can improve the forecast skill. Therefore, the data of hindcasts of precipitation, MSLP, and H500 for the period 1983-2010 computed with the SL–AV model at the 2.5° grid for the area of 20-90°N, 50°W-180°E are taken for further computation.

5.1.3 SPI-1 calculations based on different data sets

As the first step of our analysis, we compare the SPI-1 values obtained from station-based precipitation observations with those derived from the two candidate data sets, CAMS and ERA-Interim (based on the respective neighbouring grid point at the original higher spatial resolution of these data sets of $0.5° \times 0.5°$). Figure 5.2 shows the local correlation values between the time series of station-based and gridded SPI-1 values for all boreal summer months, obtained by computing the classical Pearson correlation coefficient between each station and the respective closest grid point and spatially interpolating the obtained values over the study region. Note that the particular values shown in the resulting maps are affected by the spatial interpolation, especially in regions with sparse station coverage, as well as by the fact that precipitation is a small-scale property that can vary markedly between a particular station location and the location of the neighbouring grid point. In this spirit, the results shown should be considered only in qualitative terms, allowing us to assess the relative representation quality of observed monthly precipitation sums in the two data sets under consideration. However, high correlations can still be accompanied by strong bias.
It is observed that the typical local correlation values for the CAMS data set are clearly higher than those for ERA-Interim (Fig. 5.3). Table 5.1 summarizes the corresponding mean local correlations taken over the complete set of stations, where the corresponding correlation values have been obtained individually for each boreal summer month (June, July, August) during the period 1979-2014. In addition, the table displays the results of two other common verification metrics already introduced in Section 3.5. The spatial field correlation describes the correlation between the SPI-1 values of all stations and their respective closest grid point during the same month and is represented here by its mean value taken over all months. The reliability characteristic ρ is defined as the difference between the numbers of true and false classifications of SPI-1 values

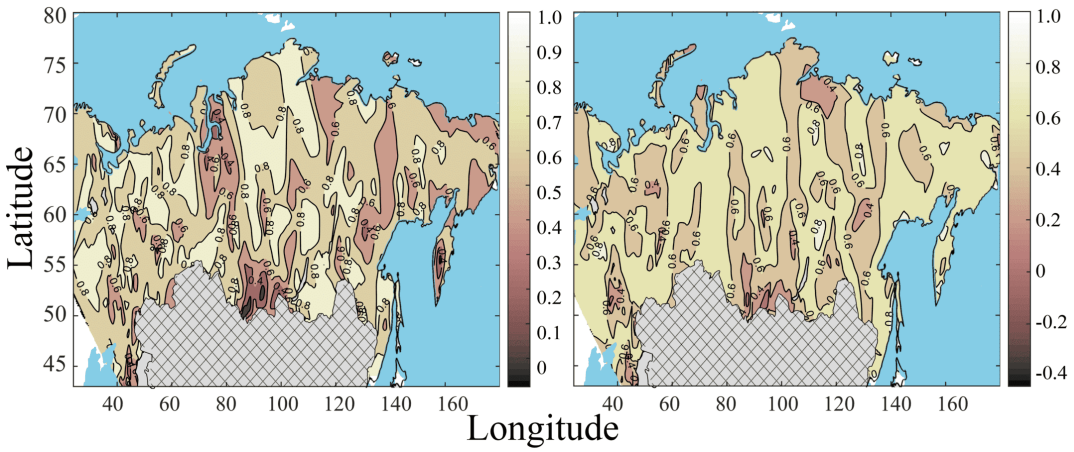

Figure 5.2: Spatial patterns of local (point-wise) correlations between SPI-1 values obtained from direct measurements made at meteorological stations across Russia and monthly precipitation data from the neighbouring grid points in the CAMS_CPC (left) and ERA–Interim (right) data sets.

in the gridded data as compared to the station-based reference data, divided by the total number of comparisons made, and is estimated using all stations and all years of observations. Here, a corresponding classification is obtained by coarse-graining the SPI-1 values into seven distinct classes defined by the WMO[5] (Table 3.1). All three measures clearly demonstrate that CAMS reproduces the true precipitation patterns with higher accuracy than ERA-Interim. Consequently, for further SPI-1 calculations the monthly precipitation data from CAMS is used.

Next, the behaviour of SPI-1 values obtained from the raw NWP data taken from the SL-AV model output is studied. It is found that one-month lead-time SPI-1 forecasts based on direct precipitation estimates from hindcast simulations of SL-AV indicate relatively poor predictability (see Table 5.2 for details). As an example, Figure 5.4 displays the calculated SPI-1 values based on CAMS and SL-AV for one randomly selected month (August 2010), indicating a remarkable discrepancy in the resulting spatial patterns. In fact, when computing the local correlations between the SPI values derived from both data sets for the different boreal summer months (Fig. 5.5), we find correlation values distributed around zero, with absolute values rarely exceeding 0.3. While the SL-AV model is capable of capturing the timing of drought and wet events with reasonable confidence, the geographical extent of these events is not correctly represented. This observation again underlines the necessity of developing and applying an alternative approach for seasonal precipitation forecasts that improves the poor accuracy of predictions for the Russia.

[5] See, e.g., http://www.wamis.org/agm/pubs/SPI/WMO_1090_EN.png, p. 4.

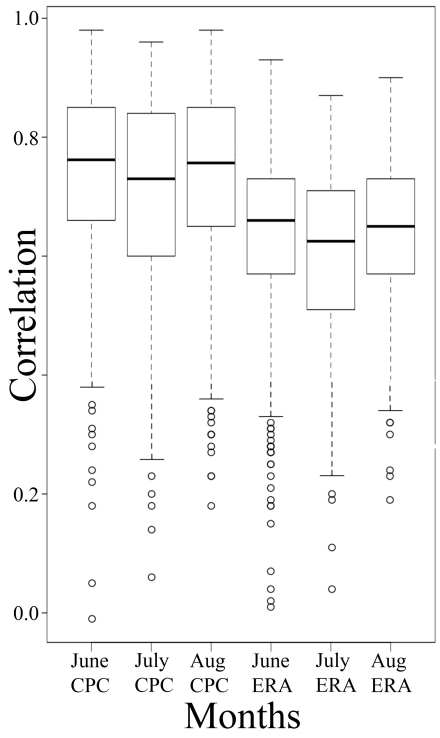

Figure 5.3: Box plots of local (point-wise) correlations between SPI-1 values obtained from direct measurements made at meteorological stations across Russia and monthly precipitation data from the neighbouring grid points in the CAMS and ERA–Interim data sets.

Table 5.1: Statistical characteristics of CAMS and ERA-Interim derived SPI-1 fields compared with station data.

Month	Local correlation	Field correlation	Reliability characteristics ρ
CAMS			
June	0.76	0.72	0.59
July	0.71	0.68	0.53
August	0.75	0.73	0.57
ERA-Interim			
June	0.65	0.63	0.45
July	0.62	0.60	0.42
August	0.64	0.62	0.44

Table 5.2: Summary of verification criteria for SL–AV based SPI-1 hindcasts and deterministic forecasts using the scheme proposed in this thesis (see Section 5.6.1 for details).

Month	Local correlation	Field correlation	Reliability characteristics ρ
SL-AV hindcast			
June	0.14	0.13	0.11
July	0.12	0.11	0.07
August	0.15	0.14	0.09
Deterministic forecast			
June	0.58	0.56	0.54
July	0.52	0.51	0.48
August	0.55	0.53	0.50

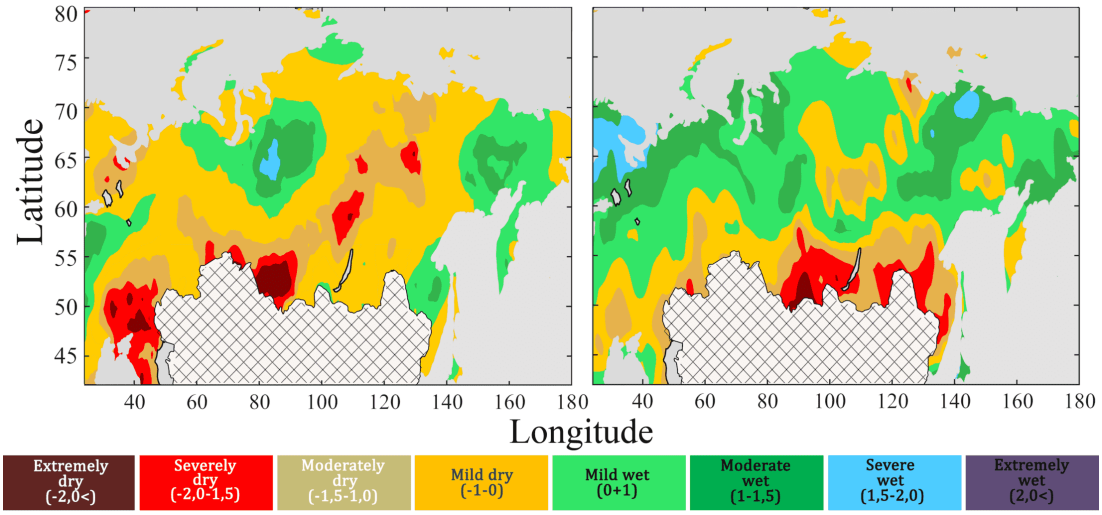

Figure 5.4: Example of resulting SPI-1 estimates for August 2010 based on CAMS (left) and SL–AV hindcast data (right). For this month, the spatial field correlations between the different fields are 0.65 (CAMS vs. rain gauges), 0.61 (ERA- Interim - not shown here - vs. rain gauges), 0.14 (SL-AV hindcast vs. rain gauges), 0.21 (CAMS vs. SL-AV hindcast), illustrating the poor agreement between the SL-AV hindcasts and both the station-based precipitation records and the selected spatially homogeneous reference data set (CAMS).

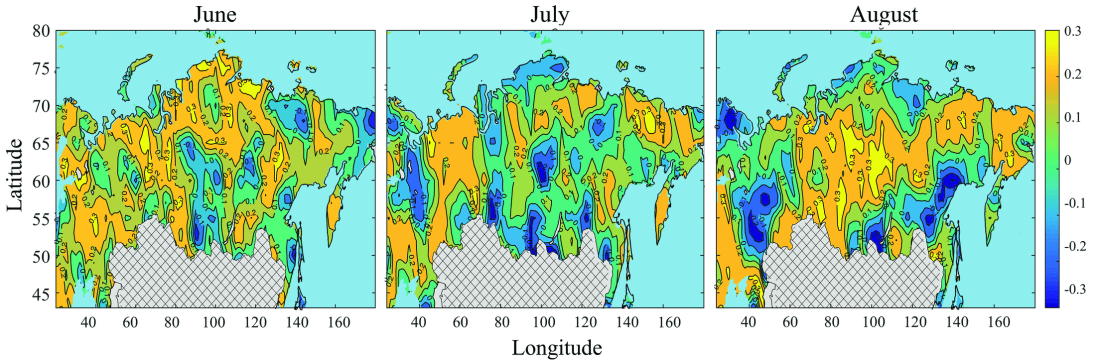

Figure 5.5: Local (point-wise) correlations between CAMS and SL-AV hindcast-derived SPI-1 values during the boreal summer.

5.2 Statistical analysis of extreme SPI

5.2.1 Spatio-temporal patterns of extreme SPI

Observed variations in regional and global climate require re-evaluation of the consequences and environmental impact of large-scale circulation processes. Previous statistical conclusions should be reviewed to account for new data and techniques for climate data analysis and interpretation. Climatic conditions for large-scale processes have changed; therefore, methods for estimation of the frequency and duration of extreme events, including drought and wetness, are of rising interest.

Changes in the climate conditions in Russia can be accompanied by drought intensification (Pachauri et al. 2007) and an increase in the occurrence frequency of drought events over the Kalmykiya, Astrakhan, Volgograd, and Rostov regions (Lopatin et al. 2005). The authors of that paper also confirmed a trend towards aridification of Russia, with its consequences being evident in the spring and summer months.

For spatio-temporal analysis of such events, the SPI calculations based on observed rain-gauge data (obtained from RIHMI-WDC) are used. The data includes monthly precipitation sums for the boreal summer (June-August) during the period 1966-2010 obtained from 518 weather stations inhomogeneously distributed over the territory of Russia (Fig. 5.1). Stations with many gaps in measurements have been excluded from this analysis, thus data from 500 stations have been used for the index calculations. Insignificant gaps (1-2 months) in the measurements have been filled with monthly mean values for a given station.

Two of the most extreme recent droughts in Russia during the boreal summer occurred in 1972 and 2010 (Fig. 5.6). In the summer 1972, a catastrophic drought developed in most parts of Russia, mainly due to the formation of a blocking anticyclone over the centre of the APR in June and in the southern EPR in late July. During that year an abnormally cold winter with deep-frozen soil were observed, thereby much of the winter and spring precipitation had run off, which promoted the drought from the be-

ginning of May. In June, the drought formed over the APR (Fig. 5.6) and decreased toward July, while the situation worsened for the EPR over the same period. A permanent inflow of dry Arctic air toward the south of the EPR resulted in the formation of a stable anticyclone, which was broken only at the end of July. Cherenkova et al. (2012) assume that the Azores High played a significant role in the formation of the drought in the summer of 1972.
A similar blocking anticyclone settled over the EPR in the summer of 2010, causing hot and dry weather, but the prerequisites that worsened the conditions are similar to those present in the summer 1972: a precipitation deficit in winter and spring and low temperatures in the winter months with concomitant deep freezing and slow thawing of soil. The soil was insufficiently wet; a powerful high-pressure centre settled over the EPR in the third week of June, which stabilised for 55 days and disturbed the usual eastward air mass transport. Moreover, this pressure situation prevented formation of clouds and, hence, precipitation, which finally resulted in a catastrophic drought (Shakina et al. 2010). A drought peak with maximum intensity and distribution was observed in July.
As seen in Figure 5.6, the spatial distribution of SPI adequately shows the drought distribution. To estimate quantitatively the SPI spatial distribution over a region, we use the areal parameter Pl, which shows the percentage of area covered by drought/extreme wetness relative to the total area of a macroregion. The EPR and APR are mainly impacted by different air masses and, hence, different pressure centres; therefore, areas of extreme drought/wetness have different genesis mechanisms. Thus, the areal distribution is analysed separately for each macroregion.
Table 5.3 shows extreme dry/wet events with wide coverage of the study region. The six most extreme droughts and the six most extreme wet events are selected for the EPR; seven droughts and six wet events for the APR. Thus, the higher Pl, the larger the region affected by the event. For example, “extreme dry" Pl values are maximal in the EPR in August 1972 and in the APR during June 1972. Indeed, the drought of 1972 was catastrophic and covered most of the territory of the former USSR.

5.2.2 Frequency distribution of extreme SPI

In order to analyse the frequency distributions of extreme events, we separated the research period (1966-2010) into eleven-year periods in order to observe the short-term climatic changes (period I: 1966-1976; period II: 1977-1987; period III: 1988-1998; period IV: 1999-2010) and obtain the SPI-1 values. For each period we estimated several statistical parameters including the 90% quantile, kurtosis, asymmetry, standard deviation (SD), median and amplitude and summarized the results in Table 5.4. An increase in the number of extreme drought events in July and August is observed during the study period; the number of wet events decreased over the same period. The standard deviation allows to estimate the spread of the SPI values about the mean. Notably, there is a trend towards left-side asymmetry, which indicates the prevalence of wet over drought events.

Table 5.3: Areal parameter Pl of significant drought and wet peaks in the EPR and APR.

Month	Year	Extreme dry EPR	Year	Extreme dry APR	Year	Extreme wet EPR	Year	Extreme wet APR
June		3		12		3		3
July	1972	5	1972	1	1981	0	1970	0
Agust		31		2		0		0
June		12		4		1		0
July	1979	0	1981	3	1998	4	1973	2
Agust		1		8		3		1
June		0		7		0		2
July	1994	14	1983	0	2000	4	1979	0
Agust		1		1		0		0
June		0		2		0		1
July	1996	0	1998	8	2003	0	1980	2
Agust		17		5		5		0
June		1		0		3		1
July	2002	3	2000	1	2005	0	1988	2
Agust		14		6		0		4
June		11		2		0		1
July	2010	18	2003	3	2006	1	2006	0
Agust		0		6		4		4
June						2		
July	-	-	-	-	2007	5	-	-
Agust						3		

Table 5.4: Statistical parameters of extreme SPI for the EPR and APR.

Period I (1966-1976) II (1977-1987) III (1988-1998) IV (1999-2010)	Left quantile 0.05 dry	Right quantile 0.95 wet	Median	SD	Asymmetry	Kurtosis	Min	Max
EPR								
June								
I	−1.78	1.38	−0.09	0.93	−0.25	3.14	−3.53	2.66
II	−1.70	1.63	0.13	1.02	−0.40	3.52	−4.52	2.85
III	−1.49	1.65	0.16	0.96	−0.19	3.04	−3.46	2.89
IV	−1.91	1.59	0.08	1.06	−0.39	3.21	−4.10	2.78
July								
I	−1.71	1.43	0.07	0.94	−0.47	3.49	−4.04	2.68
II	−1.57	1.54	0.18	0.96	−0.50	3.66	−3.93	2.72
III	−1.77	1.67	0.11	1.02	−0.24	3.17	−4.12	3.00
IV	−1.93	1.57	−0.04	1.05	−0.20	2.89	−3.53	3.17
August								
I	−1.87	1.41	−0.01	0.99	−0.41	3.70	−4.53	3.20
II	−1.51	1.59	0.15	0.95	−0.22	3.23	−3.72	3.12
III	−1.75	1.54	0.13	0.99	−0.40	3.10	−3.45	3.04
IV	−1.74	1.66	0.03	1.04	−0.13	3.00	−3.77	3.63
APR								
June								
I	−1.63	1.58	0.04	0.96	−0.09	3.13	−3.86	3.39
II	−1.87	1.58	0.01	1.04	−0.25	3.19	−4.14	3.24
III	−1.67	1.52	0.05	0.98	−0.31	3.13	−3.80	3.04
IV	−1.65	1.67	0.12	1.01	−0.08	2.91	−3.49	3.60
July								
I	−1.65	1.56	0.13	0.98	−0.33	3.21	−3.65	3.05
II	−1.52	1.56	0.06	0.94	−0.11	3.03	−3.77	3.36
III	−1.98	1.57	0.02	1.07	−0.34	3.17	−4.09	3.57
IV	−1.67	1.59	0.04	1.00	−0.27	3.31	−5.00	3.14
August								
I	−1.72	1.56	0.07	1.00	−0.27	3.05	−3.90	3.06
II	−1.79	1.61	0.06	1.03	−0.21	3.04	−3.78	3.97
III	−1.80	1.59	0.08	1.03	−0.32	3.32	−4.30	3.47
IV	−1.60	1.53	0.06	0.95	−0.19	3.15	−3.89	2.97

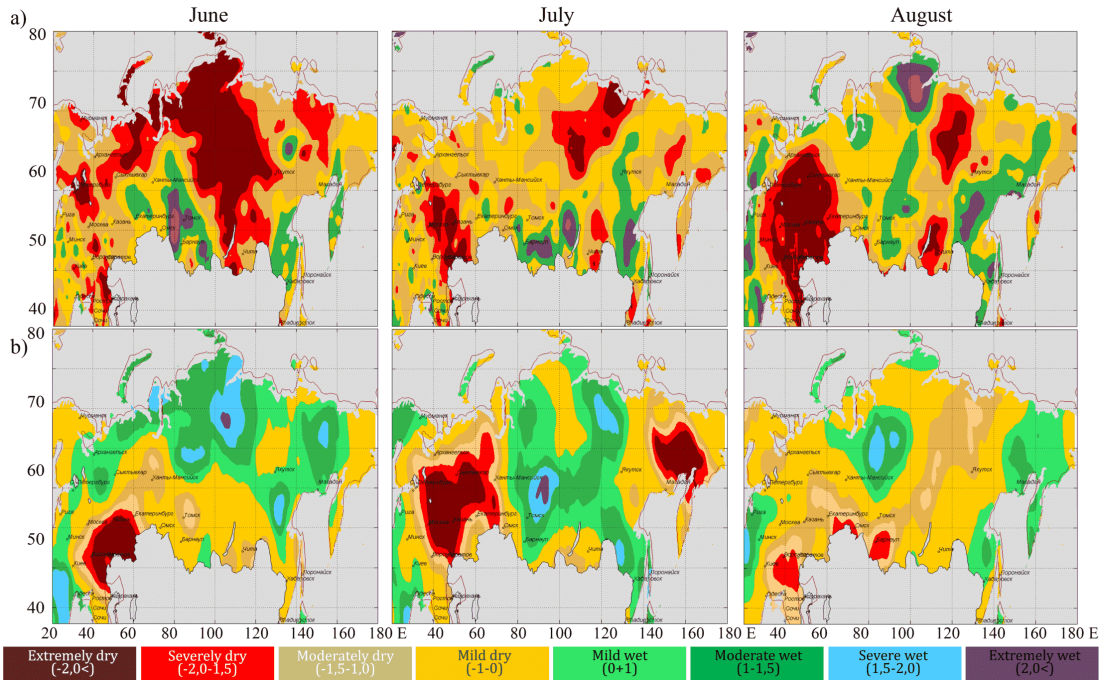

Figure 5.6: SPI-1 values for the most extreme drought events in Russia in a) 1972 and b) 2010 during the boreal summer (left to right -June, July, August).

In the EPR we observed a tendency towards more droughts in June, in turn the wetness increases by August and drought decreases accordingly. Both gradations clearly manifest themselves in June in the APR: drought prevails and wetness decreases by July; as mentioned above, they both tend to decrease in August. This situation has become more pronounced in recent years (period IV).

For further analysis we identified cases corresponding to values below the 5% quantile for dry and above the 95% quantile for wet evens. Since the 5/95% quantiles identify the most extreme cases and are different for each point, we classify them according to the SPI gradation and visualise the spatial distribution for each case (Fig. 5.7 a, b). Both maps identify by green color all values where the corresponding quantiles correspond to absolute SPI values of >2 (indicating extreme events); the purple color is for SPI values within the gradation $[-2, -1.5]$ and $[1.5, 2]$ for dry and wet events, respectively (severe events), and finally, the yellow color represents moderate events with SPI within $[-1.5, -1]$ or $[1.0, 1.5]$. Figure 5.7 (a) highlights that droughts have been especially recorded in the southern and western regions, in the European North, Southern Siberia, Primorye and Khabarovsk regions. Lower frequency of droughts is observed in the northern regions. The spatial distribution of drought changes during the summer: extreme droughts mainly accumulate in the southwestern regions in June, cover the whole south, however they also noticed in the Murmansk region in the north, and the southern part of the Far East, especially in July. In August droughts propagate to cover almost the whole territory of Russia. Figure 5.7 (b) shows the same analysis

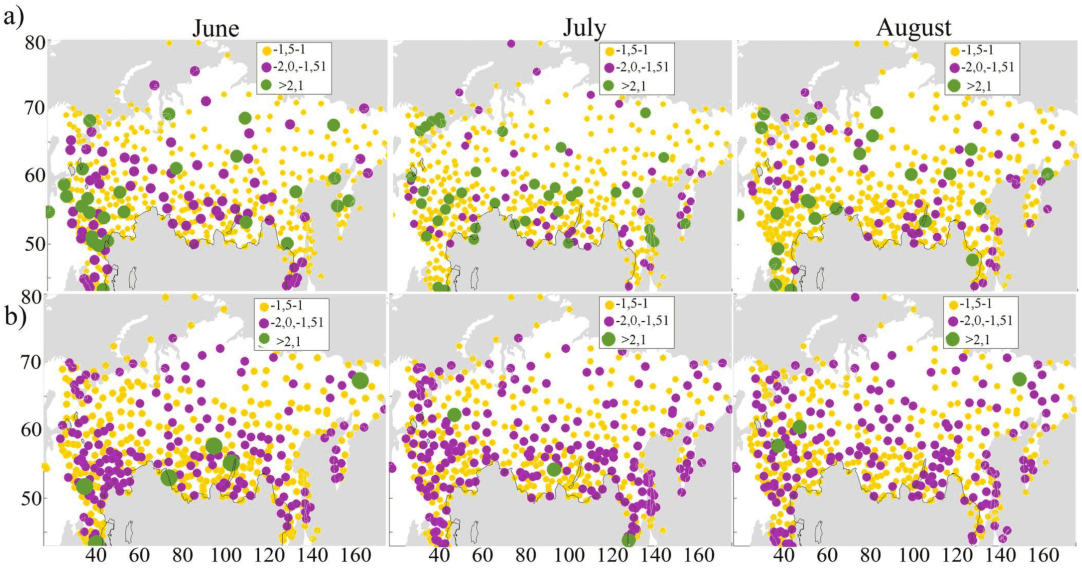

Figure 5.7: Spatial distribution of the a) 5th percentile for drought events b) 95th percentile for wet events over Russia (left to right: June, July, August in the SPI gradations).

for wet events. It is found that the severe gradation is the most frequently observed. Wet events can be observed almost over whole Russia as opposite to droughts, as well as in the northerneast regions (e.g., Yakutia, Chukchi Peninsula) and western Siberia (Krasnoyarsk regions) wet events are observed more often. The highest number of wet events are recorded in June, and the fewest in July.

5.2.3 Long-term variability

Regarding the long-term trends of drought and wet events over the EPR and APR for the study period, we identify a decrease in drought events for the EPR in June and August, with an increase in July (Fig. 5.8 a). The results are opposite for wet events: an increase in June and August and a decrease in July. The coefficients of the linear trends for both types of events are maximal in July with different signs, i.e., drought increases and wetness decreases. The statistical significance of the coefficients of the linear trend is confirmed with a confidence of 93% for drought and 92.5% for wetness in June, while the p-values of Student's t-test indicate statistical insignificance for both, dry and wet events in July and August. The behaviour of drought and wetness in the APR is similar to that observed for drought and wetness in the EPR, with an increase of drought (Fig. 5.8 b) and decrease in wet events.

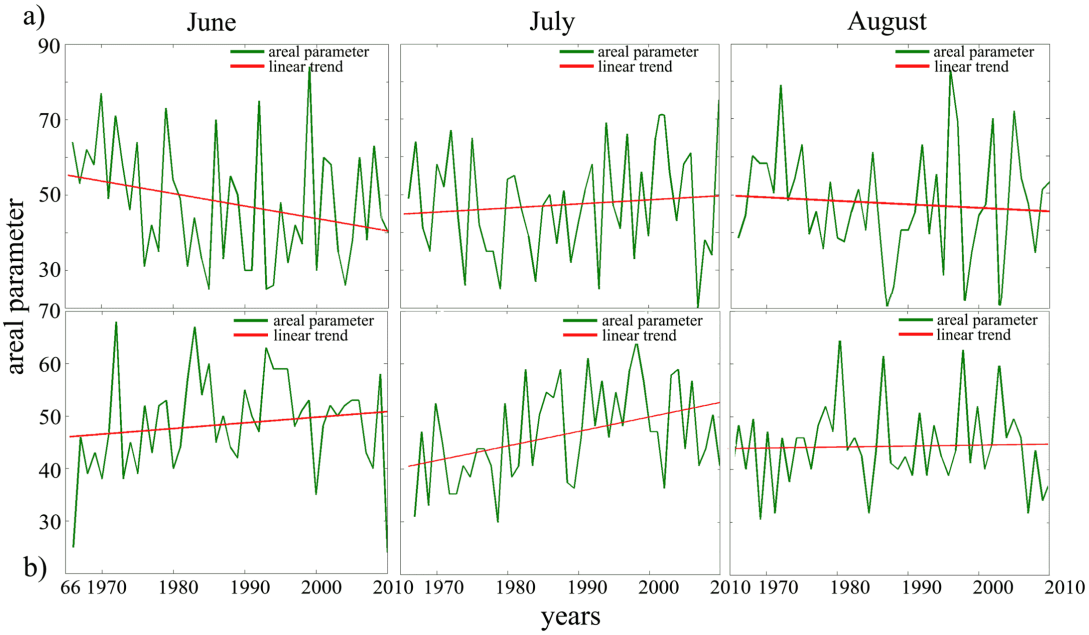

Figure 5.8: Long-term trends of drought distribution in terms of Pl value in the a) EPR and b) APR (left to right - June, July, August).

5.3 Synoptic analysis of extreme SPI events

Variations in atmospheric circulation regimes associated with changes in the global and regional climate affect the frequency and intensity of climatic extremes, which in turn exert considerable influence on overall biodiversity (Barry et al. 2009). The formation of droughts and extreme wet events of different duration and intensity is caused by many factors, and by the complex physical mechanisms of their interactions ("Adoption of the Paris Agreement" 2015).

Macrocirculation processes are among the most important factors contributing to the development of drought and wet conditions. Cherenkova et al. (2015) described relationships between the development of large-scale circulation and the corresponding influence on the frequency of extreme events within the period 1936-2000. Climate forecasts demonstrate that the general planetary temperature rises and, hence, the frequency of extreme droughts is increasing (IPCC 2013). In addition, arid areas currently cover up to 1/5 of the whole surface of the Earth (Cherenkova 2007). Studying the climate dynamics of arid zones will enable to make correct strategic and management decisions, since phenomena like desertification and persistent droughts have a direct influence on socio-economics.

5.3.1 Drought events

Cherenkova et al. (2015) provided an analysis of extreme drought frequency over Russia using different drought indices, including the Russian agricultural drought index (Selyaninov GTK) and the Palmer index (PSDI) - along with a typification of elementary circulation mechanisms (ECMs) in the Northern Hemisphere (NH) developed by Dzerdzeevskii (1968). This study revealed spatio-temporal key features of drought conditions and a trend towards the formation of more frequent drought conditions in the NH based on the analysis of the dynamics of durations of circulation types, especially blocking processes in the European sector. The blocking processes and, as a result, extreme weather events are oftenly caused by highly amplitude quasistationary midlatitude planetary waves (Petoukhov et al. 2016). Coumou et al. (2014) demonstrated that most of the summer extremes have been associated with anomalous jet stream circulation patterns characterized by persistent high-amplitude quasi-stationary Rossby waves. Also, they noticed a weakening of the zonal mean jet, which causes, in turn, meridional circulation patterns. Furthermore, the anomalous circulation regimes cause persistent surface weather conditions resulting in a midlatitude synchronization of extreme heat and rainfall events on monthly time-scales. One of the most extremely persistent blocking anticyclones was observed in 2010. That summer experienced catastrophic droughts, which became subjects of high research interest not only in Russia but worldwide. Some studies explaining the genesis and detailing the formation of this extreme event (Cherenkova et al. 2015; Lupo et al. 2012; Volodin 2011) sought to reveal the regularities of extreme event formation and potential localisation and indicated that the obtained information can be effectively implemented into forecasting of extreme weather conditions.
Here a synoptic analysis is provided by applying composite maps (Fig. 5.9) representing superimposed fields of mean sea level pressure (MSLP) with visualized SPI. The MSLP maps play an important role in such analyse, since they demonstrate the distribution of pressure systems in the atmospheric boundary layer. This helps us to associate the zones of extreme drought/wet events with the pressure systems (anticyclones/cyclones) causing these extremes. In turn, the location of pressure systems explains the weather situation and helps to predict future conditions of the atmosphere by using different types of typifications of weather processes. In this thesis, we described the identified extreme weather events with Katz' typification of atmospheric processes (Katz 1960), commonly used by long-range operational weather predictions in weather agencies of the former USSR countries. Katz grouped the cases of extreme drought and wet events into several classes according to the configuration of the pressure fields involved. This enables referring to a certain type of process for each extreme drought or wet event. The analysis of maps obtained for 500 and 850 geopotential height reveal the presence of blocking processes in all cases of extreme events presented in Table 5.3. In this part of the work, the identified cases are separated into groups within a synoptic description characterising each group.

1. *Group I with the centre of the pressure system over Eastern Europe* includes the

following cases: June 1979, July 1994. Both events have been characterized by similar locations of the main synoptic structures. Drought formation was caused by an anticyclone, located in the area of 40-60°N and 10-40°E. East of it a deep cyclone was found (50-100°E) that provided air masses from the Arctic (Fig. 5.9 a, b).

2. *Group II with the centre of the pressure system over the EPR* includes three cases: August 1972, August 1996, and July 2010. These anticyclones were located further to the east compared with the first group and encompassed almost the whole EPR up to 70°E. In comparison with group I, the cyclones also shifted to the east up to 140°E (Fig. 5.9 c, d, e).

3. *Group III with the centre of the anticyclone over the Urals and West Siberia* includes the following cases: June 1972, August 1981, and July-August 2013. In this group the high-pressure formation covered almost the half of the territory of Russia (50-120°) and caused an extreme drought over a larger region. West and east of the anticyclone, two troughs were located which cause intensive moisturisation in these regions. Figure 5.10 clearly demonstrates the location of pressure formations (cyclones and anticyclones) caused such event.

4. *Group IV with the centre of the anticyclone over Siberia and West Yakutia* includes the following cases: June 1983, July 1998, August 2003, and June-July 2012. One main anticyclone can be identified, with the covered area being about two times smaller than for those areas in the third group, which favours a precipitation deficit in the region. The pressure field on the east of this anticyclone was unstable. The anticyclones in these cases were located within the range of 65-100°E. A striking example of this group was found in 2012. An extreme drought accompanied by forest fires has been observed over Siberia, especially over its central and southern parts, during the period of early June to the first ten days of August (Fig. 5.11).

For the cases from the EPR (groups I and II), the separated groups have been compared with Katz's weather typification (Katz 1960). In this typification, the author divided the weather processes into two types: zonal and meridional. Both are described using circulation indices, which characterise the intensity of air mass transport in zonal and meridional directions. The zonal index is the mean pressure gradient between the meridians bounding the region of interest; the meridional index is the mean pressure gradient between parallels bounding the region of interest; the general index is the ratio between zonal and meridional circulation indicies (Katz 1960). Different combinations of pressure gradient signs indicate the geographic localization of pressure systems in the upper-air (850 and 500 hPa) pressure fields. For instance, the consecutive combination of two positive and two negative signs of geopotential zonal gradients means that the axis of the upper-level trough (the centre of the cyclone) is located in the area where the gradient sign changes from positive to negative. In the zonal type air

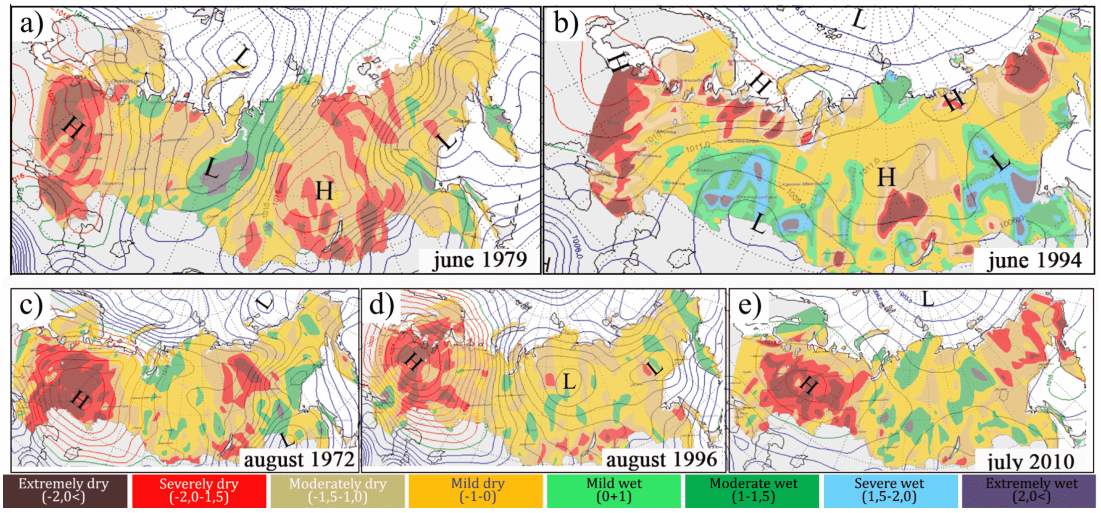

Figure 5.9: Composite maps of SPI and MSLP for the first group: a) June 1979, b) July 1994; second group: c) August 1972, d) August 1996, e) July 2010. L - low pressure, H - high pressure, the lines are isobars.

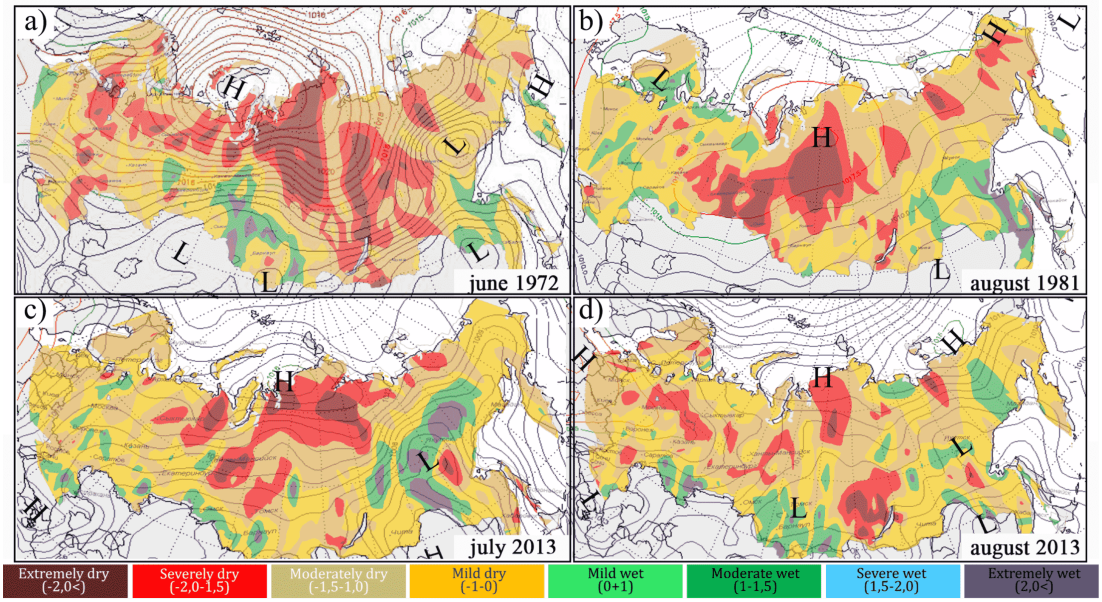

Figure 5.10: Same as in Figure 5.9 for the third group: a) June 1982, b) August 1981, c) July 2013, d) August 2013.

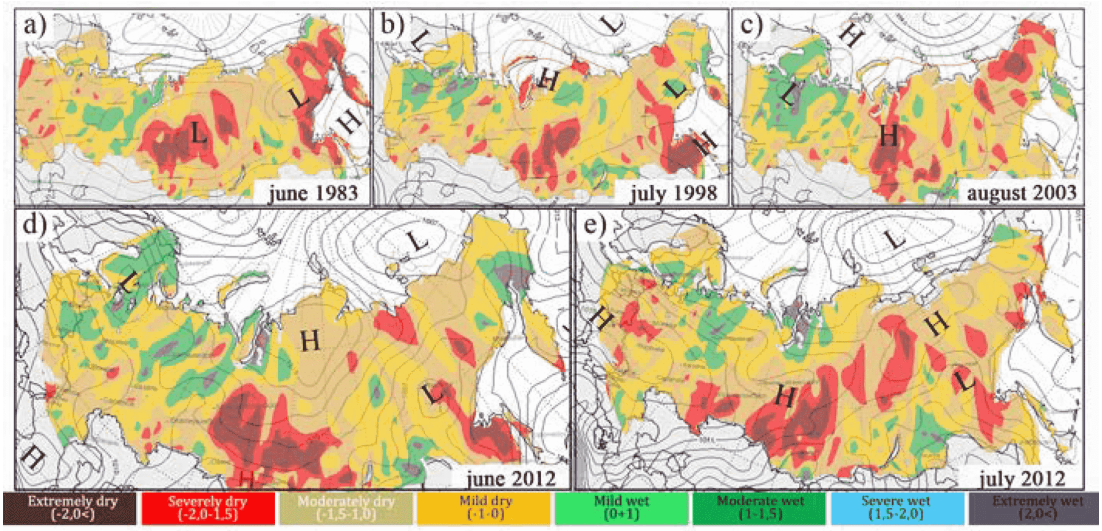

Figure 5.11: Same as in Figure 5.9 for the fourth group: a) June 1983, b) July 1998, c) August 2003, d) June 2012, e) July 2012.

masses flow from west to east along around a latitudinal band. Different combinations of gradient signs are used to define four types of meridional circulation.

- In the *"C" circulation type* (with central position of the ridge relative to Europe and West Siberia), an upper-level ridge is located over the centre of the EPR with the upper-level troughs on its eastern side.

- The *"E" circulation type* (eastern position of the upper-level ridge) presupposes the presence of an upper-level trough over Western Europe and an upper-air ridge in the east of the EPR and over West Siberia.

- The *"W" circulation type* (western position of the upper-level ridge) experiences an upper-level ridge over Western Europe (or over the British Isles) and an upper-level trough east of it, with the axis directed to the southeast part of the EPR/West Siberia.

- The *"N" circulation type* (mixed type) represents two ridges located west and east of an upper-level trough with the axis passing through the centre of the EPR. Thus, this circulation type can be seen as a combination of the "W" and "E" types (Katz 1960).

Visual assessment of the separated groups for extreme drought episodes demonstrates that the first and second groups (anticyclones over the EPR) correspond to the "C" circulation type (central type), while the third and fourth groups (anticyclones over the APR) coincide with the "N" circulation type.

5.3.2 Wet events

According to the SPI gradation, all values above zero characterize wet conditions. In most parts of Russia, wetness is associated with precipitation observed along atmospheric fronts. To carry out a synoptic analysis of precipitation genesis, information about natural synoptic periods (NSPs) for every month is obtained. Normally, a NSP has a duration 3-7 days. Some preliminary explanations and definitions at NSP and natural synoptic regions (NSR) have been already given in the Section 2.1. Information about NSP for the first NSR is stored at the Division for Long-Range Weather Forecasting at the Hydrometcentre of Russia. Due to the absence of data on NSP for the second NSR covering the APR, a similar analysis for the APR is not provided here. The synoptic analysis is based on the charts of the 500 and 850 hPa geopotential height levels and MSLP for each observed extreme wet event. To complete the analysis, we use the observed values for daily precipitation in the gradation of "very heavy rain" (15-49 mm per 12 hours) and "extreme rain" (50 mm or more per 12 hours) according to the Hydrometcentre of Russia[6]. The plotted precipitation maps and pressure maps are enabled us to explain the genesis of heavy and extremely heavy precipitation in certain regions (see an example of such map in Figure 5.12).

These exists a clear relation of the amount of precipitation and the duration of NSP with the prevailing cyclonic activity affecting the moisture content of the region. As shown in Section 5.3.1, blocking processes are observed over the study region in cases of extreme drought formation. In contrast, extreme wet gradations can be established not only during meridional circulation, but also within zonal circulation, where a series of active humid cyclones pass over the same region multiple times during one month or sometimes both circulation types (zonal and meridional) can be observed during the same month in different NSPs causing extreme precipitation amounts.

The episode in June 2005 describes such situation clearly (Fig. 5.12); "extreme rain" was registered during two different NSPs within one month. The first period was observed from June 6 to 11, when a series of active cyclones with the zonal circulation type and producing heavy rain passed over the midlatitudes of the EPR. During the second period, June 20 to 23, transformation of the planetary upper level frontal zone (PUFZ) took place and an active moisturised cyclone was generated over the EPR and blocked by two anticyclones in the west and east. This configuration of the PUFZ caused enduring precipitation.

The episodes of extreme wetness are compared with the catalogue of Katz's typification of weather processes. The assessment of the separated cases of heavy precipitation (Table 5.3) over the EPR revealed that the events during June 1981, June 2005, and August 2006 can be referred to as "C" - type circulation, and those of July 1998, July 2000, August 2003, and July 2007, as "E" - type circulation. Both types of patterns are characterised by transition zones in the troposphere between high cold cyclones and high warm anticyclones, called upper-level frontal zones (UFZs). Separate UFZs can merge and form PUFZs that trigger the processes of formation and devel-

[6]https://meteoinfo.ru/images/ media/books-docs/RHM/nast-KPP-2009.pdf

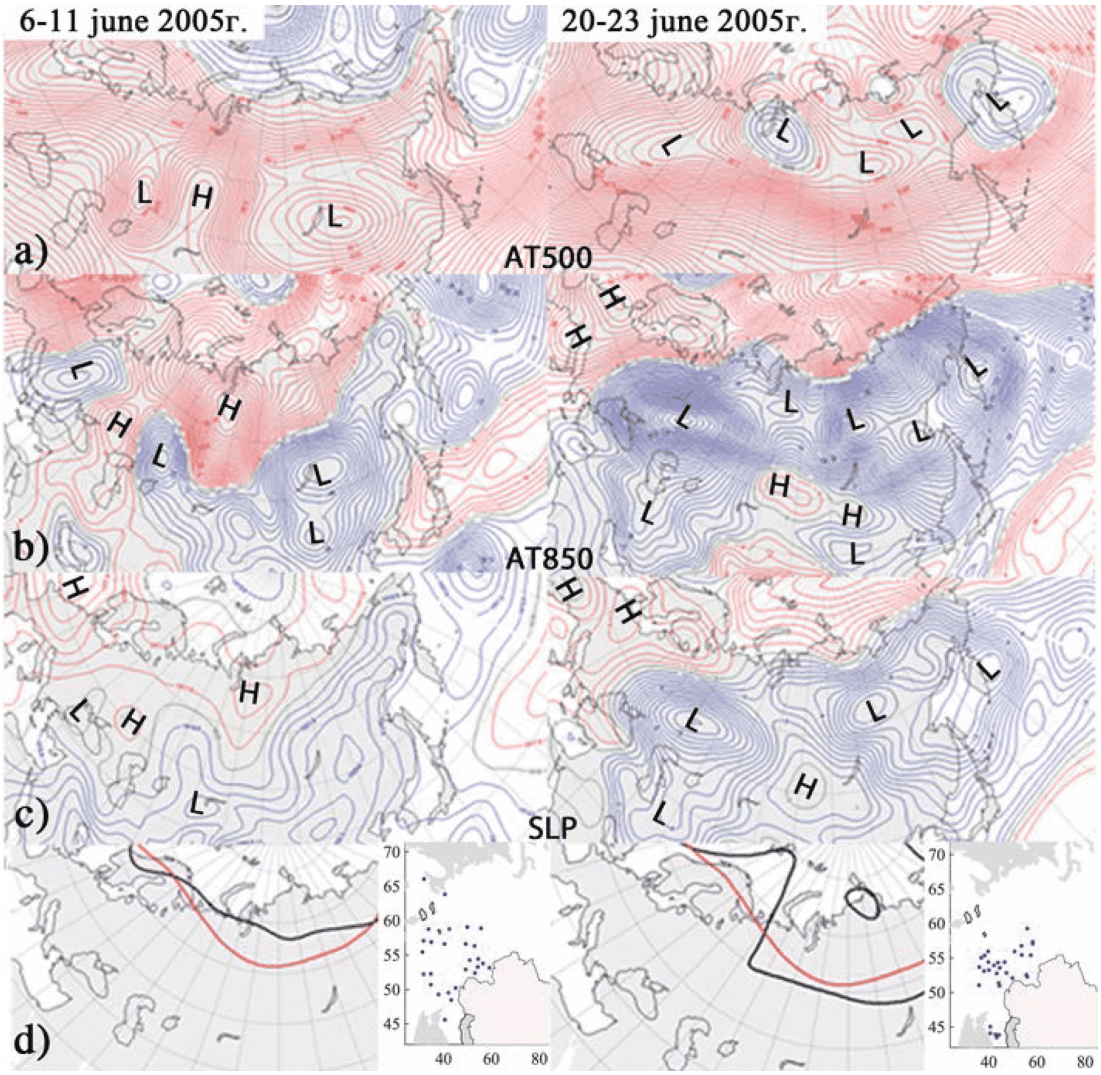

Figure 5.12: The charts for the synoptic analysis of wet events in EPR for June 2005 for two NSPs. a) 500 hPa, b) 850 hPa, c) MSLP, d) maps of actual planetary upper-level frontal zones (PUFZs) and mean normal PUFZs obtained for the period from 1966 to 2013 for the second and fourth NSPs in July 2005 separately. The maps of actual precipitation (right panels of the sub-figure d) for both cases are in "heavy" and "very heavy" gradations. L is low pressure, H is high pressure, the lines are isobars.

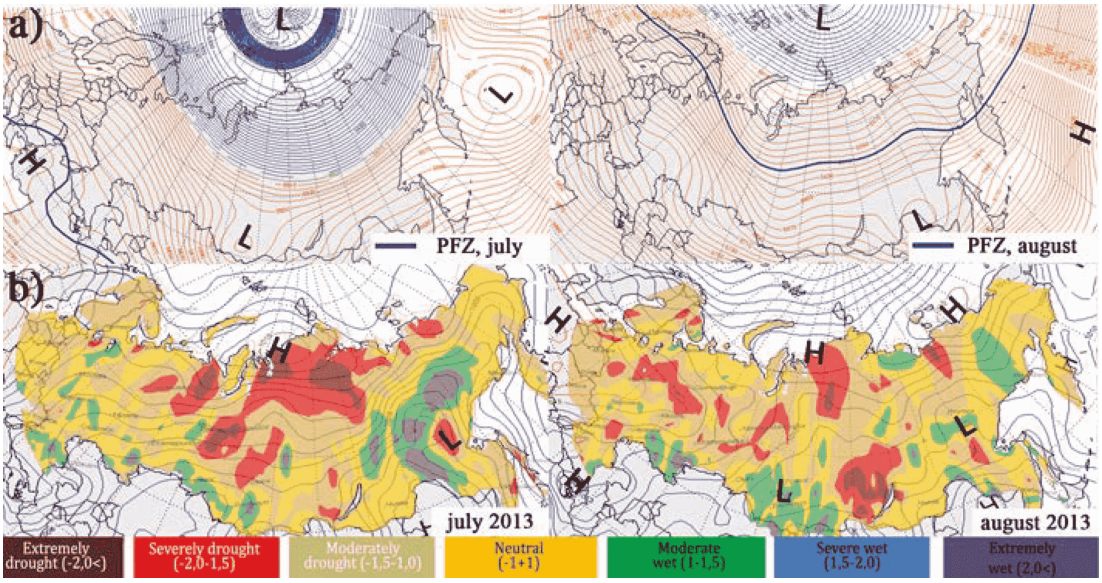

Figure 5.13: a) 500 hPa charts and b) composite maps of SPI and MSLP for the case of extreme floods in July - August 2013 in Far East of Russia. L is low pressure, H is high pressure, the lines are isobars.

opment of cyclones and anticyclones and, hence, the generation of wave processes in the atmosphere. Since heavy and extreme rain in deep cyclones are associated with considerable deviations of PUFZ from its climatological position (for each month) toward the south, we focused our attention on the dynamics and transformation of these frontal zones. We demonstrated the position of PUFZ (Fig. 5.13 a) and composite SPI map (Fig. 5.13 b) for one of the most extreme floods in Far East, happened in July-August 2013. The detailed analysis of existed weather situation shown in Utkuzova et al. (2015b). By comparing contour lines of climatological PUFZ with observed PUFZ during extreme precipitation cases, we noticed a southward shift of the observed PUFZ according to climatological line by 5-25° with the "E" - type circulation (Fig. 5.13 a).

5.4 Correlation of the SPI with teleconnection indices

In Sections 5.3 and 5.2 we have shown that synoptic analysis can help to explain the formation of extremely dry and wet events, and that statistical analysis can help to quantify the occurrence of these events. To continue the discussion on synoptical influences on precipitation formation in Russia we next present an analysis of the associated teleconnection patterns.

In Section 2.3.1, we discussed important teleconnection patterns that influence precipitation formation in different areas of the world. Since teleconnections play a crucial role in long-range precipitation forecasts, and formation of precipitation is controlled by the atmospheric dynamics at different scales, it is necessary to identify meteorolog-

ical variables connected with precipitation that have the potential to serve as predictors. In the present context, the North Atlantic and North Pacific circulation patterns are known to influence meteorological conditions in vast parts of the NH extratropics (Wallace et al. 1981). Specifically, both types of atmospheric circulation patterns have been shown to have an influence on weather in Russia during the boreal winter and spring (Kiktev et al. 2015). In the following, we report statistical evidence that relevant relationships also exist during summer.

In order to uncover the role of the most relevant NH centres of action for the emergence of the summer precipitation patterns over the territory of Russia, we performed a correlation analysis between indices (Barnston et al. 1987; Bell et al. 1995; Wallace et al. 1981) representing these large-scale variability patterns and the observed regional SPI-1 values. Specifically, we focus on the East Atlantic/West Russia pattern (EA/WR); East-Pacific/North Pacific pattern (EP/NP); Polar Eurasian pattern (POL), describing a long-range connection from the Atlantic to Eurasia; and the Scandinavian pattern (SCA), a dipole pattern west and east of the Caspian Sea, all with monthly resolution. High correlation values between the respective indices and observed SPI-1 values during a certain month of the year highlight regions for which possible wet and dry events can be expected to coincide with the respective positive or negative phases of the associated pattern.

The results of our corresponding analysis are shown in Figure 5.14 and confirm that precipitation formation during the summer in the study region is statistically related with (and, thus, most likely influenced by) different large-scale atmospheric circulation patterns in the NH. The strongest positive correlations between the EA/WR index and the monthly SPI-1 fields are found in July and confined to the Southern Ural. A very similar correlation structure is also present for the EP/NP index in July. The latter also shows a notable positive correlation in northwestern Russia during June. In parallel, both patterns also exhibit strongly negative correlations across Western to Central Siberia (especially EP/NP in July), while August lacks any particularly relevant correlation patterns with both indices. POL and SPI-1 exhibit strongly positive mutual correlations, especially in July in the Northern part of Siberia, and marked negative correlations in the EPR. As the summer proceeds, the positive correlations gradually vanish, while the region with negative correlations persists. Finally, the SCA pattern presents strongly positive correlation values during all boreal summer months (especially in July and August) in Southern Yakutia, Eastern Siberia and the western part of the Russian Far East, while strong negative correlations are mainly concentrated in the north of the EPR. All aforementioned statistical interdependencies are characterized by maximum absolute values of correlations between 0.5 and 0.7.

From the analysis detailed above, it is concluded that regions closer to the Atlantic and Pacific Oceans have a tendency toward stronger correlations between SPI-1 values and their possible predictors (related to the aforementioned patterns) in comparison with the more continental parts of Russia. In June, the Northern European and Far-Eastern parts of Russia can be expected to be the regions with the most reliable pressure-based SPI-1 forecasts (especially regarding the significant correlations with the POL and

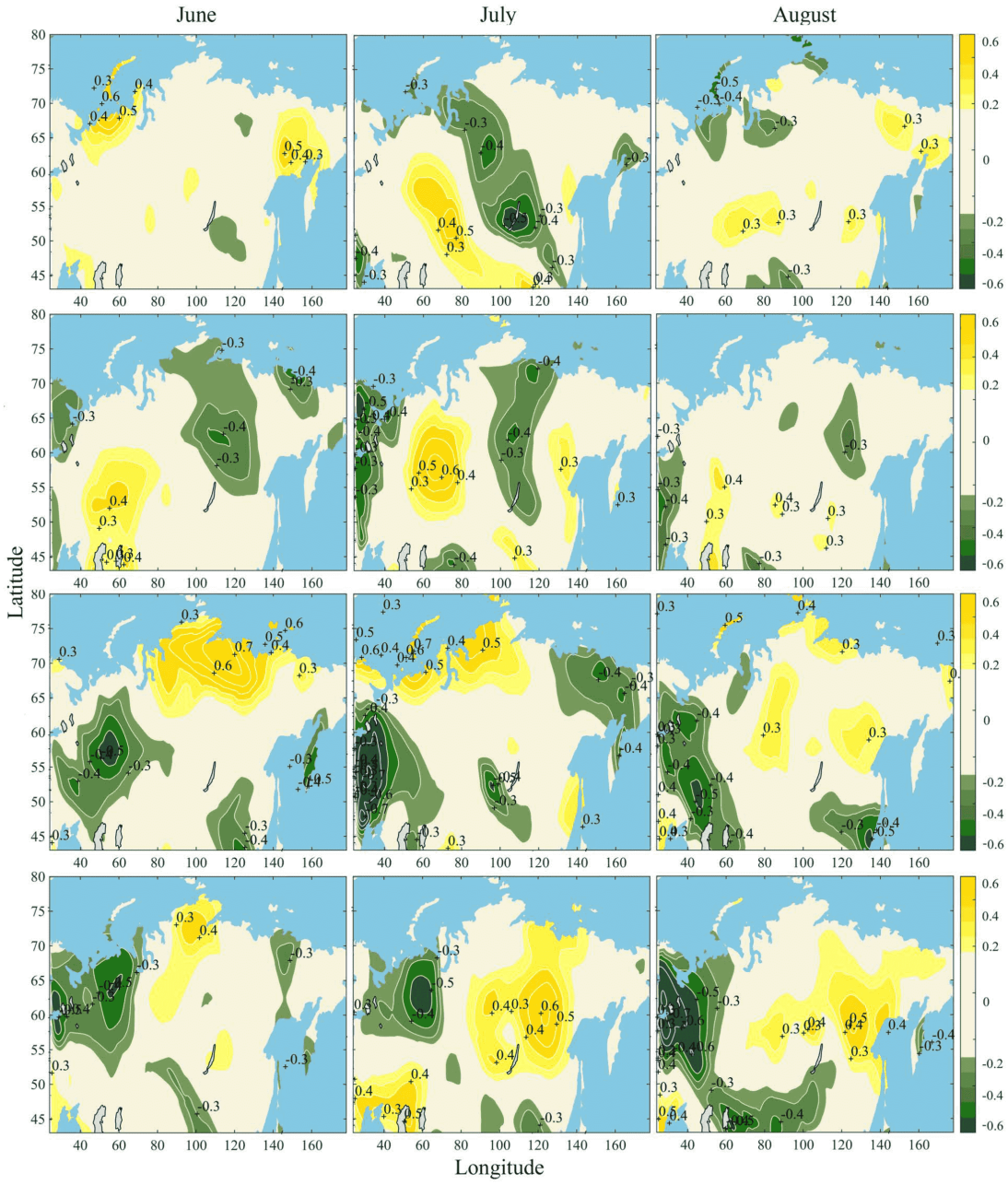

Figure 5.14: Results of local (point-wise) correlation analysis between the CAMS-derived SPI-1 data and different atmospheric circulation patterns: a) EP/NP, b) EA/WR, c) POL and d) SCA) for the boreal summer (from left to right: June, July, August).

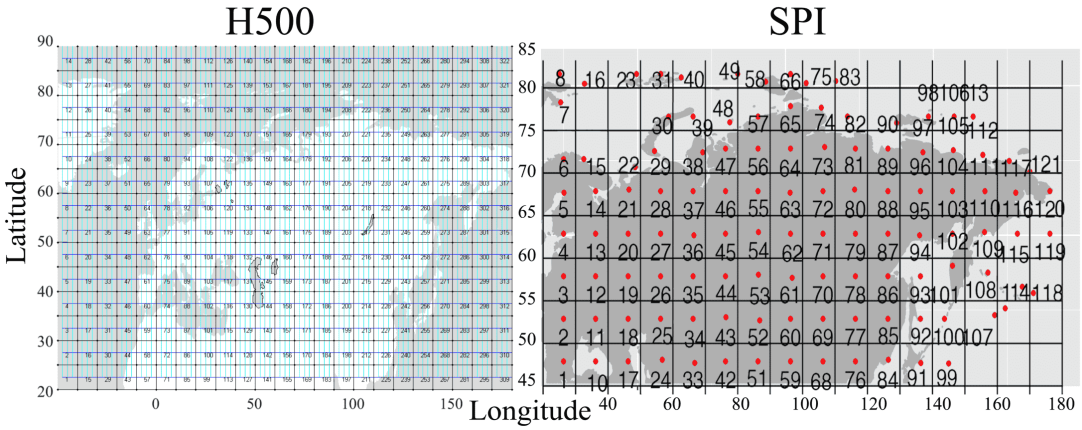

Figure 5.15: Grids with FRs for a) H500 and b) SPI.

SCA patterns in these regions). In July, the regions between 45-60°N and 20-40°E as well as 120-160°E display the strongest correlations with the EA/WR, EP/NP and POL indices. Finally, during August, the region between 50-70°N and 30-60°E presents the highest correlations with the SCA and POL indices. Taken together, these results increase confidence in the potential to estimate the SPI-1 fields based on predictors that are properly selected (independently for each region) using linear regression analysis, which will be demonstrated in the following sections.

5.5 Statistical forecasting scheme for Russia

5.5.1 Selection of predictors

In order to identify potential informative predictors for the regional SPI-1 fields over entire Russia, we perform a detailed cross-correlation analysis of the H500 and MSLP of the SL-AV hindcast data sets. For evaluating possibly relevant cross-correlations, we fix the spatial range for both predictands to 20-90°N and 50°W to 180°E. This area is chosen to cover the Northern part of the Atlantic, Pacific and Arctic oceans as well as continental parts of Northern Eurasia. The SPI-1 fields are obtained from the CAMS precipitation data within the region of 40-90°N and 20-180°E. In order to reduce the corresponding amount of pairwise correlations and account for the fact that very detailed regional resolution is hard to achieve and interpret, we divide the aforementioned regions into larger spatial sub-regions, each covering 5 (10°) in latitude (longitude) instead of working with the native spatial resolution of the data (2.5°). This coarse-graining procedure resulted in 322 grid cells for the SL-AV data sets. From the CAMS-derived SPI-1 data, 121 of the resulting cells are considered as FRs, all of which cover at least some part of the land surface of Russia (Fig. 5.15).
The coarse-graining of the predictor (H500 and MSLP) and target (SPI-1) fields is achieved by representing each resulting grid cell by its geographical centre and com-

puting a weighted mean (with weights according to the spatial distance to the centre of each cell) over the data for all original grid points that contribute to each respective cell. Based upon this, reduced data sets are obtained, defining potential predictors for the SPI-1 values in each FR as spatial regions in which the respective pressure variable exhibited an absolute correlation value above 0.4 (with statistical significance beyond the 95% confidence level) with respect to the target SPI-1 value for a given calendar month (i.e., separately for the three boreal summer months June, July and August). By this analysis we identify a set of candidate regions in the H500 and MSLP fields from SL-AV that might serve as informative predictors for each FR and each calendar month for which SPI-1 is to be predicted. Notably, these candidate regions have a tendency to cluster in space.
In order to obtain a robust and numerically feasible forecasting scheme, we further reduce the number of individual candidate regions to a set of predictors by selecting the weighted mean value for each group of candidate regions that meets the following conditions (see Figure 5.16 for a schematic illustration): (i) minimum size of three sub-regions, (ii) spatial connectedness (i.e., each region in a group needed to have at least one direct neighbour region that belongs to the same cluster) and (iii) stability (i.e., groups used for predicting SPI-1 values at neighbouring regions need to have a sufficiently large overlap). For the purposes of this case study, the latter requirement is manually checked for all pairs of FRs, while a more formal and automatically testable criterion for spatial overlap is used in the later West African case study (see Section 6.4.1) to increase its objectivity. Taken together, our reduction procedure results in a comparatively small set of predictors, which are subsequently used in the forecasting step (see below). Note that while most FRs are associated with several predictor combinations (typically of the order of 5-10), there are others for which our approach does not result in any suitable pair of predictor variables from the MSLP and H500 fields. As a consequence, from the initial 121 FRs, the predictor selection left us with pressure covariates allowing SPI-1 forecasts for 81, 73 and 78 FRs for June, July and August, respectively.

5.5.2 Scheme description and implementation

In Section 5.5.1, it has been demonstrated that both H500 and MSLP exhibit regions that show strong co-variability with local SPI-1 changes over the Russian Federation. Motivated by this finding, we hypothesize that combinations of potential H500 and MSLP predictors thus derived can be utilized to constrain the expected SPI-1 values for any given grid point, together with their associated uncertainty. Specifically, we propose using model 1 (Section 4.3.1) in which all possible pairwise combinations of individual H500 and MSLP predictors identified in Section 5.5.1 are considered to form a set of linear regression equations for the predictand (local SPI-1 value) for the corresponding FR and calender month of interest. Note, that it would be equally possible to utilize combinations of more than two predictor variables from the considered set of candidate predictors, as well as pairs of variables stemming from the

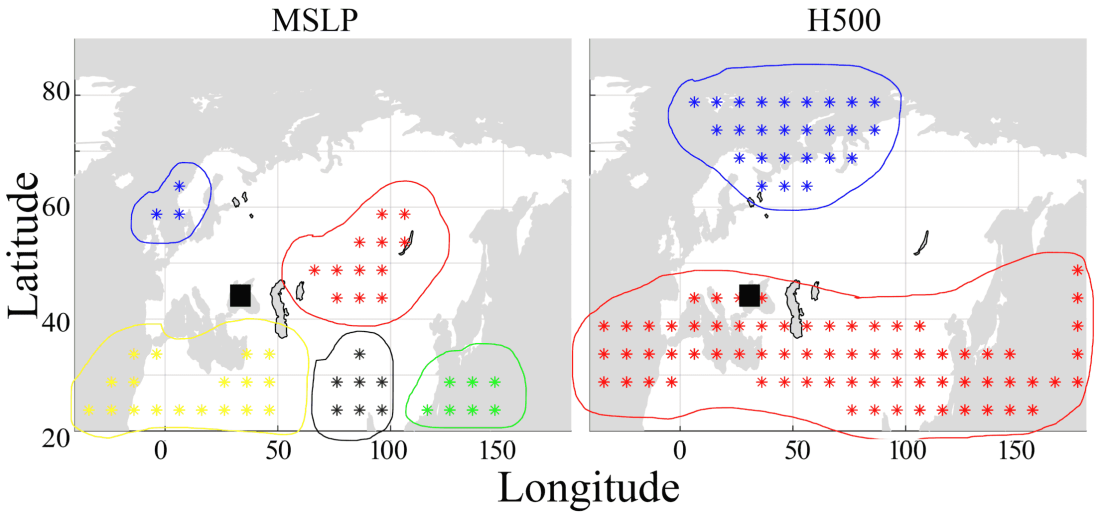

Figure 5.16: Schematic illustration of the selection of informative predictors. The black square depicts the forecast region (FR) for which a prediction is to be made for a certain calendar month (for all years with the same set of statistical models, see text), while groups of dots with different colors indicate different informative predictors. In the example illustrated here, 10 independent regression equations can be formed by combining 5 MSLP and 2 H500 predictors to generate the forecast ensemble.

same pressure field. To this end, we use only pairs of H500 and MSLP predictors on one hand, to reflect the fact that both fields influence SPI-1 and, on the other hand, to keep the regression models as sparse as possible, so the corresponding regression parameters could be well constrained and minimize numerical problems due to a possible collinearity of predictors. Instead, the maximal possible variety of combinations of predictors from the H500 and MSLP fields are utilized to explore the full space of possibilities in the probabilistic forecasting task and capture as much of the associated forecast uncertainty as possible.

Following this rationale, we consider all combinations of pairs of previously identified H500 (x_i) and MSLP (y_j) predictors to provide individual forecasts of the SPI-1 (z_{ij}) for a given FR and month in terms of a set of linear regression equations, as described in Section 4.3.1. By this procedure, each forecasting site is associated with an individual set of linear equations, which are independently solved to generate an ensemble of individual SPI forecasts based on one-month lead-time H500 and MSLP forecasts of the SL-AV model. This set of forecasts can then be exploited in both deterministic and probabilistic ways.

Table 5.5: Summary of verification metrics.

Event type	*BS*	*BSS*	*AUC*
June			
BN	0.16	0.27	0.79
NN	0.20	0.07	0.76
AN	0.17	0.25	0.79
July			
BN	0.17	0.20	0.75
NN	0.21	0.04	0.70
AN	0.19	0.16	0.73
August			
BN	0.14	0.29	0.78
NN	0.18	0.14	0.73
AN	0.16	0.27	0.77

5.6 Forecast verification

5.6.1 Deterministic forecast

In this work we use a deterministic forecast for multiple categories. It is obtained from the set of linear equations by computing the mean over all ensemble members in a single SPI-1 value. This value characterises dry or wet conditions in the SPI-1 gradations for each given FR.

Table 5.2 summarizes verification metrics for characterizing the skills of the direct SPI-1 hindcasts of the SL-AV model together with those of our forecasting model 1 based on one-month lead-time forecasts of H500 and MSLP from SL-AV. Here, "true" and "false" indicate whether or not the deterministic forecast made by our algorithm falls into the same of the seven SPI classes defined by the WMO as the corresponding observation.

In our case, the reliability characteristic ρ (see Section 3.5.1) takes values of around 0.5, with the weakest results for July (0.48), slightly better values in August (0.5) and the highest in June (0.54). The local correlation coefficients vary between 0.27 and 0.73 (Fig. 5.17 a), with the best results again being obtained for June, whereas in July and August, the correlation is generally weaker. Figure 5.17 (a,b) highlights areas with relatively good, as well as such with relatively poor forecast accuracy. Specifically, a good forecast can be expected in June in the northwestern, southern European and far-eastern parts of Russia. In July, reasonable results can be obtained, especially in the Far East and some parts of southern Russia. Finally, in August, we expect acceptable forecasts in the westernmost EPR as well as in the western to central parts of Siberia. The model generally tends to exhibit lower forecast skill for the central

parts of Russia, with maximum values of about 0.5 for both ρ and local correlation, which meets the expectations raised by the spatially distinct influences of different large-scale atmospheric circulation patterns (see Section 5.4).
As additional verification metrics, we also calculated the Mean Absolute Error (MAE) and root mean square error (RMSE) of the SPI-1 forecasts for each FR. Both characteristics indicate good accuracy. In accordance with the metrics discussed above, June is found to be the month with the lowest forecast error (values of 0.11 and 0.35 for MAE and RMSE, respectively). In August, both error measures have slightly higher values (0.15 and 0.38, respectively), whereas July shows the highest values (0.20 and 0.45, respectively). Figure 5.17 (c) shows the corresponding spatial patterns of the RMSE. As expected, in general the lowest errors are found in areas with the highest local correlation and forecast reliability ρ. In turn, large errors together with low correlation and reliability indicate regions with poor forecast accuracy.
In June, small errors can be observed on the Taymyr peninsula, in northern Siberia, some smaller areas in the centre of the EPR, close to the Ural Mountains, and in the Far East of Russia close to the Sea of Okhotsk. In July, larger errors are found in several smaller areas across the entire study region, with the highest values in the southern parts of Russia. In August, much of the EPR, Eastern Siberia on the south of the Russian Far-East exhibit the largest forecast errors. However, there are some regions with relatively small forecast error during all months, like the westernmost part of Russia and some areas in the Far-East.
An additional verification of our deterministic forecasts is provided by the scatter plots between observed and predicted SPI-1 values shown in Figure 5.18. The curves demonstrate the different capabilities of model 1 in catching dry, normal and wet episodes and their intensity in the boreal summer. Based on these results, it is concluded that months classified as having normal weather conditions are not necessarily well-represented in the SPI forecasts. The actual forecast scores depend strongly on the specific region, reflecting different dominant atmospheric circulation patterns in different regions. In general, the deterministic forecasts showed the best accuracy in June and somewhat lower ones in August and July.

5.6.2 Probabilistic forecast

A big advantage of probabilistic forecast is the explicit consideration of forecast uncertainty. Specifically, the probabilistic forecast takes all ensemble members explicitly into account and produces the prediction along with a certain probability of the occurrence of the event of interest. To check the quality of the obtained forecasts, we use two metrics for probabilistic forecast verification: ROC curves and reliability diagrams (as discussed in Section 3.5.2). The corresponding results for our pressure-based forecasts for each class of conditions and each boreal summer month are presented in Figure 5.19 and Table 5.5. The best accuracy is found in June, with a maximum area under the ROC curve (AUC) value of 0.79 for below normal (BN) and above normal (AN) conditions, while a generally lower prediction accuracy is observed for normal

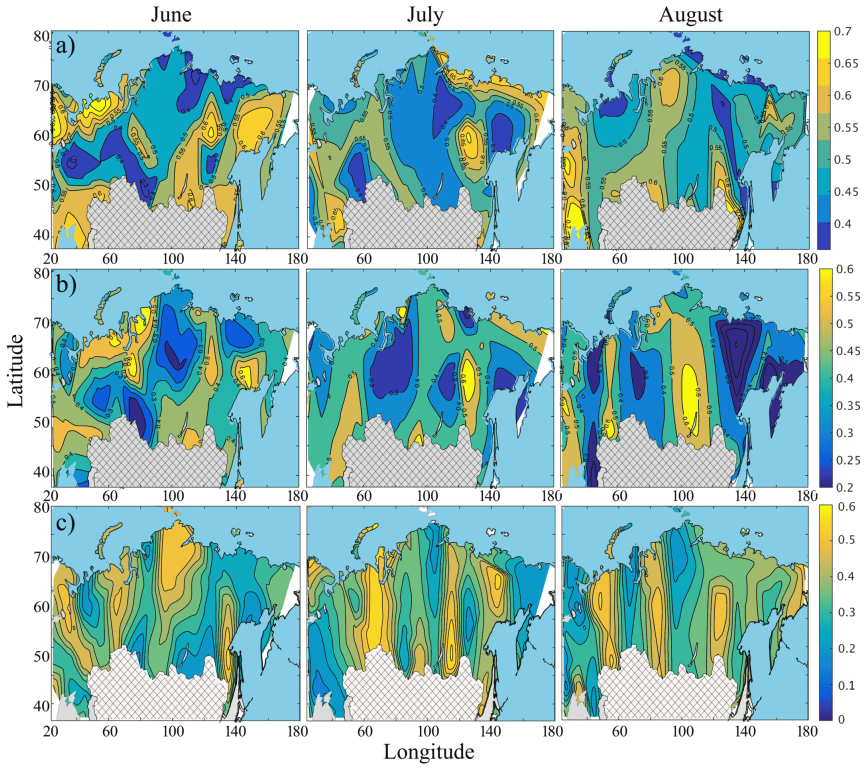

Figure 5.17: Deterministic forecast accuracy: a) local (point-wise) correlation, b) forecast reliability characteristic ρ and c) RMSE between deterministic forecast and CAMS-derived SPI-1 values.

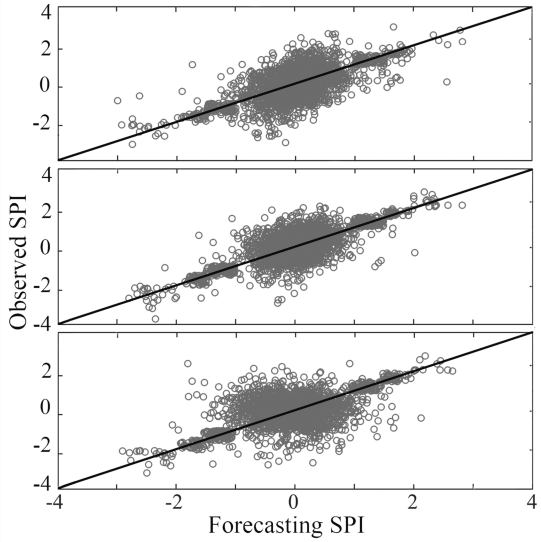

Figure 5.18: Scatter plot between observed and predicted SPI-1 values for the deterministic forecasts for the months June, July and August (from top to bottom).

conditions (0.76). The same ranking between the different types of events is recovered for the two other summer months (with AUC generally slightly higher for dry than for wet conditions). However, the corresponding AUC values are consistently lower for August than for June and indicate the lowest forecast accuracy for July.
Figure 5.20 shows the resulting reliability diagrams. The corresponding values of Brier Score (BS), Brier score baseline (BSB) and Brier Skill Score (BSS) are provided in Table 5.5. The best skills are identified (highest BSS) for all three types of conditions during August, slightly less skilful forecasts for June, and the lowest skills for forecasts in July, which resembles the outcome of the ROC analysis. In general, the reliability diagrams indicate the highest reliability (despite not possessing the highest BSS) for the prediction of dry conditions in June. According to Wilks (2011) and Weisheimer et al. (2014) and their classification of characteristic forms in reliability diagrams, in our case, dry and wet conditions generally exhibited good forecast calibration. For wet conditions, the forecast line often lay slightly above the diagonal during June and July, indicating a minor tendency towards underforecasting, except for very high forecast probabilities. In contrast, for dry conditions during August, the reliability curves fall below the main diagonal, revealing a loss of predictive skills at low-to-moderate forecast probabilities. Unlike for wet and dry conditions, the reliability diagrams for normal conditions indicate generally poorer skills of our probabilistic forecasts (yet slightly higher skills than pure climatological forecasts) and reveal a general and stable tendency towards overforecasting at all but the very low forecast probabilities for all boreal summer months.
As for the deterministic forecasts, it should be underlined that the accuracy presented here exhibits large differences among the different regions of Russia due to the differential impact of large-scale atmospheric circulation patterns (not shown). Specifically,

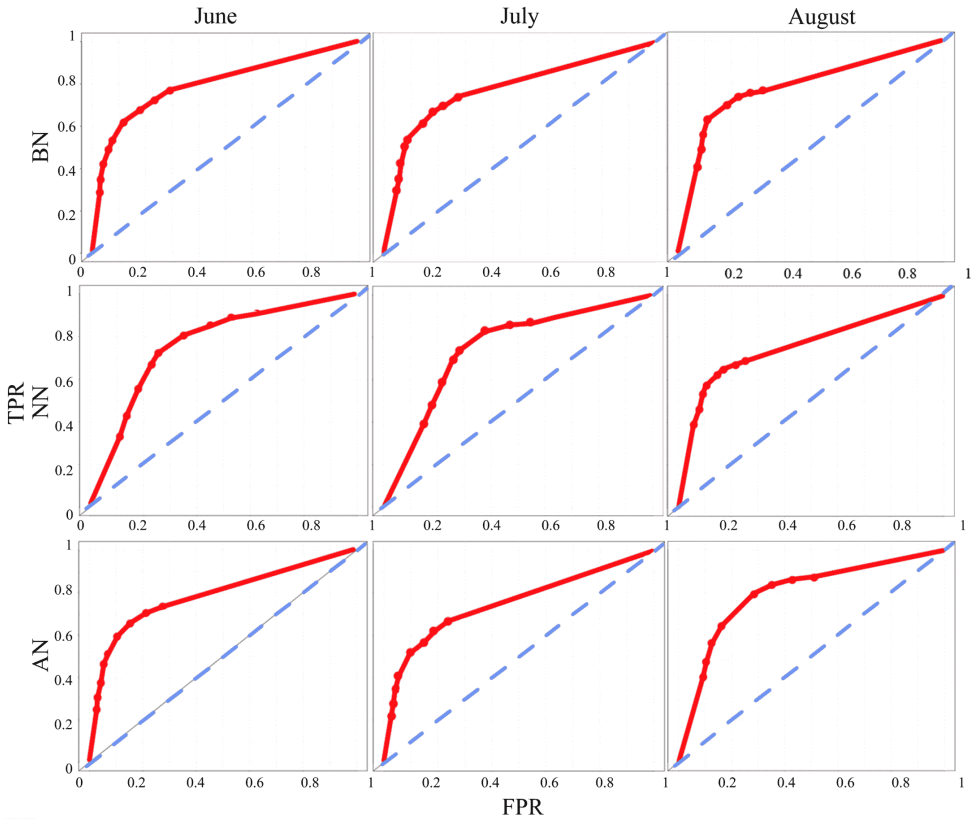

Figure 5.19: ROC curves describing the forecast accuracy for different groups of SPI-1 conditions over Russia during the three boreal summer months.

the influence of the oceans on the formation of extreme precipitation patterns clearly plays a major role for prediction purposes. In summary, it is concluded that the proposed scheme (model 1) provides an improvement of existing direct SPI-1 forecasts based on the SL-AV model. The obtained results are acceptable but still far from being fully satisfactory. Potential improvements to our approach include the replacement of linear by nonlinear statistical relationships, the introduction of probabilistic weights to the individual members of the forecast ensembles according to their expected individual forecast skills, and the reduction of possibly redundant information due to potentially collinear predictors by backward elimination, as in the method introduced by Runge et al. (2015). However, some of these possible improvements are likely to suffer from the small ensemble size (a few decades of one monthly value per year for each regression model).

5.7 Discussion

In this chapter, we compared two data sets (CAMS and ERA-Interim) with monthly precipitation values. We found that CAMS satisfies our needs (good coverage over

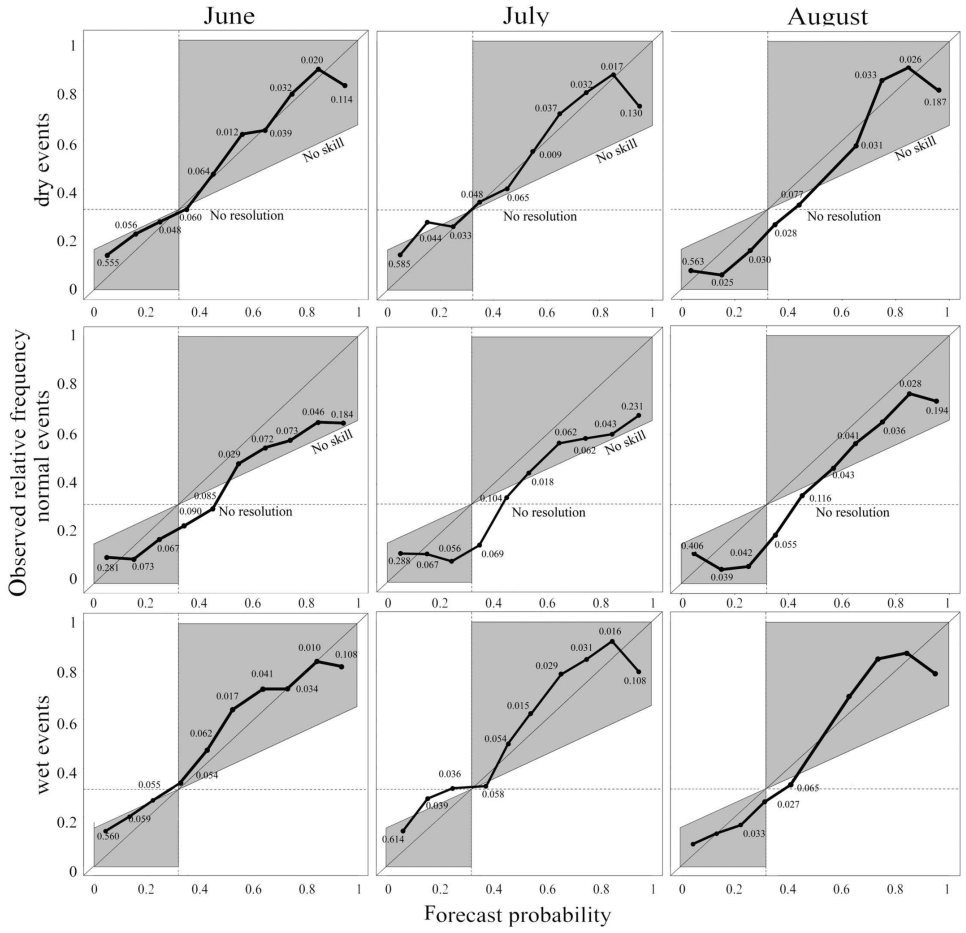

Figure 5.20: Reliability diagrams for probabilistic SPI-1 forecasts of below normal, normal and above normal precipitation conditions over Russia during the three boreal summer months. Point labels give the relative frequencies of use of each forecast probability.

Russia, high quality of precipitation reconstructions, including low amount of missing data in time-series, long period of records and quick update of the archive with the new data) and provides higher quality of data than ERA-Interim. In order to inspect the behaviour of monthly precipitation in terms of the SPI-1 index, we reconstructed this index for the period 1966-2010. During the research period, the SPI-1 index was employed to identify the most extreme dry and wet events observed in Russia. These cases were compared with historical data and confirmed that the SPI-1 provides an adequate and easy-to-understand picture of the spatial distribution of extreme events. Identified cases were analysed by implementing statistical and synoptic analysis tools. Within our statistical analysis, we found an increase in the amplitude of extreme (dry/wet) events during the past 20 years, with a prevalence of wet events over dry events. Trends in the drought distribution over Russia in the summer months have also

been identified. Accordingly, the spread of drought is becoming reduced in June and August and increased in July; wetness propagation increases in June and August and is reduced in July in the EPR.
A catalogue of extreme dry and wet events over Russia was created based on the SPI calculations for the period from 1966 to 2013. This catalogue can be used for different scientific purposes and provided the basis for synoptic analysis. The episodes obtained were categorised into four groups following their synoptic features and subsequently compared with the catalogue of Katz's weather typification. Despite the fact that this weather typification was developed around 50 years ago, the weather charts proposed by Katz still accurately describe weather processes and help to predict atmospheric circulation over the NH in the short (during one NSP) and long range (in this study, up to one month). The analysis of upper-level (850 and 500 hPa) charts demonstrated that extreme wet events can form in cases of both meridional and zonal circulation. With the zonal type, an extreme wet event is possible if a series of cyclones are passing through the same region during a certain period of interest. The duration of NSPs affects the intensity of wetness over Russia. In all extreme drought and wet episodes, the cyclones and anticyclones existed on sea level, 850 hPa and 500 hPa charts.
According to the PUFZ, we observed some common facts in the transformation and dynamics during extreme events. In cases of extreme wetness with cyclones of an "E" circulation type, the planetary frontal zone was displaced by 5-25° to the south relative to the climate mean position. The features of the PUFZ configuration and sea level pressure fields revealed by this study can be used as prognostic indicators for forecasting extreme drought and wet events with different lead-times, e.g., when forecasters observe the southward displacement of PUFZ by 5° and more, they may expect the process of stabilisation of a pressure system in the observed region.
The analysis of teleconnection patterns extended the atmospheric circulation analysis of precipitation formation over Russia. Long-term teleconnection patterns play a crucial role in predicting precipitation for longer periods. We identified that the EA/WR, EP/NP, POL and SCA patterns all have a significant correlation with SPI-1, influencing the summer precipitation formation over Russia. This analysis also shows a tendency for strong correlation between possible pressure-based predictors (H500, MSLP) and SPI-1. This raises confidence in the potential to estimate SPI-1 fields using linear regression analysis based on these variables.
The implementation of the SPI-1 forecasting model 1 was also presented in this Chapter. The detailed procedure of obtaining predictors and regression equations was described. By making use of cross-correlations between SPI-1 and atmospheric pressure fields at sea-level and 500 hPa geopotential height, we developed a new forecasting scheme utilizing selected pressure covariates as informative predictors for regional summer precipitation in a linear regression framework. Regions with significant covariability between observed SPI-1 values and corresponding pressure variables turned out to coincide with spatial locations for which forecasting model 1 commonly yields acceptable results and outperforms previous direct precipitation forecasts. The regression approach developed in the present work can be directly used to formulate both

probabilistic and deterministic forecasting schemes.
We have found that, for the territory of the Russian Federation and the proposed model 1, both deterministic and probabilistic forecasts exhibit good accuracy, with the highest accuracy during June mainly for wet and dry episodes, though some problems persist in capturing normal conditions. The prediction results have been compared to hindcast data, revealing that the proposed prediction scheme (model 1) has great potential for improving forecasts beyond the existing direct precipitation forecasts of the underlying SL-AV model. Thus, the proposed model 1 benefits from the existence of large-scale controls on precipitation formation across Russia, which are most relevant in the western and eastern parts of the country and gradually lose their significance toward central Russia with its more continental climate.

Chapter 6

Spatio-temporal pattern of extreme SPI over West Africa and 0-3 months lead-time SPI-1 forecasts

The region of West Africa (WA) has recently been intensively studied, motivated by its diverse weather conditions and extreme vulnerability to climate change. Weather in the region is shaped by different types of phenomena (monsoon, tropical cyclones, etc.) bringing more frequent natural disasters. Agriculture and the economy are heavily dependent on the rainy season, requiring resilience to constantly adapt to the new conditions resulting from climate change. Year-to-year variations in the timing and amount of precipitation result in economic and human losses. Consequently, it is crucial to perform in-depth analyse on the reasons of such fluctuations and to predict future consequences. In this Chapter we present a comparison between two forecasting models for WA based on the forecasting scheme presented in Section 4.2.

6.1 Data and model

6.1.1 Precipitation data

To understand the changing climatology and for monitoring the rainy season, reliable data is of paramount importance. A dataset suitable for operational precipitation monitoring and forecasting must have consistent time series (without gaps) and be statistically homogeneous (Guttman 1999). By homogeneous, we mean that observation stations should cover the region with the high resolution, have equipment and measuring techniques recommended by WMO and record meteorological parameters at certain times (presented by WMO) with minimal gaps between the measurements. On

a global scale, it is difficult to acquire data with such standards. Of course, the quality and accessibility of observation data depend on the region, e.g., for WA we encountered the problem of accessing high quality observations. Several data sources were considered, but inconsistencies in the amount of precipitation and a lack of a suitable observation period were discovered.

One of the available data sources is provided by NOAA[1] via the Climate Data Online (CDO) tool covering different types of meteorological information with open access. These data initially looked homogeneous, with long term records. However, the monthly precipitation amounts for several stations in WA are undervalued (e.g., for an area with August monthly mean of around 400 mm/month it reported 0-10 mm/month, a value that is obviously too low to be correct). Another potential data provider with higher accuracy is the Koninkijk Nederlands Meteorologisch Instituut (KNMI)[2] in partnership with the WMO Regional Climate Centre, giving the possibility to directly analyse and download climate data for multiple regions. After checking both archives, we found that KNMI provides more realistic values for WA, thus we obtained observational data for the reference period 1983-1997 from 166 weather stations in WA (Fig. 6.1). Years outside this reference period had to be omitted due to missing data.

Since the spatial coverage of observation data is not high enough in order to use these data directly in the forecasting models, huge efforts are currently undertaken to create new reliable precipitation. Today, one of the most popular ways of generating high quality and resolution observation data is combining observed precipitation together with satellite data, providing estimates for every grid point at the required resolution. One of the most popular and reliable data archives providing such estimates is the NOAA/NCEP CPC CAMS (shortly CAMS) data set. It was successfully used in our previous analysis in Russia (see Chapter 5) and has been proven to be a reliable data source (Dutra et al. 2013; Kidd 2001; Manzanas et al. 2014; Rowell et al. 2015; Siebert et al. 2011; Sohn et al. 2012). Also, CAMS is a recommended archive by the African Regional Climate Centre (ARCC). With such recommendation, we expect that CAMS is a good alternative for WA. In order to verify our expectations, we compared it to the reference data. We used monthly data for the period of June-September 1982-2016 with a spatial resolution of 2.5°. In comparison with Russian case study, where we upscaled the initial resolution of CAMS due to decrease computations over such huge area, in WA it was decided to stay with the initial resolution of CAMS, to be able to cover diverse precipitation conditions in details on relatively small area and at the same time to have enough forecasting regions for running the statistical scheme over the region.

In order to provide a detailed drought/wet analysis (see Section 6.2) of the WA region we use high resolution precipitation data. Among others, CHIRPS (Climate Hazards Group InfraRed Precipitation with Station data) is commonly used for seasonal

[1] https://ncdc.noaa.gov/cdo-web/

[2] https://climexp.knmi.nl/

drought monitoring in the African region (June-September, 1982-2016). It presents precipitation obtained by coupling satellite images with meteorological station data with a resolution of 0.05° (Verdin et al. 2016). It is a quasi-global rainfall dataset available for the period from 1981 through to the present day for 50°S - 50°N.

6.1.2 Operational model description

As an operational model, we used the second-generation Climate Forecasts System, CFSv2, running at the National Centers for Environmental Prediction (NCEP). This is a fully coupled ocean-atmosphere-land prediction system, with advanced physics, high resolution, and refined initialization to improve the seasonal climate forecasts (Yuan et al. 2011). The second generation of the CFS model contains improvements of its four technological components, an upgrade of the four-level soil model, an interactive three-layer sea-ice model, and historical prescribed CO_2 concentrations. The four technological components of the CFSv2 model were independently designed. The R2NCEP/DOE Global Reanalysis contains global atmospheric and land surface conditions (Kanamitsu et al. 2002). GODAS is a global ocean data assimilation system that has been operating at NCEP since 2003 (Behringer 2007) and provides the ocean initial states. GFS is a Global Forecasting System and atmospheric model run at a lower resolution (T62L4). MOM4 is the fourth version of an ocean forecasting model from GFDL (Griffies et al. 2004).
The atmospheric model has a spectral triangular truncation in the seven horizontal layers and a finite differencing in the eight vertical layers, with 64 sigma-pressure hybrid layers. The vertical coordinates are the same as in the operational Global Data Assimilation System (GDAS; Saha et al. 2014). As a land surface model, the Noah model is used in CFSv2 for medium-range forecasts (Ek et al. 2003). It should be mentioned that the predictive skill of the model is higher in boreal winter and for target phases when enhanced convection is present in the central Indian and Pacific oceans (Barnston et al. 2013; S. Li et al. 2015; Wang et al. 2014).
CFSv2 produces outputs for 4 different time ranges: subseasonal, 2-6 week predictions over the continental US and for MJO predictions; long-lead seasonal predictions of up to 9 months; decadal and centennial predictions. The model provides hindcast data for the period from 1981 to 2010 with the initial conditions at 0, 6, 12, and 18Z (here Z is the Universal Time Zone) cycles for every 5th day (Saha et al. 2014). For our purpose, we used 9-month retrospective predictions and extracted predictions for the first four months, resulting in 0, 1, 2, and 3lt forecasts for the initial conditions' 12Z cycle. To increase the time period covered by data, we combined re-forecasts with forecast data for 2011-2016. Thus, for further work, we have a period from 1982 to 2016 for the boreal summer months including September (June-September).

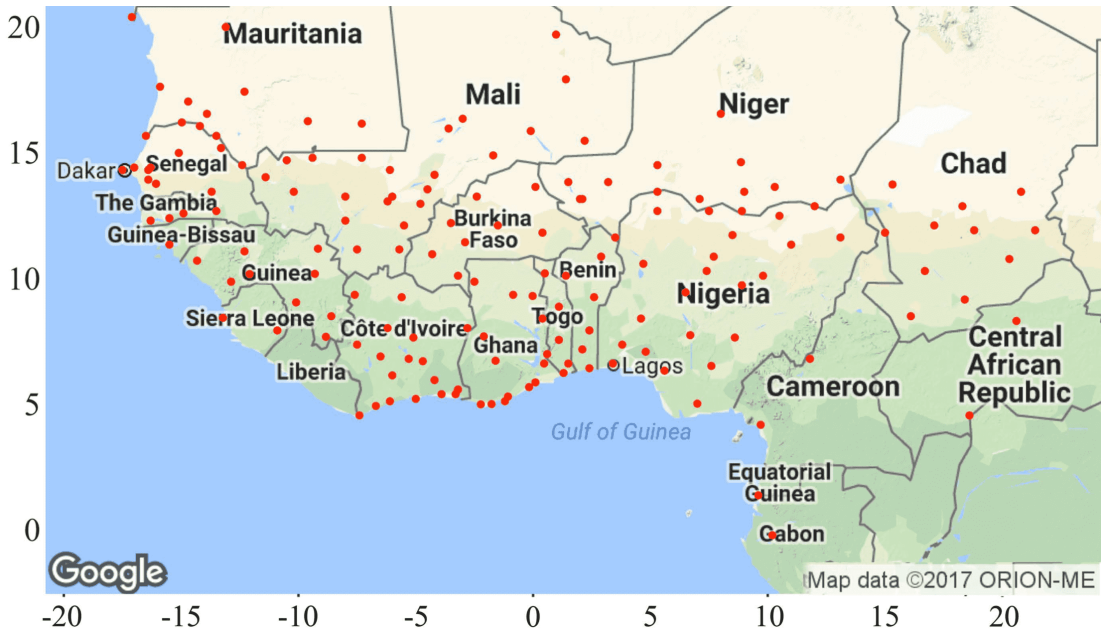

Figure 6.1: Spatial distribution of meteorological stations (red dots) in WA with continuous rain gauge records that have been used as reference data in this study.

6.1.3 SPI-1 calculations based on different datasets

Comparison between precipitation estimates from data archives and observations is essential to this work. Here, we compared the SPI-1 values obtained from station-based precipitation observations with gridded data from CAMS. As displayed in Figure 6.1, station data are not homogeneously distributed, while precipitation varies in WA on a small scale, producing various weather conditions. As it was mentioned before, the observation network is not homogeneous, especially in the southeastern part the distance between stations is quite large. Another problem with the data is the short time series of available good quality observations. Only 16 years are available, and even within this period (1982-1997), there are some gaps found, which have been filled by averages (for stations with not more than 2-3 gaps per considered time period).
As first step, obtained the SPI values from the rain gauge stations and performed correlation analysis between SPI-1 for observational data and CAMS. As seen in Figure 6.2, the correlation between the two data sets is not high. The highest correlation coefficients are found in June in the Sahel area, with the highest concentration of weather stations. In June, August and September, a statistically significant high correlation over Nigeria is noticed. In August and September an area with low correlation is observed over Cameroon, the Central African Republic and the Guinea Coast. The root mean square error (RMSE) values of CAMS compared with observation data range from 0.9 (September) to 1.15 (August).
For drought analysis, the high-resolution CHIRPS archive is used. Gauge and satellite estimates are compared for the period 1982-1997 in terms of SPI-1. We calculated

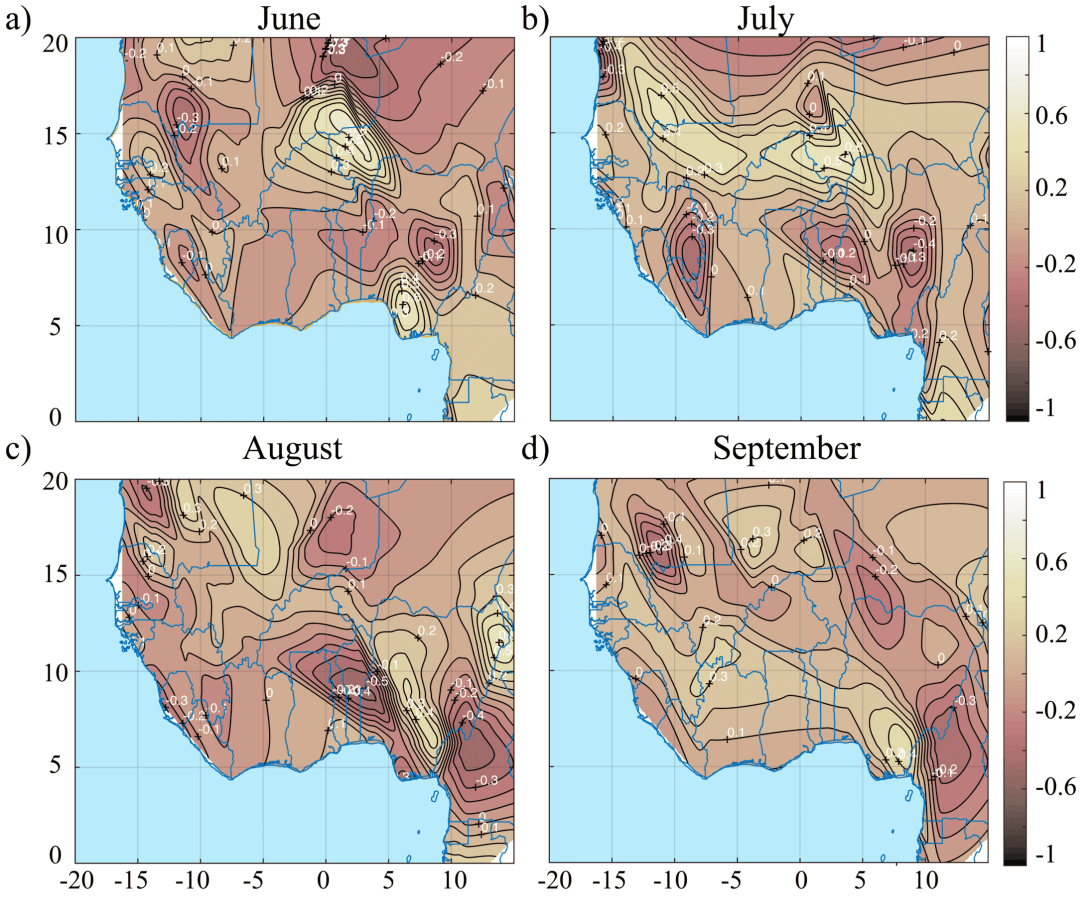

Figure 6.2: Spatial patterns of local (point-wise) correlations between SPI-1 values obtained from direct measurements made at meteorological stations across WA and monthly precipitation data from the neighbouring grid points in the CAMS data sets for the period 1982-1997. a) June, b) July, c) August and d) September.

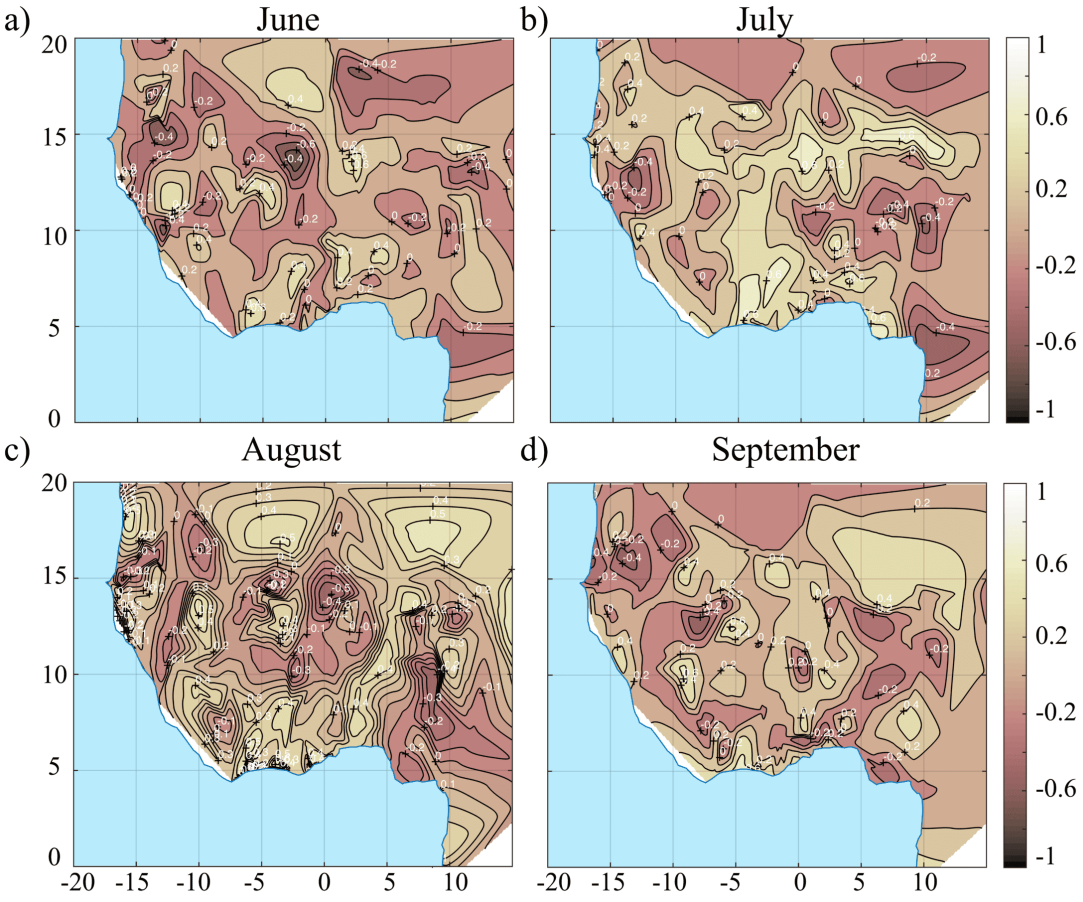

Figure 6.3: Same as in Figure 6.2, but for the CHIRPS data set.

point-wise correlations between CHIRPS and station data (Fig. 6.3). Generally, there is a strong correlation between satellite estimates and observation data; however, the locations of high and low correlation areas are roughly the same as in the analysis with CAMS. The mean values of correlations cluster is around 0.3, whereas the mean correlation for CAMS is lower, around 0.2, and RMSE is identical to CAMS, with the lowest error in July (0.85) and the highest in August (1.2). The results from the correlation analysis for the two data archives are similar, with some fluctuations, however there are no high correlation coefficients obtained. African meteorological centres[3] recommended to use both archives for research and forecasting work, since the quality of observation data is poor.

Next, we studied the behaviour of SPI-1 based on CAMS and raw forecast data taken from the CFSv2 model. We obtained pure precipitation forecasts with up to a three-month lead-time; thus, we had four first month forecasts from the nine-month seasonal hindcasts for the period June-September. The WMO describes lead-time forecasts as follows: 3lt forecast, 2lt forecasts, 1lt forecasts, 0lt forecasts, where the forecast is created for four months, three months, two months, one month ahead and current month, respectively. Normally, these forecasts are obtained in the beginning of the forecasting month (1st day of the month). Following this idea, 0lt forecast is given 1st day of the forecasting month in order to describe weather conditions for the whole month.

An example of SPI-1 patterns based on CAMS and CFSv2 for a randomly selected year, 1988 (all 4 months), a case with extremely wet conditions observed throughout WA is presented in Figure 6.4. This figure indicates differences in spatial patterns; however, the forecast is not always worse at longer lead-times. For example, in the plots shown in Figure 6.4 (c) we observe that the 2lt and the 3lt forecasts predict the current situation with wet events better than at 0lt, which, logically, should be the best forecasts. The reason for this could be the uncertainties of the model, rendering the first forecasting month to be less stable than others because the forecasting system is dynamic. In time, by the second month the system stabilizes and starts to produce more accurate forecasts.

The differences between observational data and forecasts are not only in the localisation, but also in the intensity of the predicted events. In some cases (e.g., August 1988), the model predicted absolutely the opposite situation of what was observed, but for others (e.g., July 1988) the model predictions are acceptable. The correlation analysis also shows a weak relationship between SPI-1 from CAMS and CFSv2 for which the mean correlation values are distributed around 0.1 and the highest absolute values rarely exceed 0.6. These results underline the necessity of the application of a statistical postprocessing scheme to improve the quality of the forecast.

[3] http://acmad.net/rcc/dataservice.php

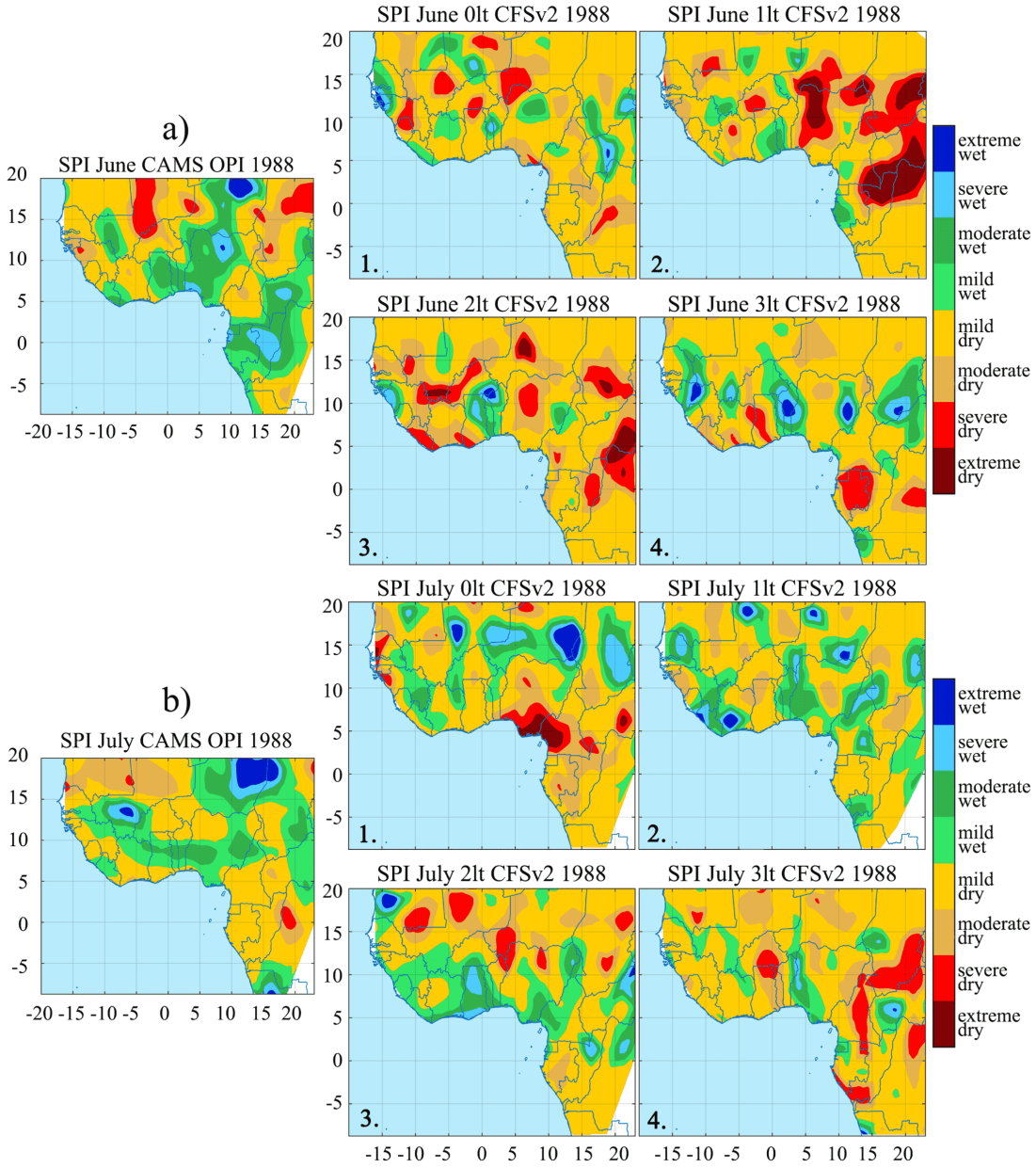

Figure 6.3: An example comparison of SPI-1 estimates for 1988 based on CAMS (left) and CFSv2 hindcast data (right, (1) 0lt, (2) 1lt, (3) 2lt, (4) 3lt) and a) June, b) July, c) August, d) September.

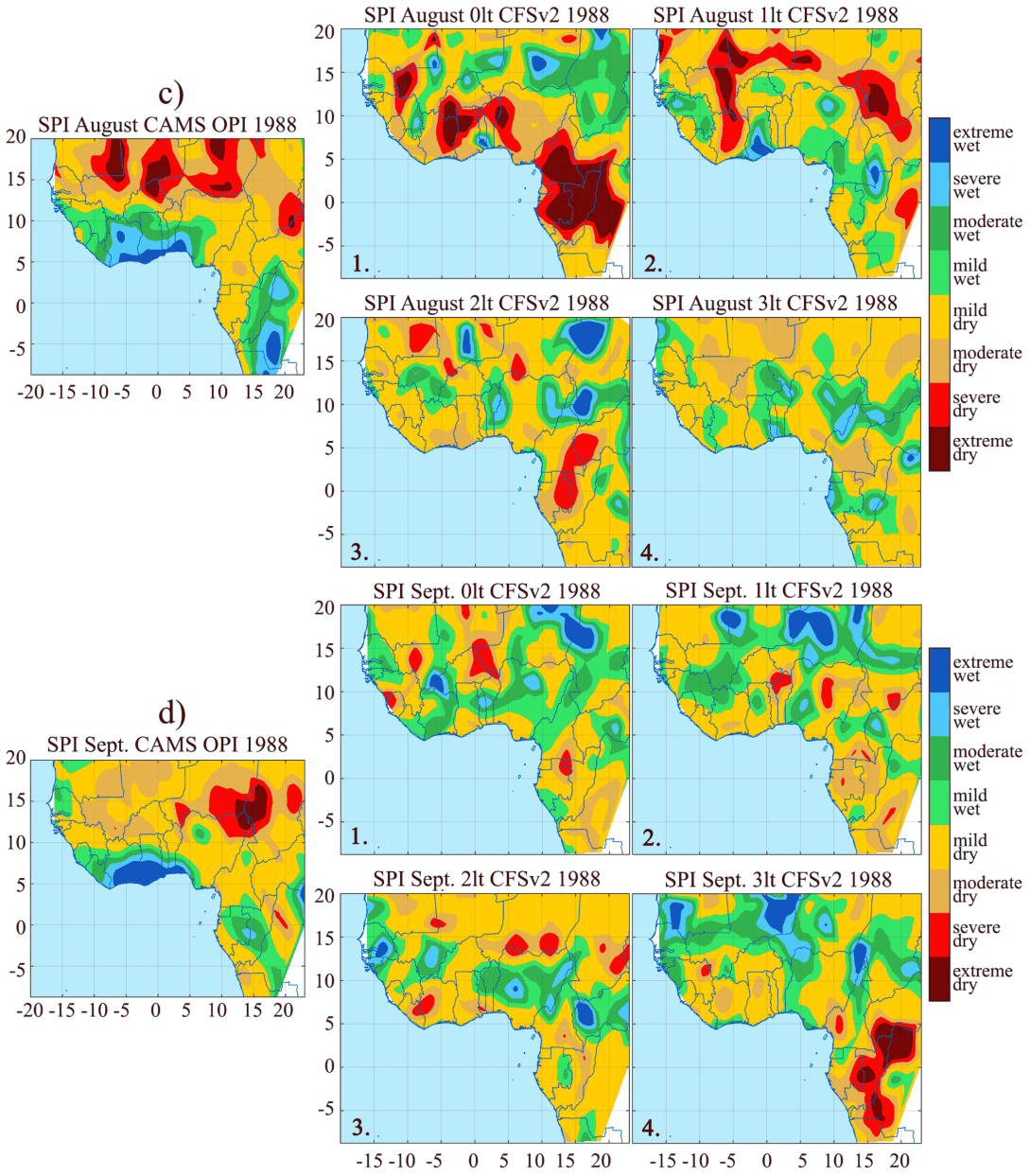

Figure 6.4: See the previous page for caption and panel c, d

6.2 Statistical analysis of drought and wet events in West Africa

Drought is a naturally occurring climate phenomenon that impacts human and environmental activity and can be considered one of the most destructive natural disasters

(Below et al. 2007). Drought can be exacerbated by human activities such as deforestation, improper land use, and poor management of water resources that influence water storage and climate. According to Sheffield et al. (2014), sub-Saharan "Tropic of Cancer" African droughts represent 20% of the natural disasters in WA and influence over 80% of the population there (Thomas 2004). While a detailed overview of the relevant precipitation regimes has been given in Section 2.2, it is necessary to mention that some areas of WA are exposed to droughts even during the rainy season. For example, the southwest of Nigeria and the coastal parts of Benin, Togo, Ghana and Cote d'Ivoire experience a "little dry season" (Parker 2017), which normally occurs between July and August, is characterized by negative precipitation anomalies, and is linked to the northward progression of the Intertropical Discontinuity (ITD). Bad weather conditions occur during this period, usually including cold winds, low temperature, morning drizzles, and partly cloudy conditions; however, afternoon sunshine may be observed. The little dry season occurs annually, although its duration varies from year to year. During this period, high pressure accumulates in the Gulf of Guinea and St. Helena, where it exhibits anticyclogenesis. The little dry period is intense, when the coastal upwelling is strong and sea surface temperature is lower than normal (along the coasts of Ghana, east of the Cape of the Three Points, and along the coasts of Togo and Benin), but weak where both the warm onshore waters persist and the coastline is perpendicular to the southwest monsoonal winds (Parker 2017; Sultan et al. 2003).

For further analysis of the propagation of dry and wet events over WA we use the Pl value (see Section 5.2.1). As a threshold, we consider only those cases where a spatial coverage of dry/wet events is more than 10% of the whole area of WA (see Table 6.1). A comparison between dry and wet events outlines that during the period 1982-2016, the frequency of severe and extremely wet events has been larger (16 times within 35 years) as compared to dry events (10 times within 35 years), with a high persistence of wet events. However, a large spatial coverage of drought events is evident compared with wet events, which have more local effects, implying a recovery of the rainy season in the WA region in late 1970s. Since the early 1970s, the frequency of rainfall events has significantly increased, and moderate to severe drought years have occurred at approximately 9-year intervals (Kasei et al. 2010). Thus, though occurring more frequently, wet events do not propagate as widely as drought events, which may be explained by the generation of rain in this area happening locally in high convective clouds during the monsoon. The strong variability at the start and end of the rainy season together with intensity fluctuations leads to problems for long-range forecasting. Since the WA region has complex synoptic conditions, with dry and wet events occurring in small regions, it is important to analyse not only the statistical frequency of events, but also to visualise their spatial distribution (Fig. 6.5).

Naresh Kumar et al. (2012) introduced a simple, but important parameter called the "drought resistance", which is a monthly measure of the persistence of drought and wet events during the rainy season. This parameter is adopted here for the calculation of the areas with drought and wet resistance from June till September for time periods

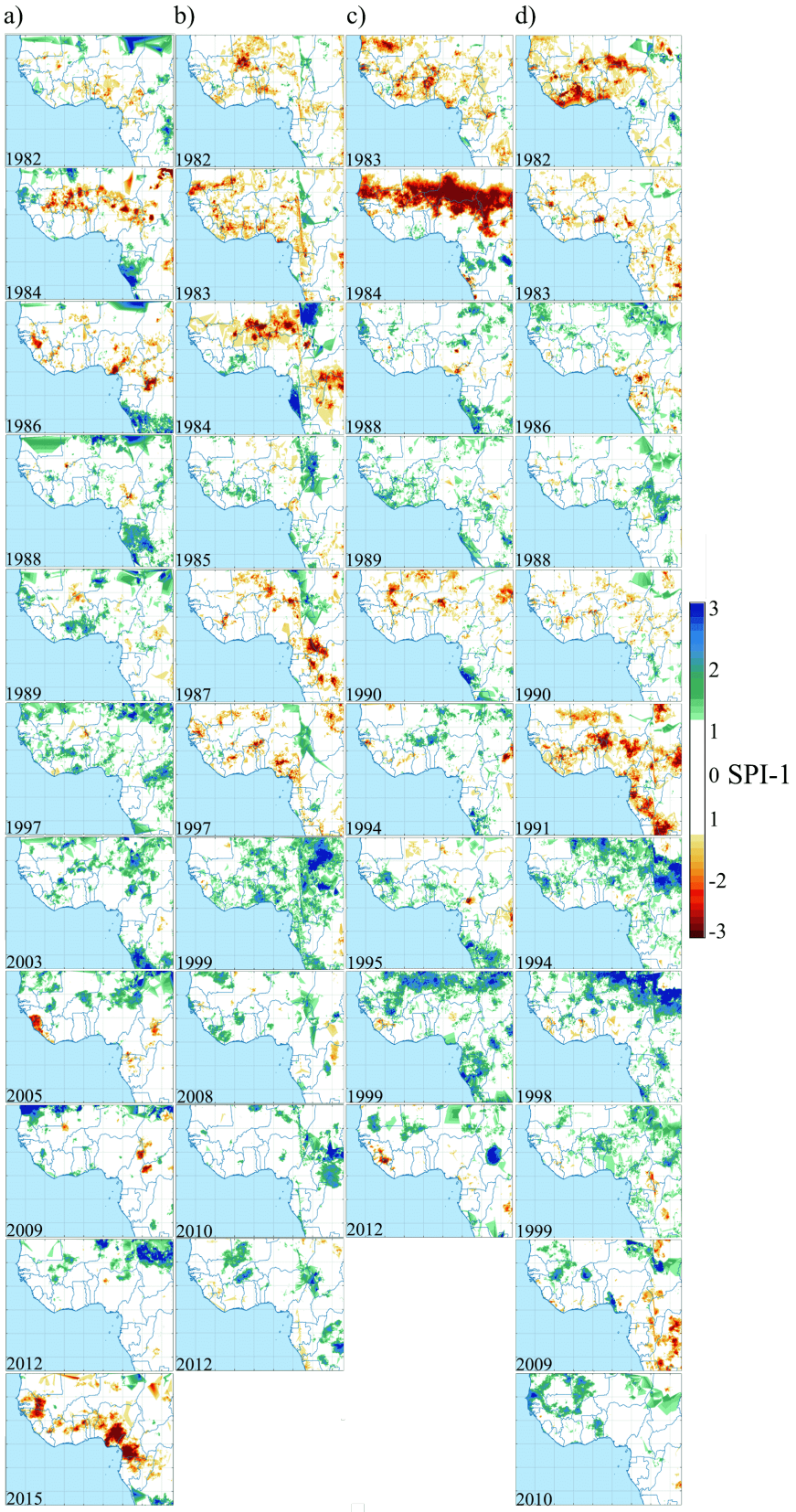

Figure 6.5: Spatial distribution of severe and extreme dry/wet events for a) June, b) July, c) August and d) September.

Table 6.1: Pl values for the most extreme drought events in WA describing the percentage of areal coverage of WA during the boreal summer for the period 1982-2016.

Drought					Wet				
Year	June	July	August	September	Year	June	July	August	September
1982		12.34		20.41	1984	10.07	11.24		
1983		17.37	23.48	15.95	1985		10.59		
1984	14.56	16.70	41.61		1986				10.87
1986	12.55				1988	16.87	12.35	16.07	11.83
1987		16.00			1989	11.96		14.25	
1990			13.07	11.51	1994			14.15	27.97
1991				32.49	1995			11.82	
1997		13.69			1997	21.22			
2009				13.63	1998				32.92
2015	22.73				1999		31.12	36.09	15.48
					2003	22.47			
					2005	14.36			
					2008		10.53		
					2009	12.22			
					2010		14.31		15.68
					2012	12.78	12.82	11.75	

of 2-4 months. For example, resistance-2 indicate situations were the event is observed in June-July, July-August or August-September, whereas resistance-3 correspond to the three-month periods June-August or July-September, and resistance-4 identifies the most persistent dry/wet events affecting all 4 months (the most dangerous cases).
The bar plots in Figure 6.6 display the area coverage (in number of grid cells) of dry and wet events in different persistence gradations (described above) during the reaserch period. The resistance value (2, 3, 4) characterises the Persistence Score (PS; characterising the duration of the observed event in months), which is a direct indicator of the magnitude and intensity of drought (DPS) and wet (WPS) events. The PS-2 shows stable events covering a large surface area, while PS-4 values characterise a higher resistance of the event, but with lower covered surface area, with PS-3 possessing an intermediate stability and areal coverage. In each year, the numbers of grid cells under different combinations of persistent drought/wet and non-persistent events are identified. The highest values of DPS-2, DPS-3 and DPS-4 indicate the most intense drought events in 1982, 1983, 1984 and 2013. The beginning of the 1980s is known as the most extreme drought period in WA (Dai 2011; Druyan 2011; Lebel et al. 2009; Mishra et al. 2010). While the drought events started in 1982-1983, the precipitation deficits worsened the drought situation in the following year in the Sahel region, and thereby worsened any resulting consequences of the drought; only 60% of normal crop areas were available for planting during this period (Giannini et al. 2008). The main reason for this catastrophic drought event has been the monsoonal rainfall deficit, which may have been the result of a very strong El Niño phase (1982-1983). However, the spatial distribution of DPS-4 values for drought events is not wide in comparison with PS-2 or PS-3 (Fig. 6.6 b). The highest values of WPS for a 2, 3, and 4-month stability are found in 1984, 1989, 1999 and 2012, i.e., years with a strong La Niña phase (Parker 2017).
Since teleconnection patterns have a strong impact on the SST and the resulting precipitation formation in WA, with catastrophic consequences for the region, they are further investigated in the next section.

6.3 Correlation with teleconnection indices

According to Parker (2017), SST is one of the most important factors influencing the climate in WA. The SST anomalies play a crucial role in energy transport from the ocean to the atmosphere, influencing the drought and wet seasons in WA (Bjerknes 1969; Namias 1972). Reduction of evaporation causes deficits of moisture in the air, which, in turn, reduces the formation of clouds and precipitation. Long periods of no precipitation can lead to serious droughts in the region and cause severe consequences (Parker 2017). Gómara et al. (2017) have described the inter-annual variability of the most prominent SST patterns. These systems are: 1) ENSO (El Niño Southern Oscillation), 2) Eastern Mediterranean Pattern (EMPI) and 3) Atlantic Equatorial Mode (ATL3). In order to investigate the effect of teleconnection patterns on precipitation

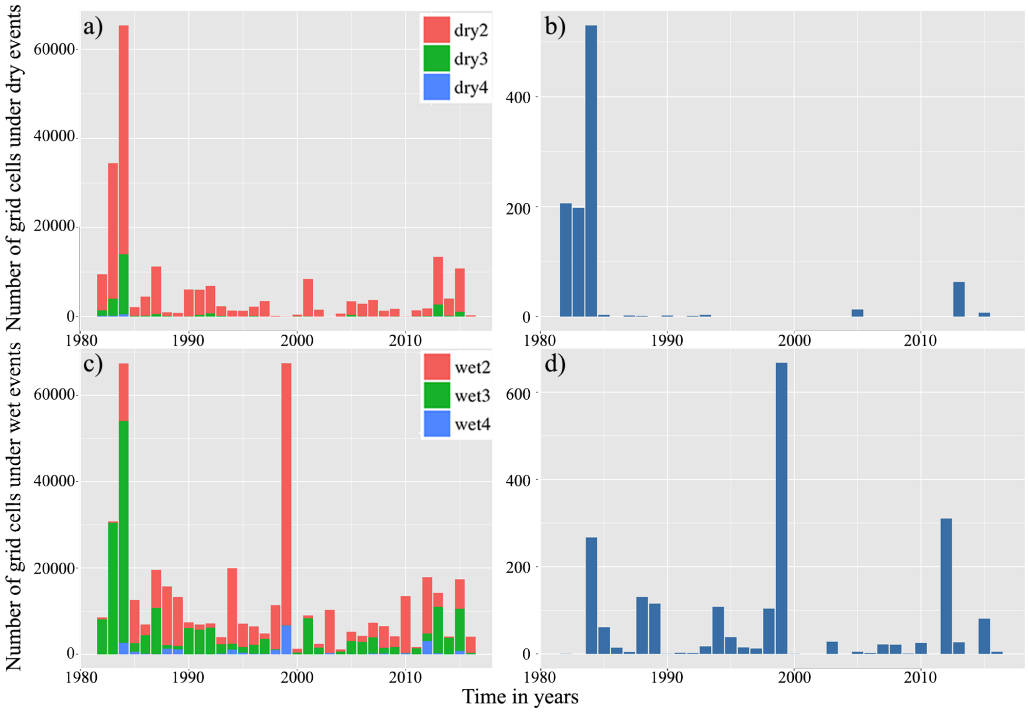

Figure 6.6: Drought (a, b) and wet (c, d) persistence of different years with different persistence levels (2-4). Panels b) and d) show the persistence-4 characteristics separately.

in WA, we decided to increase the list of indices and selected in total 14 indices describing the fluctuations in the Atlantic, Indian and Pacific oceans (as introduced in Section 2.3). Cross-correlation analysis is performed between these teleconnection indices and SPI-1 during the rainfall season (June-September, 1982-2016) with monthly resolution. The majority of the indices are taken from NOAA[4] except for ATL3 and EMPI, which are calculated for this analysis. The ATL3 is computed based on SST values taken from the NOAA Optimum Interpolation (version 2) with 1° resolution and for EMPI calculations we obtained geopotential height field at 500 hPa from the NCEP Reanalysis 2, provided by NOAA/OAR/ESRL PSD, Boulder, Colorado, USA[5]. The SPI-1 fields are calculated from the CAMS data set with a resolution of 2.5°.
Since we found significant correlation with the majority of indices during our study period, we decided to divide them into 3 groups. The first group has the strongest correlation with the SPI-1 during all 4 months and indices AMM, TNA, WHWP and MJO_E (MJO with the centre around 10°E), the second group has strong correlation during 3 months found for MJO_W10 (with the centre around 20°W) and PNA; the third group includes indices with significant correlation during 2 months (ATL3, QBO, EMPI, NAO, SOI, TSA). The results obtained from correlation analysis between CAMS SPI-1 and the teleconnection indices from our first group are shown in Figure 6.7. The strongest positive correlation between almost all indices in the first group and SPI-1 is seen in June and September, when the rainfall season begins and ends. However, areas responding to different indices vary. For instance, the influence of TNA, WHWP and AMM distributes as followes: in June, on the eastern part of the Sahel region, in July, the affected area spreads through the Sahel and Sudan regions and along the Guinea coast, in August and September a stronger correlation over whole WA is observed. For the MJO_E20 index, at first the results are less clear. Since MJO is calculated for different longitudes (every 30°), we have chosen two indices having the closest location to our study area: MJO_W10 and MJO_E20. We found that MJO_W10 has strong positive correlation with precipitation in WA, whereas in July, when a "little dry season" occurs in many regions/areas, a strong negative correlation is noticed. Conversely, with MJO_E20, the correlation is stronger in June and July than in August and September. Parker (2017) provides MJO composite maps of weekly rainfall probabilities and 850 hPa wind anomalies for the May-July period, where he showed how the probabilities of rain occurrence change during the eight MJO phases in WA. Notably, precipitation in phases 1 and 5 can be caused by the occurrence of anomalous low-level westerly winds, and in the phases 3 and 7 due to easterly wind anomalies. In such way, MJO events are taken into account for predicting precipitation with a time lag of approximately 15-20 days.
The second group includes only two indices: PNA and MJO_W10 (Fig. A1). Here we observed significant correlations only in June, August and September. Since the indices are defined based on variability in the Pacific and Atlantic oceans basins, they

[4]https://esrl.noaa.gov/psd/data/climateindices/list/
[5]https://esrl.noaa.gov/psd/

clearly affect the different parts of WA differently. In June, a positive correlation between PNA and SPI-1 is noticed in the southern part of WA, in the area of Zaire and Angola. In August, this moves to the north and is split into two main areas, with negative (south of WA) and positive (central Sahel) correlation. In September the effected area covers the western and southern coastal parts of WA. Conversely, for MJO_W10 the response areas with positive and negative correlation are observed in the northern parts of WA. In June, there is a strong positive correlation in the centre of the Sahelian and the Sudanian regions. In August, the area moves eastward, and in September it divides into two parts, both with strong negative correlation to MJO_W10, one over the centre of Guinea, and the second beyond our area of interest, in the northeastern part of Chad, southeast of Libya, and northwest of Sudan.
SPI responds to the variability of different indices in different months, for instance, a strong connection was observed in September between SPI-1 and ATL3, QBO and SOI (Fig. A2). ATL3 has a positive correlation with the Sahelian region and negative with the centre of the Guinea coast region. Folland et al. (1991), Gray et al. (1997), Rowell et al. (1995), and Ward (1998) found that decadal precipitation variations over the Sahel and Sudan areas are related to negative anomalies in SST over the Atlantic. SST modes (generating favourable atmospheric conditions over the Atlantic) strongly influence the development of tropical storms, which affect the precipitation regime (over the Sahel and Sudan regions). Analysis of the QBO index and SPI showed a strong positive correlation with almost the entire western part of WA. Such correlation can be explained by increasing latent heat release in the tropics and the varying position of a sub-tropical standing wave within the associated Hadley anomaly (Jury et al. 1994). Gray et al. (1992b) demonstrated a connection of ENSO and QBO, such that the QBO eastern phase supports the development of El Niño, while its western phase promotes La Niña events. We therefore expect that, El Niño and La Niña strongly influence the precipitation in WA. Indeed, SOI is found to have a correlation with the precipitation in the southern part of WA region (Janicot et al. 1996).
Following the previos consideration, we conclude that SST variability influences the precipitation formation in different areas of WA and that it is possible to identify those response areas using teleconnection indices. Not only the Atlantic influences WA climate, but the Pacific and Indian oceans also play a significant role. This effect has been investigated in many studies (Gray et al. 1992b; Jury et al. 1994; Nnamchi et al. 2011; Rowell et al. 1995; Williams et al. 2011). Cooler-than-average SST in the equatorial and South Atlantic is the reason for wet periods, while warmer-than-average SSTs lead to droughts in the Sahel region. The influence of the Mediterranean Sea on WA is presented through the EMPI index, with affecting precipitation in the Sahelian region and southern parts of WA in June. A weaker correlation between the EMPI index and precipitation is evident for July, where positive anomalies lead to wet conditions in the Sahel, and negative anomalies to dry conditions. Therefore, variations in the SST of the Atlantic, Indian, and Pacific oceans and the Mediterranean Sea have a large impact on the regional variation in precipitation in WA, especially in the coastal areas (Guinea Coast) and the Sahelian and the Sudan regions during

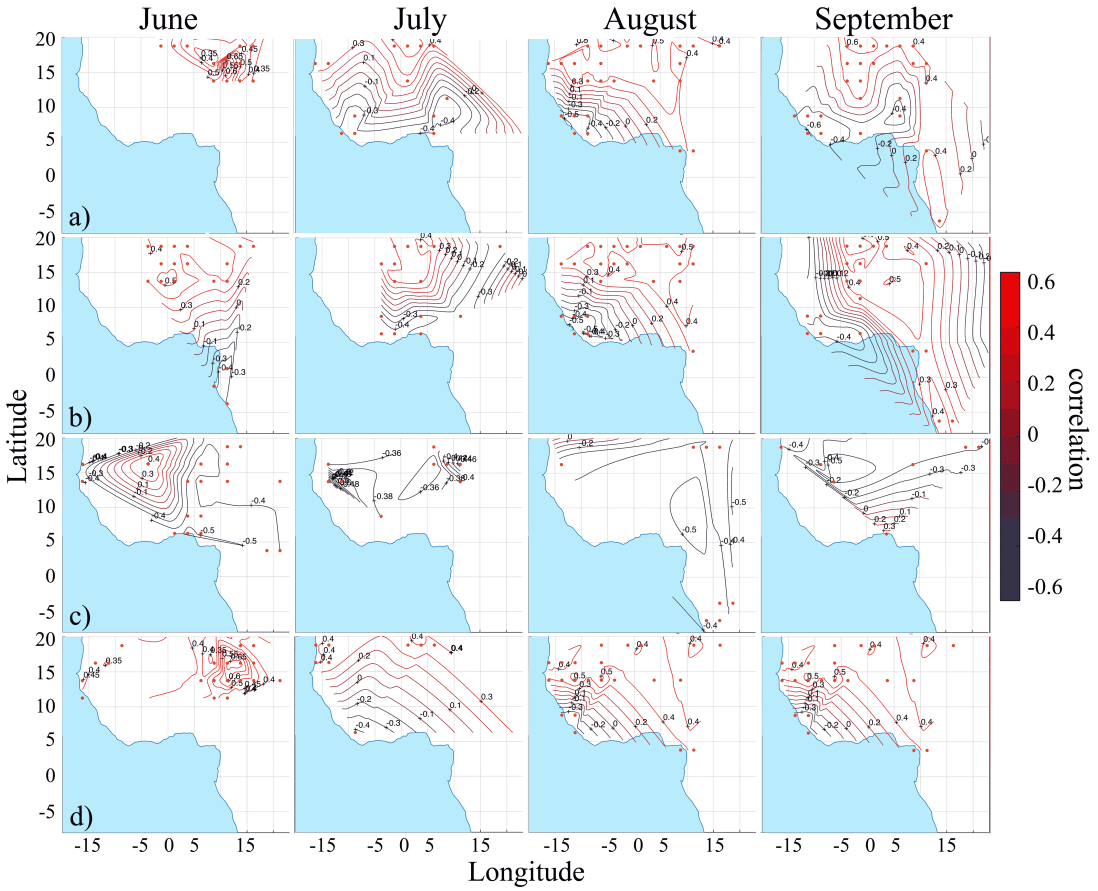

Figure 6.7: Results of spatial correlation analysis between the CAMS-derived SPI-1 observations and different atmospheric circulation patterns. a) TNA, b) WHWP, c) MJO_E20, d) AMM, for the boreal summer (from left to right: June, July, August, September).

the boreal summer (June-September). Based on the performed analysis, we conclude that areas showing strong correlation with teleconnection indices, should have strong statistical connection with predictors, which we can use in the proposed statistical post-processing scheme to provide better forecasts. In June, we expect good skills in the eastern and coastal parts of the Sahel and Sudan regions (south of Mali, Niger, north of Burkina Faso, Nigeria, coastal parts of Mauritania, Senegal, Guinea), whereas in July, the connection is not as strong compared with other months, which can cause lower predictability. In August and September, forecasts for the northern parts of the central Sahel and areas close to the coast should be skilful. Therefore, the closer the region to the Atlantic, the better we expect the forecast to be, since precipitation in this area has a strong connection to SST.

6.4 Statistical forecasting scheme for West Africa

6.4.1 Predictor detection and cluster analysis

In order to test the statistical forecasting model 1 (see Section 4.3.1) for a region from Russia (see Section 5.5.2) we apply it to WA, which is well-known as a complex area with intensive drought and wet regimes during the June-September period. In section 6.3 we demonstraited the influence of large-scale teleconnection patterns on precipitation formation in the region. The seasonal anomalies in WA have been linked to SST variability (Folland et al. 1991; Janicot et al. 1996; Ropelewski et al. 1987). Changes in SST control the transfer of large amounts of energy from the ocean to the atmosphere, which significantly influences the formation and duration of dry and wet events (Bjerknes 1969). Thus, SST plays a crucial role in WA climate and the corresponding forecasts. However, the impact of SST anomalies on WA differs from one part of the region to another and it is necessary to take into account the regional aspects of climate. Of course, SST is not the only variable that influences monthly weather conditions in this area; among other factors, pressure fields H500 and MSLP also have effects on precipitation, since all atmospheric dynamics are pressure based. In section 6.3, we have outlined the significance of the connection between teleconnection indices (many of them being pressure-based) and precipitation in WA. In addition, section 4.2 demonstrated the necessity of using pressure fields in precipitation reconstructions. Therefore, we used surface temperature (ST, combined sea and land surface temperature) instead of standard SST to increase the covered area and take into account the boundary level temperature, along with H500 and MSLP as possible predictors, and each was subjected to cluster analysis in order to detect areas that could be influencing precipitation.

Before performing cross-correlation analysis, the resolution of the FR is selected. In WA, an initial resolution of 2.5° for the field to be forecasted and 1° for the predictors are used. Another new idea implemented in the WA case study is to check the forecasting ability of the model for 0-3lt periods. Since WA is a complex region which is influenced by all three tropical oceans as well as the Mediterranean Sea (the north of WA, the Sahel region), ST is obtained in the area 40°S-40°N, 180°W-180°E (Fig. A3 a). Both pressure fields (H500, MSLP) should cover the processes in the Pacific and Atlantic oceans, we therefore used the ranges of 40°S-60°N, 180°W-10°E (Fig. A3 b). Based on these three potential predictor fields, we perform the cross-correlation analysis between each grid cell from each predictor field and each grid cell from the SPI-1 field separately for the entire research period and each lead-time separately. To identify the closest connection between predictor fields and predictand, we limit the correlation values by the 1 and 99th percentiles for all empirical correlation values. Here we should draw parallels with the corresponding analysis for Russia, where we defined the regions as exhibiting an absolute correlation value above 0.4. Using the 1 and 99th percentiles points for the predictor selection procedure, allows us to identify a threshold for each forecasting region (FR), which in turn is a more sensitive and accurate

approach to detect candidate regions. We noticed (as in Russia) that the candidate regions in WA have a tendency to cluster in space.
Candidate regions further subjected to cluster analysis are performed using the R functions *hclust* for hierarchical clustering (Murtagh et al. 2014) and *mclust* for normal mixture modeling for model-based clustering classification and density estimation (Fraley et al. 2012). The second package, *mclust*, is used to check if the obtained results from the *hclust* are robust. The idea behind *hclust* procedure is to check the Euclidean distance between grid points and provide as output only those cells, having the minimum spatial distance to each other, i.e., neighbours (single-linkage/minimum-distance clustering, Section 3.3). Outputs of the clustering procedure produces several spatially distributed potential predictor clusters for each FR. Afterwards, the geographical centre is found and the weighted mean of all time series within respective cluster is computed for further usage in the regression model. Notably, ST has more potential clusters than H500 and MSLP, which again indicates that statistical precipitation variability in WA is directly influenced by ST.

6.4.2 Implementation of forecasting schemes

In this section we shortly describe the implementation of the previously identified predictors into both forecasting models. Model 1 follows the strategy discussed in section 4.3.1. For this purpose, we consider all combinations of ST (x_i), H500 (y_j) and MSLP (z_k) predictors to provide individual forecasts of SPI-1 (M_{ijk}) for a given FR and month in terms of a set of linear regression equations (as discussed in Section 4.3.1). By this procedure, each FR is associated with an individual set of linear equations that are independently solved to generate an ensemble of individual SPI forecasts based on 0-3lt ST, H500 and MSLP predictions obtained from the CFSv2 model. This set of forecast equations can then be evaluated in both deterministic and probabilistic ways.
The number of possible predictive clusters is only limited by the number of sub-regions considered and the requirement that different clusters need to be spatially disconnected. The procedure for probabilistic forecasts is fully described in Section 5.6.2; as the result in this case, we obtain forecasts in three gradations, BN, NN and AN, with probabilities of each event type to occur for the period June - September for each lead-time.
The detailed description of model 2 is given in Section 4.4.1. In this case, all identified predictors from ST, H500, MSLP fields are combined in one multiple linear regression equation and evaluated, as previously mentioned, in both deterministic and probabilistic ways.

6.5 Forecast verification

6.5.1 Deterministic forecast

6.5.1.1 Traditional spatial verification methods

Deterministic forecasts obtained from model 1 and model 2 are checked firstly by using traditional spatial metrics, such as RMSE, MAE and point-wise correlation. The results for all four months and 0-3lt results are presented in Table 6.2. Comparing both models according to the listed metrics, we find that model 1 predicts SPI-1 more accurately than model 2. For model 1, the correlation is higher, by around 0.2, and the errors are almost half lower. The best forecast is achieved for June, with low RMSE and MAE. The month with the second highest accuracy is September, while for August, the forecast is slightly worse, and the worst forecast is obtained for July, with the largest values for RMSE and MAE and lowest correlation values (Table 6.2). The lowest values are observed in the southern parts of WA (Angola, Zaire; Fig. 6.8), near the Gulf of Guinea and in the eastern parts of the Sudan region. These patterns strongly resemble the areas of high and low correlation between SPI-1 and teleconnection indices, identified in Section 6.3. The northern part of WA shows high predictability, as also expected from the teleconnection analysis.
The derived verification parameters for model 2 show a slightly different picture of the distribution of forecast accuracy for boreal summer in WA. In general, model 2 predicts precipitation with the lowest errors in August, with mean values for RMSE of 1.12, MAE of 0.89, and a mean correlation value of 0.54. Thus, the errors are significantly higher, and correlation is much lower than for model 1. Next, in July, both errors are higher (1.20 and 0.95, respectively) and the mean correlation is just 0.46. In September, the results for the errors are similar, with an RMSE of 1.21 and MAE of 0.95; however, the mean correlation is a little higher (0.51). Finally, June has the highest error values (1.65 and 1.03, respectively) and the highest mean correlation, 0.54. Maps of the spatial distribution of correlation coefficients (Fig. 6.9) display an area of low values in the central (continental) part of WA. Having high correlation and high error means the bias of obtained results is also high and we do not catch the mean values good enough, however the bias is not checked explicitly. Again, as described for model 1, the July 2lt case shows very low values compared to other months and lead-times. We also observe more northern areas with low values compared to model 1. However, coastal areas exhibit good forecasts, with correlation coefficients of 0.7 to 0.8.
Next, the outputs of deterministic forecasts are analysed by conditional quantile plots (Wilks 2011) derived for each forecasting month for both models. Here, we use a modified version of classical Q-Q plots, plotting 10/90%, 25/75% quantiles, median and histogram (Fig. 6.10 and 6.11). Conditional quantile plots (CQP) are a convenient method for graphical representation of the joint distribution of forecast and observations. Quantiles are derived from the conditional distributions p $(o_j \mid f_i)$ in relation

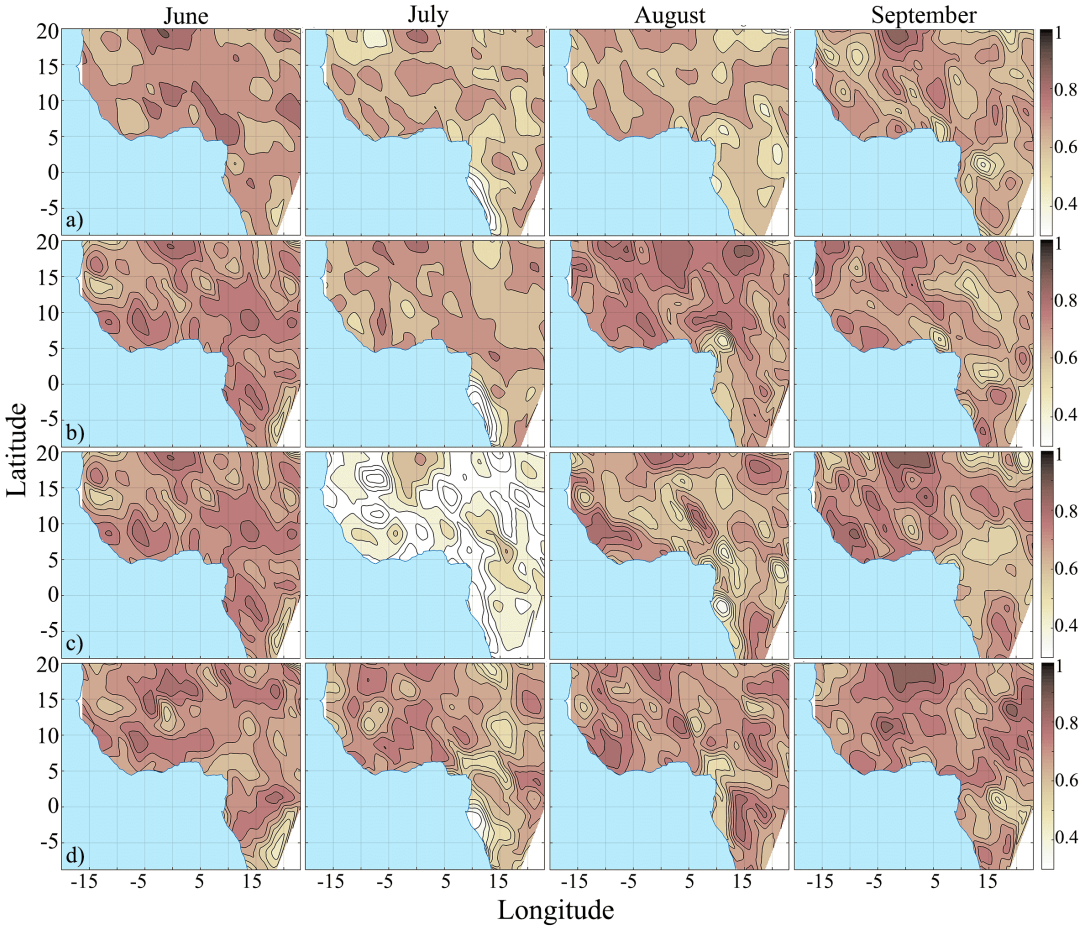

Figure 6.8: Point-wise correlation between the forecasts obtained by model 1 and observed SPI-1 for June, July, August, September for a) 0lt, b) 1lt, c) 2lt, d) 3lt forecasts.

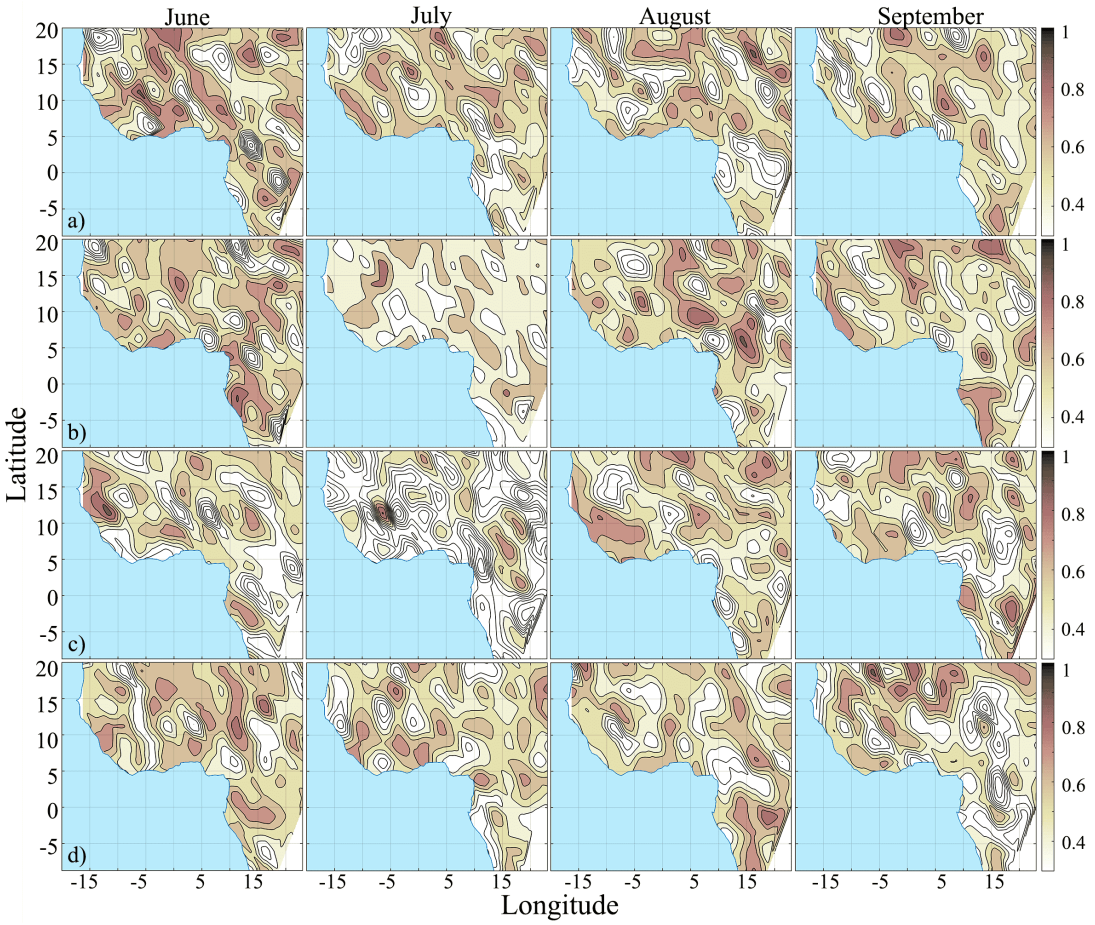

Figure 6.9: Same as for Figure 6.8, but for model 2.

to the line of identity, and the lower parts of the figure show the unconditional distributions of the forecasts, p(f_i) (Murphy et al. 1987). In the best forecast, the red line characterising the median must be positioned on the main diagonal. Any deviation from this line shows uncertainties in the forecasts and SPI values that are poorly forecasted. For better comparison, we fix the axis on the figures at the interval [-4, 4] (in the SPI-1 gradation, values of -4 and 4 characterise extreme drought and wet events).
Comparing both forecast models, it is clearly seen that model 1 provides acceptable results (except for June 2lt, August 0lt; Fig. 6.10). The median line intersects with the diagonal line for normal events; however, there are forecasts for dry and wet events that significantly deviate from the diagonal line. There are even some cases where the median line becomes almost flat (June 0lt, July 2lt) and these forecasts are less reliable. In general, dry events are more closely following the diagonal line than wet events; however, with different lead-times, various situations can be observed.
We cannot conclude that with a larger lead-time the quality of the forecast is reduced. On the contrary, for August and September, the 3lt forecast presents the current situation more accurately than the 2lt or 1lt forecasts. For model 2 (Fig. 6.11), it can be clearly seen that the forecasts are much further separated from the diagonal line than in model 1. The intensity of dry and wet events is also much more strongly overestimated by model 2 than by model 1. From the figures it is hard to select "good" and "bad" forecasts, since they all look more or less similar and present low accuracy.
Additionally, we present comparison maps with observed and deterministic forecasts for one randomly selected case with forecast values of all lead-times for both model 1 and model 2 (Fig. 6.12). The left panel presents the observed SPI pattern and deterministic forecasts for both schemes with 0-3lt are presented on the right side. In June 1984 we clearly observed an intense and extreme drought in WA. Both models predict the actual drought and wet events accurately. However, the spatial distribution is not accurate, especially for model 2. Moreover, 0lt and 1lt forecasts from model 2 underestimate wet events and produce forecasts in the wrong areas. More accurate visualisations of deterministic forecasts are presented by model 1, where spatial localisation and intensity of dry and wet events are presented reasonably well. Less accuracy is achieved for 2lt, where both wet and dry events are underestimated. Conversely, for the 3lt forecast wet events are predicted in the southern part of the study region with high accuracy for both spatial distribution and intensity.
In summary, traditional forecast verification methods show that model 1 produces deterministic forecasts more accurately, compared to the more classical model 2. That means, using combinations of predictors and obtaining ensembles of forecast equations for each forecast region can increase the probability of getting better forecasts compared to the use of only one deterministic model.

6.5.1.2 Fractions Skill Score

Spatial verification methods have recently become popular in the meteorological community (Radanovics et al. 2018). To keep up with the state-of-the-art we compute

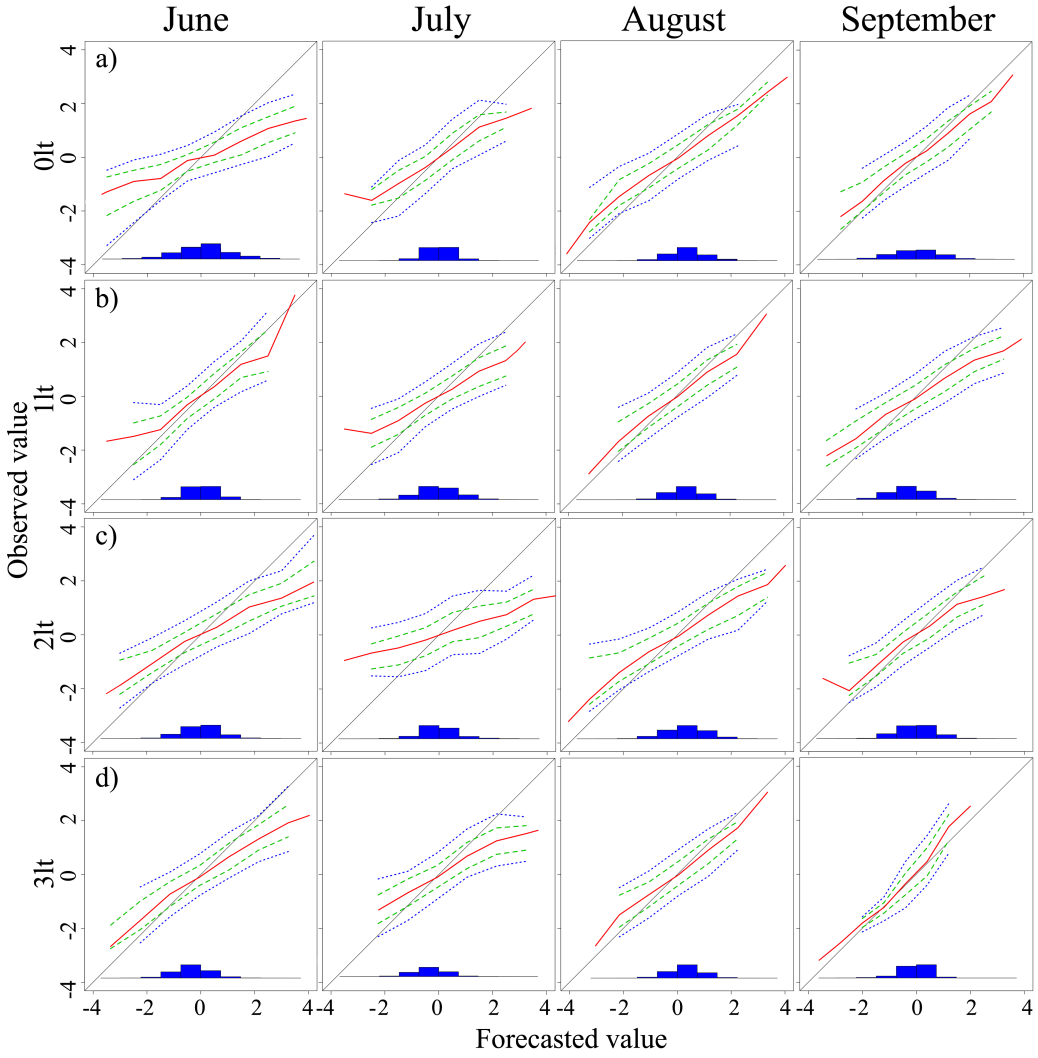

Figure 6.10: Conditional quantile plots for model 1: a) 0lt, b) 1lt, c) 2lt, d) 3lt forecasts. The red solid line presents the median, the green dashed line the 25th and 75th percentiles, the blue dashed line the 10th and 90th percentile; the blue histogram shows the frequency of forecasted values.

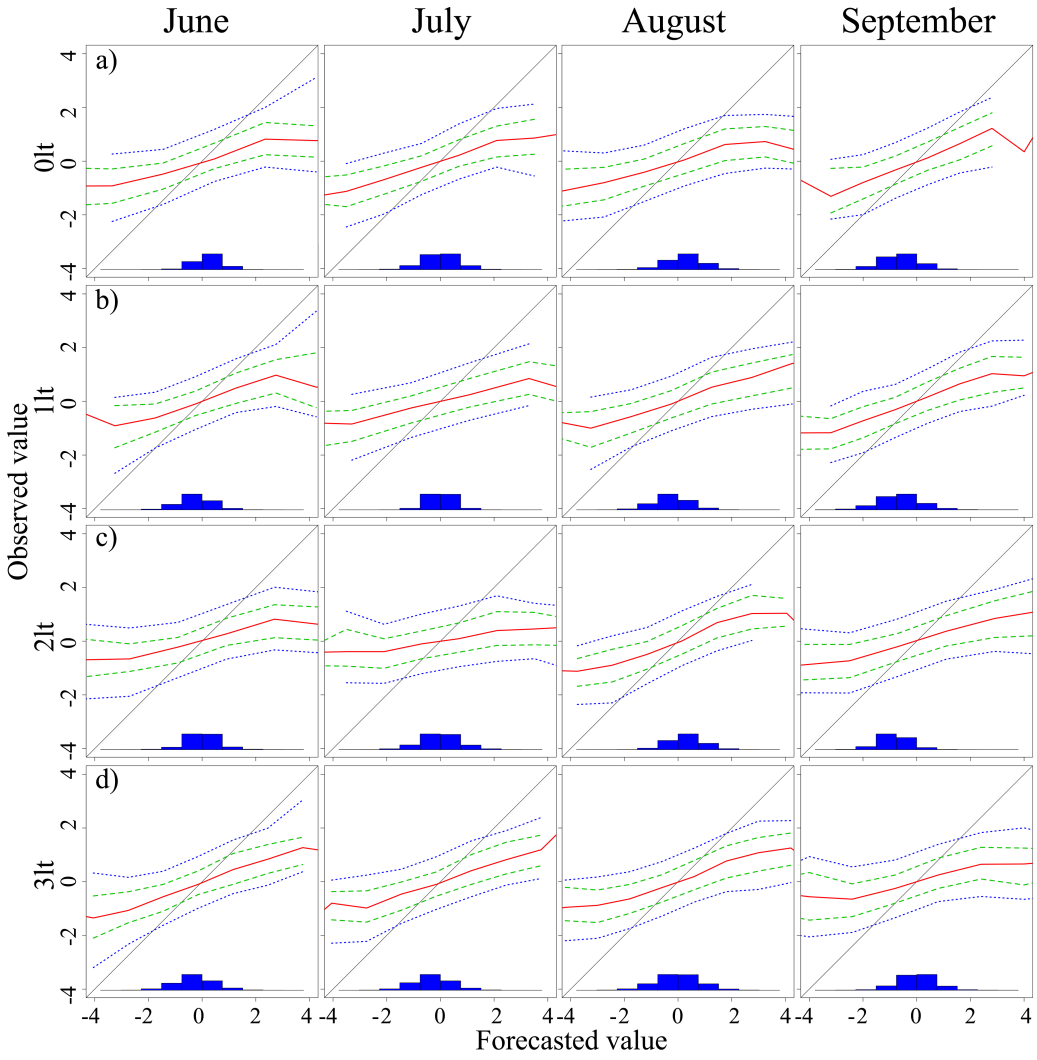

Figure 6.11: Same as for Figure 6.10, but for model 2.

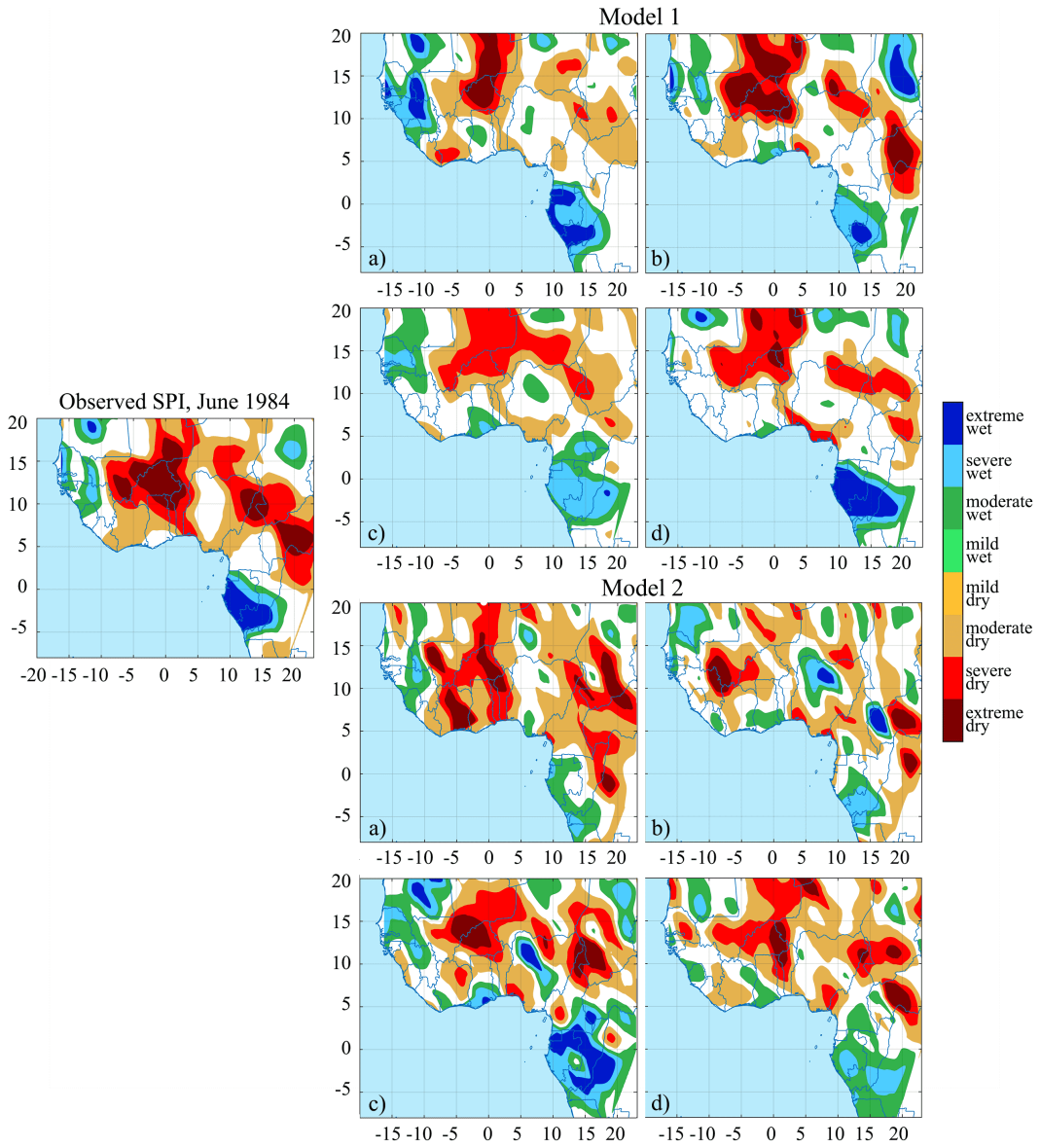

Figure 6.12: Example results of observed SPI and deterministic forecasts of spatial SPI-1 patterns for June 1984 using model 1 (top 4 panels) and model 2 (bottom 4 panels) for a) 0lt, b) 1lt, c) 2lt, d) 3lt forecasts.

Table 6.2: Summary of forecast verification parameters.

Model 1												
	0lt			1lt			2lt			3lt		
Month	RMSE	MAE	Corr	RMSE	MAE	Corr	RMSE	MAE	Corr	RMSE	MAE	Corr
June	0.7004	0.5348	0.7285	0.7111	0.5473	0.7109	0.7227	0.5510	0.6808	0.7129	0.5463	0.7033
July	0.7699	0.5786	0.6372	0.7682	0.5801	0.6655	0.8767	0.6653	0.3855	0.7668	0.5788	0.6596
August	0.7978	0.6129	0.6488	0.7366	0.5686	0.7163	0.7612	0.5925	0.6603	0.7489	0.5784	0.7007
September	0.7536	0.5914	0.6675	0.7408	0.5769	0.6930	0.7386	0.5762	0.6921	0.7274	0.5696	0.7193
Model 2												
	0lt			1lt			2lt			3lt		
June	1.0592	0.8463	0.5629	1.0592	0.8463	0.5629	3.4357	1.6214	0.4806	1.0503	0.8404	0.5567
July	1.0847	0.8620	0.5199	1.1843	0.9427	0.5011	1.4205	1.1226	0.3010	1.0966	0.8721	0.5191
August	1.2495	0.9879	0.5103	1.1139	0.8949	0.5481	0.9993	0.7887	0.5474	1.1253	0.8987	0.5343
September	1.0198	0.8189	0.5147	1.1056	0.8741	0.5500	1.2301	0.9807	0.5132	1.4883	1.1328	0.4848

Fractions Skill Score (FSS) in our study to check the obtained deterministic forecast for both models. Most of the spatial verification characteristics are available in R within the package *SpatialVx*[6]. For FSS calculations we use a combination of the *SpatialVx* package and R code provided by Dr. M. Hoff (DWD, Germany) for better visualisation.

The FSS calculations require to identify thresholds and scales (numbers of neighbourhood boxes), where the model produces different scores. In deterministic forecasts, it is important to identify intensity thresholds of dry and wet events (from -1 to -2 for dry events and from +1 to +2 for wet events). As neighbourhood size, we take the highest value equal to 8 (in our case the WA domain is containing 13 by 18 grid points, if we take n = 8, it fully covers the study area). We obtained the FSS for dry and wet events for deterministic forecasts for both models, 0-3lt, and the years 1982-2016. FSS can be obtained for each year separately or for a whole period of interest, depending on the specific purposes.

The results of FSS calculations are shown in Figures 6.13, A4, A5 and A6 as a function of dry/wet intensity threshold (x-axis) and spatial scale (y axis). Within these plots, the numbers present the FSS score values; dark red, red and orange colors indicate good performance, whereas all colors below the blue dividing line represent poorer performance. The edge between those two areas (indicating the range of "useful forecasts") can be calculated using the formula $FSS > 0.5 + f_{obs}/2$, where f_{obs} is the fraction of observed events in the full domain (Mittermaier et al. 2010). Values below the blue line in the FSS diagrams display the skill that would be achieved using traditional grid box matching and a low threshold. All other values of n (from 2 to 8 in this case) on the y-axis present FSS scores for upscaled boxes. Following this logic, it is easy to achieve high skills for the forecast with n = 8, since all domains are taken into account and the higher n, the higher the FSS. Comparing the forecast for different box sizes helps to overcome the biggest problem of weather forecast verification — the double penalty

[6]SpatialVx: Spatial Forecast Verification https://CRAN.R-project.org/package=SpatialVx

problem (see Section 3.5.1), and thus the fact that traditional techniques consider two errors — the first when the forecasted event did not occur at the corresponding location, and the second when the event happened where it was not forecasted (Gilleland et al. 2009). Therefore, matching observed and forecast values for large box sizes decreases the chance of double penalty and increases the accuracy of the forecast.
Forecasted dry events presented in Figures 6.13 and A5 for both models show high FSS values with similar qualities, as found using traditional verification methods. The FSS values for model 1 are in most cases (except for July), especially for box sizes 1 and 2, above the blue threshold. Only in July, the forecasts for all four lead-times show much lower values, with FSS below the usefulness criterion (July, 2lt). For other box sizes, we found acceptable scores. August and September forecasts are more accurate than June and July, however, FSS values in June are also high, especially for 1lt and 3lt forecasts. The highest accuracy can be observed again for the September 3lt forecast. FSS values for model 2 are slightly higher, and values are equally distributed among all months and lead-times; however, none of the cases covers the first two box sizes. That behaviour allows us to conclude that model 1 shows higher accuracy compared to model 2 for dry events.
FSS values for wet events are presented in Figs. A4 and A6. The FSS values for wet events have similar behaviour and distribution as for dry events. According to Figure A4, FSS values are higher in August and September, whereas slightly worse forecasts are obtained in June, with the lowest values presented in July. The 2lt forecast is again useful for boxes with sizes $n = 1,2$, as we noticed using other verification characteristics. For wet events, different thresholds have different accuracy. Boxes with sizes $n = 1,2$ show low FSS, with values in the gradation below the value of useful forecasts. However, as the box size increases, FSS rises for thresholds (of the SPI-1 values) from 1 to 1.6 and in June, 0lt for all thresholds. The model does not produce a score for thresholds above 1.6, meaning that the model can better predict low intensity wet events compared to such with high intensity.
Wet events in model 2 have lower FSS values, and the boxes with sizes n=1, 2 for all months and lead-times also show skills below the usefulness threshold. July shows bad forecast accuracy compared to other months, but without large differences among lead-times. The highest accuracy is obtained in September, while the accuracies for June and August are similar.
We conclude that the FSS is a useful tool to verify the quality of forecasts for SPI gradations and helps the user becoming aware of incorrect event gradation. An advantage of the SPI (particular using SPI in FSS analysis, instead of pure precipitation) is its gradation system. Thus, the main challenge for a forecaster is to predict the gradation correctly (not predict an exact value), which is increasing the chance of obtaining a high accuracy of a forecast. Generally, the FSS is better when verifying larger domains with many grid points; otherwise, with smaller domains, the results must be interpreted more carefully. The FSS helps to overcome the problem of a double penalty and to identify the frequency of its occurrence. This score reflects the general behaviour of the forecast accuracy obtained from traditional methods and can be used

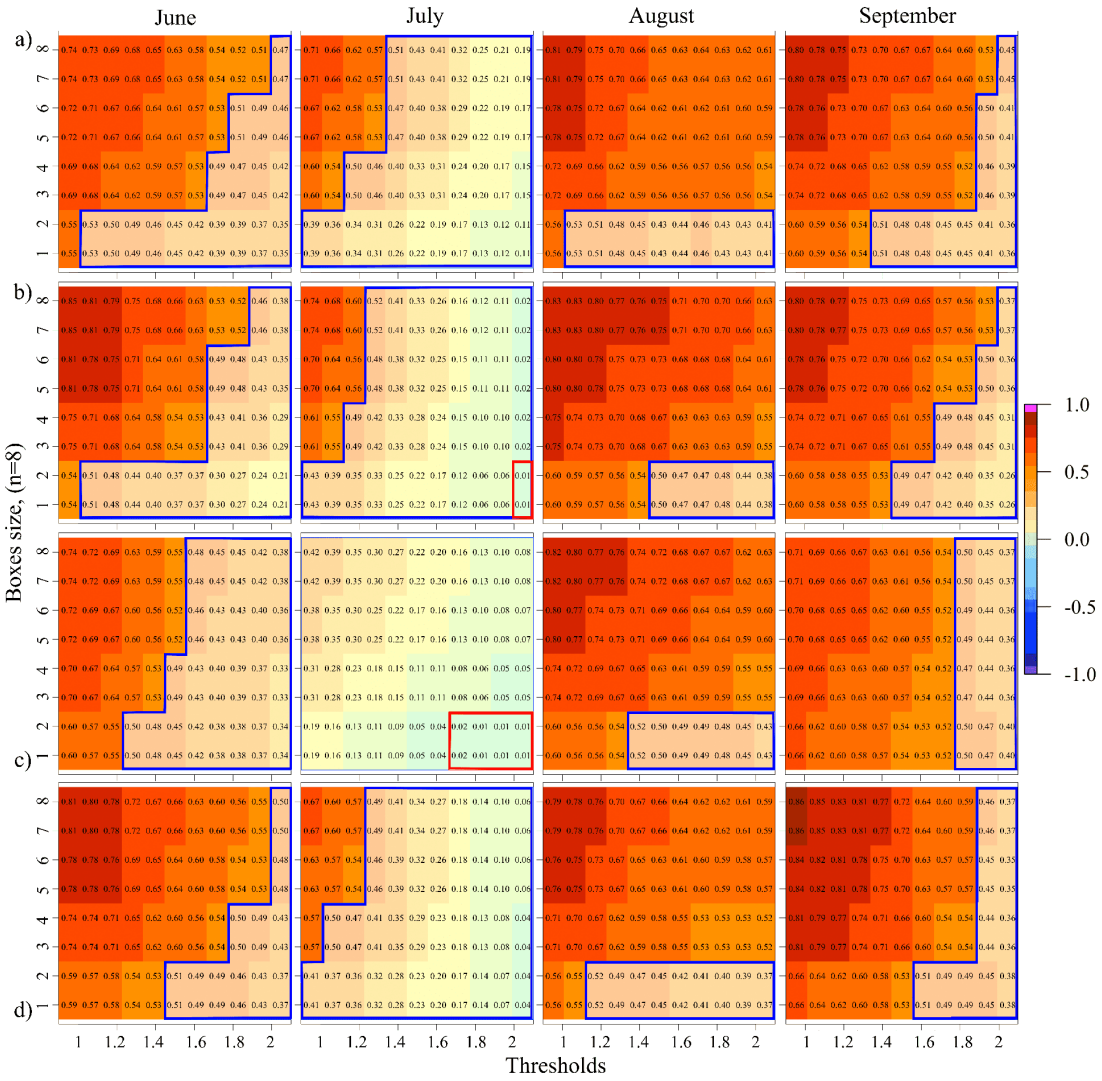

Figure 6.13: Neighbourhood verification scores using the FSS method for dry events for the period 1982-2016 verified against observed SPI for the same period. a) 0lt, b) 1lt, 2) 2lt, 3) 3lt, for model 1.

as an extra verification tool.

6.5.2 Probabilistic forecast

Probabilistic forecast comparison of both regression models for WA is done using ROC curves, attribute diagrams and CRPS, since they accurately quantify the skills of probabilistic forecasts. All these characteristics are calculated for each month and lead-time to show the deviation in skills when moving from 0 until 3lt during the June-September season for both forecasting models.

6.5.2.1 ROC curves

ROC curves are constructed for all three event types (AN, NN, BN) for both models and include 3lt cases on each graph presented in Figure 6.14 for model 1 and Figure 6.15 for model 2. The resulting prediction accuracy (AUC parameter) for model 1 and 2 is presented in Table 6.3.
The presented ROC curves and the AUC parameter clearly show that the probabilistic forecast derived from model 1 has good accuracy. All curves are far from the horizontal line and AUC values vary between 0.65 and 0.85 for dry events, 0.67 and 0.82 for wet events, and 0.47 and 0.62 for normal events. Again, the model has a low accuracy for normal events, as also found for Russia in Section 5.6. However, the model's skills are good (around 0.8 for most cases) for dry and wet events. We also compared different forecasts with lead-times from 0-3 months, and the best predictability for dry events is achieved in June (0lt), followed by September (3lt), August (1lt) and July (1lt); for wet events the results are almost the same, apart from July. The highest values are observed in June (0lt), September (2lt), July (0lt) and August (1lt). We notice a lack of linear dependence between increasing lead-time and decreasing accuracy, as the behaviour is different for each month. In June, the highest accuracy for dry events is observed for 1lt, then for 0lt, 3lt and finally for 2lt; however, the differences between the AUC values for different lead-times are only in the decimals, and thus too small to be significant. In July, dry events are forecasted to be much worse, with the best results being achieved for 0lt and 3lt, then for 1lt and 2lt. In August, the best forecast is in 1lt and 3lt, then 2lt and 0lt. Unexpectedly, in September the best forecast is achieved for 3lt, then a bit worse AUC value is obtained for 0lt and values similar to each other are observed for the 2lt and 1lt predictions.
The ROC curves and AUC values derived from model 2 show clearly worse results (Table 6.3). Dry and wet events are forecasted well enough, with AUC values around 0.7; however, neutral events are presented insufficiently, with AUC around 0.5. Between different lead-times, the highest AUC values are obtained from the 3lt and 0lt forecasts; between months, the values are similar with small deviations and it is difficult to emphasize the best and the worst forecasting month within model 2. According to neutral events, they were also found to be poorly forecasted.

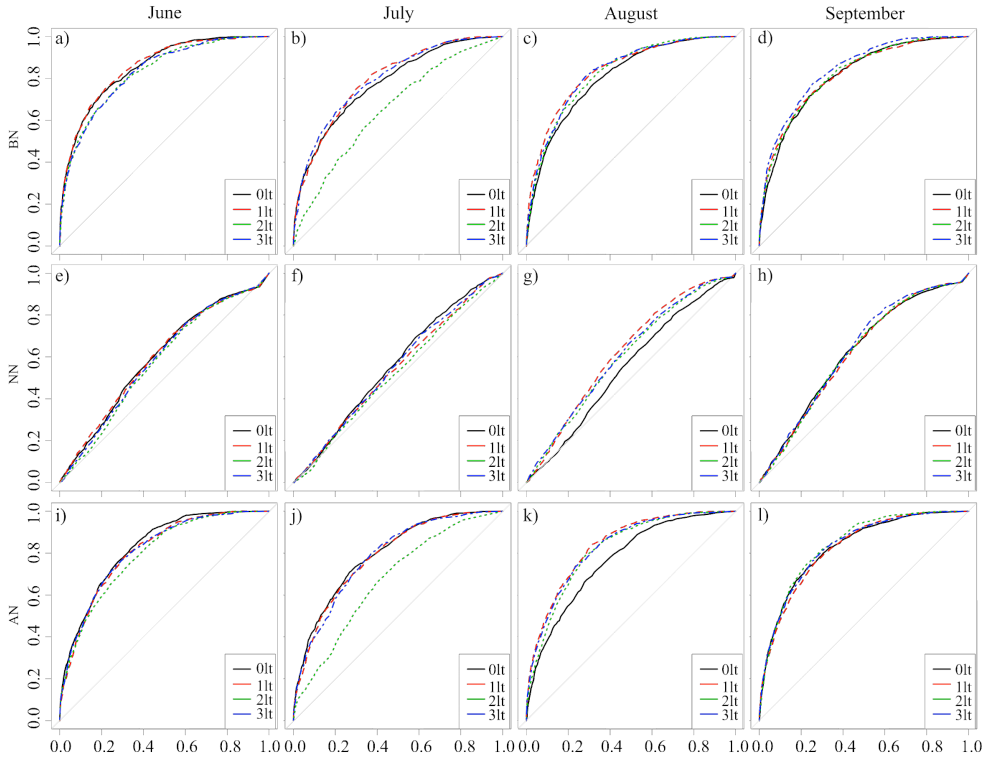

Figure 6.14: ROC curves describe the forecast accuracy for different groups of SPI-1 conditions over WA during the four boreal summer months and a-d) BN, e-h) NN and i-l) AN for model 1.

Table 6.3: Summary of AUC values for WA.

Month	0lt			1lt			2lt			3lt		
	BN	NN	AN	BN	NN	AN	BN	NN	AN	BN	NN	AN
Model 1												
June	0.850	0.5957	0.8252	0.8527	0.5960	0.8258	0.8258	0.5746	0.7933	0.8270	0.5850	0.8112
July	0.7783	0.5596	0.7942	0.7963	0.5417	0.7863	0.6550	0.4770	0.6711	0.7953	0.5494	0.7848
August	0.8060	0.5499	0.7670	0.8371	0.6226	0.8389	0.8244	0.6015	0.8194	0.8316	0.6113	0.8292
September	0.8122	0.6231	0.8273	0.8177	0.6182	0.8240	0.8200	0.6206	0.8402	0.8411	0.6306	0.8313
Model 2												
June	0.7580	0.5355	0.7519	0.7437	0.5275	0.7495	0.7243	0.5209	0.7108	0.7587	0.5533	0.7611
July	0.7453	0.5592	0.7544	0.7219	0.5465	0.7220	0.6417	0.5300	0.6220	0.7425	0.5603	0.7353
August	0.7357	0.5430	0.7367	0.7540	0.5721	0.7369	0.7620	0.5578	0.7605	0.7518	0.5702	0.7434
September	0.7440	0.5531	0.7363	0.7531	0.5553	0.7490	0.7377	0.5454	0.7232	0.7138	0.5486	0.7076

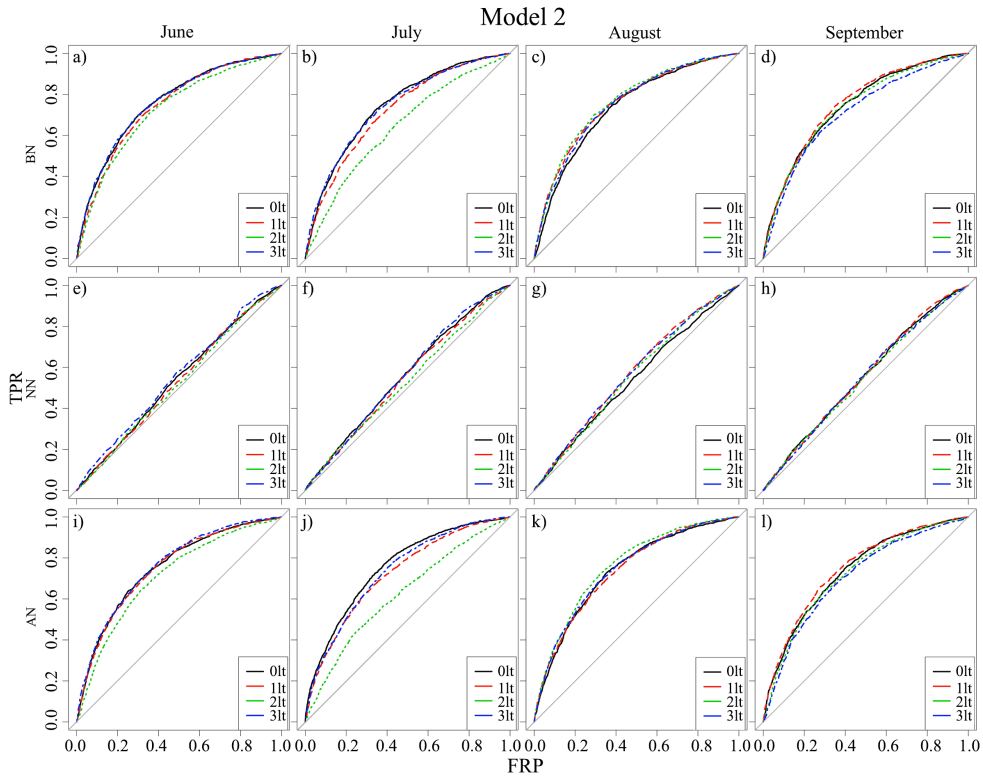

Figure 6.15: Same as Figure 6.14, but for model 2.

6.5.2.2 Reliability diagrams

Further verification analysis for probabilistic forecasts is performed by considering attribute diagrams, Brier Score (BS) and Brier Skill Score (BSS) values obtained for both models. Attribute diagrams are generated for all months and lead-times separately and are presented in Figures 6.16, A7, A8 and A9. In general, all reliability diagrams for model 1 show high skill scores and good calibration, except for neutral events. According to Wilks (2011) descriptions of different types of attribute diagrams, dry events at all lead-times show good calibration and in some cases are underestimated (dry bias), wet events are forecasted slightly worse, also with good calibration and overestimation (wet bias). Unfortunately, forecasts of neutral events are overconfident and have poor resolution.
The Brier Skill Score (BSS) characteristics of reliability diagrams are derived by using the *verify* function of the *verification* package in R for both models and are presented in Table 6.4. For model 1, the BSS parameter has similar behaviour as the correspondingly AUC values. The best forecast is achieved for dry events for 0lt, then slightly smaller BSS values are found for 1lt, 3lt and 2lt, respectively. In July, the BSS values are distributed such that the highest value is observed for 1lt, then for 3lt, 0lt and 2lt. In August and September, again the best forecasts are achieved for 3lt, then for 1lt, 2lt and 0lt. Wet events are forecasted a bit worse; however, the BSS values are still significantly high. In June, the best forecast is derived for 0lt, then for 1lt ,3lt, and 2lt, while in July the ranking is (best to worst) 3lt, 0lt, 1lt and 2lt.
It should be mentioned that as for the ROC curves in July, for all events the BSS shows low values, and for 2lt the forecast skills is not significant. In August, the highest BSS values are observed for 1lt, then for 3lt, 2lt and 0lt, while in September - for 3lt, 0lt, 1lt and 3lt. Neutral events are forecasted with low, but positive, BSS values for all lead-times and during all months, except for one case (July, 2lt). In June and August, the best forecast is obtained for 0lt, 1lt, 3lt and finally for 2lt. In July, the accuracy ranking is almost the same, with a difference between the first two lead-time forecasts, so the best prediction is obtained for 1lt, with results a little bit worse for 0lt, then for 3lt and 2lt. In September, the best forecasts are for 3lt, 1lt, 2lt and 0lt.
The results obtained for the model 2 are presented in Figures 6.17, A10, A11, and A12. Here, all diagrams have minimal resolution, as all the curves are positioned far from the diagonal. The below and above normal events in all cases are overestimated (wet bias) and due to that, normal events are forecasted relatively poorly. For normal events, the BSS is always negative, which means that a climatological forecast gives better results than model 2, and the attribute diagrams are showing rare events.
The BSS and BS parameters for model 2 are presented in the second part of Table 6.4 for all months, lead-times and dry, wet and neutral events separately. The BS values are high for all cases, compared with model 1, and since the BS and the BSS are related to each other, the BSS values are quite low. However, for dry and wet events only in some cases the BSS values are negative: for 0lt, 1lt and 3lt in August, and for 2lt in June. The best forecast is obtained for June and August for 0lt-2lt; for 3lt the best

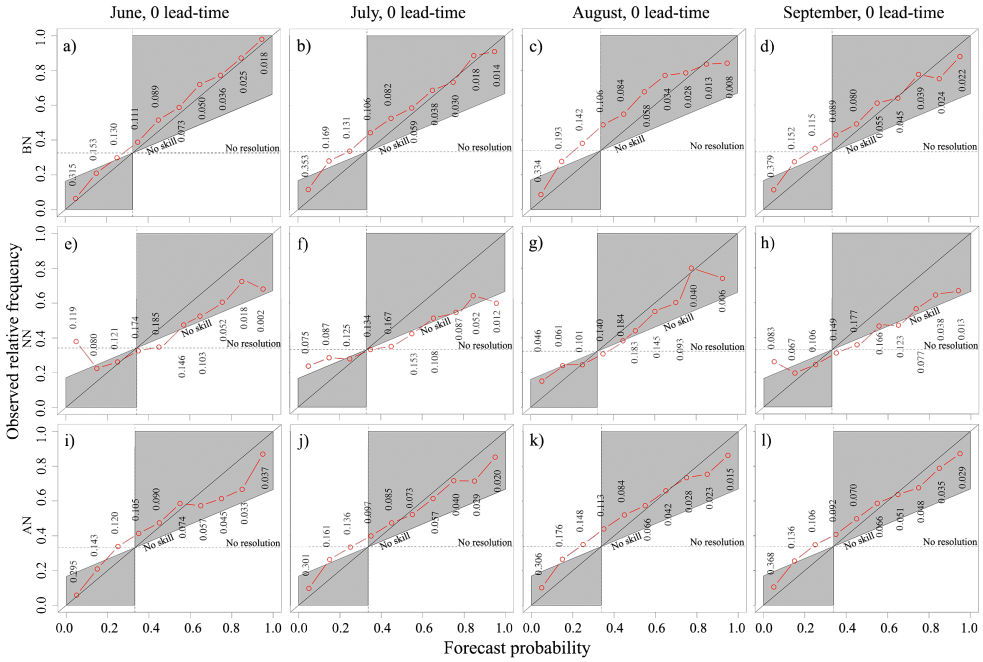

Figure 6.16: Reliability diagrams for probabilistic SPI-1 forecasts for model 1 of below normal, normal and above normal precipitation conditions over WA during the four boreal summer months (June - September) for 0lt forecasts. Point labels give the relative frequencies of use of each forecast probability.

forecast is found in June and July.

6.5.2.3 Continuous ranked probability score

An additional verification parameter is used in order to check the quality of probabilistic forecasts obtained from both models. The continuous ranked probability score (CRPS; Matheson et al. 1976) is one of the most popular verification metrics in the meteorological community. The best CRPS is the lowest (i.e., 0 indicates the best forecast), since it generalizes an absolute error (see Section 3.5.1).
The CRPS is calculated for each month and each lead-time for both models. Based on the results (Table 6.5), we conclude again that model 1 tends to perform better, since the values for model 1 are lower than those for model 2. The lowest values are distributed between different lead-times; however, the smallest value is observed in September for the 3lt forecast. Based on the CRPS, the forecast for June is slightly more accurate compared to other months. However, the differences are not large; thus, little higher values are observed in August, with the most accurate forecast obtained for 1lt. The best forecasts in September are found at 2lt and 3lt. In July, as mentioned before, we obtained the lowest accuracy, with a CRPS of around 0.52.
The CRPS obtained from model 2 have higher values. It is difficult to name the best forecasted month, since the values vary between lead-times. However, the lowest score

Table 6.4: Summary of verification parameters: Brier Score (BS) and Brier Skill Score (BSS) for Model 1 (top part) and Model 2 (bottom part)

Model 1						
0lt						
	BN		NN		AN	
Month	BS	BSS	BS	BSS	BS	BSS
June	0.1590	0.2765	0.2071	0.0805	0.1734	0.2179
July	0.1844	0.1710	0.2188	0.0106	0.1857	0.1677
August	0.1821	0.1866	0.1883	0.1385	0.1879	0.1613
September	0.1795	0.1910	0.2089	0.0539	0.1761	0.2134
1lt						
Month	BS	BSS	BS	BSS	BS	BSS
June	0.1640	0.2531	0.2134	0.0525	0.1811	0.1829
July	0.1812	0.1854	0.2114	0.0442	0.1861	0.1659
August	0.1728	0.2283	0.1951	0.1072	0.1669	0.2549
September	0.1720	0.2247	0.2065	0.0650	0.1762	0.2131
2lt						
Month	BS	BSS	BS	BSS	BS	BSS
June	0.1713	0.2201	0.2210	0.0185	0.1887	0.1490
July	0.2368	0.0650	0.2652	-0.1991	0.2411	-0.0806
August	0.1797	0.1976	0.2092	0.0427	0.1781	0.2052
September	0.1691	0.2381	0.2066	0.0643	0.1725	0.2297
2lt						
Month	BS	BSS	BS	BSS	BS	BSS
June	0.1706	0.2233	0.2160	0.0408	0.1814	0.1818
July	0.1836	0.1744	0.2205	0.0030	0.1842	0.1747
August	0.1711	0.2357	0.2028	0.0721	0.1713	0.2354
September	0.1683	0.2416	0.2024	0.2239	0.1680	0.2498
Model 2						
0lt						
	BN		NN		AN	
Month	BS	BSS	BS	BSS	BS	BSS
June	0.2149	0.0305	0.3011	-0.3371	0.2154	0.0191
July	0.2205	0.0053	0.3025	-0.3432	0.2179	0.0078
August	0.2316	-0.0447	0.2983	-0.3246	0.2374	-0.0810
September	0.2136	0.0363	0.2995	-0.3300	0.2115	0.0372
1lt						
Month	BS	BSS	BS	BSS	BS	BSS
June	0.2178	0.0238	0.2847	-0.2876	0.2129	0.0427
July	0.2329	-0.0438	0.2901	-0.3118	0.2332	-0.0487
August	0.2628	-0.1780	0.2686	-0.2146	0.2753	-0.2379
September	0.2178	0.0238	0.2869	-0.2973	0.2250	-0.0117
2lt						
Month	BS	BSS	BS	BSS	BS	BSS
June	0.2259	-0.0084	0.2804	-0.2831	0.2251	-0.0053
July	0.2155	0.0383	0.2824	-0.2926	0.2250	-0.0050
August	0.2038	0.0902	0.2741	-0.2546	0.2066	0.0773
September	0.2171	0.0312	0.2811	-0.2863	0.2228	0.0050
3lt						
Month	BS	BSS	BS	BSS	BS	BSS
June	0.2134	0.0470	0.2748	-0.2447	0.2161	0.0263
July	0.2141	0.0441	0.2855	-0.2928	0.2180	0.0177
August	0.2247	-0.0034	0.2858	-0.2945	0.2330	-0.0501
September	0.2381	-0.0634	0.2867	-0.2982	0.2424	-0.0926

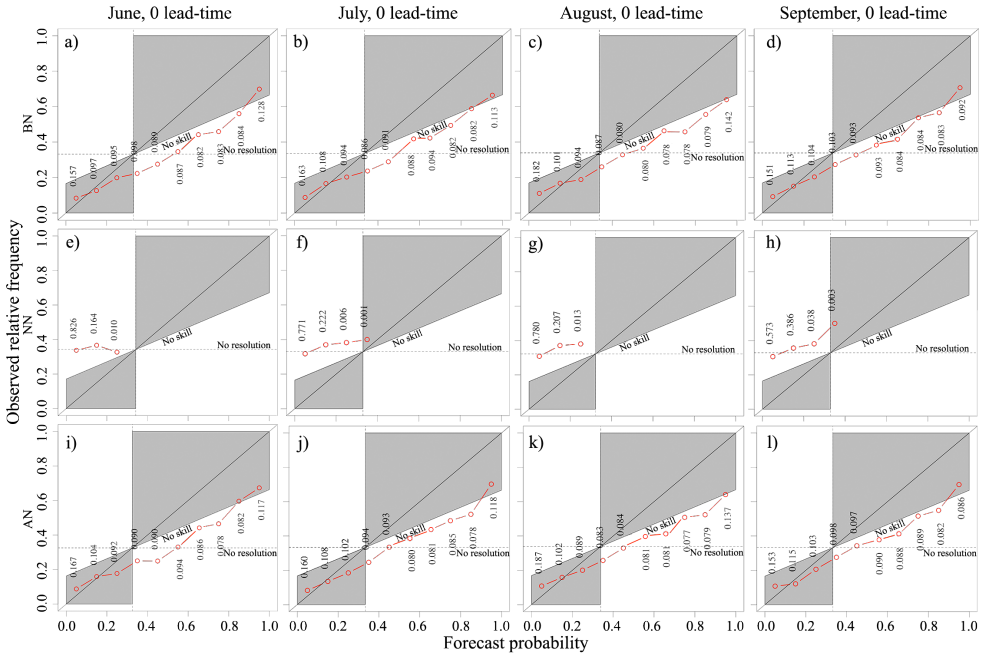

Figure 6.17: The same as in Figure 6.16, but for model 2.

is observed in August for the 2lt forecast (0.65). The worst forecast is obtained in September for 3lt, while interestingly enough, the same forecast is the best according to model 1. In general, in June and July the CRPS values are similar, except for June 1lt forecast, where the score is relatively high. In August and September, the situation is not stable at all, skills are different and range from 0.65 (August, 2lt) to 0.86 (August 0lt). In September, the values are slightly higher, with the lowest observed for the 0lt forecast and the highest for 3lt. Thus, August exhibits the most accurate forecast in model 2. We conclude that the CRPS values are mostly consistent with the corresponding results obtained from the other verification metrics.

6.5.3 Example: June 1984

A visual comparison between the two forecasting models and the observed SPI, transferred into the three gradations, is presented in Figure 6.18 for the same example month (June 1984) as in Section 6.5.1. The observed SPI values are transferred into the categories of dry, neutral and wet conditions and visualised. Five significant regions of dry and wet events are evident in Figure 6.18. Regarding the wet events, the first area is located in the western part of WA, covering the Guinea Coast and western part of Mauritania; the second is in the north-eastern part of WA, and finally, the third part is located in the south of WA. Dry events cover central areas of WA, except for small regions over Nigeria, dividing the big dry domain into two parts.
Comparing both models with observational data, we conclude that model 1 reproduces dry and wet events slightly more accurately than model 2. The western wet area is not

Table 6.5: Summary of CRPS values for WA for model 1 and model 2.

Month	0lt	1lt	2lt	3lt
Model 1				
June	0.4137	0.4320	0.4245	0.4108
July	0.5094	0.5101	0.5805	0.5105
August	0.4344	0.4070	0.4345	0.4148
September	0.4472	0.4440	0.4210	0.3998
Model 2				
June	0.7318	0.7410	0.9286	0.7238
July	0.7275	0.8203	0.9183	0.7414
August	0.8558	0.7685	0.6461	0.7724
September	0.6598	0.7422	0.8469	0.9413

reproduced well by both models; only the 2lt in the model 1 and model 2 presented forecasts relatively close to the observed situation. The eastern wet area is also forecasted insufficiently: only the 1lt forecast from model 1 and 0lt, 2lt forecasts from model 2 represented this area with a reasonable approximation to the observations. Both models for all lead-time forecasts capture the dry area in the south, where inaccuracy is mostly noticed in the spatial distribution. We observe that the spatial pattern of model 1 is more precise, especially in the 0lt and 2lt forecasts. Dry events are reproduced by model 1 correctly for 0lt and 3lt forecasts, for 2lt, the forecasted dry area moves towards the north and the 1lt forecast is too smooth, although it is still possible to recognize dry events. Model 2 produces good enough results for 0lt and 2lt forecasts, while the figures for 3lt and 1lt are again forecasted too smooth.

6.6 Discussion

We have considered a second region in order to study the applicability of the proposed forecasting scheme to different regions and for different lead-times. We focused on a study period of 1982-2016 and four months (June-September) to characterise dry and wet periods in the WA region. We have first provided an analysis of the precipitation data used, reconstructed the SPI-1 index for further calculations, checked the quality of precipitation forecasts obtained from the CFSv2 forecasting model and motivated the necessity of implementing statistical post-processing methods in order to increase the quality of long-range precipitation predictions. The chapter also included an analysis of the most extreme cases of drought and wet events in WA during the study period. The analysis was complemented by an evaluation of long-term variability of extreme drought and wet events, where both types of events were checked for persistence in time, identifying the historically most extreme events with their duration and spatial

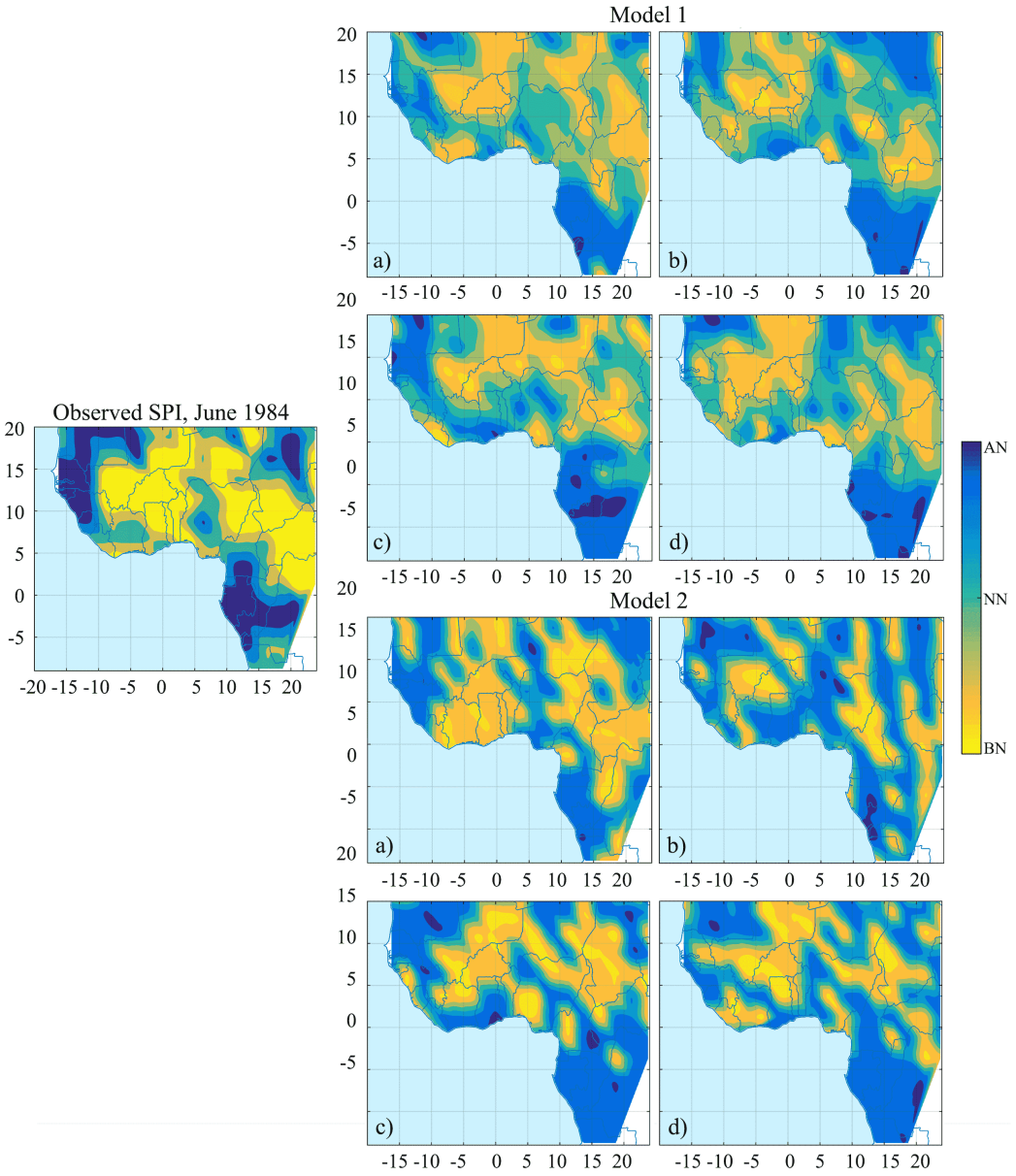

Figure 6.18: Example results of observed SPI (in terms of below, normal and above normal events) and probabilistic forecasts of spatial SPI-1 patterns for June, 1984 for model 1 (top 4 panels) and model 2 (bottom 4 panels) for: a) 0lt, b) 1lt, c) 2lt and d) 3lt forecasts.

extent.

Further, we have described the possible influence of teleconnection patterns on precipitation formation and have identified the strongest correlations between certain patterns occurring not only in the Atlantic, but also in the Pacific and Indian oceans, as well as the Mediterranean Sea. Based on this teleconnection analysis, we conclude that, since some regions of WA have strong statistical relations with different indices, using these

indices as predictors could allow obtaining better forecasts in those areas.
Based upon these observations, we have demonstrated the selection of informative predictors for WA SPI values necessary for constructing the forecasting models. We have considered three candidate fields of potential predictors (ST, H500 and MSLP) to identify interconnections with the SPI-1, calculated from the CFSv2 model and CAMS data, respectively. Combinations of potential predictors were identified and used in the forecasting models.
Another new feature introduced in the analysis of WA described in this chapter is the comparison of two regression based forecasting models. The model 1 presents the approach as used for Russia in Section 4.3.1, with an ensemble of simple linear regression equations obtained for each FA, while model 2 (see Section 4.4.1) presents a classical multiple linear regression approach, where all possible predictors are included in one single equation.
To identify the best forecasting model, we have employed various verification metrics. We have found that for WA, model 1 produces more accurate forecasts for both deterministic and probabilistic predictions. The highest accuracy was achieved in June followed by September, August and July for dry events, while slightly worse accuracy was achieved for wet events, and acceptable accuracy for normal situations. We demonstrated the absence of a linear relation between predictability and lead-time. However, the 3lt forecast was even better than 0lt (e.g., in the September case).
Comparison of deterministic and probabilistic forecasts for model 2 demonstrated lower accuracy and higher errors than for model 1, and much stronger overestimation of the predicted events. Model 2 also showed different accuracy behaviour in deterministic forecasting during the study period. It was noticed that SPI values in maritime regions and areas with less continentality (closer to the ocean) are predicted better. According to the probabilistic forecasts, model 2 exhibits poor accuracy and even produced the forecasts worse than climatological forecast. However, visual analysis demonstrated for the example of June 1984 that both models may be able to describe the general patterns of all three types of events (BN, NN, AN) with acceptable accuracy.
To this end, the proposed model 1 produces higher accuracy for deterministic and probabilistic forecasts and can be implemented for different regions and models. We could not identify a strong decrease in its accuracy with an increase of lead-time. For this reason, at least the first four months' outputs, which have been checked for ST, H500 and MSLP fields, can be taken from the CFSv2 model for further work.

Chapter 7

Conclusions and outlook

Obtaining consistent and reliable precipitation forecasts beyond the time-scales of normal synoptic patterns is a challenging task. The results obtained from such forecasts are important for a variety of different applications including (but not limited to) agricultural and hydrological planning, decision making in engineering and industry, etc. Accordingly, since the topic is important, there is an increasing interest in the development of improved forecasting schemes.
The main goal of this study was to develop a statistical post-processing scheme based on linear regression models, reconstructing precipitation in terms of the SPI index and thereby improving the quality of long-term precipitation forecasts based on the identified predictors. To test the regression models, two case studies and two forecasting models were selected. The first experiment was based on the application of the SL-AV model to a case study in Russia, where monthly precipitation data for boreal summer (June-August) were forecasted for the period 1983-2010. The second experiment applied the CFSv2 model for West Africa (WA), with the period of interest being the summer wet seasons (June-September) from 1982-2016. In WA, we focused on monthly precipitation predictions with different lead-times (0-3 months). After discussed the two cases, we now return to the original research questions that are presented in the introduction, summarize the main results of this study, and provide an outlook for further work that could be continued on the topic of further improvement of precipitation forecast.

7.1 Conclusions

- *Since numerical weather prediction (NWP) models do not produce good precipitation estimates, are there further statistical methods to improve precipitation predictions?*

  Statistical methods are popular tools that aim to improve different lead-time forecasts, especially long-range precipitation predictions, due to their relatively simple implementation procedures, potential for fast calculations, and relatively

easy-to-implement methods to identify significant connections between predictors and the predictand.

The methods applied to NWP outputs are called post-processing methods. They quantify the relationship between forecasted predictors and observed predictand in order to obtain new, calibrated forecasts. Statistical post-processing methods can significantly improve raw NWP calculations and thus have become quite popular. In this work, we presented an improved monthly precipitation forecasting scheme for different lead-time forecasts, starting at the initialization time for the Standardized Precipitation Index (SPI) over Russia and WA based on two prediction models: the SL-AV operational model (for the Russian case study) and CFSv2 model (for the WA case study). Notably, contemporary NWP models used for producing seasonal forecasts, like SL-AV and CFSv2, often perform relatively poorly at this task. This insufficiency results from differences between the observation and interpretation data in the model, incomplete representation of physical processes in the atmosphere, systematic biases, and other problems. Here, we have proposed a new statistical post-processing scheme that includes some ingredients of other existing schemes but combines them in a way that (to the best of the author's knowledge) has not been attempted previously in the context of SPI forecasting. With this method, we developed an improvement in the monthly precipitation forecasts of both case studies.

- *Can we construct statistical forecasting models for predicting precipitation based on large-scale predictors?*

  In this work, we presented two forecasting models that display the potential of this approach. We were motivated by the substantial influence of large-scale atmospheric teleconnection patterns on precipitation formation in the two study regions. Accordingly, our analysis provided a detailed characterization of statistical interrelationships between some of the most prominent Northern and Southern Hemispheric centres of action in atmospheric dynamics and the regimes of boreal summer precipitation across Russia and WA. In regions with significant co-variability between observed SPI-1 values and corresponding pressure variables, our new forecasting scheme commonly yields acceptable results and outperforms previous direct precipitation forecasts. In order to identify potential informative predictors for the regional SPI-1 fields over Russia and WA, we provided a cross-correlation analysis for the absolute geopotential at 500 hPa level (H500) and mean sea level pressure (MSLP) predictors for Russia, and H500, MSLP and surface temperature (ST) predictors for the WA case study, where the predictors were taken from hindcasts obtained from the SL-AV and CFSv2 models, respectively. Based on these datasets, we defined potential predictors for the SPI-1 values in each forecasting region with respect to the target SPI-1 value for a given calendar month. By this analysis, for each forecasting region, calendar month and lead-time for which SPI-1 was to be predicted, we identified a set of candidate regions in the H500, MSLP and ST fields. In order to

obtain a robust and numerically feasible forecasting scheme, we further reduced the number of individual candidate predictors to a set of regions by selecting the weighted mean value for each group of spatially contiguous grid points with strong enough correlations with an target variable. We also introduced extra conditions that the potential predictors had to satisfy.

Essentially, we prepared sets of possible predictors and they (and their combinations) were used in a forecasting scheme to reconstruct past precipitation in Russia and WA. In this approach, the detection of predictors played a crucial role; thus, the procedure for identifying potential predictors had to be as accurate as possible. We noticed that since precipitation in WA has a strong connection with ST, we obtained more strong candidate predictors from this variable (in comparison with MSLP and H500), and as a result, achieved higher accuracy for precipitation reconstructions in WA than in Russia.

The prediction results achieved by the new approach have been compared to hindcast data, revealing that the proposed prediction scheme has great potential to improve forecasts for both study regions beyond the existing direct precipitation forecasts of the underlying SL-AV and CFSv2 model. We also showed the absence of a linear connection between predictability and lead-time for different months: the accuracy between lead-times is different. However, in most cases, the last 3lt forecast was even better than 0lt; we noticed that the 2lt and 0lt forecasts were often less accurate.

- *Can the statistical forecasting models be implemented for any region and be constructed by various NWP models?*

  In this study, the statistical forecasting model is based on linear regression. The classical interpretation of linear regression is that it shows the linear relationships between dependent variable(s)/predictor(s) and a predictand. Such relationships can be identified between any predictors and predictand. We checked the forecasting scheme for two case studies - Russia and WA - to show how the scheme works on such regions, with extremely diverse circulation patterns and precipitation regimes. The good results obtained from the proposed forecasting scheme show its flexibility and the potential to implement the model for different study areas.

  The most important step of using such scheme is to identify relevant statistical connections between predictor and predictand. The connection can be identified by correlation analysis between selected candidate predictors that influence precipitation in the region of interest. The predictors should be well-presented by NWP models, e.g., in this thesis we employed two different forecasting models: SL-AV and CFSv2 for Russia and WA correspondingly.

  When we checked the SPI-1 index, obtained from the raw NWP precipitation we got poor predictability for both NWP models. That is why the implementation of further corrections is required. One possible way to solve this problem is

post-processing techniques. In short, the identified potential informative predictors can be used to constrain the expected SPI-1 values for any given grid point, together with their associated uncertainty. Specifically, we proposed an SPI-1 forecasting scheme in which all possible combinations of individual predictors from H500, MSLP (for the case of Russia) and H500, MSLP, ST (for WA) are considered to form a set of linear regression equations for the predictand (local SPI-1 value). The maximum possible variety of combinations of predictors from the H500, MSLP and ST fields are used to explore the full space of possibilities in the probabilistic forecasting task and capture as much as possible of the associated forecast uncertainty. Following this rationale, we provided an ensemble of linear regression equations for each forecasting region. The result of such regression approach can be delivered in probabilistic and deterministic ways.

7.2 Outlook

The work on the proposed methodology revealed several topics for future research that may result in further improvements of the proposed forecasting scheme.

- *Different precipitation data sets* can be tested and used. Recently, many new high-quality high-resolution and open source precipitation archives have been published. However, these archives must be comprehensively reviewed in order to identify the most appropriate ones for forecasting purposes. Their high resolution may be another challenge, since it requires more computational resources, especially to perform cross-correlation analysis. In such cases, it is important to provide a procedure of upscaling, which can cause errors and require approximations. Within this topic, it is necessary to adopt a strategy that balances reasonable resolution and computation time requirements, while providing accurate predictions.

- *Additional predictors* could be identified and used to construct the regression models. In the presented study we used only three predictors - two pressure covariates and surface temperature. However, other possible predictors (e.g., wind velocity), should be also considered, since they may have a strong physical connection with precipitation formation and may increase the quality of resulting forecasts. Additional work can be done on implementing different statistical approaches for cluster analysis to identify possible potential predictors more carefully (e.g., network analysis, principle component analysis, Bayesian model averaging and others).

- *Identifying different approaches for obtaining deterministic forecasts* is the most important part of further work in this area. The current way of extracting deterministic forecasts from a system of linear regression equations in Model 1 should be reconsidered (e.g., the simple averaging approach should be replaced

by a more accurate one). A better solution should increase the accuracy of deterministic forecasts.

- *Other precipitation indices*: In the beginning of the work related to this thesis, we produced a comparison of the most popular precipitation indices currently in use (Utkuzova et al. 2015a). This analysis showed that the SPI is the most appropriate index for representing drought and wet conditions in the mid-latitudes. Moreover, SPI recommended by the World Meteorological Organisation (WMO) to detect drought and wet events (Svoboda et al. 2012). Recently, we have become interested in the SPEI index, which is a slightly modified version of the SPI. The SPEI includes evapotranspiration, making it more sensitive to droughts, since it plays an important role in the formation of serious drought and wet events, especially in regions with low monthly precipitation totals (subtropics, tropics). Contextually, it makes sense to provide a comparison between forecasting models applied to SPI and SPEI for different climate regions in order to identify areas where each index gives the most reliable precipitation forecasts.

Figures

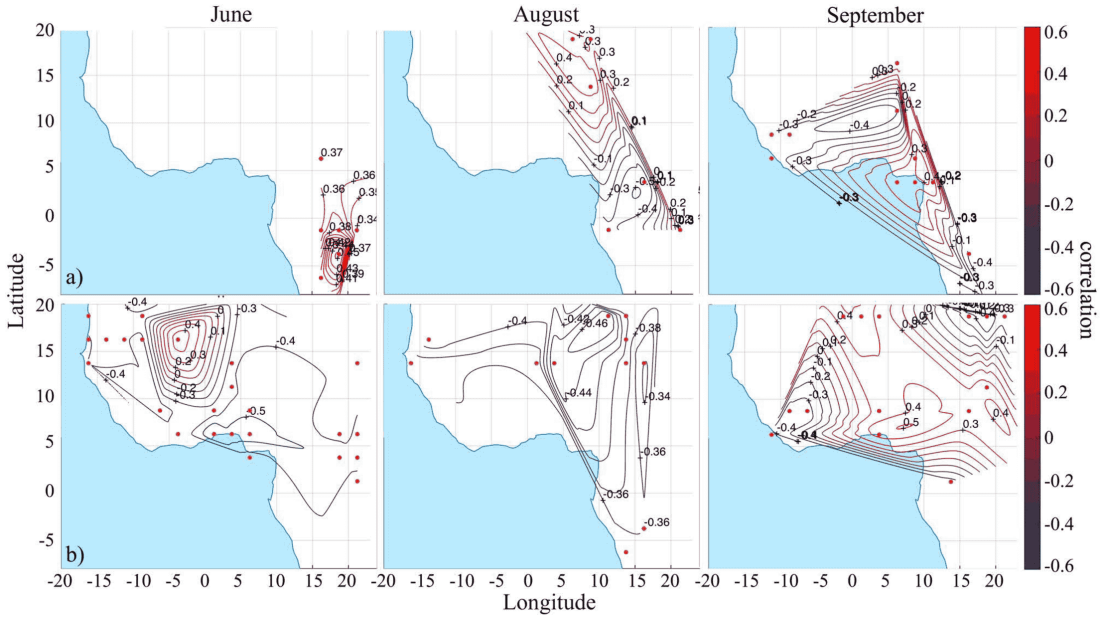

Figure A1: Results of spatial correlation analysis between the CAMS-derived SPI-1 observations and different atmospheric circulation patterns a) PNA, b) MJO_W10, for the boreal summer (from left to right: June, August, September.)

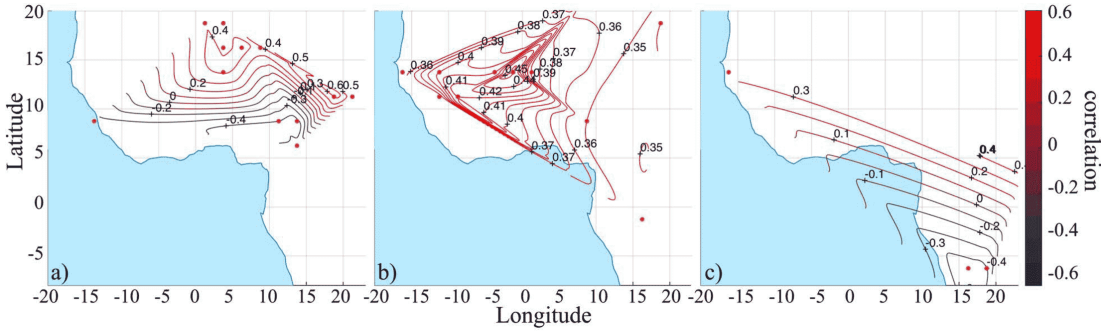

Figure A2: Results of spatial correlation analysis between the CAMS-derived SPI-1 observations and different atmospheric circulation patterns a) ATL3, b) QBO, c) SOI for September.

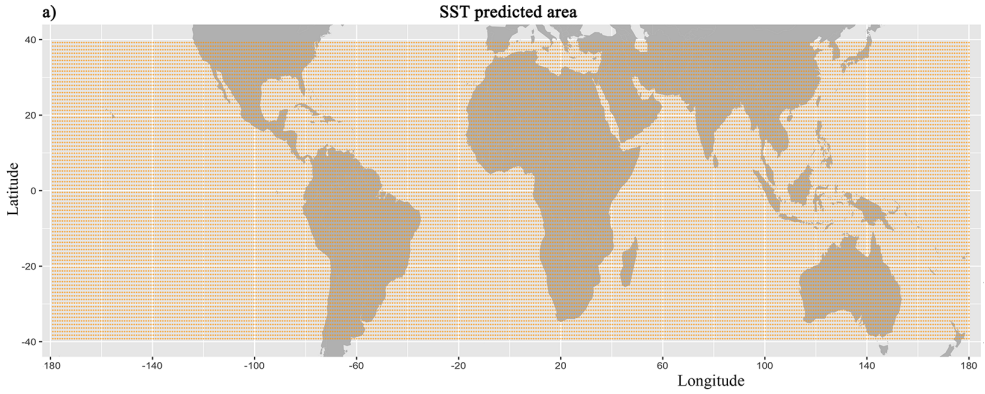

Figure A3: Grids for potential predictors: a) ST, b) MSLP and H500.

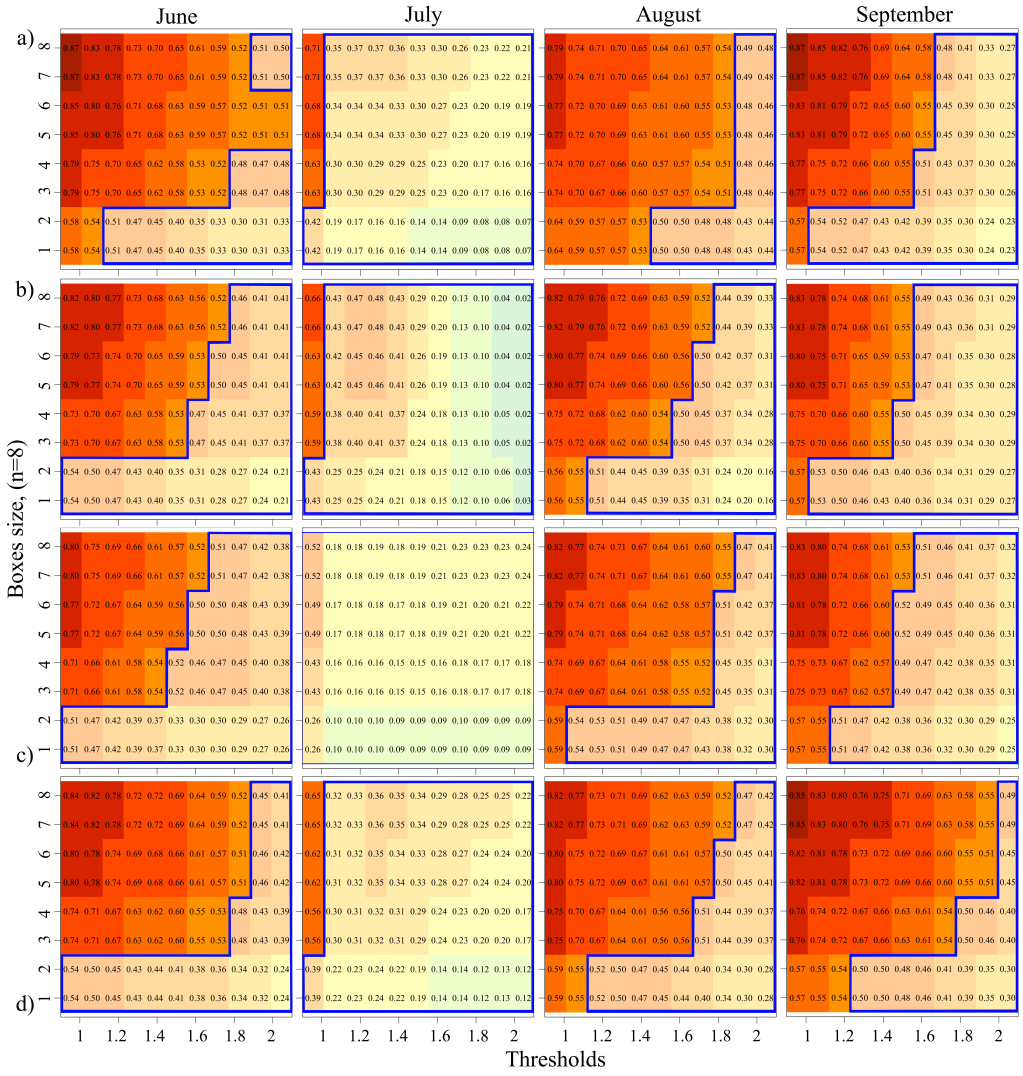

Figure A4: Neighbourhood verification scores using FSS method for *wet* events for the period 1982-2016 verified against observed SPI for the same period for Model 1. a) 0lt, b) 1lt, c) 2lt, d) 3lt.

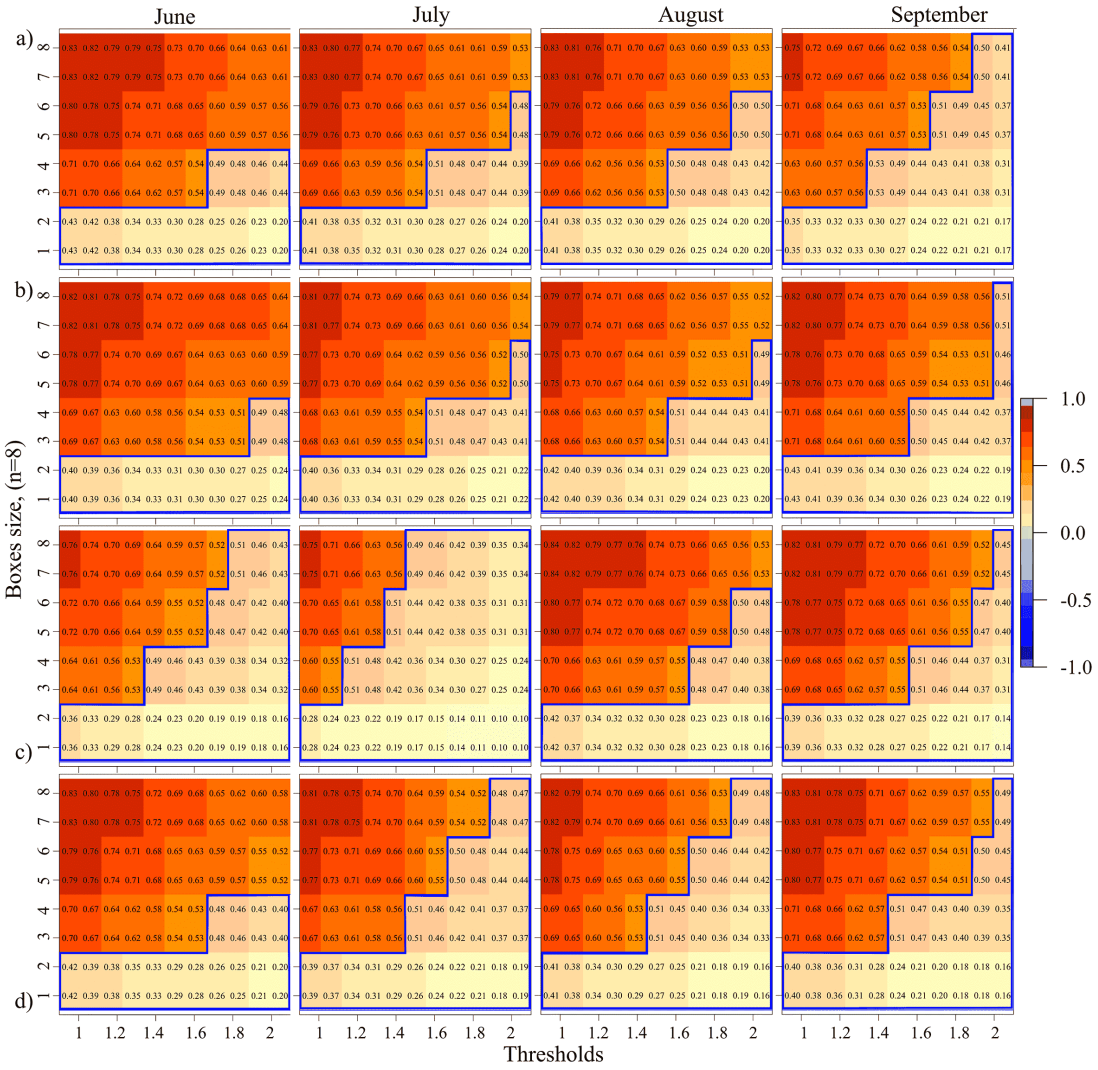

Figure A5: Same as in Figure A4, but for dry events, Model 2.

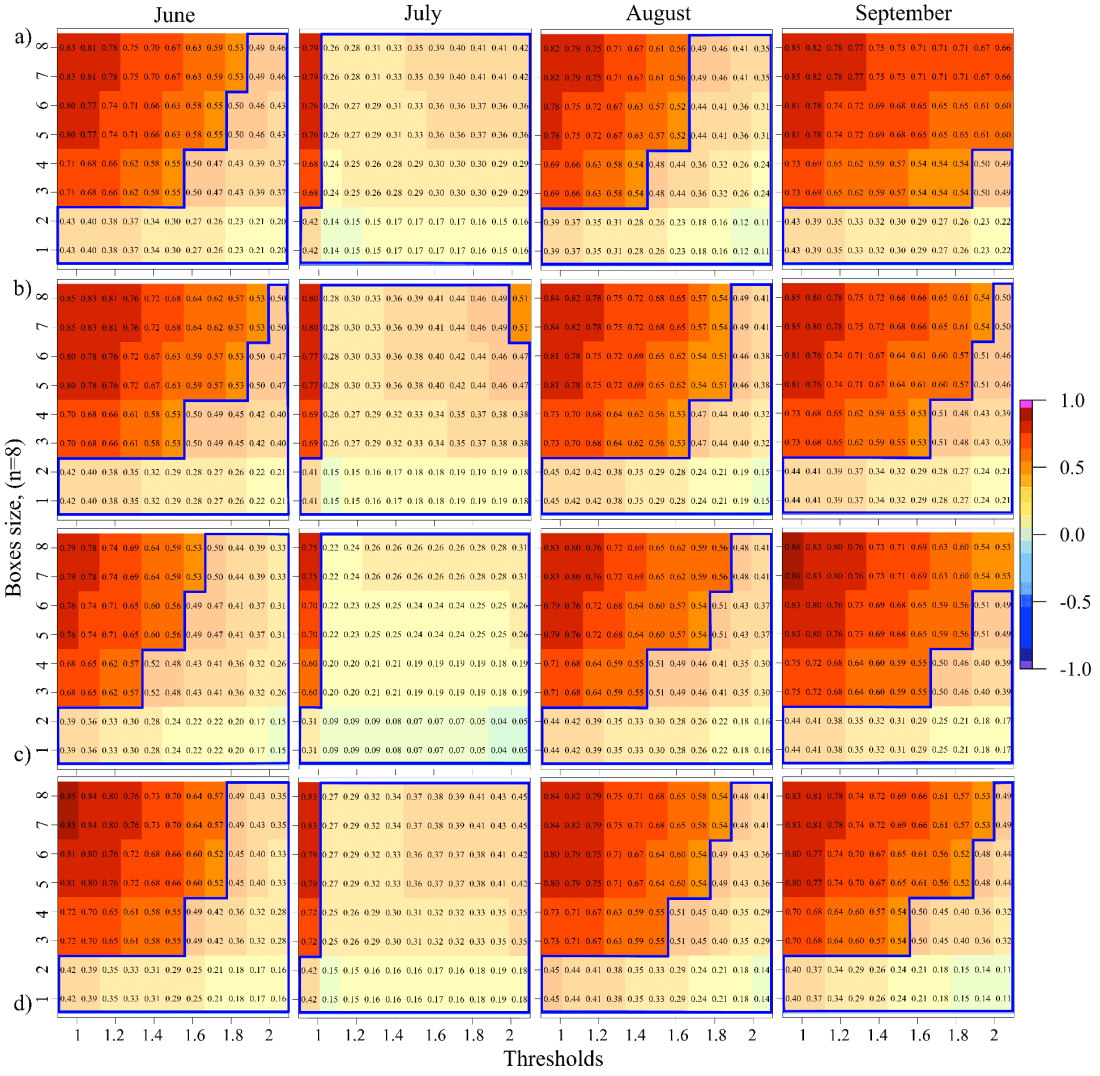

Figure A6: Same as in Figure A4, but for wet events, Model 2.

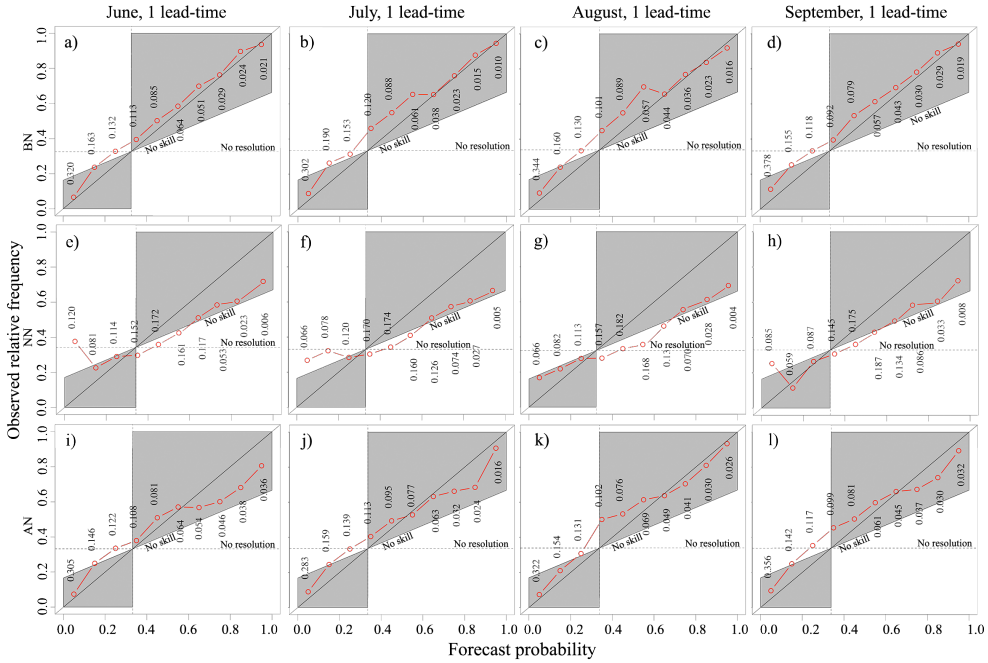

Figure A7: Reliability diagrams for probabilistic SPI-1 forecasts for Model 1 of below normal, normal and above normal precipitation conditions over WA during June-September for 1lt. Point labels give the relative frequencies of use of each forecast probability.

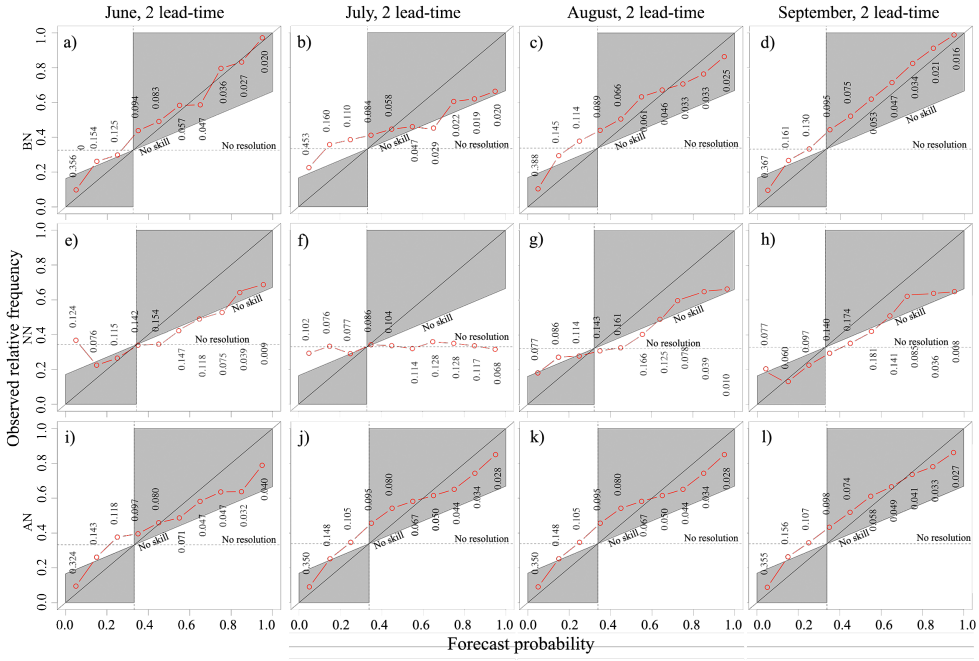

Figure A8: Same as in Figure A7, but for 2lt forecast, Model 1.

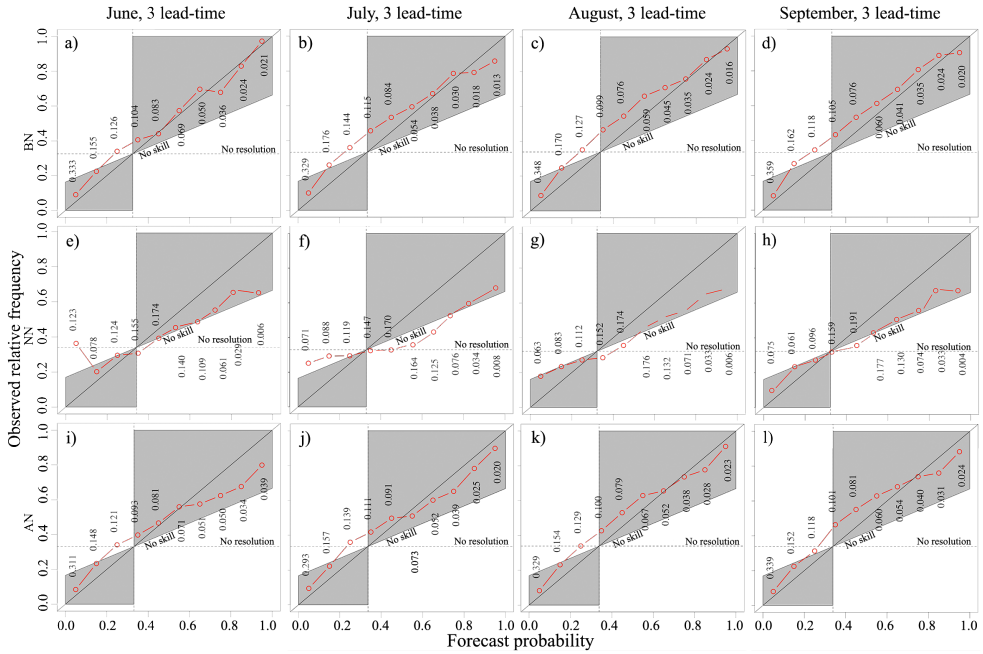

Figure A9: Same as in Figure A7, but for 3lt forecast, Model 1.

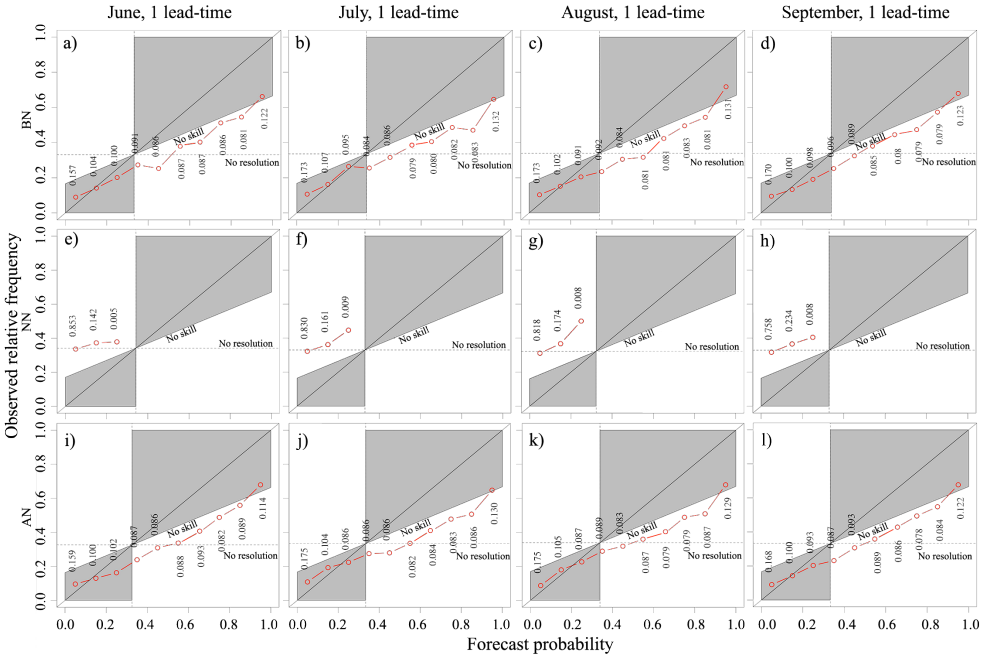

Figure A10: Same as in Figure A7, but for 1lt forecast, Model 2

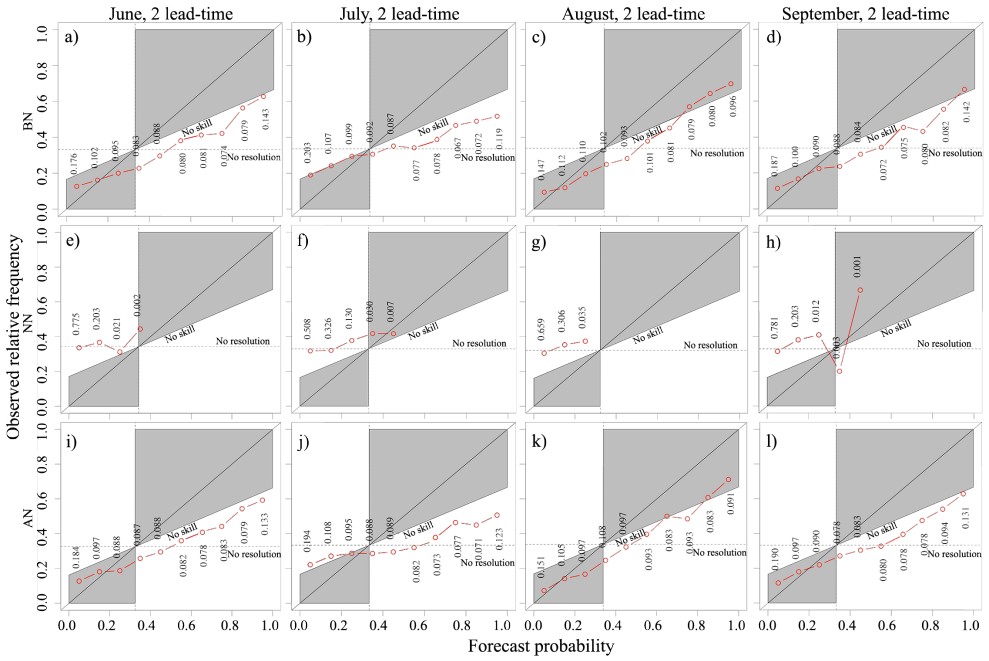

Figure A11: Same as in Figure A7, but for 2lt forecast, Model 2.

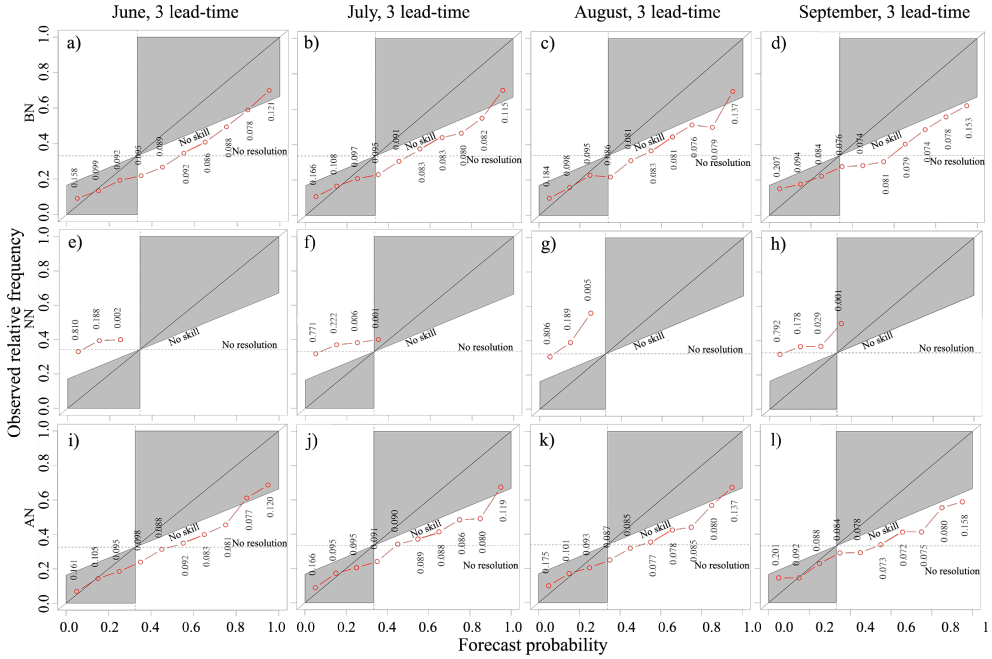

Figure A12: Same as in Figure A7, but for 3lt forecast, Model 2.

Bibliography

Abramowitz, M. and Stegun, A. (1965). "Handbook of mathematical formulas, graphs, and mathematical tables". In: *National Bureau of Stand Mathematics Series* 55.

"Adoption of the Paris Agreement" (2015). In: *Conference of the Parties Twenty-first session* L.9, p. 31.

Arkhangelskiy, V. (1956). "Tracks and speeds of cyclones and anticyclones movements in Eastern Siberia and Far Eastern part of USSR. [Пути и скорости перемещения циклонов и антициклонов в Восточной Сибири и на Дальнем Востоке]". In: *Proceedings of FERHRI, [in Russian]* 1, pp. 97–113.

Balsamo, G., Albergel, C., Beljaars, A., Boussetta, S., Brun, E., Cloke, H., Dee, D., Dutra, E., Muñoz-Sabater, J., Pappenberger, F., Rosnay, P. de, Stockdale, T., and Vitart, F. (2015). "ERA-Interim/Land: a global land water resources dataset". In: *Hydrology and Earth System Sciences* 19, pp. 389–407.

Bardossy, A. and Plate, E. J. (1992). "Space-time model for daily rainfall using atmospheric circulation patterns". In: *Water Resources Research* 28(5), pp. 1247–1259.

Barnston, A. G. and Livezey, R. E. (1987). "Classification, seasonality and persistence of low-frequency atmospheric circulation patterns". In: *Monthly Weather Review* 115(6), pp. 1083–1126.

Barnston, A. G. and Tippett, M. K. (2013). "Predictions of Nino3. 4 SST in CFSv1 and CFSv2: a diagnostic comparison". In: *Climate dynamics* 41(6), pp. 1615–1633.

Barry, R. G. and Chorley, R. J. (2009). *Atmosphere, weather and climate*. Routledge.

Behringer, D. (2007). "3.3 The Global Ocean Data Assimilation System (GODAS) at NCEP". In: *Proceedings of the 11th Symposium on Integrated Observing and Assimilation Systems for the Atmosphere, Oceans, and Land Surface*.

Bell, G. D. and Janowiak, J. E. (1995). "Atmospheric circulation associated with the Midwest floods of 1993". In: *Bulletin of the American Meteorological Society* 76(5), pp. 681–695.

Below, R., Grover-Kopec, E., and Dilley, M. (2007). "Documenting drought-related disasters: A global reassessment". In: *The Journal of Environment & Development* 16(3), pp. 328–344.

Berezhnykh, T., Marchenko, O. Y., Abasov, N., and Mordvinov, V. (2012). "Changes in the summertime atmospheric circulation over East Asia and formation of long-lasting low-water periods within the Selenga river basin". In: *Geography and natural resources* 33(3), pp. 223–229.

Bjerknes, J. (1969). “Atmospheric teleconnections from the equatorial Pacific”. In: *Monthly Weather Review* 97(3), pp. 163–172.

Bondell, H. D. and Reich, B. J. (2008). “Simultaneous regression shrinkage, variable selection, and supervised clustering of predictors with OSCAR”. In: *Biometrics* 64(1), pp. 115–123.

Brown, B. et al. (2009). “Spatial Verification Methods”. In: *Presentation at the âFourth International Verification Methods Workshop*. Vol. 4(10.06), p. 2009.

Byshev, V., Kononova, N., Neiman, V., and Romanov, Y. A. (2002). “Peculiarities of the Climate Dynamics in the Northern Hemisphere in the 20th Century”. In: *Doklady earth sciences*. Vol. 385. Springer, pp. 538–545.

Carslaw, D. C. and Ropkins, K. (2012). “Openairâan R package for air quality data analysis”. In: *Environmental Modelling & Software* 27, pp. 52–61.

Carter, G. M., Dallavalle, J. P., and Glahn, H. R. (1989). “Statistical forecasts based on the National Meteorological Center’s numerical weather prediction system”. In: *Weather and Forecasting* 4(3), pp. 401–412.

Casati, B. (2010). “New developments of the intensity-scale technique within the Spatial Verification Methods Intercomparison Project”. In: *Weather and Forecasting* 25(1), pp. 113–143.

Chen, S.-F. and WU, R. (2017). “An enhanced influence of sea surface temperature in the tropical northern Atlantic on the following winter ENSO since the early 1980s”. In: *Atmospheric and Oceanic Science Letters* 10(2), pp. 175–182.

Cherenkova, E. (2007). “Dynamics of severe atmospheric droughts in European Russia”. In: *Russian Meteorology and Hydrology* 32(11), pp. 675–682.

Cherenkova, E. and Kononova, N. (2012). “Analisys of a severe atmospheric drought in 1972 and 2010 and mac-rocirculation conditions of its formation over the European part of Russia”. In: *Tr. Gl. Geofiz. Obs. im. AI Voei-kova* 565, pp. 165–187.

Cherenkova, E. and Popova, E. (2015). “Dynamics of soil moistening in spring and summer 2010 in the European Russia on the basis of the analysis of remote sensing data”. In: *Sovr. Probl. Distantsionnogo Zondirovaniya Zemli Kosmosa* 12(4), pp. 119–130.

Conte, M., Giuffrida, A., and Tedesco, S. (1989). “Mediterranean Oscillation: Impact on Precipitation and Hydrology in Italy”. In: *Conference on Climate and Water*. Vol. 1.

Cook, E. R., Seager, R., Cane, M. A., and Stahle, D. W. (2007). “North American drought: reconstructions, causes, and consequences”. In: *Earth-Science Reviews* 81(1), pp. 93–134.

Cotillon, S. E. and Tappan, G. G. (2016). “Landscapes of West Africa: A window on a changing world”. In:

Coumou, D., Petoukhov, V., Rahmstorf, S., Petri, S., and Schellnhuber, H. J. (2014). “Quasi-resonant circulation regimes and hemispheric synchronization of extreme weather in boreal summer”. In: *Proceedings of the National Academy of Sciences* 111(34), pp. 12331–12336.

Dai, A. (2011). "Drought under global warming: a review". In: *Wiley Interdisciplinary Reviews: Climate Change* 2(1), pp. 45–65.

Davis, C. A., Brown, B. G., Bullock, R., and Halley-Gotway, J. (2009). "The method for object-based diagnostic evaluation (MODE) applied to numerical forecasts from the 2005 NSSL/SPC Spring Program". In: *Weather and Forecasting* 24(5), pp. 1252–1267.

De Geer, G. (1926). "On the solar curve: as dating the ice age, the New York Moraine, and Niagara Falls through the Swedish Timescale". In: *Geografiska Annaler* 8, pp. 253–283.

Dee, D. P., Uppala, S. M., Simmons, A., Berrisford, P., Poli, P., Kobayashi, S., Andrae, U., Balmaseda, M., Balsamo, G., Bauer, d. P., et al. (2011). "The ERA-Interim reanalysis: Configuration and performance of the data assimilation system". In: *Quarterly Journal of the royal meteorological society* 137(656), pp. 553–597.

Dormann, C. F., Elith, J., Bacher, S., Buchmann, C., Carl, G., Carré, G., Marquéz, J. R. G., Gruber, B., Lafourcade, B., Leitão, P. J., et al. (2013). "Collinearity: a review of methods to deal with it and a simulation study evaluating their performance". In: *Ecography* 36(1), pp. 27–46.

Dracup, J. A., Lee, K. S., and Paulson, E. G. (1980). "On the definition of droughts". In: *Water resources research* 16(2), pp. 297–302.

Druyan, L. M. (2011). "Studies of 21st-century precipitation trends over West Africa". In: *International Journal of Climatology* 31(10), pp. 1415–1424.

Duncan, G. and Job, B. L. (1978). "Crisis forcasting using the Markov Renewal model". In: *International Interactions* 4(3), pp. 225–246.

Dutra, E., Di Giuseppe, F., Wetterhall, F., and Pappenberger, F. (2013). "Seasonal forecasts of droughts in African basins using the Standardized Precipitation Index". In: *Hydrology and Earth System Sciences* 17(6), p. 2359.

Dzerdzeevskii, B. (1968). "Circulation mechanisms in the atmosphere of the Northern Hemisphere in the Twentieth Century". In: *Institute for Geography, Soviet Academy of Sciences, Moscow [in Russian].[Goedecke R (translator), Berryman BF (ed), University of Wisconsin Press, Madison, WI, 1970]*.

Ebert, E. E. (2008). "Fuzzy verification of high-resolution gridded forecasts: a review and proposed framework". In: *Meteorological applications* 15(1), pp. 51–64.

Ebert, E. E. (2009). "Neighborhood verification: A strategy for rewarding close forecasts". In: *Weather and Forecasting* 24(6), pp. 1498–1510.

Ebert, E. E. and Gallus Jr, W. A. (2009). "Toward better understanding of the contiguous rain area (CRA) method for spatial forecast verification". In: *Weather and forecasting* 24(5), pp. 1401–1415.

Ebert, E. E. and McBride, J. (2000). "Verification of precipitation in weather systems: Determination of systematic errors". In: *Journal of Hydrology* 239(1), pp. 179–202.

Ek, M., Mitchell, K., Lin, Y., Rogers, E., Grunmann, P., Koren, V., Gayno, G., and Tarpley, J. (2003). "Implementation of Noah land surface model advances in the

National Centers for Environmental Prediction operational mesoscale Eta model". In: *Journal of Geophysical Research: Atmospheres* 108(D22).

Enfield, D. B., Mestas-Nuñez, A. M., Mayer, D. A., and Cid-Serrano, L. (1999). "How ubiquitous is the dipole relationship in tropical Atlantic sea surface temperatures?" In: *Journal of Geophysical Research: Oceans* 104(C4), pp. 7841–7848.

Folland, C., Owen, J., Ward, M. N., and Colman, A. (1991). "Prediction of seasonal rainfall in the Sahel region using empirical and dynamical methods". In: *Journal of Forecasting* 10(1), pp. 21–56.

Fontaine, B., Trzaska, S., and Janicot, S. (1998). "Evolution of the relationship between near global and Atlantic SST modes and the rainy season in West Africa: statistical analyses and sensitivity experiments". In: *Climate Dynamics* 14(5), pp. 353–368.

Fovell, R. G. and Fovell, M.-Y. C. (1993). "Climate zones of the conterminous United States defined using cluster analysis". In: *Journal of climate* 6(11), pp. 2103–2135.

Fraley, C., Raftery, A. E., and Gneiting, T. (2010). "Calibrating multimodel forecast ensembles with exchangeable and missing members using Bayesian model averaging". In: *Monthly Weather Review* 138(1), pp. 190–202.

Fraley, C., Raftery, A., and Scrucca, L. (2012). "Normal mixture modeling for model-based clustering, classification, and density estimation". In: *Department of Statistics, University of Washington* 23, p. 2012.

Gaffney, S. and Smyth, P. (1999). "Trajectory clustering with mixtures of regression models". In: *Proceedings of the fifth ACM SIGKDD international conference on Knowledge discovery and data mining*. ACM, pp. 63–72.

Galvin, J. (2008). "The weather and climate of the tropics: Part 6–Monsoons". In: *Weather* 63(5), pp. 129–137.

Giannini, A., Biasutti, M., and Verstraete, M. M. (2008). "A climate model-based review of drought in the Sahel: desertification, the re-greening and climate change". In: *Global and planetary Change* 64(3), pp. 119–128.

Gilleland, E., Ahijevych, D., Brown, B. G., Casati, B., and Ebert, E. E. (2009). "Intercomparison of spatial forecast verification methods". In: *Weather and forecasting* 24(5), pp. 1416–1430.

Glahn, H. R. and Lowry, D. A. (1972). "The use of model output statistics (MOS) in objective weather forecasting". In: *Journal of applied meteorology* 11(8), pp. 1203–1211.

Glantz, M. (1977). "The value of a long-range weather forecast for the West African Sahel". In: *Bulletin of the American Meteorological Society* 58(2), pp. 150–158.

Gneiting, T. and Raftery, A. E. (2007). "Strictly proper scoring rules, prediction, and estimation". In: *Journal of the American Statistical Association* 102(477), pp. 359–378.

Gneiting, T., Raftery, A. E., Westveld III, A. H., and Goldman, T. (2005). "Calibrated probabilistic forecasting using ensemble model output statistics and minimum CRPS estimation". In: *Monthly Weather Review* 133(5), pp. 1098–1118.

Gómara, I., Mohino, E., Losada, T., Domınguez, M., Suárez-Moreno, R., and Rodrıguez-Fonseca, B. (2017). "Impact of dynamical regionalization on precipitation biases and teleconnections over West Africa". In: *Climate Dynamics*, pp. 1–26.

Gordon, N. D. and Shaykewich, J. (2000). *Guidelines on performance assessment of public weather services*. World Meteorological Organization.

Gray, W. M., Landsea, C. W., Mielke Jr, P. W., and Berry, K. J. (1992a). "Predicting Atlantic seasonal hurricane activity 6–11 months in advance". In: *Weather and Forecasting* 7(3), pp. 440–455.

Gray, W. M., Sheaffer, J. D., and Knaff, J. A. (1992b). "Influence of the stratospheric QBO on ENSO variability". In: *Journal of the Meteorological Society of Japan. Ser. II* 70(5), pp. 975–995.

Gray, W. M., Sheaffer, J. D., and Landsea, C. W. (1997). "Climate trends associated with multidecadal variability of Atlantic hurricane activity". In: *Hurricanes*. Springer, pp. 15–53.

Griffies, S. M., Harrison, M. J., Pacanowski, R. C., and Rosati, A. (2004). "A technical guide to MOM4". In: *GFDL Ocean Group Tech. Rep* 5, p. 371.

Grimit, E. P., Gneiting, T., Berrocal, V., and Johnson, N. A. (2006). "The continuous ranked probability score for circular variables and its application to mesoscale forecast ensemble verification". In: *Quarterly Journal of the Royal Meteorological Society* 132(621C), pp. 2925–2942.

Groisman, P. Y., Knight, R. W., Easterling, D. R., Karl, T. R., Hegerl, G. C., and Razuvaev, V. N. (2005). "Trends in intense precipitation in the climate record". In: *Journal of climate* 18(9), pp. 1326–1350.

Guttman, N. B. (1999). "Accepting the standardized precipitation index: a calculation algorithm". In: *JAWRA Journal of the American Water Resources Association* 35(2), pp. 311–322.

Hamill, T. M. and Colucci, S. J. (1997). "Verification of Eta–RSM short-range ensemble forecasts". In: *Monthly Weather Review* 125(6), pp. 1312–1327.

Hartmann, H. C., Pagano, T. C., Sorooshian, S., and Bales, R. (2002). "Confidence builders: Evaluating seasonal climate forecasts from user perspectives". In: *Bulletin of the American Meteorological Society* 83(5), pp. 683–698.

Hatzaki, M. and Wu, R. (2015). "The south-eastern Europe winter precipitation variability in relation to the North Atlantic SST". In: *Atmospheric research* 152, pp. 61–68.

Hersbach, H. (2000). "Decomposition of the continuous ranked probability score for ensemble prediction systems". In: *Weather and Forecasting* 15(5), pp. 559–570.

Higgins, R., Leetmaa, A., and Kousky, V. (2002). "Relationships between climate variability and winter temperature extremes in the United States". In: *Journal of Climate* 15(13), pp. 1555–1572.

Hoeting, J. A., Madigan, D., Raftery, A. E., and Volinsky, C. T. (1999). "Bayesian model averaging: a tutorial". In: *Statistical science*, pp. 382–401.

Hortal, M. (2002). "The development and testing of a new two-time-level semi-Lagrangian scheme (SETTLS) in the ECMWF forecast model". In: *Quarterly Journal of the Royal Meteorological Society* 128(583), pp. 1671–1687.

Huang, B., Schopf, P. S., and Pan, Z. (2002). "The ENSO effect on the tropical Atlantic variability: A regionally coupled model study". In: *Geophysical Research Letters* 29(21), pp. 35–1.

Huffman, G. J., Adler, R. F., Arkin, P., Chang, A., Ferraro, R., Gruber, A., Janowiak, J., McNab, A., Rudolf, B., and Schneider, U. (1997). "The global precipitation climatology project (GPCP) combined precipitation dataset". In: *Bulletin of the American Meteorological Society* 78(1), pp. 5–20.

Huo, L., Guo, P., Hameed, S. N., and Jin, D. (2015). "The role of tropical Atlantic SST anomalies in modulating western North Pacific tropical cyclone genesis". In: *Geophysical Research Letters* 42(7), pp. 2378–2384.

Hurrell, J. W. et al. (1995). "Decadal trends in the North Atlantic Oscillation: regional temperatures and precipitation". In: *Science-AAAS-Weekly Paper Edition* 269(5224), pp. 676–678.

Huth, R., Beck, C., Philipp, A., Demuzere, M., Ustrnul, Z., Cahynová, M., Kysel, J., and Tveito, O. E. (2008). "Classifications of atmospheric circulation patterns". In: *Annals of the New York Academy of Sciences* 1146(1), pp. 105–152.

Inness, P. M. and Dorling, S. (2012). *Operational weather forecasting*. John Wiley & Sons.

IPCC (2013). "Summary for policymakers". In: *Climate Change 2013: The Physical Science Basis. Contribution of Working Group I to the Fifth Assessment Report of the Intergovernmental Panel on Climate Change*. Cambridge University Press, Cambridge and New York.

Jacob, D. (1999). *Introduction to atmospheric chemistry*. Princeton University Press.

Janicot, S., Moron, V., and Fontaine, B. (1996). "Sahel droughts and ENSO dynamics". In: *Geophysical Research Letters* 23(5), pp. 515–518.

Janowiak, J. and Xie, P. (1999). "CAMS-OPI: A global satellite-rain gauge merged product for real-time precipitation monitoring applications". In: *Journal of Climate* 12(11), pp. 3335–3342.

Jolliffe, I. T. and Stephenson, D. B. (2012). *Forecast verification: a practitioner's guide in atmospheric science*. John Wiley & Sons.

Jordan, A., Krüger, F., and Lerch, S. (2017). "Evaluating probabilistic forecasts with the R package scoringRules". In: *arXiv preprint arXiv:1709.04743*.

Jury, M., Mc Queen, C., and Levey, K. (1994). "SOI and QBO signals in the African region". In: *Theoretical and Applied Climatology* 50(1), pp. 103–115.

Kafadar, K. and Spiegelman, C. H. (1986). "An alternative to ordinary qq plots: Conditional qq plots". In: *Computational Statistics & Data Analysis* 4(3), pp. 167–184.

Kalkstein, L. S., Tan, G., and Skindlov, J. A. (1987). "An evaluation of three clustering procedures for use in synoptic climatological classification". In: *Journal of climate and applied meteorology* 26(6), pp. 717–730.

Kanamitsu, M., Ebisuzaki, W., Woollen, J., Yang, S.-K., Hnilo, J., Fiorino, M., and Potter, G. (2002). "Ncep–doe amip-ii reanalysis (r-2)". In: *Bulletin of the American Meteorological Society* 83(11), pp. 1631–1643.

Karavitis, C. A., Alexandris, S., Tsesmelis, D. E., and Athanasopoulos, G. (2011). "Application of the standardized precipitation index (SPI) in Greece". In: *Water* 3(3), pp. 787–805.

Kasei, R., Diekkrüger, B., and Leemhuis, C. (2010). "Drought frequency in the Volta basin of West Africa". In: *Sustainability science* 5(1), p. 89.

Katz (1960). *Seasonal changes in gereral atmospheric circulation and long-range forecasts.* [Сезонные изменения общей цир- куляции атмосферы и долгосрочные прогнозы]. Gidrometeoizdat, Leningrad, [in Russian].

Katz, A. (1988). "Use of cross correlations in the search for teleconnections". In: *International Journal of Climatology* 8(3), pp. 241–253.

Khromov, S. and Petrosyants, M. (1994). *Meteorology and climatology*.

Kidd, C. (2001). "Satellite rainfall climatology: a review". In: *International Journal of Climatology* 21(9), pp. 1041–1066.

Kiktev, D., Kruglova, E., and Kulikova, I. (2015). "Large-scale modes of atmospheric variability. Part I. Statistical analysis and hydrodynamic modeling". In: *Russian Meteorology and Hydrology* 40(3), pp. 147–159.

Kilsby, C., Cowpertwait, P., O'connell, P., and Jones, P. (1998). "Predicting rainfall statistics in England and Wales using atmospheric circulation variables". In: *International Journal of Climatology* 18(5), pp. 523–539.

Klein, W., Lewis, B., and Enger, I. (1959). "Objective prediction of five-day mean temperatures during winter". In: *Journal of Meteorology* 16(6), pp. 672–682.

Kononova, N. (2009). *Classification of Circulation Mechanisms of the Northern Hemisphere According to BL Dzerdzeevskii*.

Kossin, J. P. and Vimont, D. J. (2007). "A more general framework for understanding Atlantic hurricane variability and trends". In: *Bulletin of the American Meteorological Society* 88(11), pp. 1767–1781.

Lang, X. (2011). "A hybrid dynamical-statistical approach for predicting winter precipitation over eastern China". In: *Acta Meteorologica Sinica* 25, pp. 272–282.

Larson, J., Zhou, Y., and Higgins, R. W. (2005). "Characteristics of landfalling tropical cyclones in the United States and Mexico: Climatology and interannual variability". In: *Journal of Climate* 18(8), pp. 1247–1262.

Lebel, T. and Ali, A. (2009). "Recent trends in the Central and Western Sahel rainfall regime (1990–2007)". In: *Journal of Hydrology* 375(1), pp. 52–64.

Lebel, T., Diedhiou, A., and Laurent, H. (2003). "Seasonal cycle and interannual variability of the Sahelian rainfall at hydrological scales". In: *Journal of Geophysical Research: Atmospheres* 108(D8).

Legg, T., Mylne, K., and Woolcock, C. (2002). "Use of medium-range ensembles at the Met Office I: PREVIN-a system for the production of probabilistic forecast information from the ECMWF EPS". In: *Meteorological Applications* 9(3), pp. 255–271.

Lemcke, C. and Kruizinga, S. (1988). "Model output statistics forecasts: three years of operational experience in the Netherlands". In: *Monthly weather review* 116(5), pp. 1077–1090.

Li, J. and Ding, R. (2011). "Temporal–spatial distribution of atmospheric predictability limit by local dynamical analogs". In: *Monthly Weather Review* 139(10), pp. 3265–3283.

Li, S. and Robertson, A. W. (2015). "Evaluation of submonthly precipitation forecast skill from global ensemble prediction systems". In: *Monthly Weather Review* 143(7), pp. 2871–2889.

Lloyd-Hughes, B. and Saunders, M. (2002). "A drought climatology for Europe". In: *International Journal of Climatology* 22(13), pp. 1571–1592.

Lopatin, V., Muravykch, A., and Gritsevich, I. (2005). "Global climate change, problems and perspectives of realisation of the Kyoto Protocol in the Russian Federation (Textbook)". In: *Russian Academy of Public Services, UNEP, WWF, Moscow [in Russian]*.

Lorenz, E. N. (1969a). "Atmospheric predictability as revealed by naturally occurring analogues". In: *Journal of the Atmospheric sciences* 26(4), pp. 636–646.

Lorenz, E. N. (1969b). "Three approaches to atmospheric predictability". In: *Bull. Amer. Meteor. Soc* 50(3454), p. 349.

Lupo, A. R., Mokhov, I. I., Akperov, M. G., Chernokulsky, A. V., and Athar, H. (2012). "A dynamic analysis of the role of the planetary-and synoptic-scale in the summer of 2010 blocking episodes over the European part of Russia". In: *Advances in Meteorology* 2012.

Madden, R. and Julian, P. (1971). "Detection of a 40–50 day oscillation in the zonal wind in the tropical Pacific". In: *Journal of the atmospheric sciences* 28(5), pp. 702–708.

Manzanas, R., Amekudzi, L., Preko, K., Herrera, S., and Gutiérrez, J. (2014). "Precipitation variability and trends in Ghana: An intercomparison of observational and reanalysis products". In: *Climatic change* 124(4), pp. 805–819.

Mariani, S., Casaioli, M., and Calza, M. (2008). *Forecast verification: a summary of common approaches and examples of application*. Università di Trento. Dipartimento di ingegneria civile e ambientale.

Marzban, C., Sandgathe, S., Lyons, H., and Lederer, N. (2009). "Three spatial verification techniques: Cluster analysis, variogram, and optical flow". In: *Weather and Forecasting* 24(6), pp. 1457–1471.

Mason, S. J. (2016). "Guidance on Verification of Operational Seasonal Climate Forecasts". In: *World Meteorological Organization. IRI Technical Report*, p. 79.

Matheson, J. E. and Winkler, R. L. (1976). "Scoring rules for continuous probability distributions". In: *Management science* 22(10), pp. 1087–1096.

Matveev, L. (1984). *Course of general meteorology*.

Mazin, I., Khrgian, A. K., and Imyanitov, I. (1989). *Handbook of clouds and cloudy atmosphere.* [Атлас облаков и облачная атмосфера], pp. 336–338.

McKee, T. B., Doesken, N. J., Kleist, J., et al. (1993). "The relationship of drought frequency and duration to time scales". In: *Proceedings of the 8th Conference on Applied Climatology*. Vol. 17(22). American Meteorological Society Boston, MA, USA, pp. 179–183.

Michaelsen, J. (1987). "Cross-validation in statistical climate forecast models". In: *Journal of Climate and Applied Meteorology* 26(11), pp. 1589–1600.

Mishra, A. K. and Singh, V. P. (2010). "A review of drought concepts". In: *Journal of hydrology* 391(1), pp. 202–216.

Mittermaier, M. and Roberts, N. (2010). "Intercomparison of spatial forecast verification methods: Identifying skillful spatial scales using the fractions skill score". In: *Weather and Forecasting* 25(1), pp. 343–354.

Mokhov, I. I., Timazhev, A. V., and Lupo, A. R. (2014). "Changes in atmospheric blocking characteristics within Euro-Atlantic region and Northern Hemisphere as a whole in the 21st century from model simulations using RCP anthropogenic scenarios". In: *Global and Planetary Change* 122, pp. 265–270.

Molteni, F., Buizza, R., Palmer, T. N., and Petroliagis, T. (1996). "The ECMWF ensemble prediction system: Methodology and validation". In: *Quarterly journal of the royal meteorological society* 122(529), pp. 73–119.

Multanovsky, B. (1933). *Basics of synoptic method implemented in long-range weather predictions.* [Основные положения синоптического метода долгосрочных прогнозов погоды].

Multanovsky, B. (1954). *Natural synoptic region.* [Естественный синоптический район]. 36(63).

Murphy, A. H. (1973). "Hedging and skill scores for probability forecasts". In: *Journal of Applied Meteorology* 12(1), pp. 215–223.

Murphy, A. H. and Winkler, R. L. (1987). "A general framework for forecast verification". In: *Monthly weather review* 115(7), pp. 1330–1338.

Murphy, A. H. and Winkler, R. L. (1992). "Diagnostic verification of probability forecasts". In: *International Journal of Forecasting* 7(4), pp. 435–455.

Murtagh, F. and Legendre, P. (2014). "Wardâs hierarchical agglomerative clustering method: which algorithms implement Wardâs criterion?" In: *Journal of Classification* 31(3), pp. 274–295.

Nachamkin, J. E., Chen, S., and Schmidt, J. (2005). "Evaluation of heavy precipitation forecasts using composite-based methods: A distributions-oriented approach". In: *Monthly Weather Review* 133(8), pp. 2163–2177.

Namias, J. (1972). "Influence of northern hemisphere general circulation on drought in Northeast Brazil". In: *Tellus* 24(4), pp. 336–343.

Naresh Kumar, M., Murthy, C., Sesha Sai, M., and Roy, P. (2012). "Spatiotemporal analysis of meteorological drought variability in the Indian region using standardized precipitation index". In: *Meteorological Applications* 19(2), pp. 256–264.

NCAR Research Applications Laboratory (2015). `verification`*: Weather Forecast Verification Utilities*. R package version 1.42.

Nicholson, S. E. (1980). "The nature of rainfall fluctuations in subtropical West Africa". In: *Monthly Weather Review* 108(4), pp. 473–487.

Nicholson, S. E. (2009). "A revised picture of the structure of the "monsoon" and land ITCZ over West Africa". In: *Climate Dynamics* 32(7), pp. 1155–1171.

Nicholson, S. E. (2013). "The West African Sahel: A review of recent studies on the rainfall regime and its interannual variability". In: *ISRN Meteorology* 2013, p. 32.

Nnamchi, H. C. and Li, J. (2011). "Influence of the South Atlantic Ocean dipole on West African summer precipitation". In: *Journal of Climate* 24(4), pp. 1184–1197.

Pachauri, R. K., Reisinger, A., et al. (2007). "Synthesis report". In: *Fifth Assessment Report of the Intergovernmental Panel on Climate Change*, pp. 151–165.

Pachauri, R. K., Allen, M., Barros, V., Broome, J., Cramer, W., Christ, R., Church, J., Clarke, L., Dahe, Q., Dasgupta, P., et al. (2014). *Climate Change 2014: Synthesis Report. Contribution of Working Groups I, II and III to the Fifth Assessment Report of the Intergovernmental Panel on Climate Change*. IPCC, Geneva.

Pagava, S., Aristov, N., Blyumina, L., and Turketti, Z. (1966). *Fundamentals of the Synoptic Method of Seasonal Weather Forecasting*.

Palmén, E. H. and Newton, C. W. (1969). *Atmospheric circulation systems: their structure and physical interpretation*. Vol. 13. Academic press.

Panofsky, H. A., Brier, G. W., and Best, W. H. (1958). *Some application of statistics to meteorology*. Earth, Mineral Sciences Continuing Education, College of Earth, and Mineral Sciences, Pennsylvania State University.

Parker, D. J. (2017). *Meteorology of tropical West Africa: The forecasters' handbook*. John Wiley & Sons.

Pelly, J. L. (2001). "The predictability of atmospheric blocking." PhD thesis. University of Reading.

Petoukhov, V., Petri, S., Rahmstorf, S., Coumou, D., Kornhuber, K., and Schellnhuber, H. J. (2016). "Role of quasiresonant planetary wave dynamics in recent boreal spring-to-autumn extreme events". In: *Proceedings of the National Academy of Sciences*, p. 201606300.

Petoukhov, V., Petri, S., Rahmstorf, S., and Schellnhuber, H. J. (2013). "Quasiresonant amplification of planetary waves and recent Northern Hemisphere weather extremes". In: *Proceedings of the National Academy of Sciences* 110(14), pp. 5336–5341.

Polo, I., Rodrıguez-Fonseca, B., Losada, T., and Garcıa-Serrano, J. (2008). "Tropical Atlantic variability modes (1979–2002). Part I: Time-evolving SST modes related to West African rainfall". In: *Journal of Climate* 21(24), pp. 6457–6475.

Preisendorfer, R. (1988). "Principal component analysis in meteorology and oceanography". In: *Elsevier Sci. Publ.* 17, p. 425.

Radanovics, S., Vidal, J.-P., and Sauquet, E. (2018). "Spatial verification of ensemble precipitation: an ensemble version of SAL". In: *Weather and Forecasting* 33(4), pp. 1001–1020.

Raftery, A. E., Gneiting, T., Balabdaoui, F., and Polakowski, M. (2005). "Using Bayesian model averaging to calibrate forecast ensembles". In: *Monthly weather review* 133(5), pp. 1155–1174.

Richman, M. B. and Lamb, P. J. (1985). "Climatic pattern analysis of three-and seven-day summer rainfall in the central United States: Some methodological considerations and a regionalization". In: *Journal of Climate and Applied Meteorology* 24(12), pp. 1325–1343.

Roberts, N. M. and Lean, H. W. (2008). "Scale-selective verification of rainfall accumulations from high-resolution forecasts of convective events". In: *Monthly Weather Review* 136(1), pp. 78–97.

Rockström, J., Karlberg, L., Wani, S. P., Barron, J., Hatibu, N., Oweis, T., Bruggeman, A., Farahani, J., and Qiang, Z. (2010). "Managing water in rainfed agriculture—The need for a paradigm shift". In: *Agricultural Water Management* 97(4), pp. 543–550.

Ropelewski, C. F. and Halpert, M. S. (1987). "Global and regional scale precipitation patterns associated with the El Niño/Southern Oscillation". In: *Monthly weather review* 115(8), pp. 1606–1626.

Roulston, M. and Smith, L. A. (2003). "Combining dynamical and statistical ensembles". In: *Tellus A* 55(1), pp. 16–30.

Rowell, D. (2001). "Teleconnections between the tropical Pacific and the Sahel". In: *Quarterly Journal of the Royal Meteorological Society* 127(575), pp. 1683–1706.

Rowell, D., Booth, B. B., Nicholson, S. E., and Good, P. (2015). "Reconciling past and future rainfall trends over east Africa". In: *Journal of Climate* 28(24), pp. 9768–9788.

Rowell, D., Folland, C. K., Maskell, K., and Ward, M. N. (1995). "Variability of summer rainfall over tropical North Africa (1906–92): Observations and modelling". In: *Quarterly Journal of the Royal Meteorological Society* 121(523), pp. 669–704.

Rugg, A., Foltz, G. R., and Perez, R. C. (2016). "Role of Mixed Layer Dynamics in Tropical North Atlantic Interannual Sea Surface Temperature Variability". In: *Journal of Climate* 29(22), pp. 8083–8101.

Runge, J., Donner, R. V., and Kurths, J. (2015). "Optimal model-free prediction from multivariate time series". In: *Physical Review E* 91(5), p. 052909.

Saha, S., Moorthi, S., Wu, X., Wang, J., Nadiga, S., Tripp, P., Behringer, D., Hou, Y.-T., Chuang, H.-y., Iredell, M., et al. (2014). "The NCEP climate forecast system version 2". In: *Journal of Climate* 27(6), pp. 2185–2208.

Saji, N., Goswami, B., Vinayachandran, P., and Yamagata, T. (1999). "A dipole mode in the tropical Indian Ocean". In: *Nature* 401(6751), pp. 360–363.

Schuhen, N., Thorarinsdottir, T. L., and Gneiting, T. (2012). "Ensemble model output statistics for wind vectors". In: *Monthly weather review* 140(10), pp. 3204–3219.

Shakina, N. and Ivanova, A. (2010). "The blocking anticyclones: the state of studies and forecasting". In: *Russian Meteorology and Hydrology* 35, pp. 721–730.

Shashkin, V. and Tolstykh, M. (2014). “Inherently mass-conservative version of the semi-Lagrangian absolute vorticity (SL-AV) atmospheric model dynamical core”. In: *Geoscientific Model Development* 7(1), pp. 407–417.

Sheffield, J., Wood, E. F., Chaney, N., Guan, K., Sadri, S., Yuan, X., Olang, L., Amani, A., Ali, A., Demuth, S., et al. (2014). “A drought monitoring and forecasting system for sub-Sahara African water resources and food security”. In: *Bulletin of the American Meteorological Society* 95(6), pp. 861–882.

Shukla, J. (1981). “Dynamical predictability of monthly means”. In: *Journal of the Atmospheric Sciences* 38(12), pp. 2547–2572.

Shver, T. (1976). *Atmospheric precipitation on the terrotory of USSR.* [Атмосферные осадки на территории СССР]. Gidrometeoizdat, Leningrad, [in Russian].

Siebert, A. B. and Ward, M. N. (2011). “Future occurrence of threshold-crossing seasonal rainfall totals: Methodology and application to sites in Africa”. In: *journal of applied meteorology and climatology* 50(3), pp. 560–578.

Siegmund, J., Bliefernicht, J., Laux, P., and Kunstmann, H. (2015). “Toward a seasonal precipitation prediction system for West Africa: Performance of CFSv2 and high-resolution dynamical downscaling”. In: *Journal of Geophysical Research: Atmospheres* 120(15), pp. 7316–7339.

Singh, N. P., Bantilan, C., and Byjesh, K. (2014). “Vulnerability and policy relevance to drought in the semi-arid tropics of Asia–A retrospective analysis”. In: *Weather and Climate Extremes* 3, pp. 54–61.

Sivakumar, M. (1992). “Climate change and implications for agriculture in Niger”. In: *Climatic change* 20(4), pp. 297–312.

Slingo, J. and Palmer, T. (2011). “Uncertainty in weather and climate prediction”. In: *Phil. Trans. R. Soc. A* 369(1956), pp. 4751–4767.

Sloughter, J. M. L., Raftery, A. E., Gneiting, T., and Fraley, C. (2007). “Probabilistic quantitative precipitation forecasting using Bayesian model averaging”. In: *Monthly Weather Review* 135(9), pp. 3209–3220.

Sohn, S.-J., Min, Y.-M., Lee, J.-Y., Tam, C.-Y., Kang, I.-S., Wang, B., Ahn, J.-B., and Yamagata, T. (2012). “Assessment of the long-lead probabilistic prediction for the Asian summer monsoon precipitation (1983–2011) based on the APCC multimodel system and a statistical model”. In: *Journal of Geophysical Research: Atmospheres* 117(D4).

Stockdale, T. N., Anderson, D. L., Alves, J. O. S., and Balmaseda, M. A. (1998). “Global seasonal rainfall forecasts using a coupled ocean–atmosphere model”. In: *Nature* 392(6674), p. 370.

Sultan, B., Janicot, S., and Diedhiou, A. (2003). “The West African monsoon dynamics. Part I: Documentation of intraseasonal variability”. In: *Journal of Climate* 16(21), pp. 3389–3406.

Svoboda, M., Hayes, M., and Wood, D. (2012). “Standardized precipitation index user guide”. In: *World Meteorological Organization Geneva, Switzerland*.

Tanaka, M., Weare, B. C., Navato, A. R., and Newell, R. E. (1975). “Recent African rainfall patterns”. In: *Nature* 255, pp. 201–203.

Temperton, C., Hortal, M., and Simmons, A. (2001). "A two-time-level semi-Lagrangian global spectral model". In: *Quarterly Journal of the Royal Meteorological Society* 127(571), pp. 111–127.

Thom, H. C. (1958). "A note on the gamma distribution". In: *Monthly Weather Review* 86(4), pp. 117–122.

Thomas, T. W. (2004). *Desert meteorology*.

Tolstykh, M., Diansky, N., Gusev, A., and Kiktev, D. (2014). "Simulation of seasonal anomalies of atmospheric circulation using coupled atmosphere-ocean model". In: *Izvestiya. Atmospheric and Oceanic Physics* 50(2), p. 111.

Tracton, M. S. and Kalnay, E. (1993). "Operational ensemble prediction at the National Meteorological Center: Practical aspects". In: *Weather and Forecasting* 8(3), pp. 379–398.

Trenberth, K. E. and Stepaniak, D. P. (2001). "Indices of el Niño evolution". In: *Journal of Climate* 14(8), pp. 1697–1701.

Ulbrich, U. and Christoph, M. (1999). "A shift of the NAO and increasing storm track activity over Europe due to anthropogenic greenhouse gas forcing". In: *Climate dynamics* 15(7), pp. 551–559.

Verdin, A., Funk, C., Rajagopalan, B., and Kleiber, W. (2016). "Kriging and local polynomial methods for blending satellite-derived and gauge precipitation estimates to support hydrologic early warning systems". In: *IEEE Transactions on Geoscience and Remote Sensing* 54(5), pp. 2552–2562.

Volodin, E. (2011). "On the nature of some super extreme anomalies summer temperature". In: *Analysis of Weather Anomaly Conditions over Russia in Summer of 2010*, pp. 48–57.

Wallace, J. M. and Gutzler, D. S. (1981). "Teleconnections in the geopotential height field during the Northern Hemisphere winter". In: *Monthly Weather Review* 109(4), pp. 784–812.

Wang, B., Wu, R., and Fu, X. (2000). "Pacific–East Asian teleconnection: how does ENSO affect East Asian climate?" In: *Journal of Climate* 13(9), pp. 1517–1536.

Wang, C. and Enfield, D. B. (2001). "The tropical Western Hemisphere warm pool". In: *Geophysical research letters* 28(8), pp. 1635–1638.

Wang, X. and Bishop, C. (2005). "Improvement of ensemble reliability with a new dressing kernel". In: *Quarterly Journal of the Royal Meteorological Society* 131(607), pp. 965–986.

Wang, Hung, M.-P., Weaver, S. J., Kumar, A., and Fu, X. (2014). "MJO prediction in the NCEP Climate Forecast System version 2". In: *Climate dynamics* 42(9), pp. 2509–2520.

Ward, M. N. (1998). "Diagnosis and short-lead time prediction of summer rainfall in tropical North Africa at interannual and multidecadal timescales". In: *Journal of Climate* 11(12), pp. 3167–3191.

Weisheimer, A. and Palmer, T. (2014). "On the reliability of seasonal climate forecasts". In: *Journal of The Royal Society Interface* 11(96), p. 20131162.

Wen, M., Yang, S., Kumar, A., and Zhang, P. (2009). "An analysis of the large-scale climate anomalies associated with the snowstorms affecting China in January 2008". In: *Monthly Weather Review* 137(3), pp. 1111–1131.

Wernli, H., Paulat, M., Hagen, M., and Frei, C. (2008). "SALâA novel quality measure for the verification of quantitative precipitation forecasts". In: *Monthly Weather Review* 136(11), pp. 4470–4487.

Wilby, R. L. and Wigley, T. (2000). "Precipitation predictors for downscaling: observed and general circulation model relationships". In: *International Journal of Climatology* 20(6), pp. 641–661.

Wilks, D. S. (2011). *Statistical Methods in the Atmospheric Sciences*. 3rd. Academic Press, Oxford.

Williams, C. (2016). "Statistical methods for post-processing ensemble weather forecasts". In:

Williams, C. and Hanan, N. (2011). "ENSO and IOD teleconnections for African ecosystems: evidence of destructive interference between climate oscillations". In: *Biogeosciences* 8(1), p. 27.

Wolter, K. and Timlin, M. S. (2011). "El Niño/Southern Oscillation behaviour since 1871 as diagnosed in an extended multivariate ENSO index (MEI. ext)". In: *International Journal of Climatology* 31(7), pp. 1074–1087.

Yao, C., Qian, W., Yang, S., and Lin, Z. (2010). "Regional features of precipitation over Asia and summer extreme precipitation over Southeast Asia and their associations with atmospheric–oceanic conditions". In: *Meteorology and Atmospheric Physics* 106(1), pp. 57–73.

Yeh, S.-W., Kug, J.-S., Dewitte, B., Kwon, M.-H., Kirtman, B. P., and Jin, F.-F. (2009). "El Niño in a changing climate". In: *Nature* 461(7263), pp. 511–514.

Yuan, X., Wood, E. F., Luo, L., and Pan, M. (2011). "A first look at Climate Forecast System version 2 (CFSv2) for hydrological seasonal prediction". In: *Geophysical research letters* 38(13).

Zanina, A. (1960). *Climate USSR, Caucasus.* [Климат СССР, Кавказ]. 2.

Zanina, A. (1968). *Climate USSR, Far East.* [Климат СССР, Дальний Восток]. 6.

Zebiak, S. E. (1993). "Air–sea interaction in the equatorial Atlantic region". In: *Journal of Climate* 6(8), pp. 1567–1586.

Zverev, A. (1977). *Synoptic meteorology*.

List of Figures

List of Tables

Acknowledgements

What is luck, and how is it connected with goals and achievements? I believe that luck is a result of hard work and plenty of thinking, dreaming and working to achieve goals - only after that you get luck and success. You set a goal and find the opportunities, people, time and motivation to go towards it, or just skip it. Of course, skipping is the easiest choice, but it doesn't bring you as much satisfaction as achieving your goal. There was no luck without working on it in my life, and this thesis is a result of many years of hard work not only from my side, but also many people more or less were involved into this. And in this acknowledgement I would like to thank all of them during my Ph.D. studies in both countries for the kindness, support, tolerance, discussions and of course, supervisory help.

The story began in Russia; it was sort of a motivation and a good "school" showed me all the good and bad things about being a Ph.D. student there. To be honest, the story could have finished in Russia, but fortunately, due to my supervisor, Reik Donner, and the support of DAAD, I changed directions and continued in Germany, at PIK and then at ATB (both in Potsdam).

I would like to first thank my two research supervisors - Prof. Reik Donner (PIK, Potsdam) and Prof. Henning Rust (Freie Universität Berlin) - who guided and supported me in order to finish this work. Warm acknowledgements must be sent to Prof. Dr. Thomas Amon (ATB, Potsdam), for his tolerance, patience and understanding due to my work on two projects at the same time.

During my stay at PIK and ATB I had the opportunity to get acquainted with many nice, smart, inspired and blessed people. I am thankful to everybody who shared ideas for current work, suggestions and simply a positive mood with me at different stages. At PIK I had a wonderful office in the middle of the forest, with lot of space for work, interesting meetings, tasty coffee and some yoga practise in between. For more than a year, my office in A56 became my home. Many dark evenings were spent there with colleagues, occupied by discussions and work. I would like to thank Prof. Dr. Jürgen Kurths, Prof. Dr. Elena Surovyatkina, Dr. Norbert Marwan (for helping with settings, plenty of things on my Mac, and solving unusual code problems in Matlab), Dr. Veronica Stolbova, Dr. Lubov Tupikina (for nice Russian atmosphere at PIK and for space/room/flatsharing and being helpful with questions all the time), Dr. Deniz Eroglu and Merve Eroglu (for flat sharing and nice tasty food, miss you very much), Dr. Efi Rousi (being so positive, helpful and kind, and also being a first meteorologist whom I met in Germany :)), Dr. Chiranjit Mitra (for lots of discussions

on different subjects and listening all my spontaneous explanations of my ideas relating to my thesis and plans for the future), Dr. Jasper Franke (for helping with decoding "someone's" (we both know who's) hand writing and able to discuss diverse questions in person and by Facebook messenger), Dr. Jonatan Siegmund, Nikoo Ekhtiari (for our nice girls talks), Dr. Catrin Kirsch, Dr. Catrin Ciemer (for being always ready to go out and support all fun ideas), Jaqueline Lekscha, Dr. Paul Schultz, Dr. Sabine Auer, secretaries of RD4 Gabi Pilz and Till Hollmann.
I would like also to thank my colleges at ATB, the whole department of Engineering for Livestock Management, and offer especially warm acknowledgements to Dr. Marcel Koenig, Dr. Sabrina Hempel, David Janke, among others for support.
My special regards have to be sent to Leipzig (TROPOS) to Dr. Oswald Knoth for an introduction to CFD modelling, weather processes modelling and many lectures about Fortran, fluid dynamics, maths, and of course, an opportunity to work 24 hours support with ASAM model. While that doesn't have a strong connection to this thesis, it helped me to better understand weather process modelling.
I should also thank Dr. Michael Hoff from German Weather Service (DWD) for helping to understand spatial verification methods, nice discussions, and tolerance in answering huge number of my questions in the last stages of writing this thesis as well as support throughout.
Many, many, many thanks and regards to my family and friends for your support and understanding. My best regards to my second mum-Professor Dr. Alla Arefyeva - for huge support, inspiration, ideas and helping to finish my Ph.D. Another person (and not only person) who help and support me all this time is my husband Geeshan and my lovely dog Manon (actually, walking with Manon gave me lots of inspiration, helped to concentrate and be able to work more productively), and my regards to my parents, parents-in-law, aunts Alla Ushakova and Raina Mingazova, and to my Oma (Nazira Mingazova), who passed away and couldn't see the moment of my defence, and whom I miss very much. My lovely cousin Eduard Khodzhaev and very good friend Dilya Slamova, who also helped me to go through all difficulties and supported me with all my decisions during my Ph.D. studies in both countries.
I send a special thanks to Russia to Prof. Dr. Mikhail Tolstykh, Prof. Dr. Vladimir Ivanov and others from the Hydrometeorological Centre of Russia for support during several working years there.
There are also some numbers of people who particularly deserve a mention, my regards to editor Sarah Knudsen, Dr. Efi Rousi, and Abdulla Hafiz for helping with reading my thesis and nice comments.
And of course, my thanks to the DAAD foundation, and especially Mrs. Elena Schmid and Dr. Thomas Prahl for the opportunity to work in Germany and for scholarship support during 2015-2016.

Eidesstattliche Erklärung

Hiermit erkläre ich dass ich die vorliegende Dissertation selbstständig verfasst und keine anderen als die angegebenen Hilfsmittel genutzt habe. Alle wörtlich oder inhaltlich übernommenen Stellen habe ich also solche gekennzeichnet. Ich versichere außerdem, dass ich diese Arbeit nur in diesem und keinem anderen Promotionsverfahren eingereicht habe. Diesem sind keine gescheiterten Promotionsverfahren vorausgegangen.

Dilya Willink